EVANESCENT WAVE AND VIDEO MICROSCOPY METHODS FOR DIRECTLY MEASURING INTERACTIONS BETWEEN SURFACE-IMMOBILIZED BIOMOLECULES

A Dissertation

by

WILLIAM NEIL EVERETT

Submitted to the Office of Graduate Studies of
Texas A&M University
in partial fulfillment of the requirements for the degree of

DOCTOR OF PHILOSOPHY

August 2007

Major Subject: Materials Science and Engineering

EVANESCENT WAVE AND VIDEO MICROSCOPY METHODS FOR DIRECTLY MEASURING INTERACTIONS BETWEEN SURFACE-IMMOBILIZED BIOMOLECULES

A Dissertation

by

WILLIAM NEIL EVERETT

Submitted to the Office of Graduate Studies of
Texas A&M University
in partial fulfillment of the requirements for the degree of

DOCTOR OF PHILOSOPHY

Approved by:

Co-chairs of Committee,	Michael A. Bevan
	Hung-Jue Sue
Committee Members,	Paul S. Cremer
	Alan R. Parrish
Head of Department,	Joseph H. Ross, Jr.

August 2007

Major Subject: Materials Science and Engineering

ABSTRACT

Evanescent Wave and Video Microscopy Methods for Directly Measuring Interactions between Surface-Immobilized Biomolecules. (August 2007)

William Neil Everett, B.S., Texas A&M University;

M.S., Texas A&M University

Co-Chairs of Advisory Committee: Dr. Michael A. Bevan
Dr. Hung-Jue Sue

Spatial and temporal tracking of passively diffusing functionalized colloids continues to be an improving and auspicious approach to measuring weak specific and non-specific biomolecular interactions. Evidence of this is given by the recent increase in published studies involving the development and implementation of these methods. The primary aim of the work presented in this dissertation was to modify and optimize video microscopy (VM) and total internal reflection microscopy (TIRM) methods to permit the collection of equilibrium binding and sampling data from interaction of surface-immobilized biomolecules. Supported lipid bilayers were utilized as model systems for functionalizing colloid and wall surfaces. Preliminary results measuring calcium-specific protein-protein interactions between surface immobilized cadherin fragments demonstrate the potential utility of this experimental system and these methods. Additionally, quantum dot-modified colloids were synthesized and evanescent wave-excited luminescence from these particles was used to construct potential energy profiles. Results from this work demonstrate that colloids can be used as ultra-sensitive probes of equilibrium interactions between biomolecules, and specialized probes, such

as those modified with quantum dots, could be used in a spectral multiplexing mode to simultaneously monitor multiple interactions.

To my family, past and present

ACKNOWLEDGMENTS

There are numerous people I would like to thank for helping me in this endeavor. First, I need to acknowledge my co-advisors, Drs. Sue and Bevan, for their guidance through this process. Thanks to Dr. Sue, I had the opportunity to work in Singapore as a research scientist in a government lab for one year. This was a valuable experience for me, both scientifically and culturally. When I returned, Dr. Sue gave me the freedom to pursue nearly any research avenue down which my interests took me. By financially supporting me as I worked with Dr. Bevan, he allowed me to find science I was truly interested in and on which I will probably base my entire academic career. I also have to thank Dr. Bevan for taking a chance on me and allowing me to work in his lab. I feel lucky to have been mentored by him in colloidal science, and I'm glad to have been able to gain perspective into his research philosophy. I look forward to many years of collaborative work as I go my separate way.

I also need to thank everyone in my two labs. You have all been instrumental in getting me through the tough times and celebrating the successes. I need to give a special thanks to people in the Bevan lab for listening to all of my ridiculous ideas and helping me solve complex experimental problems. This dissertation is much better than it would have been without your input.

I'd like to thank my family for all of their support over the years. I am who I am because of you. As I grew up, you fostered my scientific interests and were always there to ensure that I place academic work above nearly everything else.

Finally, I need to thank my wife, Sarah, who stood by me as I completed this degree. She has been incredibly thoughtful and patient throughout: me leaving her behind for one year to work on the other side of the planet, living nearly 2 hours apart during the remainder of my Ph.D., and the inevitability of me pursuing a post-doctoral position somewhere far from her for at least another year. She is truly my rock, and I will never forget her sacrifices.

TABLE OF CONTENTS

Page

Page

Page

LIST OF FIGURES

FIGURE Page

FIGURE Page

FIGURE Page

FIGURE Page

FIGURE Page

FIGURE Page

FIGURE Page

FIGURE Page

FIGURE Page

LIST OF TABLES

1. INTRODUCTION

1.1 Significance, Objectives, and Outcomes

The experimental measurement of intermolecular forces between biomolecules is an important and longstanding problem in biophysics that has been approached through the development or adaptation of manifold techniques. Generally speaking, this collection of approaches can be subdivided into three mutually exclusive categories based on the type of force or energy gauge utilized and accessible information.[1] Probe methods, for instance, externally manipulate the separation between apposing biomolecule-modified substrates in order to directly quantify interactions (e.g., binding and bond rupture forces, dissociation constants) via displacements of actual (e.g., atomic force microscopy cantilevers) or effective (e.g., optical traps, magnetic tweezers) springs.[2,3] On the other hand, spectroscopic techniques quantify interactions between soluble and surface-bound species by measuring changes in interfacial optical or resonance signatures (e.g., fluorescence, refractive index, oscillation frequency) to indirectly obtain nonintrusive, statistically significant equilibrium binding data with imaging capabilities.[4,5] The third distinct measurement type—the one utilized throughout this work—involves passively monitoring the diffusive behavior of biomolecularly functionalized Brownian colloids as they sample equilibrium positions proximal to neighboring surfaces, also bearing biomolecules, in order to characterize either long-range interactions, tethered chain mechanics, or binding lifetimes.[6,7]

This dissertation follows the style of *Journal of Chemical Physics*.

Colloidal interactions are controlled by potentials on the scale of thermal energy, kT, which is the range wherein many important specific and non-specific biological interactions reside. Coincidentally, because of the importance of understanding colloidal interactions throughout many existing and emerging areas of science and technology (e.g., coatings, foods, photonics, sensors, etc.), a well-established and extensive theoretical framework is available to describe the forces that influence Brownian colloids—that is, self-diffusing particles.

The overarching objectives of this research, therefore, are to extend, develop, and refine methods that exploit the use of self-diffusing colloidal probes to measure weak interactions between surface-immobilized biomolecules and other biomedically relevant macromolecules. The key results from this dissertation include:

- Utilizing total internal reflection microscopy (TIRM) to measure non-specific protein-protein and protein-synthetic macromolecule interactions
- Development of a semi-empirical method to identify surface heterogeneity using diffusing probes
- Demonstration of a combinatorial approach to measuring colloidal (or biomolecular) interactions using QD-modified particles in a spectral multiplexing mode
- Examination and fine-tuning of several protein immobilization strategies, such as the use of functionalized supported lipid bilayers (SLBs), for diffusing colloidal probe applications

- Identification of the mediating factors that influence fusion, neck formation, and lipid exchange between two apposing SLBs
- Evaluation of PEGylated lipid bilayer stability using TIRM and video microscopy (VM) methods
- Assessment of criteria and development of protocols to yield particles with uniform surfaces that contain negligible defects
- Preliminary measurements of specific calcium-mediated protein-protein interactions via (i) pair-potentials from VM particle-particle analyses and (ii) measured ensemble TIRM particle-wall potential energy profiles.

The colloidal techniques discussed herein exploit natural gauges for time (a^2/D), energy (kT), force (fN), and length (nm) when interrogating biomolecular interactions. The use of these gauges is motivated by the capabilities of existing techniques employed for such measurements. To date, the successful implementation of diffusing colloidal probes is by far the most sensitive measure available to interrogate forces between immobilized biomolecules, because their interactions are governed by energies on the scale of kT. The experimental section in this dissertation will outline, in greater detail, how our diffusing probe approaches have been developed, whereas this introduction merely serves to compare and contrast preexisting force/energy measurement methods with diffusing colloidal probe measurements from video microscopy and TIRM data.

1.2 Background

Although intermolecular interactions between biomolecules arise from the same forces that dictate interactions between all molecules, a “biological interaction” is

typically much different from an ordinary chemical reaction/bond. This is due, in part, to the exhibited hierarchy of self-assembling structures in biological systems that arises from a higher level of complexity. These structures range from vitamins and proteins to membranes and cells. Furthermore, biological interactions are governed by competing interactions, feedback loops, regulatory mechanisms, and branching pathways.[1,2]

Biological interactions are also never at thermodynamic equilibrium, and are not, rigorously speaking, closed systems. Experimental data is usually collected from processes in isolation, but *in vivo*, these are coupled to other interactions.[1,2] Therefore, establishing an appropriate and realistic experimental construct is crucial for extracting meaningful and useful data on biological interactions. An enormous amount of attention has been given to this general problem in the last two decades, especially since the advent of scanning probe techniques for measuring weak interactions. Note that the term "weak" is only intended to convey the sense that most biological interactions are not at a magnitude to be accurately measured through conventional mechanical methods—or even with the methods described below, for that matter. As a terminology, "weak" and "strong" interactions are subjectively defined on scales relative to each other or against the lowest resolution attainable with the experimental technique used to measure the interaction. In this dissertation, we refer to "weak" as energies on the order of kT, because larger energies ($>10kT$) are not measurable with our methods, which is explained in a later section. This introduction serves simply to outline several of these well-established approaches and how they have been utilized to collect force and energetic data from biological interactions.

Because of spatial complexity, the separation-dependent potential between two biomolecules is also not accurately represented by regular vdW and/or electrostatic potentials. Figure 1.1 is a plot of generic interactions that can exist between interacting macromolecules. Although no single system will likely display all of these characteristics combined into one single potential, many display a combination of many of these forms. For instance, cadherin interactions, under a columbic screening condition, have been shown to exhibit a short-range oscillatory biospecific-type potential in the presence of Ca^{2+}. Since the features (oscillatory wavelength) of this potential are on the length scale of a fraction of the entire molecule, some methods, as will be shown, are better suited to exploring these types of potentials. Yet, weaknesses of all methods require that complimentary approaches be employed.

1.2.1 Mechanically Operated Probe Techniques

To measure small forces between biomolecules, atomic force microscopy[8] employs a cantilever with a spring constant as low as 0.01N/m and a functionalized tip attached to the bottom. The tip interacts with the underlying functionalized substrate and can be extremely sharp, having a radius of curvature of <5nm, or made to distribute the applied load through the use of micron-sized colloidal particles[9] mounted to the bottom of the cantilever (Figure 1.2). The maximum reliable force resolution achievable with AFM is on the order of tens of pN, but AFM can be used to map out topographical features less than 1nm in size, which can be of enormous benefit in biological research.

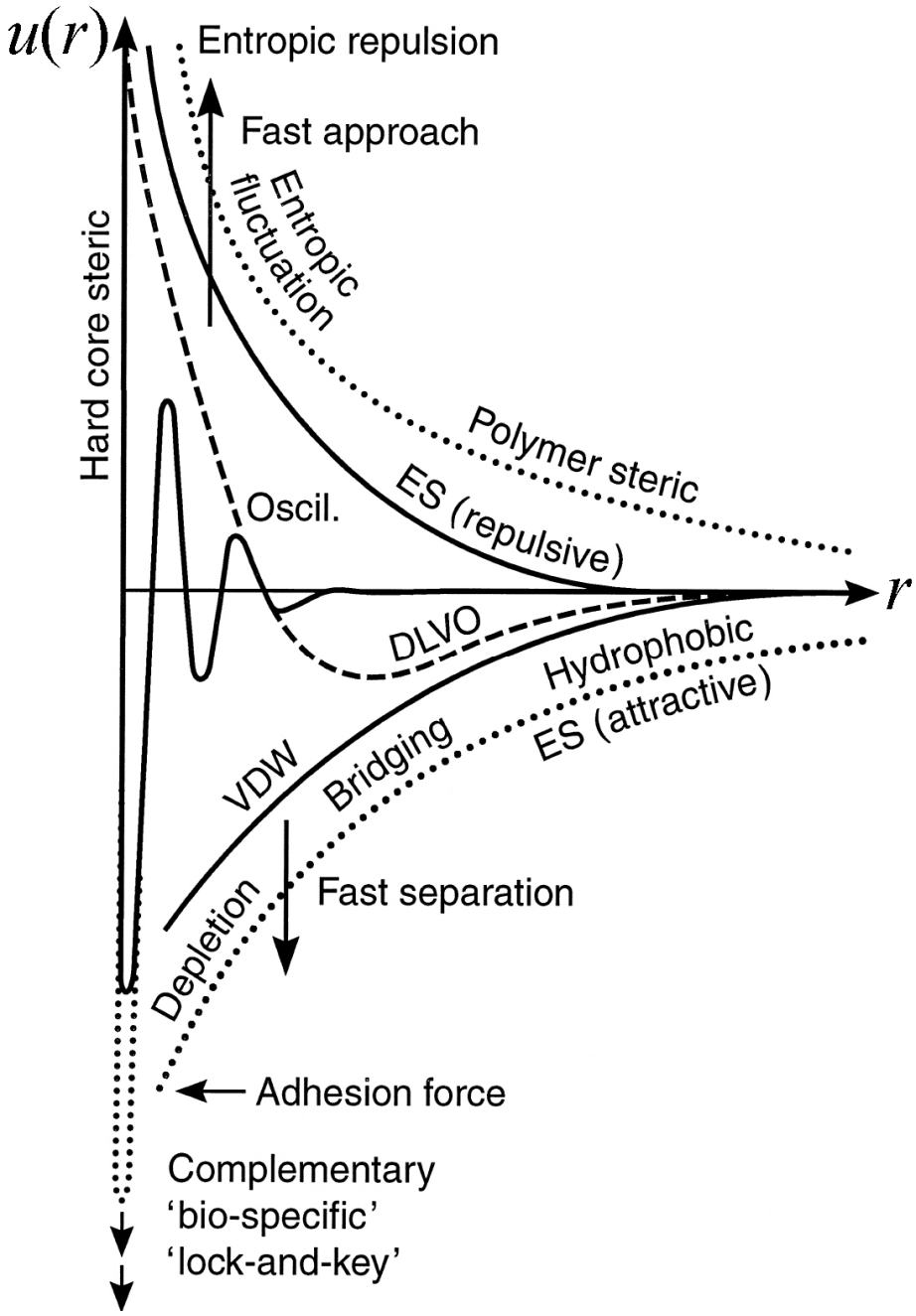

Figure 1.1. Plot of potentials that can exist for attractive and repulsive systems as a function of separation, *r*. The terms "fast approach" and "fast separation" refer to experimental conditions wherein surfaces are rapidly translated. In this work, the approach and separation rates are dictated by particle size and separation-dependent low-*Re* hydrodynamic dissipation.

Typically, the displacement of an AFM cantilever is monitored by measuring a calibrated change in incident angle of a laser beam reflected off of the top surface of the cantilever and onto a photodiode array, based on a "known" displacement applied by a piezoelectric scantube. Note that thermal drift is one drawback that accounts for a reduced accuracy in knowing the actual vertical displacement applied by the scantube. The spring stiffness of the cantilever is calibrated by displacing the tip with the scantube and measuring its deflection. Despite the promise of extremely high lateral and vertical spatial resolution, the accuracy of AFM is severely limited when measuring forces of soft matter due to thermal drift, variation in local composition and geometry of surfaces, and uncertainty in the accuracy of measured forces and displacements at separations >10nm. For comparison, TIRM and other diffusing probe techniques operate within the noise of AFM data.

The surface forces apparatus (SFA),[10,11] developed by Tabor, Winterton, and Israelachvili, is used to measure separation-dependent forces at a resolution of 10nN between two curved surfaces (typically mica) held at 90º to each other. The force is gauged with cantilevered springs, and optical interferometry is used to measure absolute separations to within to 2Å. Compared with AFM, SFA is more ideally suited to measuring surface-surface interactions and accurately collects long-range force data due its exquisite spatial resolution in the z-direction and lack of vulnerability to thermal drift. SFA is not, however, practically capable of spatially resolving lateral features below approximately 5μm. Therefore, analysis of experimental data normally assumes a uniform surface. Like AFM, SFA can collect data on bond rupture forces, dissociation

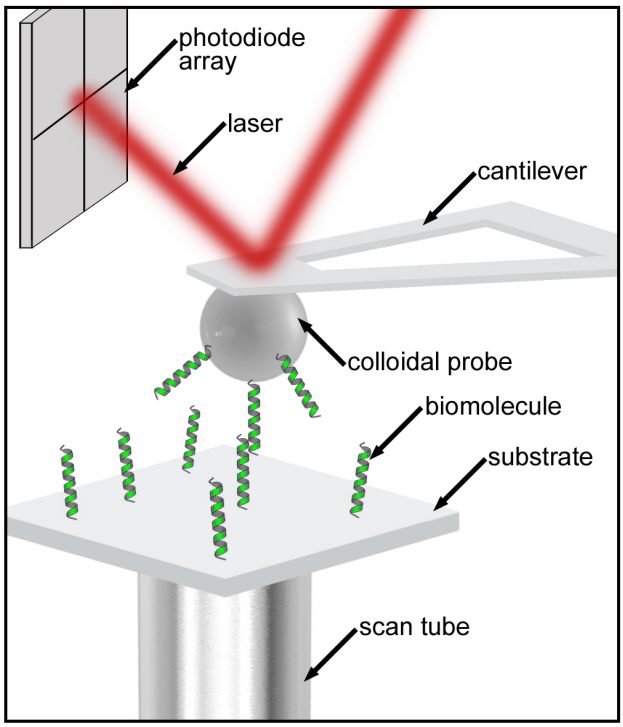

Figure 1.2. Schematic of AFM using a colloidal probe for a tip. Apposing surfaces can be modified with biomolecules, and the cantilever used as a gauge to study separation-dependent forces.

kinetics, and separation-dependent forces,[12] yet these experimental systems are incapable of creating a realistic environment, wherein biomolecules are not held in proximity for long-time durations but are constantly sampling positions at multiple separations relative to the neighbors they are interacting with.

The bioforce probe (BFP),[13] or micropipette aspiration (MPA), measures the forces between (i) a cell or giant vesicle and another cell or vesicle and (ii) functionalized microparticles and a cell, vesicle, or another functionalized microparticle (Figure 1.3). The force transducer is an elastically deformable vesicle or red blood cell, which is translated with the suction from a tip of a glass pipette. The membrane tension, intersurface force, and total interaction energy are found through micromechanical

analysis of the measured global geometries of the deformed membranes. When the two compliant membranes adhere to each other, they will distend as the aspirated portions are retracted. When the bond is ruptured, the membranes return to their spherical, undistorted shapes. Force can be varied by simply applying different gauge pressures to the interior of the micropipette. The resulting spring constants approach a resolution of μN/m. Moreover, with the capability to measure small distortions in the shape of an aspirated membrane, forces can be measured from 1μN down to 100nN, which gives the BFP method the largest range of force sensitivity of all of the methods presented here. Results from a study of cadherin bond rupture forces using the BFP are presented in Figure 1.3.[14] Bond lifetimes and frequencies are experimentally determined through multiple sampling events. Worth mentioning is one crucial drawback to these types of experiments: surface properties may change as surfaces are adhered and broken apart repeatedly. This limitation is normally handled by examining the trend in the data as a function of sample number, but the problem may still exist.

We now turn our focus towards "apparent" or pseudo springs. Under the right conditions, light brought to a diffraction-limited focus will form a radiation gradient that can achieve a stable 3D trap for dielectric objects such as colloidal particles. By steering the beam using optics, the trapped colloid will also translate along with the optical potential well. This is the foundation of an instrument called optical tweezers or an optical trap. Forces can be calibrated against the viscous drag of the surrounding medium, since low-*Re* conditions provide exact hydrodynamic solutions. Alternatively, the versatility and sensitivity of the optical trap is greatly enhanced if the force vs.

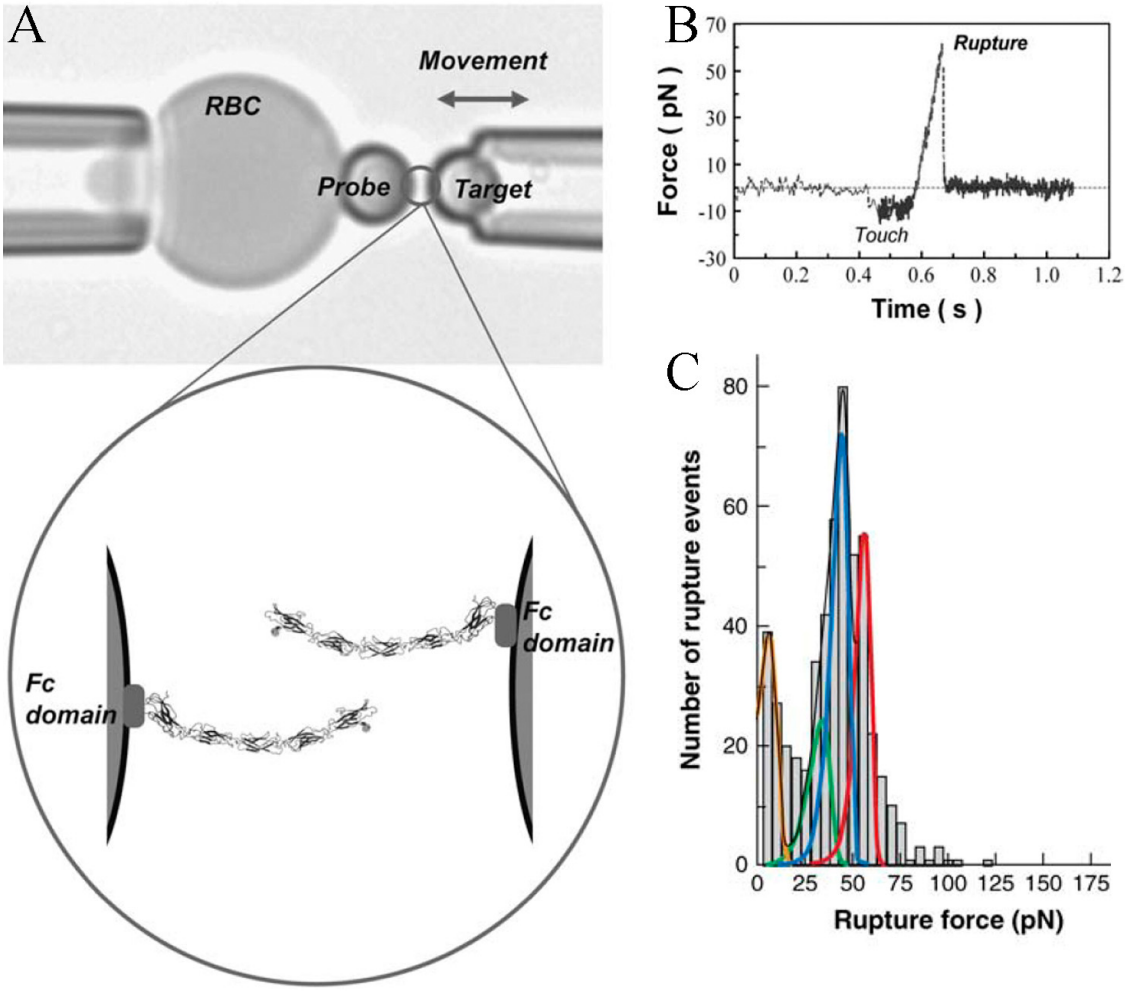

Figure 1.3. (A) Microscopy image of a BFP setup, with a red blood cell (RBC) used as the transducer membrane. Cadherin bond rupture forces (B and C) were studied through multiple approach and separation cycles. Figure is modified from previous literature.[14]

displacement (optical trap stiffness) is found; discussion of this calculation is beyond the scope of this introduction. For a detailed description of optical trapping forces, previous literature can be reviewed.[15]

Optical traps have been utilized successfully in many different studies of biomolecular interactions, from the direct observation of kinesin stepping[16] to measuring

stretching and relaxation of DNA chains (Figure 1.4).[17] This is accomplished through the modification of the surfaces of a fixed particle and an optically trapped neighbor particle with biomolecules. Using the optical trap, one particle can be held while the other is translated with a nanomanipulator to apply known displacements. The translation of the optically trapped bead is related to the interaction force with the translated particle through the applied optical stiffness.

Experiments with blinking optical tweezers are closely related to the work done in this dissertation, whereby two Brownian particles are allowed to sample equilibrium positions while transiently being relocated with two optical potential wells to proximal positions. In this manner, particle-particle sampling can be interpreted using Boltzmann's relation, and the presence of the optical traps merely reduce the sampling time necessary to gain ample statistics on particle pairs interacting in the dilute limit.

1.2.2 Spectroscopic Methods

The study of condensed phases at interfaces impacts a wide variety of technological and scientific areas, thus a multitude of techniques are available for studying chemi- and physisorption and reactions at interfaces. Here, I only describe a few that are used in the context of understanding binding kinetics and adsorption isotherms relevant to biological systems.

Surface plasmon resonance (SPR)[19] is used to characterize the refractive index and/or thickness of ultrathin biopolymer films (down to 1nm thick) at the surface of a noble metal (Au, Ag, Cu). The method works by using total internal reflection to generate a surface plasmon at the metal-liquid interface, and the local resonance angle is

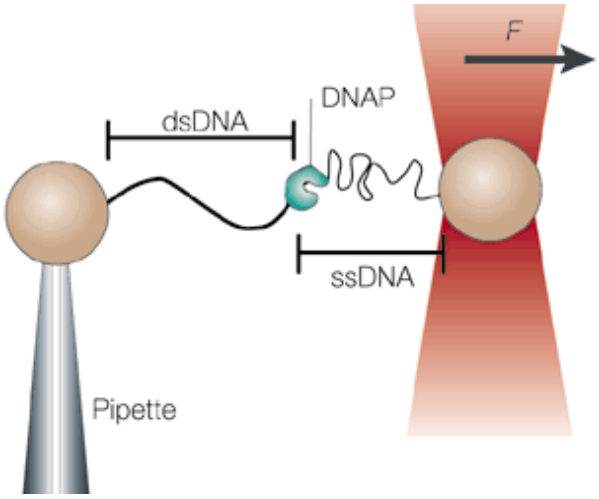

Figure 1.4. Graphic showing how optical traps can be used to research biomolecular interactions. In this figure, DNA is immobilized on two particles and stretched, with one particle fixed by a micropipette (left) and the other translated with the radiation force generated by focused light. By knowing the trap stiffness, force-separation curves can be generated. Figure modified from a literature source.[18]

tracked as material is adsorbed to the thin metal film. By relating the resonance angle to the optical thickness or refractive index of the adsorbed film, the adsorbed amount per unit area can be extrapolated if the optical properties of the biopolymer are known. In this manner, multi-stage binding can be monitored in a "label-fee" mode, which helps to diminish the effects that covalently attached labels can have on interfering with native protein-ligand function.

Generally speaking, SPR data is an integrated value from the entire spot size of the beam of light, but fairly recent advances have allowed SPR to be operated in an imaging mode,[5] where features as small as a few microns can be resolved (see Figure 1.5). Still, binding kinetics are monitored by observing average interactions between soluble and surface-bound species without collecting separation-dependent potentials. Hence, this limited information is important but incomplete.

To a lesser extent, ellipsometry and reflectometry are used to characterize the adsorption of biofilms at interfaces. These methods reply on optics principles similar to those applied in SPR studies. For example, the time-dependent formation of SLBs from vesicle adsorption and fusion was studied with ellipsometry under different conditions.[20] Most ellipsometry and reflectometry setups are accessed by researchers in the field of semiconductor fabrication, so readings under ambient conditions are the norm. Flowcell designs have, however, been incorporated into these optical techniques to allow for the real-time measurement of adsorption kinetics at liquid-solid interfaces. Moreover, ellipsometry has been modified to acquire spatially resolved (down to 1μm) thickness/absorption values.[21]

The formation of adsorbed layers can also be monitored using fluorescent labels in a technique termed total internal reflection fluorescence microscopy (TIRF). In TIRF, an evanescent wave is generated at the fluid-solid interface through total internal reflection, which excites fluorescence from labeled species. Fluorescence intensity is then gathered as a function of time with an optical microscope to obtain information nearly identical to the other spectroscopic methods mentioned above. The one major deficiency of TIRF is that the adsorbed species must be labeled in order to observe them. This leads to potential problems when studying interactions, as additional molecular complexes tend to disrupt native biomolecular interactions. Yet, TIRF is normally quite useful and appropriate for studying physisorption of macromolecules.

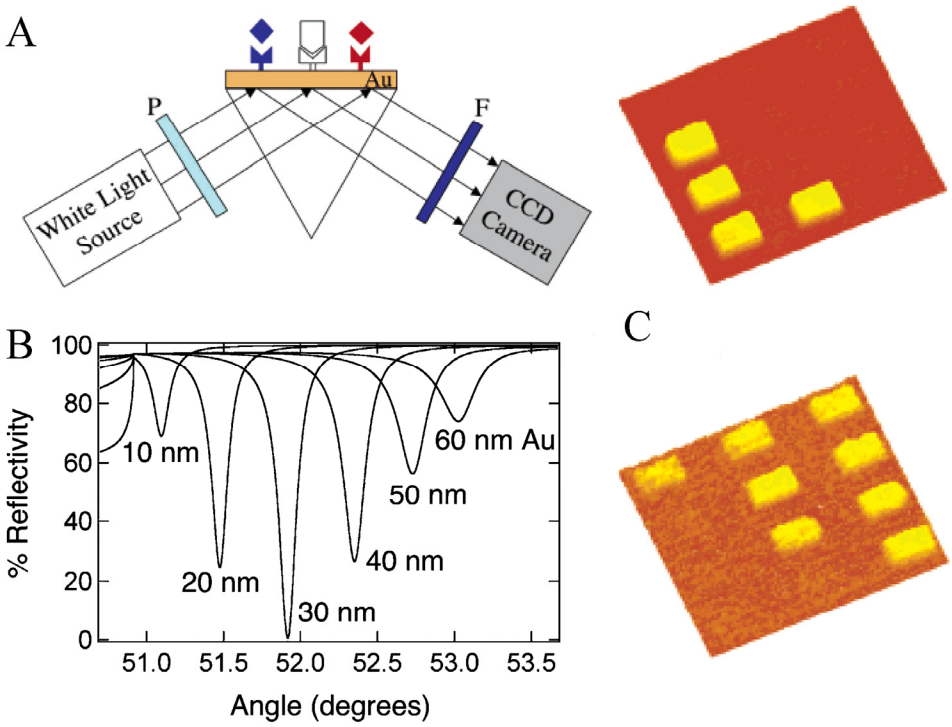

Figure 1.5. (A) Experimental arrangement for SPR. (B) Plots showing resonance angles for multiple Au layer thicknesses. (C) SPR imaging of a microarray with features around 1μm. Figure created from several sources.[22]

Up to now, the spectroscopic methods discussed herein have used light exclusively, which is why they are classified in that manner. A closely related method, and one that does not use light, is the quartz-crystal microbalance with dissipation monitoring (QCM-D). QCM-D compliments spectroscopic data as another independent measure of adsorbed mass, which is estimated by monitoring the change in resonance frequency of a piezoelectric crystal as macromolecules adsorb at the liquid solid interface. Because resonance frequency is greatly affected by an object's mass, small amounts of adsorbed matter can be detected with high temporal resolution. Film thicknesses are estimated based on knowing the molecular weight of the adsorbed

species. Just as in nearly all spectroscopic measurements—save data from specialized instruments with imaging capabilities—QCM-D integrates the signal from the entire crystal surface (>2mm^2), so local information is lost.

Additionally, acoustic waveguides can be implemented in studies of adsorbed layers. Of direct significance to this work is research conducted using acoustic waveguides to acquire time-dependent adsorption data from 1, 5 and 10mol% NTA-labeled vesicles forming SLBs.[23] The subsequent binding of His-tagged proteins to the Ni-NTA group incorporated into the SLB was also examined to calculate the binding isotherm. Results from this paper directly impacted research protocols described in this dissertation (see *Section 3.2.4*).

1.2.3 Brownian Probe Techniques

The tracking of passively diffusing functionalized colloids continues to be an improving and auspicious approach for probing weak interactions on the order of kT.[24,25] For example, interaction energies accessible with experimental techniques, such as TIRM,[26] approach those of biological significance. Recent work involving the integration of TIRM and VM[27] methods permits the tracking of 3D colloidal trajectories to within ~1.5nm for particle-wall separations and half-pixel identification of lateral positions.[25,28,29] Analyses of particle ensembles has demonstrated the simultaneous quantifying of particle-particle pair potentials, laterally resolved particle-wall potentials, and average lateral diffusion coefficients with exact multi-body hydrodynamic corrections.[25,30] Aside from collecting self-consistent data, one application of this combined experimental approach is the mapping of interfacial potential energy

landscapes (patterned or naturally occurring) with *kT*-scale sensitivity.[25,30] Extensions of this work to more complex problems such as protein arrays or cell membrane surfaces afford the opportunity to resolve interaction energies at scales inaccessible to scanning probe methods (e.g., chemical force microscopy[31]). Early work using TIRM to measure potentials between liposomes[32] and long-range attraction between receptor-ligand pairs[6] showed promise but have not been performed in a way that meaningful short-range data can be extracted. The details of these methods above are outlined in the remainder of this dissertation, thus a thorough and detailed explanation is removed here for the sake of limiting redundancy.

Two other sensitive methods that involve the passive monitoring of Brownian particles are dynamic and static light scattering. In dynamic light scattering (DLS), a monochromatic laser is passed through a colloidal suspension and the time-dependent intensity fluctuations are monitored. Brownian motion of the particles is the source of these intensity fluctuations, so the time scale of movement of the particles is related to the time scale of intensity fluctuations. The second-order autocorrelation function is generated from the intensity vs. time data and used to calculate the diffusion coefficient, which is directly related to the average hydrodynamic radius of the particle ensemble. DLS is used to measure interactions by observing changes in short-time diffusion as soluble molecules interact or surface-immobilized biomolecules on colloidal surfaces begin to change their rates of association. Studies with this technique have lead to important breakthroughs in the field of biophysics (specifically protein crystallization),[33] but separation-dependent potentials are not accessible with DLS.

The aforementioned technique of using optical tweezers has also been successfully employed as an approach to studying separation-dependent potentials. Here, optical traps are simply used to keep particle pairs from sampling positions at separations larger than that of interest. In other words, two potential energy wells are established transiently so as to keep particles in proximity, thereby reducing the sampling time needed to gain statistically relevant data between particles in the dilute limit. The one drawback to using this approach is the same for all VM techniques: spatial resolution is not fine enough to resolve the important subtle detail in separation-dependent potentials between biomolecules. Though this issue can be overcome using interference techniques that aid in tracking lateral particle positions to within 1nm.

Another method, recently developed in our group, exploits the diffusive behavior of concentrated colloids atop potential energy landscapes, either physical or chemical, in order to resolve the depth and shape of the energy well. Although only physical features were imaged with these diffusing probes, preliminary research has shown that chemical attraction in the form of vdW can also be resolved using this method. Figure 1.6 shows results from Bahukudumbi and Bevan (in press) comparing AFM scans of topographical data to the features mapped out by analyzing the behavior of a quasi-2D dispersion sampling positions within the physical features.

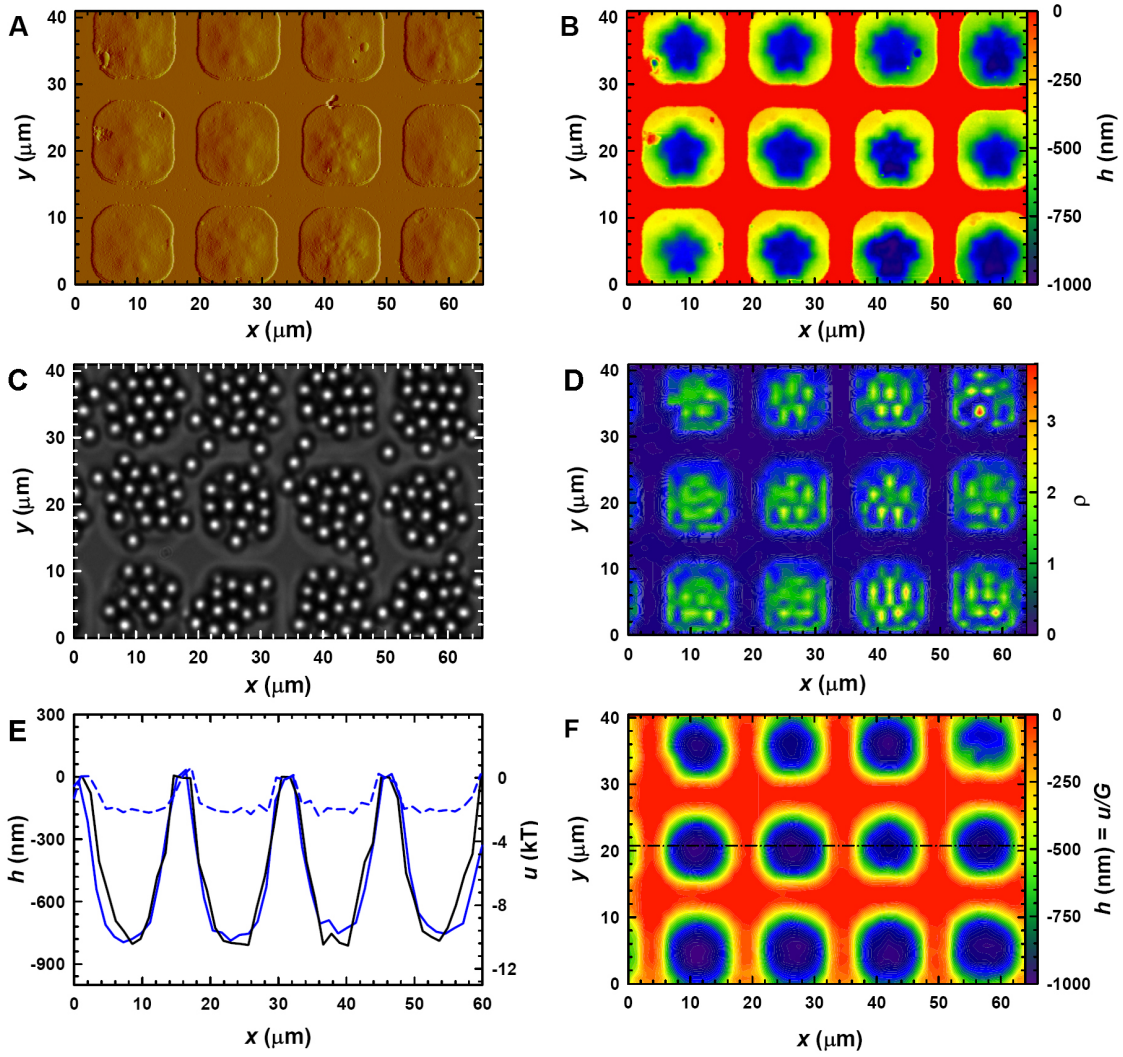

Figure 1.6. AFM (A) amplitude and (B) height images of a patterned glass surface. (C) Optical microscopy image of an equilibrium configuration of levitated 2.2μm silica colloids (ϕ_{eff}=0.28). (D) Spatially resolved time-averaged colloid density, $\rho(x, y)$. (E) Profile and (F) spatial map of potential energy landscapes plotted against AFM height data (E) and converted to height data (F).

1.3 Dissertation Outline

This dissertation is organized as follows: *Section 2* details the theoretical aspects of (i) colloidal and surface forces, (ii) TIRM, (iii) ensemble analysis TIRM, (iv) luminescence TIRM, (v) calculating, interpreting, and utilizing the pair distribution

function from particle-particle data, (vi) finding lateral mean-square displacements with correction for two-body hydrodynamics, (vii) quantitative analysis of fluorescence recovery after photobleaching data, and (viii) physiochemical descriptions of polymer brush layers with scaling theory. *Section 3* outlines every experimental detail, which includes: (i) materials and equipment used, (ii) the preparation of homogeneous and patterned surfaces, (iii) synthesis of specialized probes ranging from single quantum dots (QDs) and Stöber silica to microspheres modified with fluorophores and QDs, (iv) experimental setups for video microscopy and TIRM, (v) how confocal microscopy was utilized, and (vi) particle and surface characterization with X-ray photoelectron spectroscopy, AFM, dynamic light scattering, and pair distribution functions for colloids in crystalline configurations. *Section 4* presents an overview of cell-cell adhesion proteins and a literature survey of direct measurements of cadherin-cadherin interactions. *Section 5* presents extensive work carried out to characterize how naturally occurring heterogeneity in interfacial systems affects the interpretation of non-specific binding between particle and wall surfaces. Specifically, a set of semi-empirical criteria were established to help determine association lifetimes. That work, therefore, serves as the baseline for measurements of specific protein-protein interactions. *Section 6* contains results that identify the key conditions necessary for apposing supported lipid bilayers (SLBs) to remain stable or fuse and exchange lipids, thus helping to establish robust experimental constructs for protein-protein measurements. Additionally, lateral transport properties within SLBs are characterized as a function of protein and PEG concentration, with adjustable parameters such as separation distance from the underlying silica support

and PEG molecular weight. Preliminary results from specific protein-protein measurements conducted with TIRM and video microscopy are presented in *Section 7*. Here, calcium-dependent changes in interfacial adhesion are monitored, thus successfully demonstrating the use of diffusing colloidal probes for directly measuring weak specific interactions. *Section 8* includes results from the development of a technique I term Luminescence TIRM, wherein the luminescence intensity from QD-modified probes is collected and analyzed with conventional TIRM theory. Quantitative electrostatic profiles were collected in scattering and luminescence modes, and they showed excellent agreement. Furthermore, time-dependent behavior of QD-modified probes in EWs was quantified in order to find limitations of, and drawback to, the technique. Future and current research are outlined in *Section 10*, with particular emphasis on continuing cadherin research and novel interfacial experiments in index-matched systems with the QD-modified probes described in *Sections 3 and 8*. Also, preliminary measurements of anisotropic potentials from "patchy" particles are presented along with an explanation of how anisotropic probes can be utilized to obtain useful data. Finally, *Appendix A* presents work performed in the field of nanoparticle cytotoxicity. A slight departure from the remainder of the dissertation, this section is certainly linked to the other work through the commonality of colloidal and biological science. In this work, ZnO QDs were made to be water dispersible down to the single-nanoparticle level through functionalization with the amphiphilic polymer, polyvinyl pyrrolidone (PVP). Aggregate size was easily adjusted with the ratio of ZnO to PVP. Primary neuronal cells from a rodent (PC12 cells) were cultured along with ZnO

aggregates at different concentrations and size ranges. The cytotoxic effects were measured with LDH assays and by quantifying the degree of DNA fragmentation for all tested conditions. The findings in this work point to significant differences in cell death when exposed to single QDs. Furthermore, nanoparticles were found to be significantly cytotoxic down to concentrations as low as 5μg/ml.

2. THEORY

2.1 Colloidal and Surface Forces

The separation-dependent interaction between a colloid and an underlying wall is dictated by the balance of surface and body forces acting on the particle that arise from electrostatic, van der Waals (vdW), and gravitational contributions. Strictly speaking, there are other forces that could exist in these types of systems (e.g., magnetic, depletion, short-range secondary bonding, etc.), but we only consider these three forces in this dissertation, where continuum specific and non-specific biomolecular forces are lumped into the vdW portion; note that "long"-time bonding between biomolecular pairs is considered association and is handled differently. The net separation-dependent potential energy of the particle-wall system is given as the superposition of these three forces through

$$u(h) = u_{\text{edl}}(h) + u_{\text{grav}}(h) + u_{\text{vdW}}(h), \tag{2.1}$$

where h is the separation between the particle and underlying wall surfaces, $u_{\text{edl}}(h)$ is the repulsive interaction between overlapping electrostatic double layers on opposing surfaces, $u_{\text{grav}}(h)$ is the linear gravitational potential due to the buoyant weight of the particle, and $u_{\text{vdW}}(h)$ is the long-range, continuum vdW attraction between the colloid and wall that is mediated by the dielectric properties of the particle, wall, and intervening aqueous medium. In quasi-2D systems, particle-particle forces in a colloidal suspension can be described by

$$u(r) = u_{\text{edl}}(r) + u_{\text{vdW}}(r), \tag{2.2}$$

where r is the separation between two colloidal particle centers.

2.1.1 Electrostatic Interactions

In the case that Debye lengths are smaller than particle-wall separations ($h/\kappa^{-1}>1$) and much smaller than particle radius ($a/\kappa^{-1}>>1$), the electrostatic interactions between overlapping double layers on neighboring particles is accurately modeled utilizing the Derjaguin approximation and non-linear superposition. Specifically, for a 1:1 electrolyte, the interaction is given by

$$u_{\mathrm{edl}}(h) = B\exp(-\kappa h), \tag{2.3}$$

with

$$B = 64\pi\varepsilon a\left(\frac{k_B T}{e}\right)^2 \tanh\left(\frac{e\Psi_p}{4kT}\right)\tanh\left(\frac{e\Psi_w}{4kT}\right) \tag{2.4}$$

and

$$\kappa = \left(\frac{2CN_A e^2}{\varepsilon kT}\right)^{\frac{1}{2}}, \tag{2.5}$$

where κ^{-1} is the Debye length, ε is the dielectric permittivity of the media, k is Boltzmann's constant, T is absolute temperature, a is particle radius, e is the elemental charge, Ψ_p and Ψ_w are the Stern potentials of the particle and wall, C is the bulk electrolyte concentration, and N_A is Avogadro's number. Note that the wall is assumed infinite when deriving Eq (2.4). In the case of two identical interacting particles, the Derjaguin approximation states that the electrostatic interactions are exactly half of what they are for the particle-wall case; i.e.

$$u_{\mathrm{edl}}(r-2a)=\frac{1}{2}B\exp(-\kappa(r-2a))\,. \tag{2.6}$$

2.1.2 Gravitational Potential

The potential energy due to gravity is simply the buoyant particle weight, *G*, multiplied by its height, *h*, above the underlying wall, with the buoyant weight being merely the product of the buoyant mass (depending on the particle and medium densities) of the particle, *m*, and the gravitational constant, *g*. The gravitational potential, therefore, is described by

$$u_{\mathrm{grav}}(h)=Gh=mgh=\left(4/3\right)\pi a^{3}(\rho_{\mathrm{p}}-\rho_{\mathrm{f}})gh\,, \tag{2.7}$$

where ρ_{p} and ρ_{f} are the particle and medium densities.

2.1.3 van der Waals Attraction

Attractive vdW forces result from charge and electromagnetic-field fluctuations at all possible rates that arise due to the mismatch in dielectric properties between the particle and wall through the surrounding medium. First, vdW potentials between colloids and surfaces are determined by computing the Hamaker "function," $A_{132}(l)$, between two halfspaces composed of materials 1 and 2 and separated by a distance, *l*, containing medium 3 as[34]

$$A_{132}(l)=-\frac{3}{2}kT\sum_{\mathrm{n}=0}^{\infty}{}'\int_{r_{\mathrm{n}}}^{\infty}x\left\{\ln\left[1-\Delta_{13}\Delta_{23}e^{-x}\right]+\ln\left[1-\bar{\Delta}_{13}\bar{\Delta}_{23}e^{-x}\right]\right\}dx \tag{2.9}$$

$$\Delta_{\mathrm{jk}}=\frac{\varepsilon_{\mathrm{j}}s_{\mathrm{k}}-\varepsilon_{\mathrm{k}}s_{\mathrm{j}}}{\varepsilon_{\mathrm{j}}s_{\mathrm{k}}+\varepsilon_{\mathrm{k}}s_{\mathrm{j}}}\qquad \bar{\Delta}_{\mathrm{jk}}=\frac{s_{\mathrm{k}}-s_{\mathrm{j}}}{s_{\mathrm{k}}+s_{\mathrm{j}}}\qquad s_{\mathrm{k}}^{2}=x^{2}+\left(\frac{2\xi_{\mathrm{n}}l}{c}\right)^{2}\left(\varepsilon_{\mathrm{k}}-\varepsilon_{2}\right)$$

$$r_{\mathrm{n}}=\frac{2l\xi_{\mathrm{n}}\sqrt{\varepsilon_{2}}}{c}\qquad \varepsilon_{\mathrm{k}}=\varepsilon_{\mathrm{k}}\left(i\xi_{\mathrm{n}}\right)\qquad \xi_{\mathrm{n}}=\frac{nkT}{\hbar}$$

where $i=\sqrt{-1}$, $\hbar$ is Planck's constant divided by 2π, *c* is the speed of light in a

vacuum, and $\varepsilon_k(\omega)$ is the dielectric spectrum of material *k*. The prime (') next to the summation indicates that the first term (*n*=0) is multiplied by $0.5(1+2\kappa l)\exp(-2\kappa l)$. The prefactor of 0.5 avoids double counting, while the remainder of this factor accounts for screening of the zero-frequency contribution.[35] Physical properties of the materials enter through the function $\varepsilon_k(\omega)$, where the water and silica dielectric spectra used this work are the same as that reported by Bevan and Prieve.[36] Mahanty and Ninham[35] suggested the model which can modify the dielectric properties of a material coated with different materials (e.g., lipid bilayers, proteins, Au film). For example, if material 1 is coated with a film thickness, δ, of material 4, then

$$\Delta_{31} = \frac{\Delta_{34} + \Delta_{41}\exp(-\delta s_4 / l)}{1 + \Delta_{34}\Delta_{41}\exp(-\delta s_4 / l)}. \tag{2.10}$$

The van der Waals interaction between a sphere and a half space is accurately described using Derjaguin approximations via[36,37]

$$u_{\mathrm{vdW}}(h) = -\frac{a}{6}\int_{\mathrm{h}}^{\infty}\frac{A_{132}(l)}{l^2}dl. \tag{2.11}$$

The vdW attraction increases smoothly from the rapidly decaying far-field limit to values that are large relative to *kT* at small separations. For convenience, the particle-particle and particle-wall vdW interactions quantified in this work are well represented by non-integer power-law decay fits to the continuum Lifshitz theory and are given by[36]

$$u_{\mathrm{vdW}}^{\mathrm{pp}}(r) = -aA\left(r-2a\right)^{-p} \tag{2.12}$$

$$u_{\mathrm{vdW}}^{\mathrm{pw}}(h) = -2aA\left(h-2a\right)^{-p}, \tag{2.13}$$

where *A* and *p* are fitting parameters, with *p* typically between 2 and 2.15.

The sum of interactions relative to the minimum potential is obtained from Eqs. 2.1-

2.7 and given as

$$\frac{u(x+h_{\mathrm{m}})-u(h_{\mathrm{m}})}{kT}=\frac{aB'}{kT}\exp\left[-\kappa\left(x+h_{\mathrm{m}}\right)\right]+\frac{a^3G'}{kT}\left(x+h_{\mathrm{m}}\right)-\frac{aA}{kT}\left(x+h_{\mathrm{m}}\right)^{-p}-\frac{u(h_{\mathrm{m}})}{kT}, \quad (2.14)$$

where $B'=B/a$ and $G'=G/a^3$ from Eqs 2.4 and 2.7, $x=h-h_{\mathrm{m}}$, and h_{m} is the most probable height.

2.2 Total Internal Reflection Microscopy (TIRM)

"TIRM" was first developed by Temple[38] to probe surface defects, but the abbreviation was hijacked and became synonymous with the technique pioneered by Prieve and Alexander[39] to measure separation-dependent surface potentials. Since that first demonstration, the method has been modified and improved significantly. The technique is based on observing the instantaneous, height-dependent scattering intensity of a particle diffusing above a wall within an evanescent wave (EW). An EW is an exponentially decaying electromagnetic field generated at the interface of the wall and media via total internally reflection of a laser beam at that interface. The EW scattering intensity is related to the instantaneous height of a particle through

$$I_{\mathrm{S}}(h)=I_0\exp(-\beta h), \quad (2.15)$$

where I_{S} is the scattering intensity, I_0 is the intensity at h=0, and β^{-1} is the EW decay length calculated from

$$\beta=\frac{4\pi}{\lambda}\left[\left(n_1\sin\theta_{\mathrm{inc}}\right)^2-n_2^2\right]^{\frac{1}{2}}, \quad (2.16)$$

with n_1 and n_2 being the refractive indices of the incident and transmitted media, θ_{inc} the

angle of incidence, and λ the wavelength of the incident laser (Figure 2.1). As particles diffuse, they sample an equilibrium distribution of heights above the wall that can be acquired experimentally by determining the instantaneous particle-surface separation, h, for a statistically relevant number of perpendicular excursions. Note that the power of TIRM derives from its capability to provide height data at a resolution of approximately 1-1.5nm. Using Eq 2.15, a time-averaged height histogram, $p(h)$, can be generated with height data, $h(t)$, which can be related to the particle-wall potential using Boltzmann's equation via

$$p(h)=A\exp\left[-\frac{u(h)}{kT}\right], \tag{2.17}$$

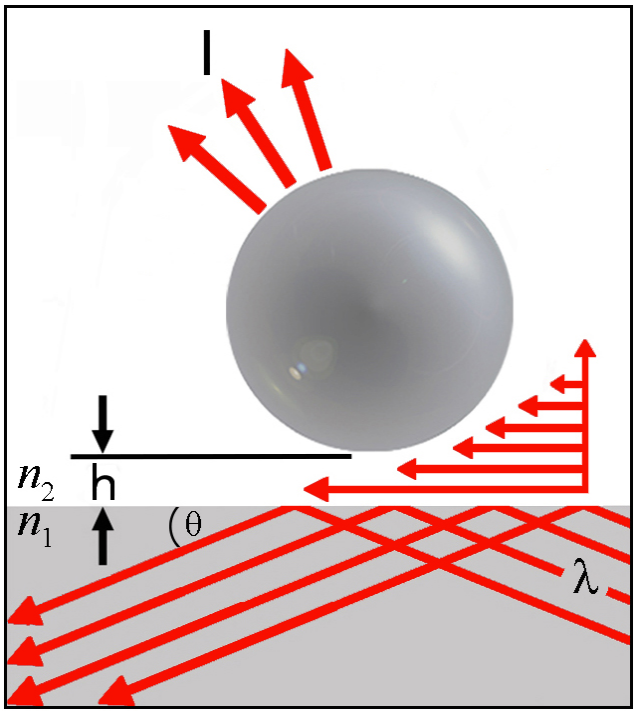

Figure 2.1. EW scattering, with intensity $I(h)$, from a particle dictated by the instantaneous height, h, above the wall.

with A being a function of the total number of height measurements. The potential energy profile, $u(h)$, is then found by inverting Eq. (2.17), and the resulting profile is an average over time and the lateral positions sampled by the diffusing particle.

2.3 Ensemble TIRM

Conventional TIRM employs a photomultiplier tube to acquire the height-dependent scattering intensity from a single particle. The novelty of ensemble TIRM, a technique developed by our group, lies in the capacity to monitor trajectories and potentials of many single particles simultaneously to allow direct comparison of spatially distributed and average properties related to particle-surface interactions. A key benefit of averaging potentials of many particles is the diminished need for time averaging, which can produce orders of magnitude faster measurement times at higher interfacial particle concentrations on homogeneous surfaces. The same concept of ensemble analysis can also be applied to heterogeneous surfaces to obtain potential energy landscapes of patterned substrates.[25]

By assuming colloids and surfaces are chemically and physically uniform (monodisperse, homogeneous, etc.), the time-dependent height fluctuations of many particles levitated above different positions on a surface can be averaged together to produce an ensemble average histogram, $\langle n(h) \rangle$, through

$$\begin{aligned} & h_1(t)\ ,\ h_2(t)\ ,\ \ldots\ ,\ h_i(t)\ ,\ \ldots\ ,\ h_p(t) \\ & \rightarrow\ n_1(h)\ ,\ n_2(h)\ ,\ \ldots\ ,\ n_i(h)\ ,\ \ldots\ n_p(h)\ \rightarrow\ \langle n(h) \rangle \end{aligned} \tag{2.18}$$

where $h_i(t)$ are the time-dependent height fluctuations of each single particle, $n_i(t)$ are the time-averaged histograms of each single particle, and $\langle n(h) \rangle$ is the time- and ensemble-

averaged histogram of p particles monitored during the course of an experiment. By analyzing both single particle and average multi-particle histograms using Eq 2.18, the ensemble TIRM method can simultaneously measure p single particles, each interacting with specific surface locations, and an ensemble particle-wall interaction averaged over all particles and surface positions. In other words, the time-averaged height histograms, $n_i(h)$, of every single particle levitated above a homogeneous surface can be created by monitoring height fluctuations of each particle.

Because all single-particle potential-energy profiles essentially match on these relative scales, it appears, from a vast amount of experimental evidence, that particle and wall properties are sufficiently uniform to consider the particles as an "ensemble." The ensemble height histogram can be represented as the combination of single particle histograms if the absolute separations are measured from scattering intensities (Figure 2.1). The absolute separations can be obtained by measuring the intensity I_0 when particles come into contact with the wall (Eq 2.15). For convenience, reference intensities, instead of I_0, are usually chosen to report potentials in relative scales. Since the scattering properties of each colloid are not identical,[40] all I_0 values are not identical despite particles having very similar optical properties. If a unique reference intensity is applied to evaluate the height fluctuations of every particle, an erroneous ensemble height histogram is constructed, since $n_i(h)$ are in different height scales. Because all particles have similar chemical and physical properties, all individual particle potential profiles essentially superimpose on the scales relative to the most probable height, h_m. Hence, the ensemble height histogram, $<n(h)>$, can be constructed from time-averaged

height histograms, $n_i(h\text{-}h_m)$, which are all aligned to h_m instead of sampling in absolute height scales.

2.4 Luminescence TIRM

This dissertation also outlines the development and validation of a technique I term luminescence total internal reflection microscopy (LTIRM) in which we simultaneously track many diffusing polystyrene (PS) particles, modified with quantum dots (QDs), which simultaneously scatter and luminesce in an evanescent wave (Figure 2.2). In this manner, probe surfaces can contain various functionalities, and distinct populations can be tracked based on their spectroscopic signature. Thus, multiple conditions can be tested simultaneously in a combinatorial fashion.

Luminescence and scattering intensities can be separated by utilizing the appropriate cutoff filter, and then, by analyzing the distribution of height-dependent luminescence intensities using Boltzmann's equation (Eq 2.17), we are able to construct particle-wall potential energy profiles in an identical manner to conventional TIRM. Therefore, instantaneous particle-surface separations are found experimentally by relating their luminescence intensity to their height, h, through

$$I_L(h) = I_0 \exp(-\beta h), \tag{2.19}$$

where I_0 is I_L at h=0, and β^{-1} is the evanescent wave decay length.

Due to the time-dependent nature of QD luminescence, it is important to consider the degree of exposure to the EW as a function of time and potential, which gives relative separations. The average exposure of particles, $\langle I \rangle$, to an EW can be estimated

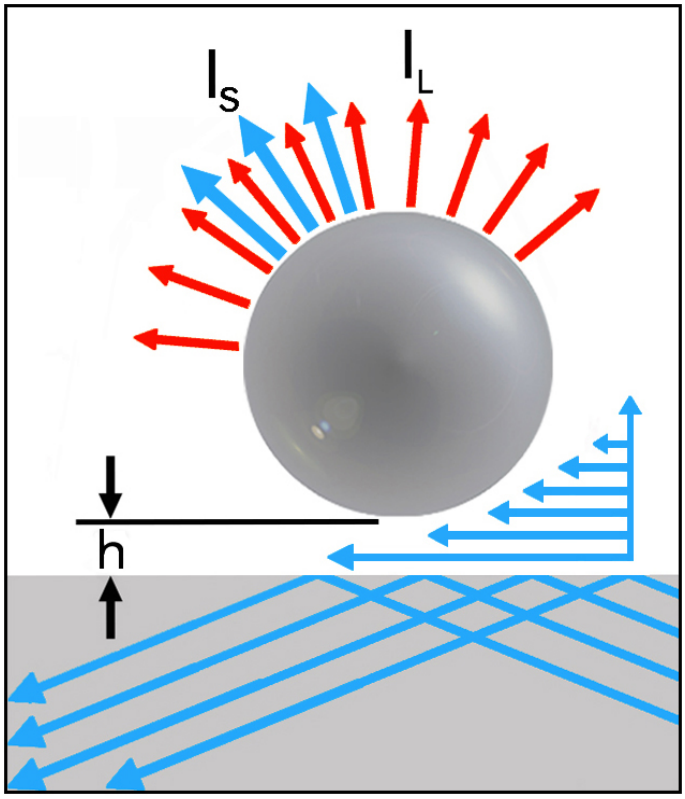

Figure 2.2. Illustration of height-dependent scattering, at λ_{inc}, and luminescence, at $<\lambda_{inc}$, from a QD-modified particle levitated above a planar surface.

via $\langle I \rangle = \int I(h)n(h)dh \Big/ \int n(h)dh$, where Eq 2.15 is used to find $I(h)$, and $p(h)$ can be obtained from the measured histogram or from $u(h)$ by inverting Eq. 2.17. Particularly for larger particles, the information gained from the previous equation could also be supplemented by an estimate of the rotational diffusivity, to give a better representation of the degree of exposure to portions of the particle as[41] $D_0^r = \left(kT/8\pi\mu a^3\right)\left[2.5/\ln\left(a/h\right)\right]$, where the correction factor, 2.5/ln(a/h), accounts for the separation-dependent hydrodynamic drag on the particle as it rotates. The above will be addressed in more detail in a later section.

2.5 The Pair Distribution Function

By using digital video microscopy to track the lateral positions of each particle within a quasi-2D dispersion, the pair potential, $u(r)$, can be, in theory, extracted with liquid structure theory. This is first accomplished through the experimental determination of the pair distribution function, PDF. Simply put, the PDF, or $g(r)$, characterizes the modulation of the local density, $\rho(r)$, around a given particle as a function of distance r from that particle. This happens in colloidal systems because, above a certain area fraction (N/A), the positions of several neighboring particles are strongly correlated, leading to the modulation of $\rho(r)$ over a few particle diameters. Therefore, $g(r)$ is related to the probability of locating a particle center at some distance from another particle center. As the distance r is increased, particle structure becomes more diffuse, so the probability of finding a particle at a given location away from the target particle tends to a constant. Therefore, this probability is related to the area fraction, which is why $g(r)$ is normalized by the particle density, thereby forcing the function to go to unity at large values of r.

To determine a $g(r)$ for a given system, each video frame is analyzed to count the number of particles residing within a distance between r and $r+dr$ from a target particle for all bins dr wide (note: the smallest bin size in our experimental setup used here is 38.5nm). This is performed for every particle in the window within a clipping zone; the clipping zone reduces the diminishment of the probability of finding particles at certain distances due to particles at the window's edge only having 0.5-0.25X the number of neighbors compared to particles in the center of the window. The total count of particles

within those radial bins is then divided by $N2\pi rdr$ to normalize the distribution. Ideally speaking, the position of the first peak of a $g(r)$ should be no less than $2a$, since particles cannot overlap; however, issues such as polydispersity, optical distortion, limited spatial resolution, and particle "hopping" (Figure 2.3B) lead to deviations in this ideality.

2.5.1 Extracting Potentials

Once a $g(r)$ is collected, the data can be analyzed to yield separation-dependent pair potentials, just as in TIRM. Here, the one caveat is that, at area fractions >0.1%, neighboring particles affect the sampling of particle pairs, so a general Boltzmann's analysis is not valid. Yet, some information can be gained from simply applying this rudimentary analysis in the form of a potential of mean force (PMF), which is obtained by

$$\omega(r) = -kT\ln\left[g(r)\right]. \tag{2.20}$$

In experiments that use optical traps to confine the sampling domain of particles, pair potentials can be analyzed in this way accurately, because two particles can be isolated and forced to sample positions within a few particle diameters. In our setup, examining particles in the dilute limit would take an enormous amount of time, simply because of the lack of spatial constraints placed on the particles. In the non-dilute limit, $\omega(r)$ is not the effective pair potential of interest but the average potential between particle pairs that are influence by the presence of all neighboring particles. This calculation, however, gives a very rough first estimate of the scale and range of pairwise interactions. In summary, for a single pair of particles not influenced by other particles,

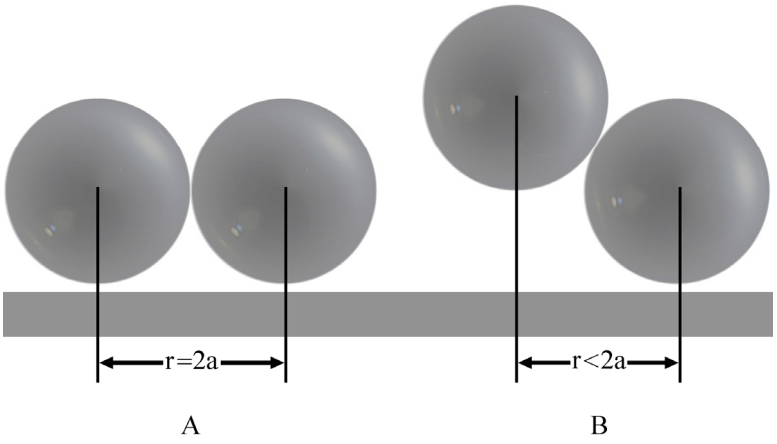

Figure 2.3. Illustration of particle "hopping" in a quasi-2D system, which leads to erroneous particle-particle separations less than 2*a*.

the radial distribution of absolute separations can be utilized to find the exact pair potential; identical to the way this equation is used in the analysis of TIRM data. On the other hand, more specialized analyses are required to interpret pair interactions in concentrated systems, and the following outlines that approach.

The pair potential, $u(r)$, is related to $g(r)$ through the Ornstein-Zernike (OZ) equation that is given by

$$h(r) = c(r) + \rho \int c(r')\, h(|r - r'|)\, dr', \tag{2.21}$$

where $h(r)=g(r)-1$ is the total correlation function, $c(r)$ is the direct correlation function, and ρ is the average particle number density. The Percus-Yevick closure relation was implemented to relate $u(r)$ and $c(r)$ and is defined through[42]

$$c(r) = \left[1 - \exp\left(u(r)/kT\right)\right]\left[1 + h(r)\right]. \tag{2.22}$$

By solving Eq 2.21 using the closure relation given above, $u(r)$ can be obtained through the application of a Fourier-Bessel transformation to Eq. 2.21 yielding[43]

$$C(k) = \frac{H(k)}{1 + \rho H(k)}. \tag{2.23}$$

Inverse Monte Carlo (MC) analyses were implemented as a numerical method to relate $u(r)$ to $g(r)$. In inverse MC simulations, a $u(r)$ is determined using iterative forward MC analyses that converge to yield an estimated $g(r)$. The initial guess for $u_i(r)$ was provided by the OZ equation (Eq. 2.21), which is then used in the forward MC to produce a simulated $g_s(r)$. An updated estimate of $u_f(r)$ is obtained from the previous value of $u_i(r)$ following the comparison of simulated, $g_s(r)$, and measured, $g_m(r)$, pair correlation functions through[44]

$$u_f(r) = u_i(r) + kT\ln\left[\frac{g_s(r)}{g_m(r)}\right]\exp\left[-(\alpha r)^2\right], \tag{2.24}$$

where α^{-1} is a damping length to prevent divergence of the inverse MC algorithm in highly structured systems. Iterations are taken until $g_s(r)$ is found to within some prescribed error from $g_m(r)$ by[44]

$$R^2 = \left[1 - \frac{\sum\left(g_m(r) - g_s(r)\right)^2}{\sum\left(g_m(r) - g_{m\_avg}\right)^2}\right], \tag{2.25}$$

where g_{m_avg} is the mean value of the measured pair correlation function. For a given noise-free $g(r)$, a unique solution is obtained through convergence of $g_s(r)$ to $g_m(r)$, provided that more than one $u(r)$ does not satisfy Eq. 2.25 within a specified value of R^2.[45]

2.5.2 Compensation for Experimental Non-idealities

No matter how well synthesized, colloidal dispersions will inevitably have a log-normal distribution of particle sizes that can be measured, for example, by dynamic light scattering or transmission/scanning electron microscopy. Because this is the case, dispersions having a polydispersity of <5% are commonly termed "monodispersed." Although this misnomer is typically unimportant for most applications, polydispersity has been proven to give misleading results (e.g., like-charge attraction[46]) if not properly accounted for, which has recently been demonstrated conclusively.[47,48] By properly accounting for variation in particle size, forward MC simulations can extract data from the measured $g(r)$ to yield more accurate potentials.

Another non-ideality to consider when analyzing video microscopy data is that of optical distortions. Many of the optical errors that arise can be handled quite nicely by general image analysis procedures,[27] but recent work[49] has shown that neighboring particles can have an optically distorting effect on each other's centroid location, thus leading to misrepresentative particle locations that make the particles appear nearer or farther apart, depending upon relative separations. This ends up resulting in error similar to effects from particle hopping mentioned above. The error in estimating particle centers as a function of distance is give by[49]

$$r' = r + 2\Delta r\left(r\right), \tag{2.26}$$

where r is the actual separation, r' is the apparent particle separation, and $\Delta r(r)$ is the optical distortion function. Although $\Delta r(r)$ depends heavily on the type of optics used

and the physical and optical properties of the particles tracked, we implement the same distortion function given in previous literature[49] due to the fact that the particle size and composition is nearly identical to those used in this dissertation.

To generate an optically distorted pair correlation function, $g'(r)$, from $\Delta r(r)$ and particle coordinates, the particle-particle separations are distorted using Eq. 2.26 to get apparent particle-particle distributions. Optical distortions are handled in the inverse MC analyses by distorting $g_s(r)$ before updating $u_f(r)$ using Eq. 2.24. As shown in the associated results section of this dissertation, these experiments reveal that the limited spatial resolution of video microscopy and the necessary corrections for systematic errors lead to a general failing of this technique to accurately describe separation-dependent potentials in attractive and weakly repulsive systems.

2.6 Lateral Mean-Square Displacements

When a particle approaches a planar surface, the lateral and normal diffusion coefficients ($D_{||}(h)$ and $D_{\perp}(h)$, respectively) and hydrodynamic mobility are expected to reduce. $D_{||}(h)$ can be expressed as

$$D_{||}(h) = f_{||}(h)D_0, D_{\perp}(h) = f_{\perp}(h)D_0 \qquad (2\ 27)$$

where $f_{||}(h)$ is a separation-dependent correction factor. A rational fit to data from Goldman et al.[41] gives

$$f_{||}(h) = \frac{-2.264 + 11.3643\delta(h) - 16.418\delta(h)^2 + 7.3205\delta(h)^3}{1 + 3.9212\delta(h) - 12.2243\delta(h)^2 + 7.3158\delta(h)^3} \qquad (2.28)$$

where $\delta(h) = (h-a)/a$. The function $f_{\perp}$ can be found elsewhere.[50] The ensemble's

average lateral diffusivity, $\langle D_{\parallel} \rangle$, can be estimated by considering $\langle p(h) \rangle$, the ensemble average distribution of heights sampled above the wall, by[51]

$$\left\langle D_{\parallel} \right\rangle = \frac{\int \left\langle p(h) \right\rangle D_{\parallel}(h) dh}{\int \left\langle p(h) \right\rangle dh} \tag{2.29}$$

where $p(h)=\exp(-u(h)/k_BT)$. Average MSDs in a single direction, x, can be quantified for lateral diffusion from multi-particle trajectory data through the following

$$W_x(t) = \left\langle \frac{1}{N_i} \sum_{i=1}^{N_i} [x_i(t) - x_i(0)]^2 \right\rangle = 2\left\langle D_{\parallel} \right\rangle t \tag{2.30}$$

where angled brackets indicate an ensemble average over multiple time origins, N_i is the number of identical particles, and $x_i(t)$ is the coordinate of particle i at time t in the x-direction. The total lateral MSD, $W(t)$, is the sum of $W_x(t)$ and $W_y(t)$.

Characteristic lateral diffusion can also be biased by an external force or superimposed convective flow field. In these experiments, this force is due to a gravitational field imposed by deliberate or incidental misleveling of the flowcell. The particles' migration velocity, V, can be found by fitting the MSD data with the following[52]

$$W_x(t) = 2\left\langle D_{\parallel} \right\rangle t + (V_x t)^2 \tag{2.31}$$

Using the generalized relation between mobility and diffusion coefficients ($D=k_BT/m$), the external force, F, can be related to the particle ensemble's velocity and average lateral diffusion coefficient by

$$F_x = \frac{\langle V_x \rangle}{\langle \mathrm{D}_{\|} \rangle} kT \tag{2.32}$$

where $F = mV_x$. Additionally, constrained lateral motion of particles due to spatially distinct potential wells can be described through interpretation of lateral MSD data with a fit to

$$W_x(t) = \langle L_x^2 \rangle [1 - A_1 \exp(-A_2 2 \langle \mathrm{D}_{\|} \rangle t / \langle L_x^2 \rangle)] \tag{2.33}$$

with L being the characteristic length of confinement of the potential well and A_1 and A_2 defined as parameters dependent upon the shape of the well.[52] Unlike, for instance, an experiment conducted on patterned templates,[53] the well shape and size is irregular and unknown before data is collected.

2.7 Fluorescence Recovery after Photobleaching (FRAP)

FRAP, a technique pioneered by Axelrod et al.,[54] is used extensively in many areas of research to estimate the diffusion coefficients of mobile fluorescently labeled species. Consequently, FRAP is now a standard procedure for studying transport of components confined within 2D biological membranes.

The fluorescently labeled membrane component under study is assumed to be initially distributed uniformly throughout the surface, and it is implied that the membrane is infinite. A laser beam at the excitation wavelength is then focused into small spot (typically <10μm in radius) within the imaging window and pulsed for a short time (<1s). The same beam is then attenuated (~5,000 times) and used to image the spatial distribution of fluorescence vs. time. If the layer is fluid and the species is

mobile, the bleached spot is recovered to some fraction of its original intensity. Illustrative examples of bleaching and recovery are given in Figure 2.4.

Basic fits to the FRAP data give reasonable estimates of component diffusion, and they are found by fitting the time-dependent intensity data with $I(t) = A\left(1 - \exp\left(-\tau t\right)\right)$, where $\tau_{1/2} = \ln 0.5/\tau$ and the diffusion coefficient if calculated by $D = \gamma_{\mathrm{D}} w^2 / 4\tau_{1/2}$, where w^2 is the radius of the bleaching spot and γ_{D} is a correction factor dependent upon the type of beam (e.g., Gaussian or step function) and the bleaching duration.[54]

A more exact theory, devised by Soumpasis,[55] utilizes the differential equation for lateral transport of a species undergoing Brownian motion:

$$I(t) = \exp\left(-2\tau_D/t\right)\left[I_0\left(2\tau_D/t\right) + I_1\left(2\tau_D/t\right)\right], \tag{2.34}$$

where I_0 and I_1 are modified Bessel functions and τ_{D} is the characteristic diffusion time. The diffusion coefficient of the labeled membrane component can be found with

$$D_{SLB} = \frac{w^2}{4\tau_{\mathrm{D}}}. \tag{2.34}$$

One caveat of this approach is that the fluorescence recovery is assumed to be complete, thus the $I(t)$ data must be normalized in order to fit the data properly. The asymptotic value of final recovery (inevitably <100%) is then found by "de-normalizing" the least-squares fit. In reality, the fluorescence intensity asymptotically approaches a value slightly below that of the prebleached intensity, due to the fact that bleached lipids redistribute uniformly throughout the membrane.

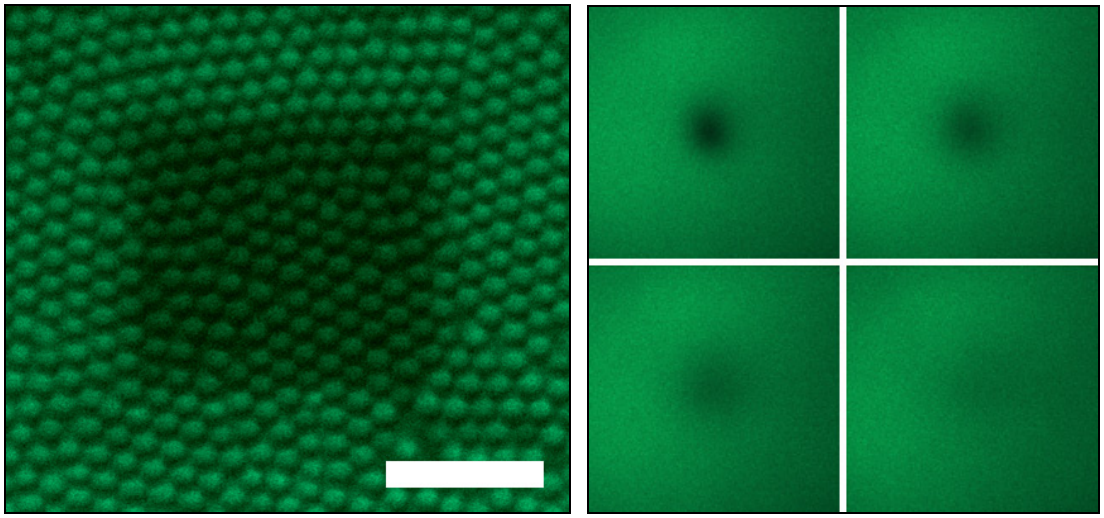

(A) (B)

Figure 2.4. (A) Bleached region within a concentrated dispersion of fluorescently tagged colloids; scale bare=20μm. (B) Series of confocal images (time interval=20s) taken immediately after bleaching, showing fluorescence recovery; window width=100μm.

2.8 Scaling Theory Description of Polymer-Grafted Lipid Membranes

Throughout much of this dissertation, polyethylene glycol (PEG), also known as polyethylene oxide (PEO), is discussed extensively. The two names are chemically synonymous, but historically, PEO is used when referring to long chains and PEG when the polymer is short. PEG is a water-soluble, inert polymer that is utilized for a variety of biomaterial applications. In this work, PEG is either part of the triblock copolymer PEO-PPO-PEO or grafted onto the head of a lipid.

This section outlines the basic theory that describes the statistical and thermodynamic configurations of the PEG chains immobilized on a supported lipid bilayer. The two main parameters that dictate the macromolecular configuration of the PEG layers are polymer mole fraction, X_p, and chain size, n_p. The most important consideration for our experiments is whether or not the PEG layer is in a mushroom or

brush state, because this layer provides the stabilizing force for particle-particle and particle-wall interactions. The mushroom-to-brush transition, $X_p^{m\to b}$, is defined as[56,57]

$$X_p^{m\to b} > \left(A_l/\pi a_m^2\right) n_p^{-6/5}, \tag{2.35}$$

where A_1 is the membrane surface area for a single lipid in the fluid phase and a_m is the size of the PEG monomer unit determined to be 0.39nm from the monomer volume in aqueous solution.[58] The value of A_1 was estimated[57] to be 0.6-0.7nm^2, so we use 0.65nm^2 here. The calculated values for $X_p^{m\to b}$ (in mole fraction) for the four PEGs of interest (followed by their n_p values) are: PEG1000 (3.15%, 23), PEG2000 (1.40%, 45), PEG3000 (0.86%, 68), and PEG5000 (0.50%, 114).

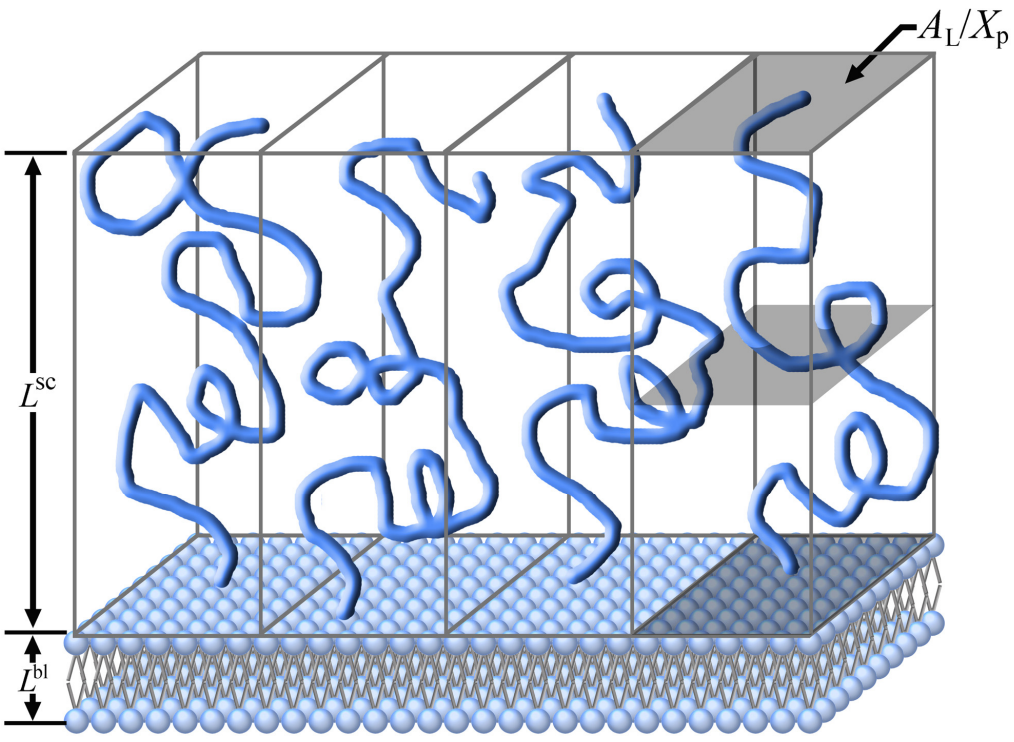

Figure 2.5. Important dimensions for PEGylated bilayers in the brush regime, where L^{SC} is the average brush thickness L^{bl} is the bilayer thickness, A_1 is the area per lipid molecule, and X_p is PEG mole fraction.

According to scaling theory, the thickness of the polymer brush layer, L^{SC}, is a function of the degree of polymerization, and PEG mole fraction within the brush and is given by

$$L^{SC} = n_p a_m^{5/3} \left(X_p / A_1 \right)^{1/3}, \tag{2.36}$$

where X_p/A_1 is called the grafting density. Figure 2.5 schematically depicts the relevant parameters that determine the average brush thickness above a lipid bilayer

Figure 2.6 gives theoretical predictions for the expected PEGylated bilayer thickness vs. *X*p for the four PEGs important to this work. Note that the layer thickness includes the PEG layers grafted to the top and bottom leaflets, $2L^{SC}$, and the thickness of the lipid bilayer, L^{bl}, which is relatively invariant.

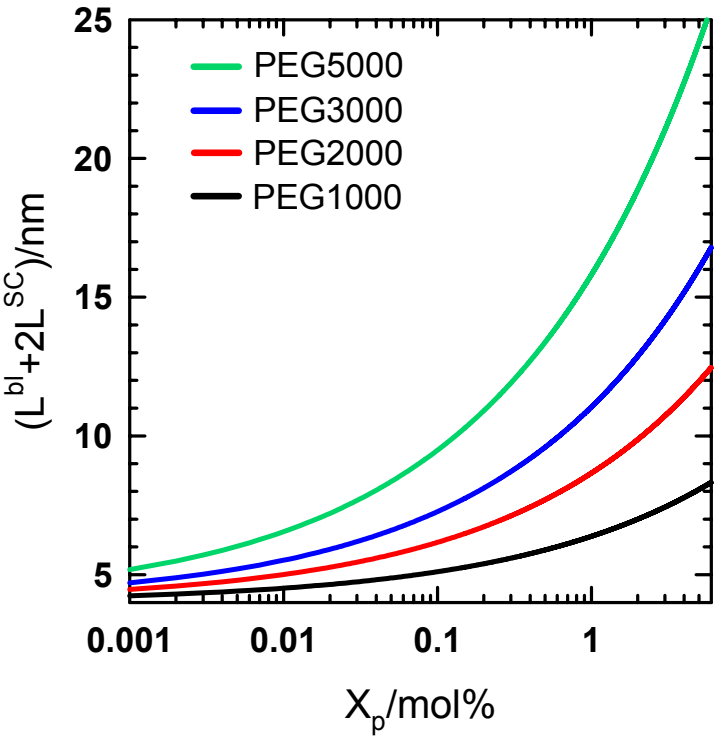

Figure 2.6. PEGylated SLB thicknesses vs. X_p for PEGs with different MWs.

3. EXPERIMENTAL METHODS

3.1 Materials and Equipment

3.1.1 Generic Chemicals

The following chemicals were used as received without further purification:

- Trioctylphosphine oxide (TOPO), trioctylphosphine (TOP), cadmium oxide, selenium, hexamethyldisilathiane, dimethylzinc, sodium chloride, hydrogen peroxide, sulfuric acid, triethylamine, N-hydroxysuccinimide, *N*-Ethyl-*N*′-(3-dimethylaminopropyl) carbodiimide hydrochloride, succinic anhydride, HEPES buffer, phosphate buffer solution, nickel(II) chloride, magnesium sulfate heptahydrate, calcium chloride, imidazole, and reagent grade chloroform, sulfuric acid, nitric acid, hydrogen peroxide, acetone, isopropanol, methanol, 1-butanol, and toluene (from Sigma-Aldrich)
- Sylgard polydimethylsiloxane (Dow Corning)
- Maleimide-nitrilotriacetic acid (Dojindo Molecular Technologies, Japan)
- Pluronic F108, F127, F68 (BASF Corp.)

3.1.2 Wall Surfaces and Particles

- Surfactant-free, sulfate-stabilized polystyrene (PS) particles with reported diameters of 4.00±0.17, 5.2±0.29, 5.9±0.58 μm and a density of ρ_{PS}=1.055g/cm^3 were purchased from Interfacial Dynamics Corporation (Eugene, OR)
- Carboxylated 0.97μm diameter silica microspheres, nominal 2.34, 4.09, 3.01μm silica colloids (ρ_p=1.96 g/ml) obtained from Bangs Laboratories (Fishers, IN)

- Nominal 1.58 and 0.99μm silica colloids (ρ_p=2.18 g/ml) purchased from Duke Scientific (Fremont, CA)
- No 1. 22×22, 18×18, 24×50mm coverslips and 24×75mm microscope slides (Gold Seal, Corning, NY)
- No 2. 22×22 selected micro coverglass (VWR)
- Costar 48- and 96-well cell culture clusters (Corning Inc.)

3.1.3 Silanes and Thiols

- >90% octadecyltrimethoxysilane (OTMS), >90% octadecyltrichlorosilane (OTS), 99% (3-aminopropyl) triethoxysilane (APS), >90% (3-mercaptopropyl) trimethoxysilane (MPS), 1-octadecanol (1-oct), >97% 3,3,3-trifluoropropyl-trimethoxysilane (TFS), >98% vinyltriethoxysilane (VTS), >98.5% 1-octanethiol, >95% 1-hexadecanethiol (HDT), >90% 16-mercaptohexadecanoic acid (MHA) were purchased from Sigma-Aldrich, with the except ion of HDT (Alfa Aesar).

3.1.4 Reactive Fluorophores

- Rhodamine Red® C_2 maleimide, succinimidyl 6-(N-(7-nitrobenz-2-oxa-1,3-diazol-4-yl)amino)hexanoate (NBD-X, SE), and AlexaFluor® 594 were purchased from Invitrogen (Carlsbad, CA).
- Fluoresceinamine (Sigma-Aldrich)

3.1.5 Photolithography Chemicals

- SU-8 2002 (MicroChem, Newton, MA), S1827 and S1805 (Shipley)
- MF 319 and SU-8 Developers; HMDS adhesion promoter

3.1.6 Lipids

- N-(4,4-difluoro-5,7-dimethyl-4-bora-3a,4a-diaza-s-indacene-3-propionyl)-1,2-dihexadecanoyl-*sn*-glycero-3-phosphoethanolamine, triethylammonium salt (BODIPY ® FL DHPE), 4-(4-(didecylamino)styryl)-N-methylpyridinium iodide (4-Di-10-ASP) (all from Invitrogen)
- 18:1 DGS-NTA (Ni) 1,2-dioleoyl-*sn*-glycero-3-[(N-(5-amino-1-carboxypentyl)iminodiacetic acid)succinyl] (nickel salt) (DOGS-NTA), 1,2-diacyl-*sn*-glycero-3-phosphoethanolamine-N -[methoxy(polyethylene glycol)-1000] (mPEG 1000 PE),1,2-diacyl-*sn*-glycero-3-phosphoethanolamine-N -[methoxy(polyethylene glycol)-2000] (mPEG 2000 PE), 1,2-diacyl-*sn*-glycero-3-phosphoethanolamine-N -[methoxy(polyethylene glycol)-5000] (mPEG 5000 PE), 16:0-18:1 PC 1-palmitoyl-2-oleoyl-*sn*-glycero-3-phosphocholine, 1-oleoyl-2-[6-[(7-nitro-2-1,3-benzoxadiazol-4-yl)amino]hexanoyl]-*sn*-glycero-3-phosphocholine (18:1-06:0 NBD PC) (all from Avanti Polar Lipids, Alabaster, AL)

3.1.7 Proteins and Antibodies

- γ-globulin-free bovine serum albumin (Sigma Aldrich)
- Monoclonal anti-human E-cadherin-allophycocyanin (lot numbers: LMK02 and LMK03) (R&D Systems, Inc.)
- Recombinant human E-cadherin/FC chimera (lot numbers: BOV07, BOV09, BOV10 and BOV13
- Recombinant human N-cadherin/FC chimera (lot numbers: FES08 and FES08)

3.1.8 Equipment and Instrumentation

- 15mW 632.8 (red), 633 (red), and 543nm (green), 10-350mW 488nm (blue), and a 20mW 450-530nm lasers (Melles Griot, Carlsbad CA)
- 12-bit CCD camera (max 43fps) from Hamamatsu (Japan)
- Axioplan 2 and Axiovert 135 optical microscopes (Zeiss, Germany)
- Axiovert 200M with LSM 5 pascal scanner (Zeiss, Germany) and Leica TCS SP5 confocal laser scanning microscopes
- FACSCalibur flow cytometer (Becton-Dickinson)
- Spectrofluoremeter (QM-4, Photon Technology Int., NJ)
- 100 (oil N.A.=1.4), 63 (oil N.A.=1.4), 63 (air N.A.=0.6) and 40× (air N.A.=0.6) objectives (Olympus)
- X-ray photoelectron spectroscopy (Kratos Axis Ultra)
- Atomic force microscopy (Nanoscope III, Digital Instruments)
- ZetaPALS particle analyzer (Brookhaven Instruments)
- Q4000 mask aligner (Quintel); SCS P6204 spin coater; reactive ion etcher (March Plasma Systems, CS-1701); metal evaporator (306, BOC Edwards), Accumet AR20 pH and conductivity meter; Branson 1510 ultrasonicator, NE-1000 syringe pump (New Era Pump Systems, Inc., NY), Dektak 3 Stylus Profilometer (Veeco Instruments, Inc. NY)
- 10ml thermobarrel vesicle extruder (Lipex Biomembranes Inc., Vancouver, Canada)

- Bruker D8 Advanced Powder X-ray Diffractometer with Cu-K_α source (λ=1.5418Å)
- JEOL 2010 high-resolution transmission electron microscope operated at 200kV
- Zeiss 1530 VP Field-emission scanning electron microscope
- Atomic absorption spectrometer (Varian SpectrAA-300)
- Absorbance microplate reader (ELx808, BioTek, Winooski, VT)
- USB2000-DT Spectrometer (Ocean Optics, Dunedin, FL)

3.1.9 Miscellaneous

- Index matching oil (n=1.518, Cargille, Cedar Grove, NJ), 68º dovetail prism (Reynard Corp., CA), TEM grids (Ted Pella), 99.99% Au shot (Premion, MA), Viton O-rings (McMaster Carr, CA), vacuum grease (Dow Corning),

3.2 Homogeneous Surfaces

Uniform surfaces enable experiments to be conducted in the most controlled manner. Although homogeneous surfaces rarely exist in biological systems, they facilitate the collection of experimental information that can be interpreted more easily. On the other hand, some unique properties in living systems are derived from chemical and physical heterogeneity. For many of the studies presented here, surfaces are prepared and assumed to be uniform so that the behavior of particle ensembles can be interpreted to yield some average response. The next major subsection in this dissertation deals with the role of patterned surfaces that are both naturally occurring (often random) and intentionally fabricated.

3.2.1 Sample and Surface Preparation

Microscope slides and coverslips were first cleaned in acetone in an ultrasonic bath for >5min. Surfaces were then rinsed thoroughly with DI water, placed in a 4:1 solution of DI:7X detergent for 20min at 100ºC (to remove inorganic debris such as silica dust), and then rinsed with running DI water for 10min to remove excess detergent. Samples were then removed and placed directly into a 3:1 mixture of 99% H_2SO_4:35% H_2O_2 (termed piranha solution) and left for 15min to removed organic contaminants and form a uniform oxide layer atop the glass surface (caution: piranha solution is a violent oxidizing agent and should be handled with care).

Particles were removed from the bottle and placed in DI water. The cleaning process began by centrifuging the particles at 14.5×10^3 rpm, removing the supernatant, and re-suspending in DI water at least 3 times. Centrifugation times varied from 15sec to 3min according to particle size and density. Particles were then suspended in a 4:1 solution of DI:7X detergent for 20min at 100ºC, centrifuged directly out of the hot bath, and rinsed >10X with DI water. A concentrated suspension of particles was added to nitric acid boiling at 80ºC and left for 20min. The suspension was diluted with an equal volume of DI water, centrifuged, and resuspended in DI water >10X to remove excess nitric acid. Cleaned particles were then used in this state or received additional functionalization such as silanes, Au films, lipid bilayers, etc.

Ionic solutions in these studies were prepared with deionized (DI) water from an in-house purification system. DI water typically had a conductivity of $1\mu S\cdot cm^{-1}$. Electrolyte solutions <5mM were tested with a conductivity meter prior to

experimentation. The pH of the electrolyte solution was maintained well above the isoelectric point of the colloidal particles to ensure a native negative charge. Solutions with concentrations <10mM were prepared by diluting a stock solution of 100mM by the appropriate amount.

3.2.2 Aqueous Cells for Studying Quasi-2D Dispersions

Depending on the type of experiment performed, sample cells were either flowcells, batch cells, or confined cells. The requirement for all cells was that they maintain a seal to avoid evaporation (so that the ionic strength would not increase) and they remain free of convective flows brought about through evaporation or thermal gradients. In the case of the confined systems, top and bottom wall separations approached that of the particles in order to keep smaller particles in a 2D state (i.e., prevent particles from diffusing over each other).

Batch cells were prepared by removing cleaned slides from DI water, drying them with a stream of nitrogen or air, and securely fashioning an o-ring coated in vacuum grease to the surface. The sample solution containing the colloidal dispersion was then pipetted into the o-ring at a volume of 100µl, and the batch cell was completed by placing a coverslip atop the o-ring and securing on the vacuum grease with tweezers.

Confined cells were prepared by taking a clean and dry sample surface, pipetting 15µl of the dispersion (10× more concentrated than in the batch system) onto it, placing a coverslip atop the drop, and securing the edges with quick-drying epoxy. Following curing, the system was permanently sealed. Furthermore, spacer particles could be

mixed in with the sample dispersion at a low concentration to ensure a precise wall-to-wall spacing.

Flowcells allow for the exchange of solution and adjustable control over the number of particles in the system. The method for creating flowcells depended on the type of experiment conducted. For instance, general adsorption experiments with unmodified glass surfaces or hydrophobic surfaces could be performed by creating a flowcell with a PDMS spacer mechanically sandwiched between a top coverslip and the bottom sample slide. In cases where superhydrophilic surfaces are used, flowcell leaking is an issue when using this technique. Instead, the PDMS spacer must be chemically bonded to the surface in order to maintain a proper seal. This is accomplished through exposure of the PDMS spacer to O_2 plasma in order to create silanol groups that can chemically react with the oxidized glass substrate. A schematic of the procedure is show in Figure 3.1. First, the cured PDMS spacer is cut to the appropriate dimensions and exposed to oxygen plasma for 20s at 100W at a O_2 flow rate of $5cm^3$/min. Next, the cleaned and oxidized glass surfaces are placed on a hotplate for 10min at 150ºC to remove excess moisture. By then placing the slide onto the activated PDMS spacer and setting it on a hotplate for 1.5hr at 100ºC, the PDMS and glass become covalently bonded. Following bonding, hypodermic needles can be inserted into the ends of the flowcell, and media can be exchanged easily. Additionally, methanol can be used as a lubricant to align features during the initial bonding step, but this is avoided for flowcell experiments with lipid bilayers, as vesicle fusion, rupture, and spreading is greatly hindered by the presence of physisorbed organic solvents.

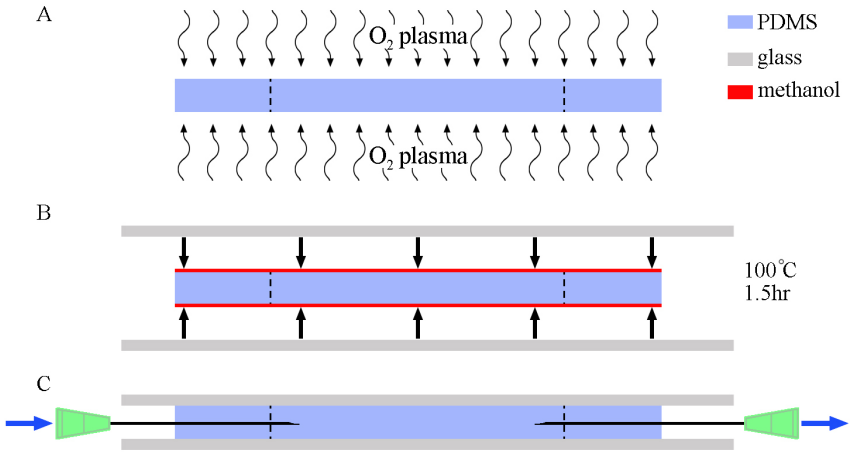

Figure 3.1. Schematic of flowcell construction showing (A) activation of PDMS spacer via O_2 plasma, which precedes (B) chemical bonding of the spacer to opposing microscope slides, which is then followed by (C) cannulation with hypodermic needles.

3.2.3 Self-assembling Monolayers

Self-assembling monolayers (SAMs)[59] in the form of silanes and thiols were produced through one of two techniques: vapor phase or solution phase deposition. All vapor phase bonding was conducted in a vacuum oven held at -20mmHg gauge pressure and 80ºC for 10hr. Solution phase self-assembly was performed at a molar concentration of 5mM for all silanes and thiols. OTMS and APS were bound in the presence of 0.1mM triethylamine to catalyze the methoxy groups, thereby exposing the Si groups. Glass slides were prepared by pretreatment with piranha solution for 15min, rinsing with copious amount of DI water, and drying of the container and slides in a vacuum over at 70ºC for 2hr to remove most of the residual water adsorbed to the glass surfaces. All solution phase bonding was carrier out in a desiccator jar for 10hr. Following the formation of SAMs, slides were removed and immediately rinsed twice with the same solvent they were immersed in during SAM formation (typically toluene for silanes and

200-proof ethanol for thiols). Hydrophobic slides were stored in toluene before use to reduce adsorption of hydrophobic debris such as dust. All slides were used less than two days after preparation.

3.2.4 Functionalized Supported Lipid Bilayers

Supported lipid bilayers (SLBs), shown in Figure 3.2, have been employed successfully as model systems for cell membranes for over two decades.[60] These surfaces mimic cell membranes in that they can undergo phase transitions, be functionalized with ligands, and possess transport properties similar to *in vivo* cell membranes. A few approaches can be taken to form SLBs on solid surfaces (patterned or uniform), but we use the method of vesicle fusion.[61] Once formed, bilayers freely float above the underlying substrate on a 0.5-2nm thick layer of water (determined by NMR, neutron reflectivity, and fluorescence interference microscopy[62]), which allows both the top and bottom leaflets to remain mobile and exhibit nearly the same degree of fluidity as freely suspended membranes. Moreover, a higher degree of separation between the bilayer and support can be achieve through the use of so-called polymer-supported membranes,[63] wherein the bilayer rests on a polymer layer residing between the bilayer and solid support. This approach reduces the frictional coupling between bilayer constituents and the underlying substrate (especially transmembrane proteins) and helps eliminate non-specific binding of membrane proteins to the solid support, thereby reducing protein denaturation and increasing lateral mobility and activity. Furthermore, the use of polymer-supported membranes has been shown to improve "self-healing" of defects within the bilayer,[64] an important criterion for the studies we perform. In this

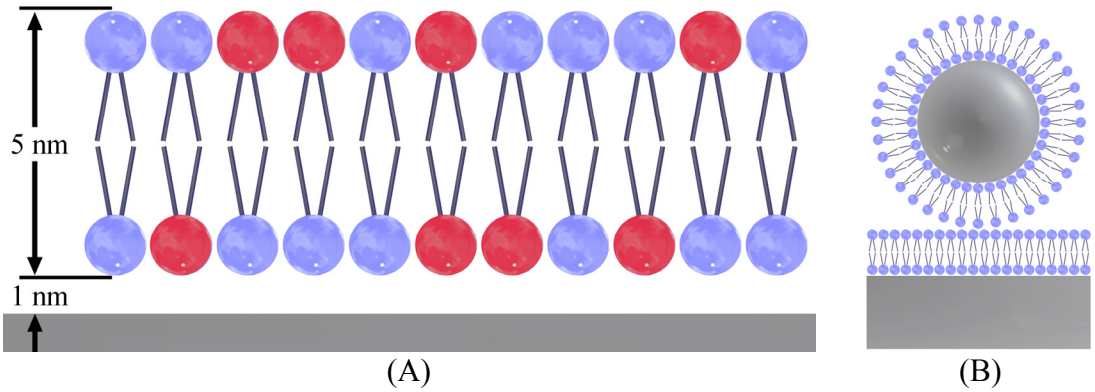

Figure 3.2. (A) Illustration of a SLB at a hydrophilic interface. A 1nm-thick water layer partitions the lower leaflet from the solid surface. Red lipid heads represent functional groups that can be incorporated into the SLB. (B) Experimental system used in this work, where particle and wall surfaces are modified with SLMs (note: (B) not drawn to scale).

work, we employ a form of polymer-supported membranes through the use of PEGylated lipids that provide a low density hydrophilic polymer brush layer above and below the bilayers. The advantage to this system, aside from imparting excellent stability to coated particles, is that the molecular weight and mole fraction can be easily tuned during the initial lipid mixing stage in order to control the brush density and thickness. Furthermore, the brush can be actively adjusted after the PEGylated bilayer is formed by utilizing specific ion effects to create poorer solvent conditioned for the PEG, thereby causing the chains to lose solvation and collapse.

Small unilamellar vesicles (SUVs)[65,66] were prepared via the extrusion method.[66,67] First, the appropriate amounts of each lipid (in chloroform) were mixed into a single solution in a glass container. Next, the chloroform was rapidly evaporated with a stream of nitrogen, and the lipids were then placed in a vacuum desiccator for 3hr to allow all of the organic solvent to be removed. The dried lipid mixture was then reconstituted with

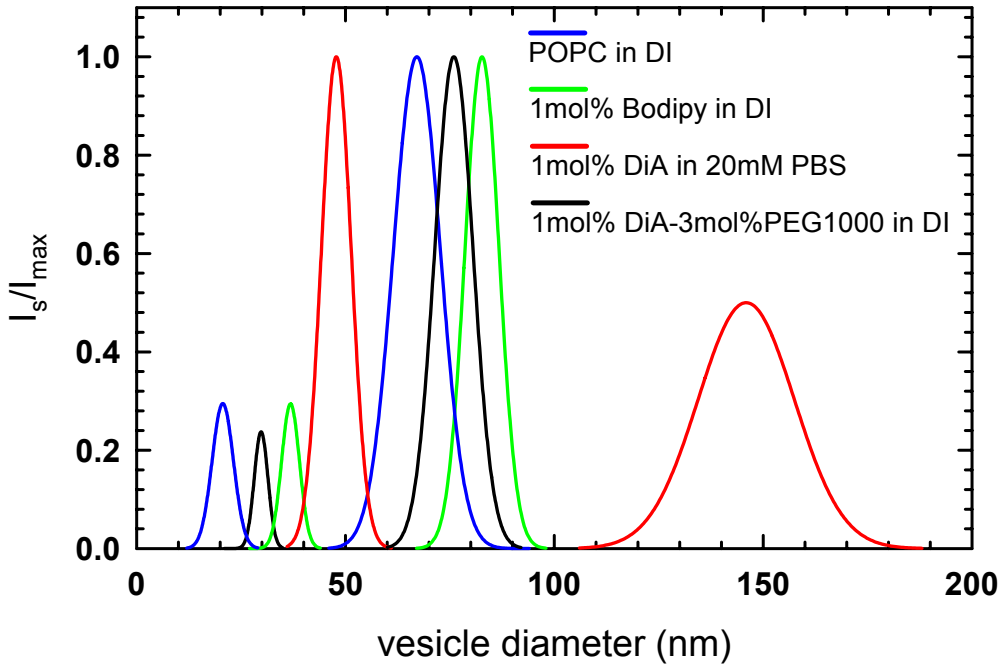

Figure 3.3. Dynamic light scattering data for vesicles, with various compositions and in DI water or PBS, extruded 10×.

10ml of DI water. This aqueous mixture was taken through 10 freeze-thaw steps using liquid nitrogen (-196ºC) and water heated to 70ºC. Note that this freeze-thaw step is critical to help break apart multi-lamellar lipid structures and ensure proper vesicle fusion and rupture during the formation of SLBs. Following the freeze-thaw cycle, the lipid solution containing highly polydispersed vesicles (ranging from 100s of nanometers to 100s of micrometers) was passed 10 times through an extruder holding a track etch membrane containing an average pore size of 50nm. The filter was replaced following the first and fifth extrusions.

After extruding, the average vesicle size was found with dynamic light scattering. Figure 3.3 gives typical data for vesicles with several different compositions. The particle size distribution of unilamellar vesicles prepared via the extrusion method is

related to the number of passes. Generally, the vesicle sizes fell within the size ranges shown in Figure 3.3. The vesicle dispersion was diluted by half with DI water to yield a final lipid concentration of 0.5mg·ml^{-1}. Vesicles were kept in DI water and at room temperature primarily to increase long-term stability. Note that the extruder used in these studies also permits the preparation of unilamellar vesicles at elevated temperatures, which is critical for producing vesicles from phospholipids with phase transition temperatures, T_m, above room temperature.

Bilayers were formed on superhydrophilic glass surfaces through vesicle fusion, rupture, and spreading.[61] Many variables dictate the manner in which vesicles fuse onto hydrophilic surfaces and eventually form continuous lipid bilayers. For instance, ionic strength can have the influence of blocking or facilitating the adsorption of vesicles, which is dictated by basic electrostatic interactions.[68] Furthermore, pH, which mediates the native charge surfaces carry, will have a similar effect,[69] depending on the charge of the hydrophilic surface (silica is negative at pH>3) and charge density and polarity of the lipid constituents. SLBs are formed as follows: (1) vesicles (Figure 3.4A) adsorb to the surface (Figure 3.4B) either through electrostatic or vdW attraction; (2) vesicles begin to flatted as vdW and/or electrostatic forces pull the lipids into contact with the underlying surface, reducing the exposed surface area of the vesicles (Figure 3.4C); (3) once vesicles on the surface reach a critical concentration, they begin to fuse with each other laterally, thereby forming two independent bilayers; (4) the top bilayer is liberated and returns to the media where it re-assembles into more vesicles; (5) the bilayer fills in small gaps (defects) by slowly diffusing across the surface and laterally connecting with

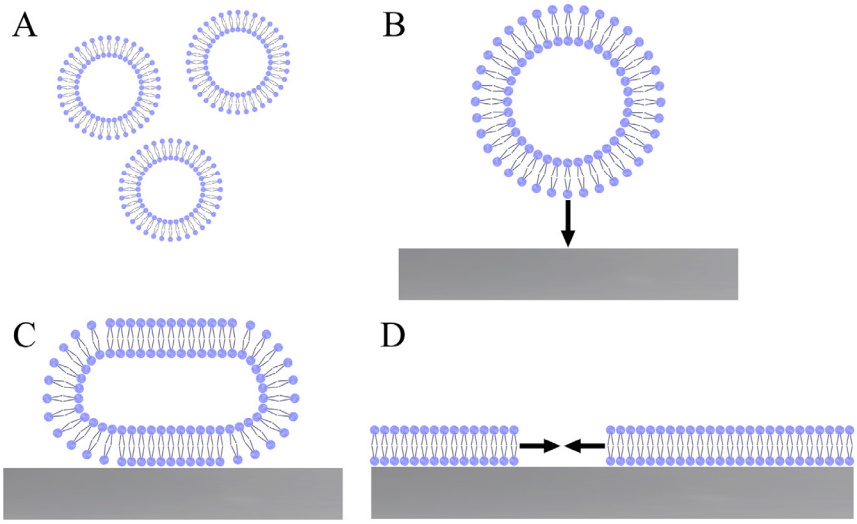

Figure 3.4. Simplified schematic of lipid bilayer coalescence following vesicle adsorption and rupture.

other lipid domains (Figure 3.4D); (6) excess vesicles adsorb to the surface and into defects smaller than the diameter of the vesicle.

In this work, vesicles were adsorbed at 150mM for 30min on pretreated glass slides and for 45min on silica particles of every size. Importantly, particles were not allowed to fully sediment in an attempt to prevent fusion of SLBs on opposing particles within the sediment; this was less of an issue for PEGylated lipids, due to the steric stabilization provided by the top and bottom PEG layers. Particles were also vortexed several times for 10s on high in order to help removed excess non-fused vesicles adsorbed to the particle surface.

One very important aspect of SLBs is that they can be functionalized with ligands subsequent to their formation. This is accomplished by incorporating reactive lipids into the initial lipid/chloroform mixture. Lipids can be functionalized with a wide variety of molecules that include, for example: PEG, fluorescent groups, metal chelators, biotin,

etc. In this research, we extensively utilize PEGylated, fluorescent, and metal chelating lipids for manifold experiments.

3.2.5 Physi- and Chemisorption of Macromolecules

Macromolecules adsorb to surfaces through two pathways: physical or chemical. The chemical pathway, also known as chemisorption, involves the formation of chemical bonds ranging from a few to several hundred *kT*, depending on the type of bond formed. For instance, strong secondary bonds such as polar or ionic can be considered in this class of adsorption, provided the bonding energy is large relative to vdW and electrostatic bonding. Simply put, the classification of bonding is subjective, aside from covalent bonding, which is strong enough to always be termed chemisorption. Physisorption is classified by weak forces such as those exhibited by "hydrophobic" interactions, electrostatic interactions near the isoelectric point, hydration forces, and vdW attraction. In these experiments, physisorption was the primary mode of adlayer formation, where F108, F127, F68, and BSA, for instance, were adsorbed to surfaces in this manner. In this research, chemisorption typically involved the bonding of his-tagged proteins to metal chelating agents, reaction of fluorophores to amine or maleimido groups, or the bonding of antibodies to their associated ligands.

3.2.6 Ni-Nitrilotriacetic Acid and His-tagged Proteins

When studying interactions between cell-cell adhesion proteins, it is crucial that the same protein activity seen *in vivo* be maintained *in vitro*. This requires that the protein: (1) not denature, (2) is oriented properly, (3) exists at the same interfacial concentration seen within the cell membrane, (4) possess the same intrinsic lateral

mobility, and (5) can interact with opposing proteins without hindrance from surrounding macromolecules.

To achieve proper orientation and activity, chemical bonding of the protein to the interface is requisite; non-specific physisorption would lead to denaturation and a loss of activity. In our system, this is accomplished through the use of polyhistidine tags (His-tags) and their affinity to the Ni-nitrilotriacetic acid (Ni-NTA) complex. First, cadherins are expressed in *E. coli* using recombinant methods to produce His-tags at the terminal end of the protein's extracellular fragment. After purification steps, proteins are available to be oriented and attached through the binding of expressed His-tags to Ni-NTA functional groups (Figure 3.5). Particles and wall surfaces were functionalized with Ni-NTA complexes through two methods: incorporation of Ni-NTA lipids into SLBs and multi-stage binding of Ni-NTA groups to silica surfaces through silane-thiol chemistry. The latter will be discussed in more detail in the following subsection, with an emphasis on patterning Ni-NTA groups on silica surfaces. Note that an advantage to using Ni-NTA incorporated into SLBs is that non-specific binding of protein is significantly reduced, therefore improving the overall performance of the surface; this is especially true for PEGylated SLBs, where the physisorption of proteins is probably completely blocked. Measurement of protein-protein interactions was performed with the SLB system, simply due to issues with colloidal stability Ni-NTA only.

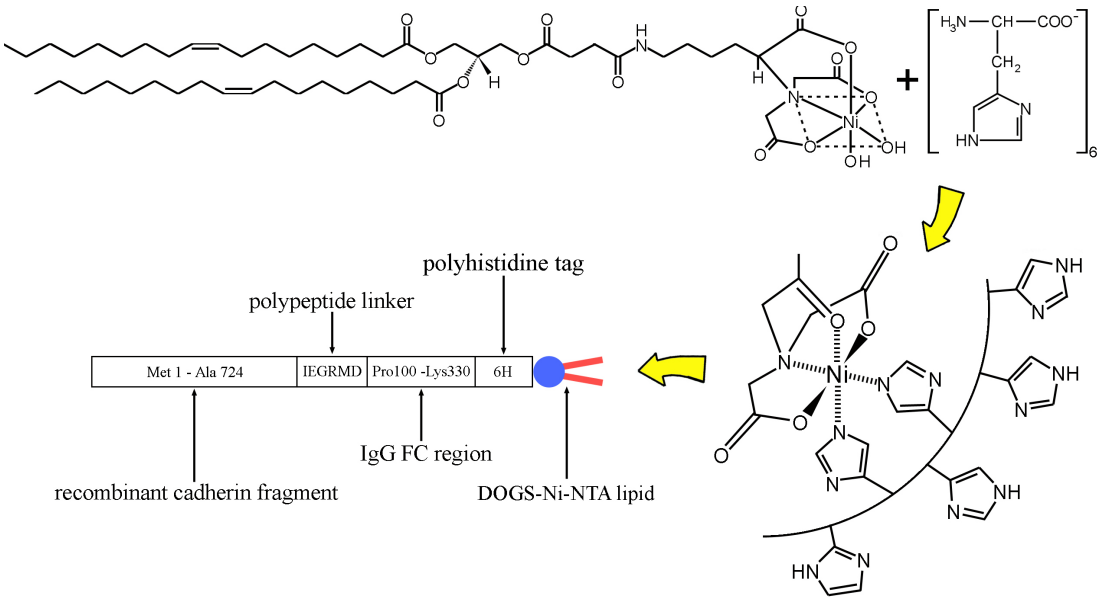

Figure 3.5. Diagram showing binding of a Ni-NTA complex with a 6XHistag linked to a cadherin fragment through a peptide linker and the FC region of an IgG molecule.

3.3 Heterogeneous Surfaces

3.3.1 Patterned Surfaces and Natural Heterogeneity

Chemical and physical surface heterogeneity is ubiquitous in synthetic materials and biological interfaces. While homogeneous surfaces are used as ideal models and often assumed in theory and experiment, real surfaces have finite, if not extensive, surface heterogeneity. The two types of heterogeneity encountered are either naturally occurring (typically random) or intentionally patterned with regular physical or chemical features.[70] Surface patterns can stand as: templates to initiate and orient colloidal assembly,[71] signaling cues in cell-cell interactions,[72] biomolecular arrays for high-throughput combinatorial measurements,[73] etc.

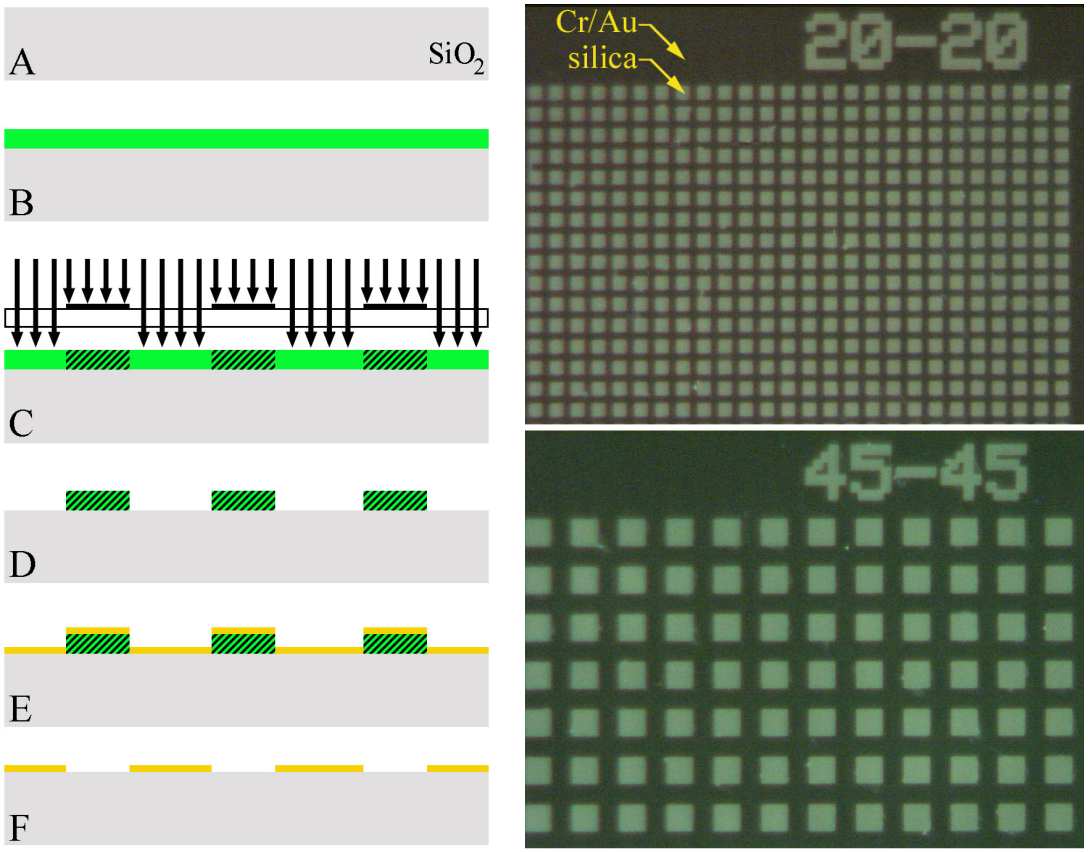

Figure 3.6. (A-F) steps for patterning metals with a lift-off technique. (G) Optical microscope images of patterned Au films with 20 and 5µm features (top) and 45 and 15µm features (bottom).

One significant advantage to employing substrates and probes with a variety of functionalities is that several interactions could be monitored simultaneously in identical environments, which would provide significant confidence when comparing the magnitude of interactions across several protein-protein interactions. The capabilities deomonstrated in this work provide the necessary basis for future research involving patterned substrates.

3.3.2 Chemical and Physical Photolithographic Patterning

Conventional photolithographic techniques were used to create both physical and chemical patterns, and all microfabrication steps were conducted in a class 1000 cleanroom. Generally speaking, the steps outlined below were carried out for all photolithography procedures. First, clean microscope slides were coated with an S1813 photoresist layer (~1.5 μm thick) was applied to the slides by dispensing 0.5 to 1 ml of photoresist onto the preheated (115 ºC) glass substrates and spinning at 3000 rpm for 30s. The photoresist was soft baked on a hotplate for 60 s at 90 ºC and then exposed to ultraviolet (UV) light through a patterned chrome mask for 4 s. Before being immersed in MF 319 developer for 60 s, the UV-exposed photoresist film was post baked for 120 s at 115 ºC. Following development, the photoresist pattern was placed in a reactive ion etcher (CS-1701, March Plasma Systems, CA) and exposed to oxygen plasma for 30 s at 200 W with an O_2 flow rate of 0.3 cm^3/s to remove any photoresist and developer residue on the glass regions.

As shown in Figure 3.6, slides with patterned photoresist were placed in a metal evaporator chamber (Edwards, BOC 306) and a 3 nm-thick layer of Cr was deposited at 1 Å/s followed by the Au layer at the same rate. Au thicknesses ranged from 3 to 15 nm, depending on the experiment conducted.

Chemical patterns with reactive functionalities were also fabricated with photolithographic methods. As a proof-of-principle example, a two lift-off techniques were devised and used to pattern reactive silanes on a glass surface. In the first (Figure 3.7A), photoresist was patterned atop a microscope slide and the reactive silane was

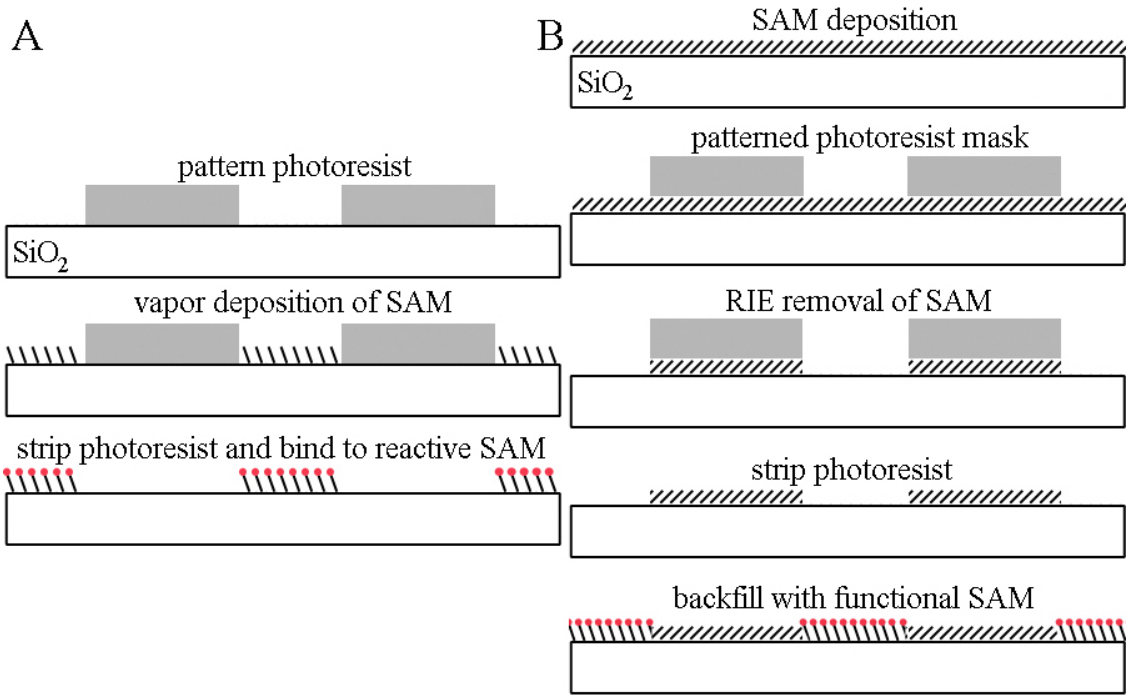

Figure 3.7. (A) Patterning silanes with a combination of vapor deposition and lift-off techniques. (B) Schematic of a method utilizing REI and backfilling techniques.

covalently deposited in a vapor phase. In the second approach (Figure 3.7B), a non-reactive blocking silane was first deposited onto the entire glass surface. Then, photoresist was patterned, and RIE was used to remove the regions with exposed silane. After stripping off the photoresist, the reactive silane was bound to the bare glass regions, and a fluorophore was subsequently covalently attached (Figure 3.8).

In glass substrates, physical patterns were created with negative photoresist (SU-8 2002) instead of positive resist, because of the reduced susceptibility to etching with the crosslinked mask. SU-8 was patterned with the above mentioned photolithographic steps, except a post exposure bake at 120 ºC was necessary to crosslink the exposed polymer prior to chemical development. Patterned slides were covered with a drop of diluted mixture of HF:DI water (10:1 or 1:1) for between 1 to 4 seconds in order to

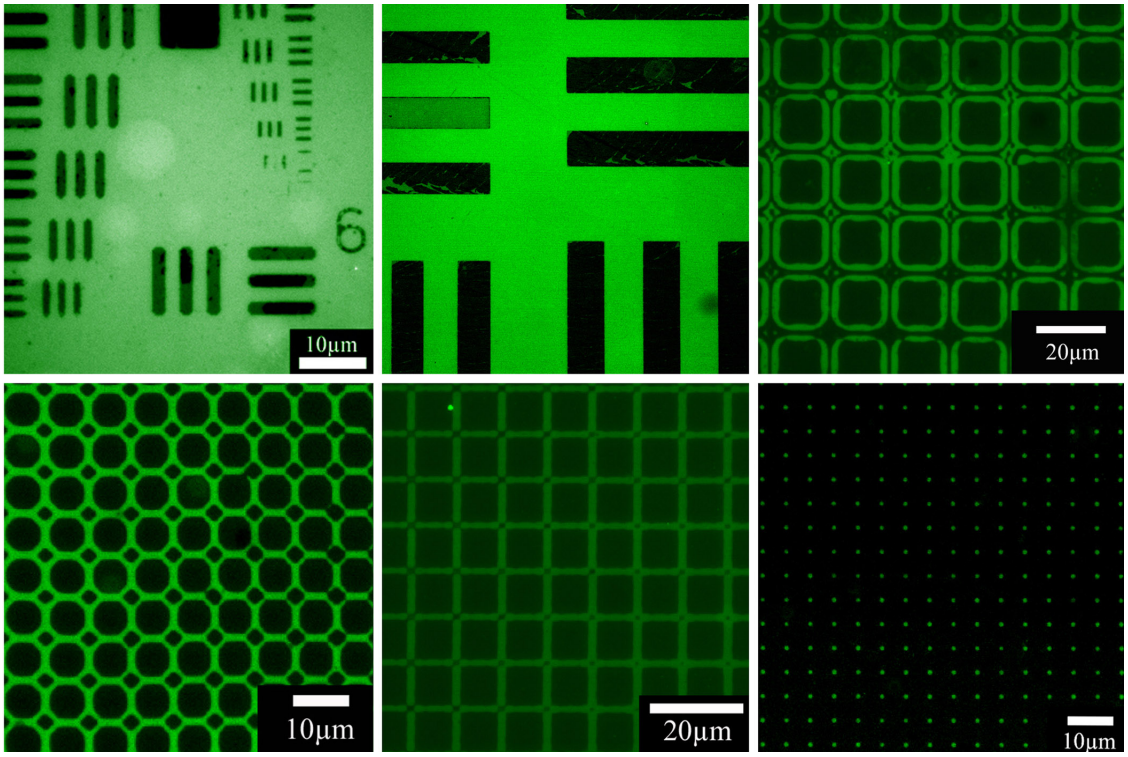

Figure 3.8. Confocal laser scanning microscopy images of patterned fluorophores in various geometries and with a range of feature sizes from 100 down to 1.0µm.

generate a range of physical depths. Etching was halted by rapidly rinsing the pattern with DI water. Results from physical patterning in glass are not presented here, but they point to the possibility of using an array of patterns to trap particle pairs and perform multiple particle-particle experiments where significant multi-body effects are negated.

In silicon wafers, physical patterns were formed using a single-step etch procedure. Briefly, silicon nitride coated <110> wafers were covered with a protective hard mask made from patterned SU-8 (patterned as described above). Chemical etching of the exposed nitride layer created a patterned region of Si vulnerable to wet etchants. 35% KOH at 70ºC was used to etch vertical sidewalls into the wafer for a predefined amount of time. A variety of physical features ranging from 150nm to 50µm were created and

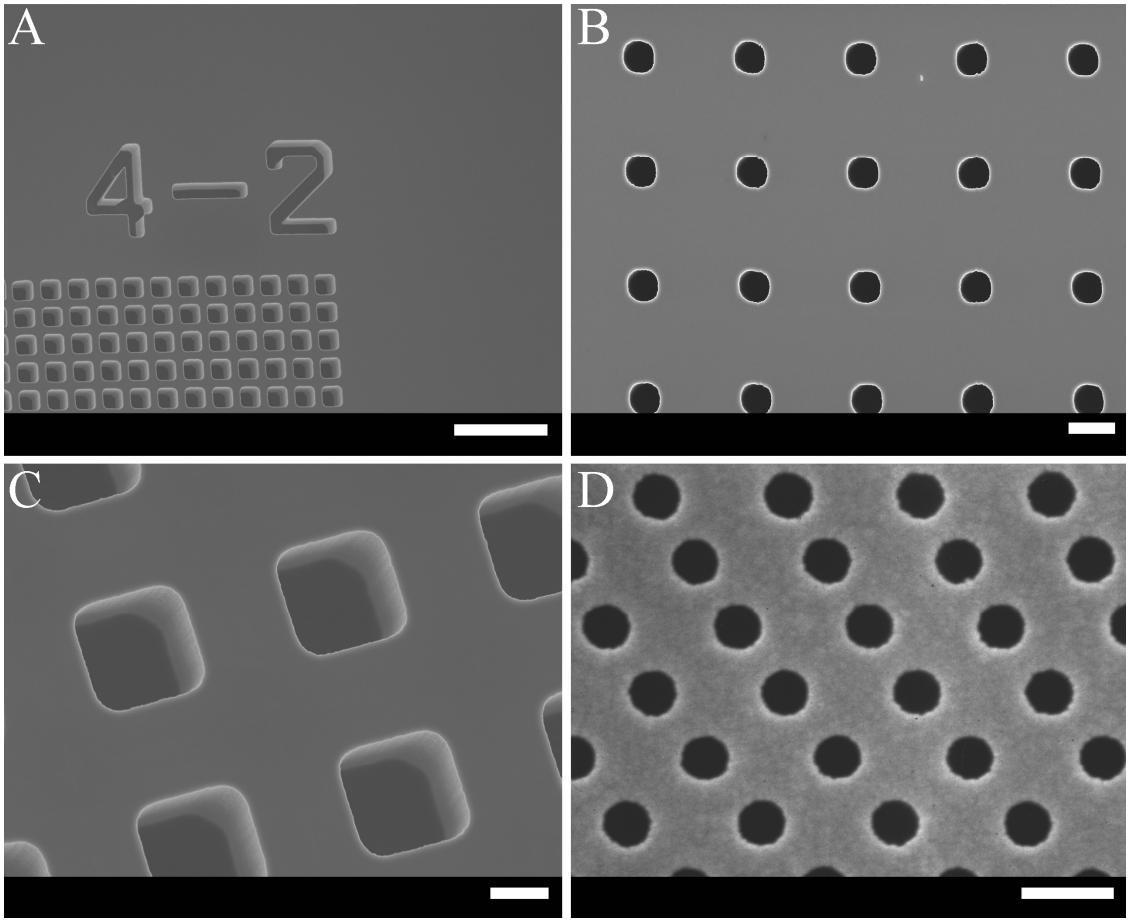

Figure 3.9. SEM image of patterned <110> silicon wafers. Scale bars: (A) 20µm (B) 3µm (C) 2µm (D) 500nm.

used for experiments such as microcontact printing and patterned of SLBs. Figure 3.9 shows several scanning electron microscopy images of physical features fabricated in Si substrates. The microscopes used in this research were not initially set up for reflection mode microscopy, thus these patterns were only used to illustrate potential applications.

3.3.3 Arranging Biomolecules on Micro- and Nanometer Scales

Patterned substrates can be useful for simultaneously comparing the behavior of multiple types of biomolecules in an identical environment, combinatorial high-throughput analysis (an extension of the previous point) on biomolecular micro-arrays,

or understanding how heterogeneity at different length scales can mediate complex interactions. The patterning work presented and outlined in this dissertation only addresses the fabrication of such patterns; testing these patterns was beyond the current purview of the research. To demonstrate feasibility, oriented and active cadherin fragments were patterned on a glass surface using an approach similar to that outline in Figure 3.7B. Briefly, OTS was deposited on the entire glass surface, photoresist was patterned on the OTS, and RIE was used ash OTS off of the exposed regions. Next, the slide was immersed in MPS (a mercapto silane) to backfill the newly oxidized region. This patterned silane was then modified with maleimido-NTA (Figure 3.10) that was chelated with Ni by immersing the surface in a 5mM solution of $NiCl_2$ for 1hr. This Ni-NTA complex was then available to bind to the His-tagged region of E-cadherin fragments. To test the activity of the protein and image the pattern, the protein-modified surfaces were incubated with 1mM fluorescent E-cadherin antibody for 1hr and then imaged with confocal laser scanning microscopy at an excitation wavelength of 633nm and long-pass filter of >650nm. Figure 3.11 shows results from this method of patterning, which proves that the E-cadherin was oriented and active on the Ni-NTA regions of the pattern. Note that a very minimal amount (<1/100th active region) of non-specific adsorption of either the antibody or protein was observed on the OTS regions.

Proteins and other biomolecules can also be patterned through the use of SLBs (Figure 3.12). An enormous collection of literature has outlined different approaches to patterning SLBs.[74] Here, we show a method that utilizes physical patterns to spatially SLBs.

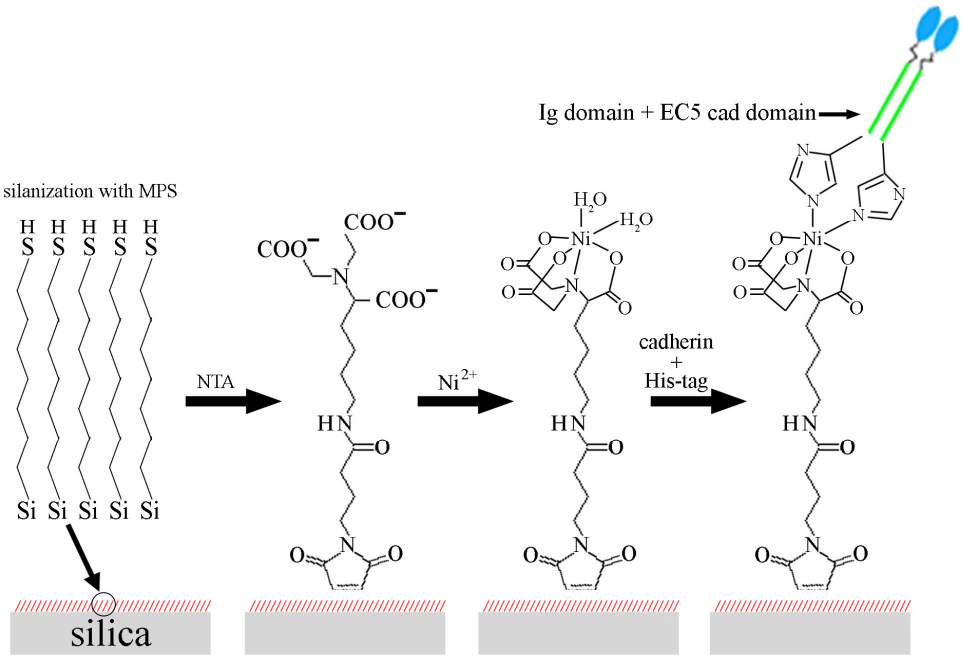

Figure 3.10. Modification scheme for attaching cadherin fragments to glass surfaces through silane and Ni-NTA chemistries.

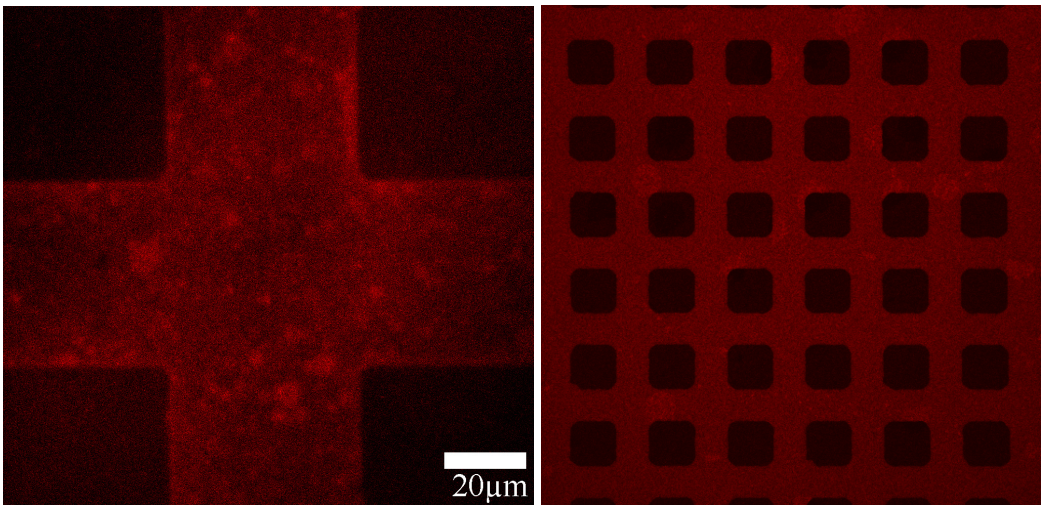

Figure 3.11. Patterned E-cadherin with fluorescently labeled antibody, compared to fluorescence from OTS regions from non-specific adsorption of antibody (dark regions). Controls run without Ni-NTA modification showed equal levels of fluorescence on the MPS and OTS regions. The scale bar is identical for both images.

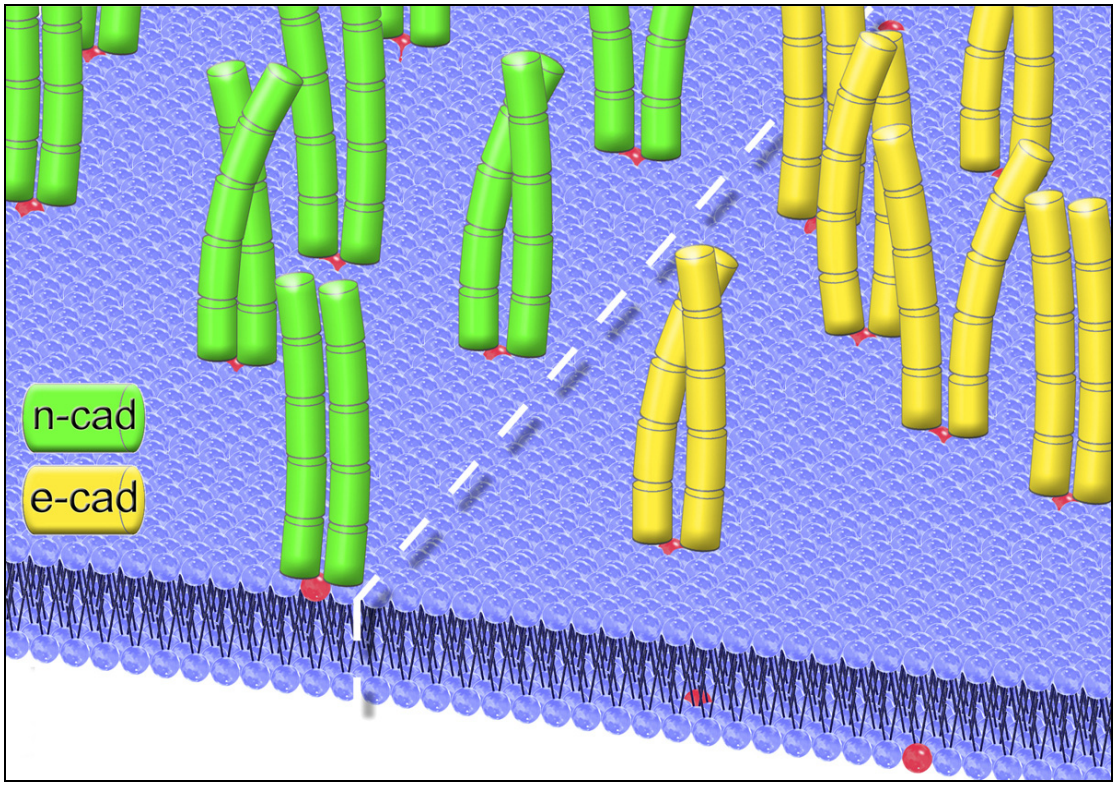

Figure 3.12. Illustrative graphic of patterned subfamilies of his-tagged extracellular cadherin fragments immobilized on a supported lipid membrane via Ni-NTA lipids, which can be fluid or gel-like.

Si substrates with etched feature sizes down to 200nm in dimension were used as supports during the formation of bilayers. Vesicles adsorbed and fused to the top Si surface but not to the regions containing holes and trenches. Confocal microscopy was used to image the resulting fluorescently labeled pattern, as seen in Figure 3.13. Further, SLBs in these arrangements may be useful in novel FRAP experiments.

3.4 Synthesis of Specialized Probes

3.4.1 Importance of Functional Particles

Particles with tailored functionalities can be a tremendous asset and often the only means through which certain data can be gathered. Functional probes range from modification with a luminescent or fluorescent tag to covalently attached macromolecules to improve colloidal stability in a system. The study of proteins in this work would not be possible without robust methods to form uniform protein layers on nearly all particles in an identical manner. Furthermore, the specialized modification of particles with quantum dots (QDs) affords an opportunity to collect data in improved ways. This section outlines the synthesis and modification of several types of colloids used in this work—from individual QD nanocrystals 2nm in diameter to microscale colloidal particles doped with QDs having different spectral signatures.

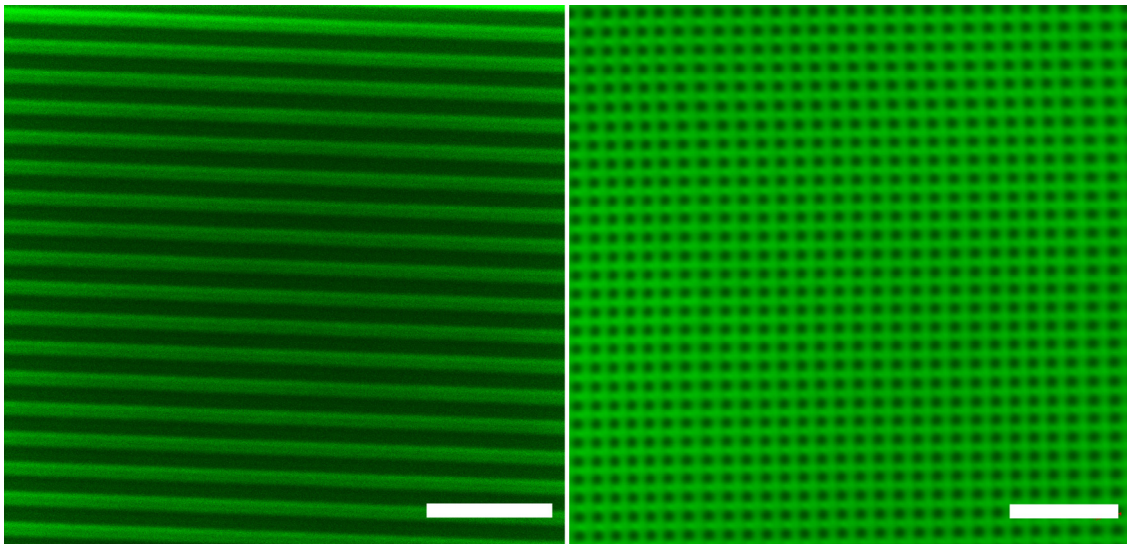

Figure 3.13. SLBs formed on patterned Si wafers. Scale bars: left = 4μm, right=2μm.

3.4.2 Stöber Synthesis of Silica

Stöber silica is prepared by reacting a tetra-alcohol-orthosilicate with water in an alcohol solvent, using a base as the catalyst. Typically, the silicate is tetraethylorthosilicate (TEOS), the alcohol is ethanol, and the base is ammonia. Other silicates and alcohols may be used, provided that water is miscible with the alcohol. Also, other bases or amines may be used; however, we have had limited success with this approach, because the higher pH values result in too fast of a reaction. It is not necessary that the alcohol attached to the silicate be the same as the alcohol (or mixture of alcohols) used as the primary solvent. For best results the (i) TEOS should be vacuum distilled, (ii) ethanol should be 200 proof (anhydrous, non-denatured), and (iii) water should be deionized and filtered. In our synthesis, we use a 29% aqueous ammonia solution (without further purification) as the ammonia source.

The ammonia concentration was maintained around 1M or less, the water concentration was held at 7M, and the TEOS concentration near 0.17M. Higher concentrations of ammonia tended to destabilize the dispersion, and values in excess of 3M typically result in too fast of a reaction. The final size of the particles depends on the concentration of the reagents—principally the ammonia concentration. Particle diameters from about 150 nm to 650 nm were possible using these concentrations. For larger particles, outer shells need to be grown by addition of TEOS, the reaction temperature needs to be lowered, other solvents need to be used, or surfactants such as SDS or Pluronic need to be incorporated into the mixture

The reaction time at room temperature was about 2 hours, but a majority of the reaction happens in the first 30min. Note that, even after a day or two, there will still be some unreacted TEOS remaining. If performing seeded growth, the TEOS concentration should not be doubled any faster than once every 2hr. During seeded growth, synthesis can last for 2-3 days before a significant number of fused doubles and clusters are formed.

Following a complete synthesis cycle, it is important to immediately dilute the reaction mixture with methanol or another alcohol to reduce the ammonia concentration, thereby ensure the stability of the particles. Water should never be used to dilute the dispersion, as this inevitably results in the formation of numerous smaller particles (probably from the unreacted TEOS). Allowing the particles to sediment under gravity and redispersing the particles in fresh alcohol (repeated 2×) will remove most of the water, ammonia, and unreacted TEOS, allowing for long-term storage without stability concerns.

3.4.3 Quantum Dot Synthesis

Three size distributions of ZnS-capped CdSe QDs (a=1.5 to 2.5nm) were prepared according to well-established protocols. Briefly, CdSe QDs were synthesized from CdO and Se in TOPO[75] and then capped with ZnS.[76] Specific size variations (i.e., emission characteristics) were achieved by quenching the reaction at predefined times. Prior to redispersion of the QDs in chloroform, excess TOPO was removed by repeated washes (>10) with methanol and hexane through centrifugation and ultrasonication.

ZnO nanoparticles (a=1.0 to 2.5nm) were synthesized via an aqueous wet chemistry method[77] and used in a cytotoxicity study outline in Appendix A. Usually, colloidal ZnO nanoparticles are formed in different types of alcohols (e.g., methanol, ethanol, propanol. etc.). The advantage of using methanol over other alcohols is that its dielectric constant is higher and it has a low ligand affinity. In this work, we use a simple sol-gel method involving methanol to synthesize ZnO. Briefly, zinc acetate dehydrate was hydrolyzed in basic methanol. Impurities such as K^+, Ac^-, and Zn-LDH were successfully removed from the final dispersion through destabilization, rinsing, and redispersion.

By including polyvinyl pyrrolidone (PVP) during synthesis, ZnO QDs could be made water soluble down to the single nanoparticle level. Additionally, the size of the ZnO aggregate could be easily controlled from several microns down to the single QD level with subsequent stabilization with PVP in weight ratios ranging from 50:1 up to 250:1 (PVP:ZnO). Results from this work are presented in Appendix A.

3.4.4 Quantum Dot-Modified Probes

Three different PS particle sizes (i.e., ~4, 5, and 6μm) were modified with three size ranges of QDs to yield a distinguishable emission range (i.e., ~540, 590, 640 nm) for each particle population. As illustrated in Figure 3.14, sets of QD-doped PS particles were prepared via a protocol similar to that given by Han et al.[78] Firstly, unmodified particles were transferred from water to 1-butanol through multiple rinses (five times each) in 200-proof ethanol and then 1-butanol using centrifugation and redispersion through ultrasonication. Next, QDs dispersed in chloroform were added to the PS/1-

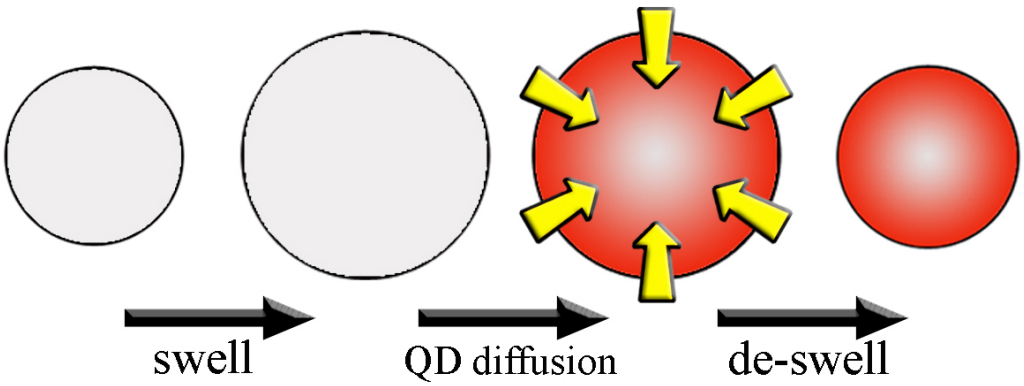

Figure 3.14. Steps for modifying polystyrene colloids with quantum dots.

butanol dispersion at 5 vol% and left for 12 hr on a shaker; chloroform swells the PS, thereby facilitating the diffusion of QDs into the interior of the particle. The doped particles were sedimented and then redispersed in 1-butanol to "de-swell" the PS. This step was repeated >3 times in order to remove any excess QDs and chloroform in the media. The modified particles were then sedimented and redispersed two times in anhydrous ethanol, transferred to DI water, and stored at 4ºC until needed.

Preliminary research was conducted to modify silica particles with a shell of QDs, followed by a shell of silica. This protocol utilizes silane chemistry in combination with the formation of disulphide bonds to covalently attach QDs to a silica matrix gown on seed particles. Two immediate applications of these particles are envisioned: studying particle-wall interactions in indexed matched systems with luminescence and using two spectral populations of particles functionalized with two different cadherin subfamilies in a particle sorting experiment (akin to those detailed in *Section 4*). In the case of the former, indexed matched systems could potentially facilitate the ensemble measurement of a surface with near monolayer probe concentration—something not achievable in

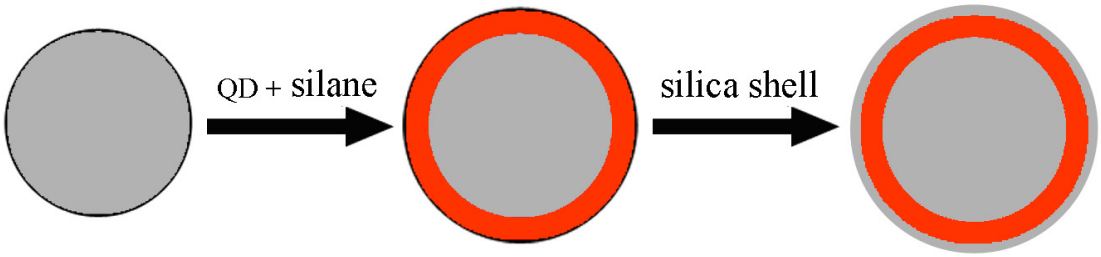

Figure 3.15. Steps for synthesizing core-shell silica with quantum dots.

scattering mode due to interference from neighboring particles in the form of noise. The one advantage to this type of cell sorting experiment is that any observed rearrangement would be strictly thermodynamic, as the active aspect of living cells is negated. Additional details concerning the previous two ideas will be better understood after reading *Sections 4 and 10*.

3.5 Video and Total Internal Reflection Microscopy

3.5.1 Experimental Setup and Data Collection

Figure 3.16 shows a schematic of the entire TIRM system and Figure 3.17 is a digital photograph of the setup. The sample cell (shown as a flowcell here) is optically coupled to a 68º dovetail prism with index matching oil (n=1.518). A laser, passed through a focusing lens, was totally internally reflected off the fluid-glass interface to produce an EW that decays exponentially into the media. As the particles diffuse and interact with the EW, they scatter light with a corresponding height-dependent intensity. This scattered (or luminescent) light is collected with an objective (a 40, 63 or 100× with a 0 or 1.6× magnifier) and directed to a monochromatic CCD camera. The schematic

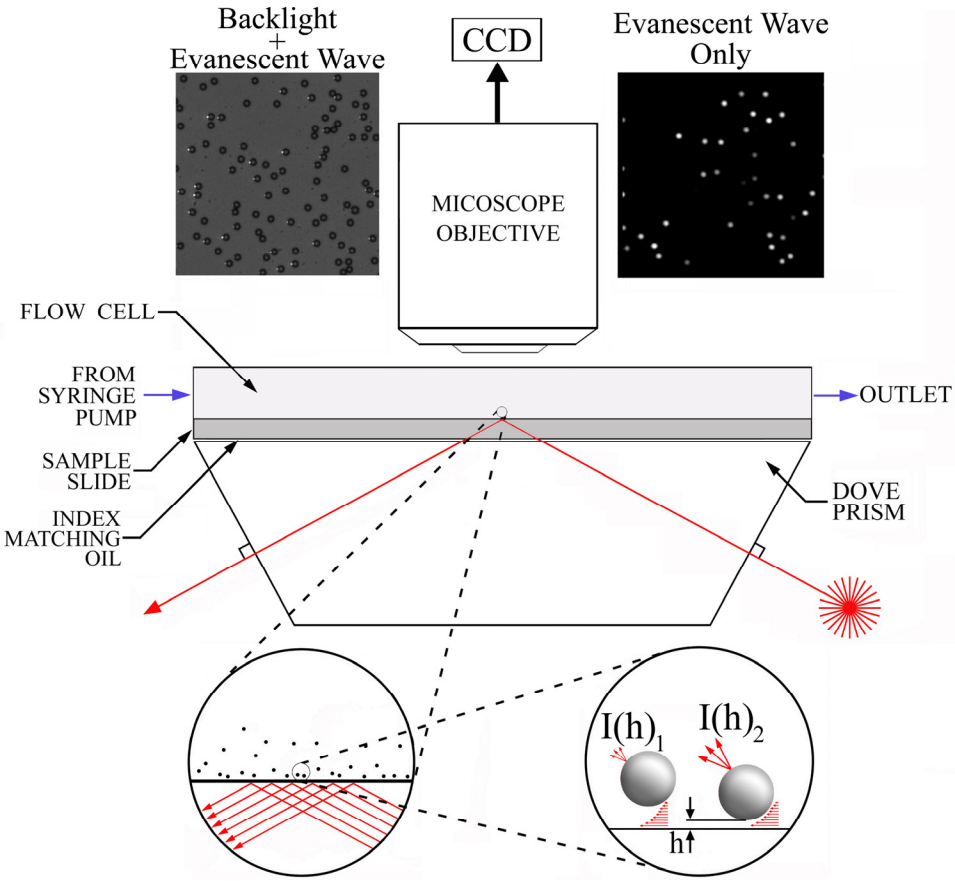

Figure 3.16. Schematic of ensemble TIRM setup.

shows images with and without the backlight. In majority of TIRM and LTIRM experiments, pixel size was set at 1214nm.

The CCD camera in this work was a 12-bit Hamamatsu (ORCA-ER) with a maximum frame rate of 43fps, which is too slow for complete dynamic data to be collected in the normal direction; higher frame rates allow for he autocorrelation function to be constructed, and from that, the perpendicular diffusion coefficient to be ascertained. The frame rate, however, was beyond the requisite speed needed to accurately assess lateral mean-square displacements. In most experiments, the camera was operated in 8-binning mode, unless excess noise mandated a higher resolution

setting. For LTIRM data collection, the exposure time was increased to approximately 0.02s, forcing the camera speed to below 10fps. Most data sets contained at least 80,000 frames, but lower or higher frame numbers would be collected depending on the number of particles and noise in the system. Data sets were normally collected within 35min, and sequence files ranged between 2 and 12GB, depending on the number of frames gathered and the camera resolution setting. Once collected, the image sequence (a multi-page TIFF file) was analyzed on a single-processor PC with Fortran codes that created a text document containing the lateral positions and integrated intensity from each particle in every frame. Image analysis algorithms are outlined in the following subsection.

Video microscopy data used to dynamically track particles for particle-particle analysis were collected on an inverted microscope through a 63× objective with a 2.5× magnifier to yield a pixel size of 38.5nm. When collecting $g(r)$ data, >2000 images were collected at a frame rate of 0.2 to 0.1 fps, depending on the size of the particle and

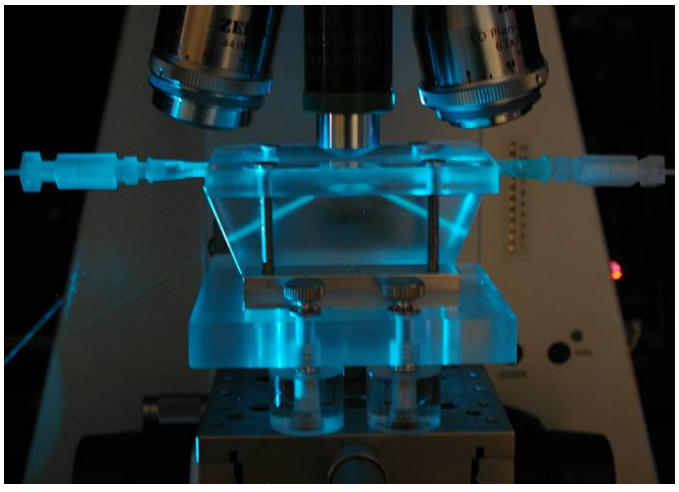

Figure 3.17. Photograph of the ensemble TIRM setup showing the flowcell, leveling stage, and total internal reflection of a 488nm Ar-ion laser beam.

system density. The lower frames rates in these experiments were to ensure particle positions were not redundantly sampled due to frame-to-frame correlative motion. In other words, the time interval between successive frames was large enough to guarantee the position of each particle exhibited no correlation to their position in the preceding frame. Thus, each particle-particle data set ranged from 4 to 5.5hr.

3.5.2 Image Analysis

Once a series of digital stills are collected with the CCD, whether it be from pair potential or TIRM experiments, particle centers and heights are found by analyzing the spatial distribution and magnitude of pixel intensities throughout each frame. Unlike a PMT, which effectively integrates the total single-particle scattering intensity in each frame, a CCD allows for multiparticle analysis, whereby the scattering signal from each particle within the window can be spatially resolved and quantified in order to track 3D trajectories. The key tradeoffs in this type of experimental approach, which have their own associated drawbacks, are: (1) lowering the binning size (i.e., increasing spatial resolution) leads to a drop in frame rate, (2) increasing the spatial resolution significantly increases the size of the sequence file, and (3) the use of higher magnifications increases spatial resolution but significantly narrows the window size.

The density of photodiodes within the CCD chip, N.A. and magnifying power of the objective, and wavelength of scattered/transmitted light dictate the adjustable spatial resolution of an optical microscopy setup. In general, the diffraction-limited resolution of any optics setup is approximated by $r_R = 0.5\lambda_0/\text{N.A.}$, but this is idealized and dependent upon factors such as illumination quality and particle-to-background contrast.

At best, one could expect to resolve features down to 200 nm using a wavelength somewhere near the middle of the visible spectrum. This resolution limit, however, severely hamstrings the accuracy of pair potential experiments, thus image analysis algorithms are needed to reach a much better lateral spatial resolution.

The tracking of particle centers from digital images is affected by imperfections that arise from contrast gradients (due to spatial CCD inconsistencies or uneven illumination), geometric distortions, analogue-to-digital conversion steps, or ambient electromagnetic noise. Crocker and Grier[27] suggest an image convolution process to correct for these distortions in order to find centers more efficiently and accurately. The final digitized noise is assumed to be purely random with a correlation length $\lambda_n \approx 1$ pixel. The convolution of an image area $A(x,y)$ with a Gaussian surface of half width λ_n is performed through

$$A_{Gauss}(x,y) = \frac{1}{B}\sum_{i,j=-w}^{w} A(x+i,y+j)\exp\left(-\frac{i^2+j^2}{4\lambda_n^2}\right) \tag{3.1}$$

where B is a normalization constant (given below), $A(x,y)$ is the set of pixel intensities of the real image at locations x and y, and i and j are the x and y coordinates in pixels. The entire frame can be smoothed to "level out" intensity variation and model the background using a simple running boxcar average algorithm via

$$A_{box}(x,y) = \frac{1}{(2w+1)^2}\sum_{i,j=-w}^{w} A(x+i,y+j) \tag{3.2}$$

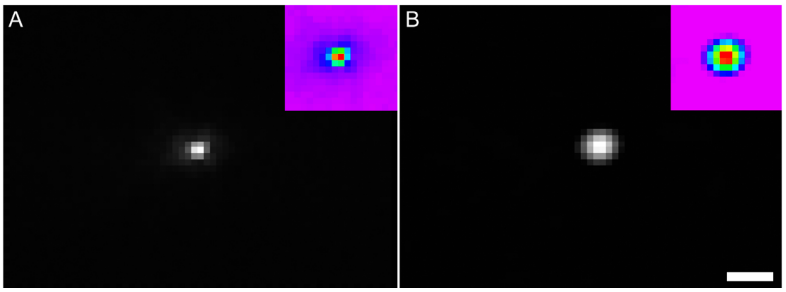

Figure 3.18. (A) Raw CCD image of single particle scattering in an evanescent wave. (B) Same image following convolution. Scale bar = 2μm. Insets are corresponding intensity contour plots for each case.

where w is an integer larger than the scattering pattern radius but smaller than the minimum separation between particles. Eqs. (3.1) and (3.2) can both be calculated in a single step using the convolution kernel

$$K(i,j) = \frac{1}{K_0}\left[\frac{1}{B}\exp\left(-\frac{i^2+j^2}{4\lambda_n^2}\right) - \frac{1}{(2w+1)^2}\right] \tag{3.3}$$

where B and K_0 are the normalization constants and are defined by

$$B = \left[\sum_{i=-w}^{w} \exp(-i^2/4\lambda_n^2)\right]^2 \tag{3.4}$$

$$K_0 = \frac{1}{B}\left[\sum_{i=-w}^{w} \exp(-i^2/2\lambda_n^2)\right]^2 - \frac{B}{(2w+1)^2} \tag{3.5}$$

with K_0, in particular, being used to make comparisons between corrected images with varying values for w. Thus, the total image convolution process is defined as

$$A_c(x,y) = \sum_{i,j=-w}^{w} A(x+i, y+j)K(i,j) \tag{3.6}$$

where A_c is the set of intensities of the final corrected image. Figure 3.18 shows a CCD frame of a single particle scattering an evanescent wave before and after the convolution process.

Following the convolution step wherein the effect of image noise is reduced, particle centers are located in each frame through a two-step process. The first step is a course search whereby the set of local brightness maxima, $[x, y]_p$ (for particles 1 to p), are found for each frame. As with Crocker and Grier's method,[27] a locally bright pixel is initially designated as a candidate particle center if there are no other local maxima within a distance of w from that pixel. In other words, this logic step is intended to discard other particle centers separated by less than one particle diameter, which would otherwise indicate overlapping particles. Since particle centers are likely to have intensities in the upper percentile of brightness, we filter out candidate particle centers belonging to the bottom 80th percentile in intensity. The final step in finding particle centers is a sub-pixel algorithm run on the original image ($A(x, y)$) that can, according to Crocker and Grier,[27] locate particle centers to at least 1/10th pixel resolution.

After the first filtering step that locates rough estimates for particle centers, a refinement algorithm can be utilized to more accurately locate particle centers based on finding the intensity-weighted centroids of groups of pixels around $[x, y]_p$ through

$$\begin{pmatrix} \varepsilon_x \\ \varepsilon_y \end{pmatrix} = \frac{1}{m_0} \sum_{i^2+j^2 \le w^2} \begin{pmatrix} i \\ j \end{pmatrix} A(x+i, y+j) \tag{3.7}$$

where

$$m_0 = \sum_{i^2+j^2 \le w^2} A(x+i, y+j) \tag{3.8}$$

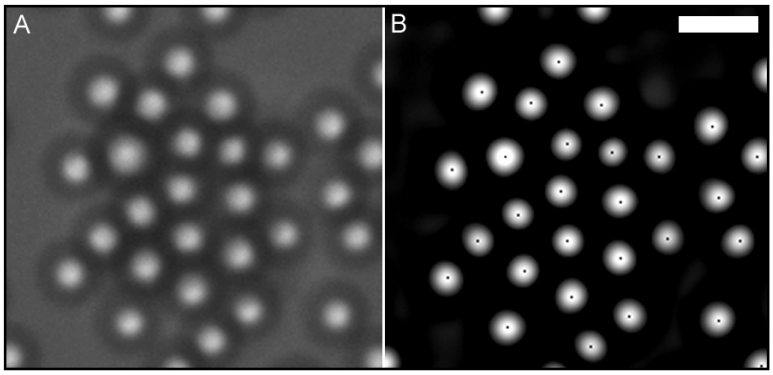

Figure 3.19. (A) Transmitted light microscopy CCD image of multiple 2.2μm silica particles (B) Same image following convolution and determination of particle centers. Scale bar = 5μm.

is the integrated intensity of a circular pattern around each local maximum (Figure 3.19). The refined, sub-pixel location of the particle's geometric center is $(x_0, y_0) = (x+\varepsilon_x, y+\varepsilon_y)$, but if $|\varepsilon_x|$ or $|\varepsilon_y| > 0.5$, the value of (x_0, y_0) is recalculated following a shift to the next pixel until the criterion is met. Importantly, the background subtraction step executed by the convolution kernel in Eq. 3.3 prevents falsely locating a particle at the center of the fitted region.

After particle centers are located in each frame, particle tracking simple involves linking particle centers in successive frames, where a characteristic distance, L, is defined to determine the minimum diffusive distance of a particle between frames. If more than one particle falls within a radius of L from a particle in the next frame, the closest centroid is considered to be the identical particle. Additionally, inaccuracies arise when identifying particle centers near the perimeter of the image, thus we discard centers found outside an inward border of $1.5a$ from the image edge.

Tracking 2D particle trajectories with the outlined steps above can be applied to both EW scattering and transmitted light modes of illuminating particle ensembles.

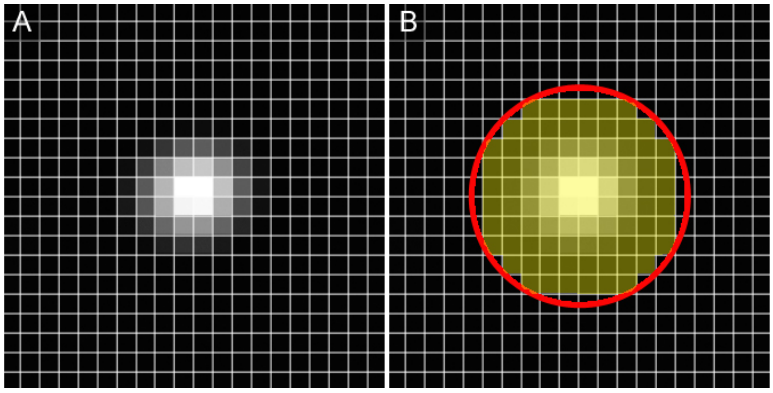

Figure 3.20. (A) Typical intensity pattern for a single particle scattering in an EW, with an apparent radius of 3 pixels (B) Example of integration area using for analyzing the type of pattern observed in (A), with an integration radius (in translucent yellow) equal to 5 pixels.

Because the EW scattering intensity from a particle is related to its instantaneous height via the exponential relation given in Eq. 2.15, normal height excursions can be found in parallel with lateral positions to generate 3D trajectory data. The scattering intensity is acquired by integrating all intensity values within a specified radius around each particle centroid, in the same manner described in Figure 3.20. Thus, the integrated scattering intensity, I_{int} is given by

$$I_{\text{int}} = \sum_{i^2+j^2 \le R^2} A(x+i, y+j) \tag{3.9}$$

where R is the integration radius and takes on an integer value. I_{int} is the combination of the background intensity and scattering intensity within the integration radius, but accurate particle-wall separations require that the background intensity, I_b, be subtracted. Hence, the actual scattering intensity from a single particle is described as

$$I = I_0 \exp(-\beta h) = \sum_{i^2+j^2 \le R^2} \left[A(x+i, y+j) - I_b \right] \tag{3.10}$$

3.5.3 Colloid Surface Association Lifetimes

Another important issue to address, especially in the context of steric experiments, is that of transients in particle stability that can be judged by lateral and normal short-time diffusive behavior. As particle-wall stabilization forces decrease (e.g., over a surface defect), particles may begin sampling locations nearer to the wall as the attractive energy well deepens. When the normal component of diffusion drops to a minute fraction of an average value for multiple successive diffusive steps, the particle can be considered deposited and temporarily in contact with the wall. Because the spatial resolution in the *z*-direction from this experiment (~1 nm) is at least two orders of magnitude more sensitive than in the lateral direction, the normal diffusive component is used as a short-time measure of particle motion. Of note is that the frame rate in these experiments was below the requisite speed needed to capture single perpendicular diffusive steps near to the wall, so small height fluctuations in successive frames correlate strongly with a deposited state. An alternative to this semi-empirical method is to employ a higher frame rate CMOS camera that can be used to deduce the average short-time diffusion coefficient of each particle normal to the wall through the autocorrelation function.

For each particle, the standard deviation of the height fluctuation, $\sigma(h_{i+j})$ (for $3 \leq i \leq n-2$ and $-2 \leq j \leq 2$ with n = total number of frames), for every five consecutive frames is calculated for the entire frame sequence. When $\sigma(h_{i+j}) < 1.5$ nm, the particle is deemed deposited during that time period and the h_ith frame is recorded as such. If this condition was satisfied in the next five frames (h_{i-1} to h_{i+3}), the h_{i+1} frame was added to the total

number of consecutive frames in which that particle was deposited, and so forth. The pixel colors in trajectory plots (*Section 5*) are indicative of the total time for which a particle was considered deposited onto the surface. Non-deposited lateral trajectories, where $\sigma(h_{i+j})>1.5$ nm, are plotted dark grey, and each deposition event at a single pixel location is illustrated graphically by an expansion to nine pixels to improve clarity. Single-pixel lateral translations of deposited particles (due to noise, stage drift, or actual diffusion) are visualized by partially overwriting the previous trajectory of the deposition event with a set of nine pixels demarcating a new deposition time. Therefore, some deposited particles appear to have two different time histories, which allows for the lateral diffusion record of a deposited particle to be more easily observed in a still diagram.

The semi-empirical value of $\sigma(h_{i+j})<1.5$nm was found through two means: (1) examination of adjusted TIRM profiles in which deposition events were accounted for and (2) single-particle Stokesian dynamics simulations using Derjaguin-Landau-Verwey-Overbeek (DLVO) separation-dependent potentials (Figure 3.21A). For the sake of brevity, details of Stokesian dynamics theory used here are omitted but can be found elsewhere.[79,80,81] In the latter, exact two-body hydrodynamics were applied in order to simulate the short-time diffusive behavior of a particle near a wall. Simulations were performed for three different well depths (0.5, 3.0 and 5.0kT) and height data was run through the height analysis code using four values for the σ_h parameter (1.0, 1.5, 2.0, and 2.5nm). Because simulated data is ideal and represents continuous diffusion, perceived deposition events determined with the code would be merely statistical in nature and not

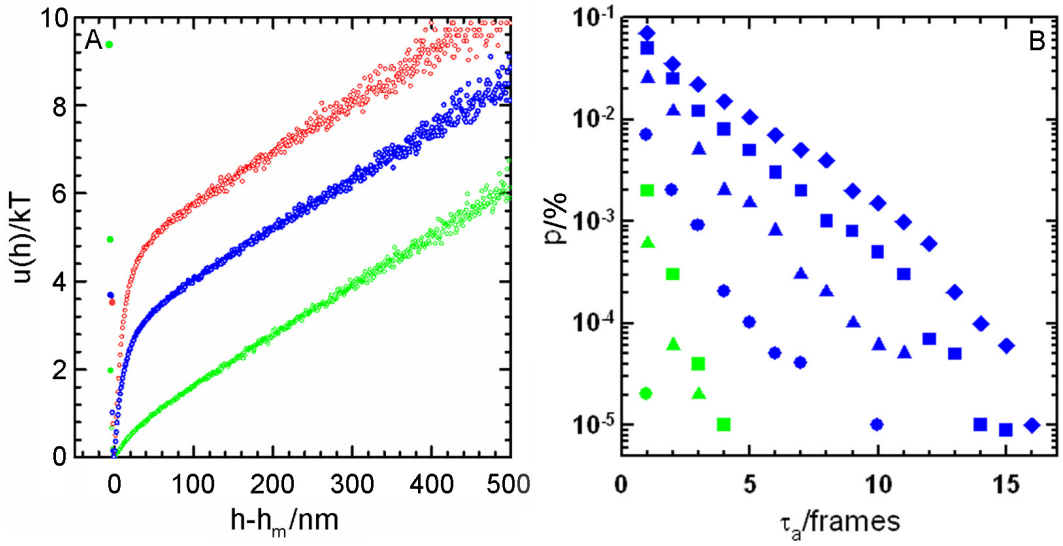

Figure 3.21. (A) Stokesian dynamics simulations of a single-particle TIRM experiment (10^8 frames) for a 2.2μm silica particle above a silica wall in a 5.0kT (red), 3.0kT (blue), and 0.5kT (green) attractive energy well. (B) Statistics from simulated data points in (A) representing the number of observed colloid "sticking" events vs. frequency using σ_h=1.0nm (●), 1.5nm (▲), 2.0nm (■), and 2.5nm (♦). Green symbols represent statistics from the 0.5kT well and blue are for the 3.0kT simulated data.

real. As can be seen in Figure 3.21B, the frequency of deposited events (in % of total frames) vs. the duration of deposition events illustrates that hindered diffusion produces statistical deposition events less than 5 frames in durations for values of σ_h<2.0nm. The more empirical estimate of the deposition parameter resulted from directly observing how changes in σ_h affected experimental profiles. Specifically, experimental data of fully levitated particles exhibiting no markers of deposition (e.g., subdiffusive behavior) were altered with various values of σ_h until a value that didn't increase noise in the profile was reached. Thus, after a complete theoretical and experimental examination of fully levitated (zero deposition events) systems, a value of 1.5nm was assigned to σ_h.

3.6 Confocal Microscopy

Confocal scanning laser microscopy (CSLM) was used to collect several types of data. Because it collects light through a scanned pinhole, ambient light is significantly blocked, thus high spatial resolution is achieved—typically around 200nm, depending on the wavelength of the emission. CSLM was performed on fluorescently patterned substrates to observe the quality and minimum dimensions of each feature. Images of QD modified colloids was gathered in order to quantify the distribution of luminescence and observe the presence of QD aggregates absorbed to the particle surface. 3D scans were taken with CSLM in order to define the geometry of neck formation between two fused SLBs. FRAP experiments were conducted on a confocal microscope in order to determine lateral transport properties within fluid SLBs. Fluorescently labeled antibodies bound to oriented and active protein fragments were imaged in order to find evidence of protein clustering. The dynamics of SLB formation were tracked in real time with CSLM to find differences in the quality of bilayers as a function of vesicle concentration. Defects in bilayers, including both excess vesicle adsorption and holes were imaged with CSLM. Finally, a multitude of control experiments were performed with confocal microscopy to determine the presence of non-specific adsorption.

3.7 Particle and Surface Characterization

3.7.1 Atomic Force Microscopy

Physical features such as surface roughness and feature step-heights were characterized by atomic force microscopy (AFM). AFM images were acquired in air under ambient conditions using a Nanoscope IIIa multimode scanning probe, from

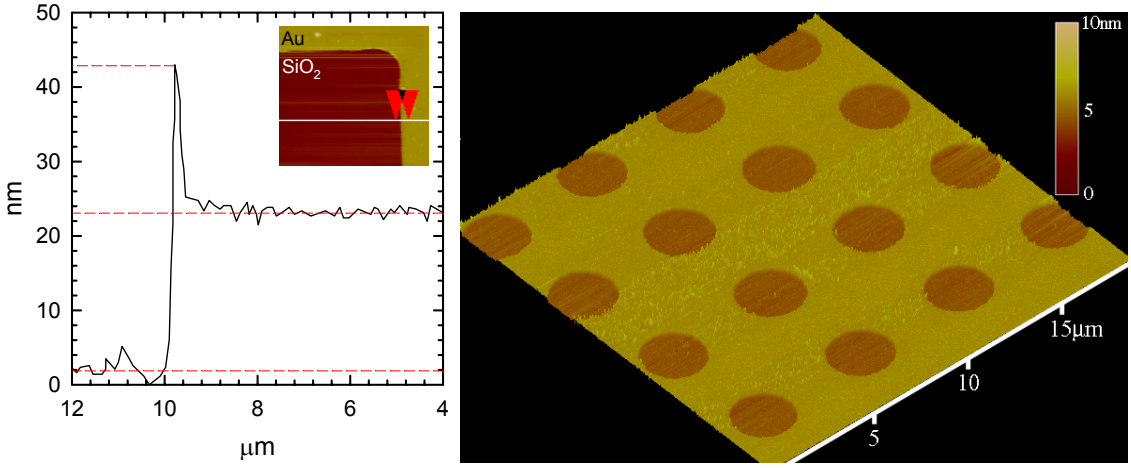

Figure 3.22. (Left) AFM profile showing pile-up near the edge of Au pattern that was fabricated using the photolithographic lift-off technique. Inset is topographic data with the white line indicating the profile location. (Right) Topographical scan on an OTS pattern on glass created using the RIE technique outlines in Figure 3.7.

Digital Instruments (Santa Barbara, CA), operated in tapping mode. Silicon nitride tips with a spring constant of 0.06N/cm and tip radius of curvature of <5nm were used. The cantilever assembly was driven with a piezoelectric crystal at a frequency just below its resonance frequency (typically around 350kHz). Scans were collected at maximum resolution (512×512lp) with window sizes ranging from 100nm to 10μm.

Unmodified glass substrates were found to have an RMS roughness (R_{rms}) of <1nm. Silanized surfaces normally exhibited R_{rms}= 2nm. Patterned features used for TIRM applications are required to have step heights less than 5nm, as larger step heights scatter the EW, leading to substantial noise. One exception to this is for lateral features aligned parallel to the EW direction. Figure 3.22 illustrates how pile-up can exist at feature edges when using lift-off methods to produce spatial patterns.

Particle surfaces were also examined with AFM to check for severe surface roughness and asperities (Figure 3.23). Particles were imaged by first drying out a

concentrated dispersion at sub-monolayer levels. In the AFM, the probe tip was positioned above a group of particles and brought into contact using a scanning are of 100nm. If the scan began successfully, the scan size was increased to 200nm and the curvature was examined. Depending on what portion of the particle was being imaged, the scan tube was repositioned towards the center of the particle and the scan size was increase to a maximum of 60% of the particle diameter; large scan sizes would lead to tips pushing the particle to the size and a loss of the image.

3.7.2 Surface Chemistry

Detailed chemical analysis of specific surfaces was carried out with X-ray photoelectron spectroscopy (XPS). XPS is a quantitative technique capable of measuring the chemical composition of the top 1-5nm of a surface. Spectra are obtained in an ultra high vacuum by irradiating a sample with an X-ray beam and simultaneously measuring the kinetic energy of photoelectrons emitted from the surface, which is directly related to their binding energy, B.E. The spectra plots photoelectron counts vs. B.E., which is used as a "fingerprint" for elemental composition.

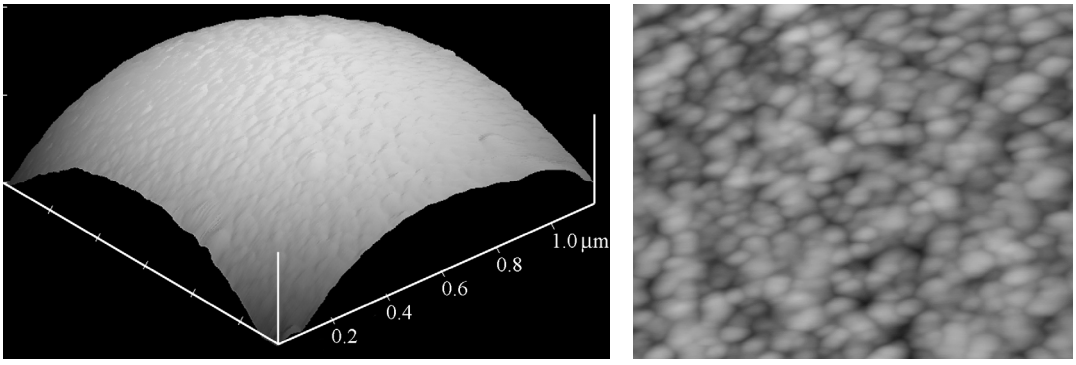

Figure 3.23. (Left) tapping-mode AFM scan of a 1-oct modified 2.2um silica particle. R_{rms} was found to be 1.7 nm (right) after modified plane fitting was applied to the data.

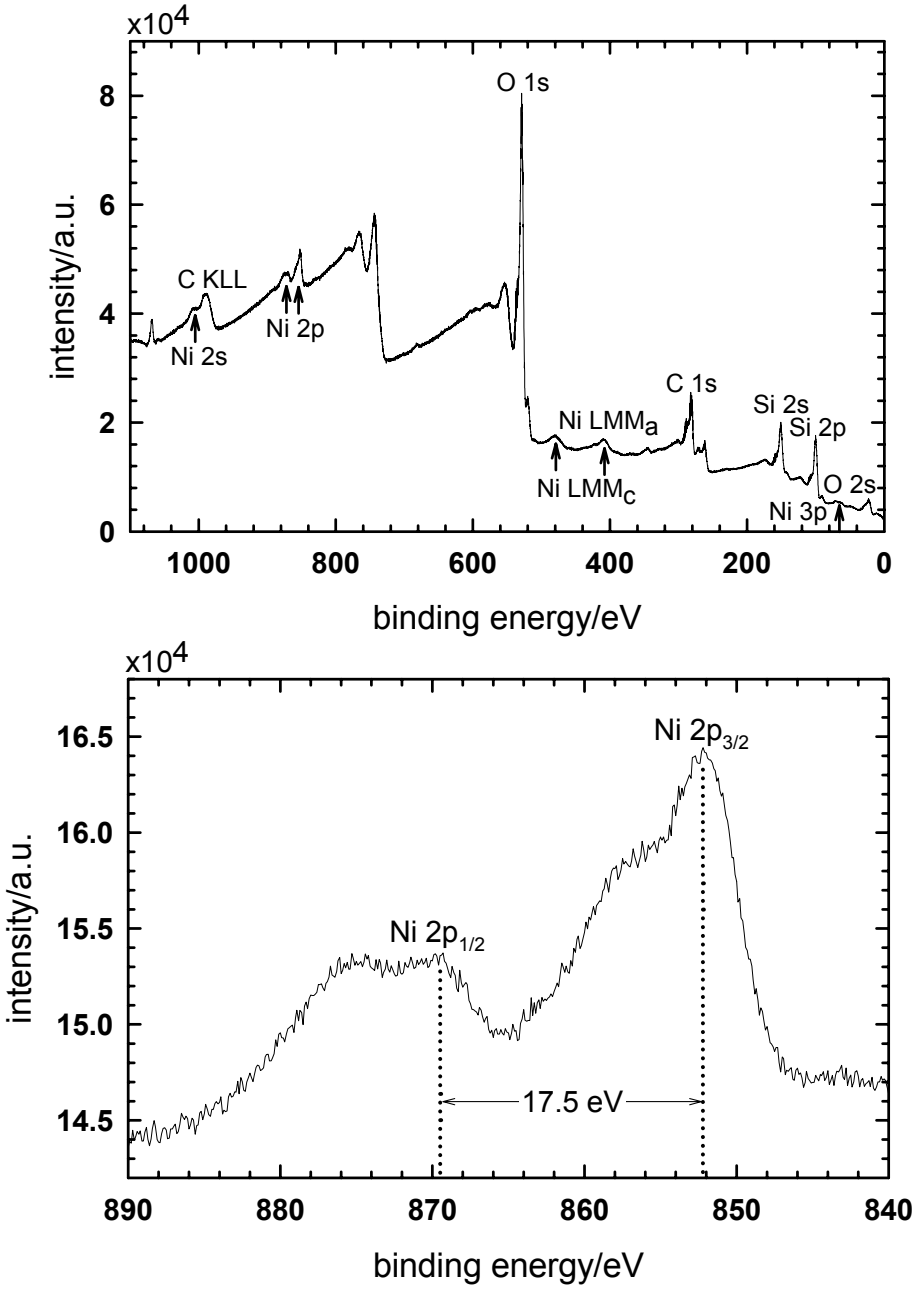

Figure 3.24. XPS survey (top) and high-resolution scan of the Ni 2p peak (bottom) of a glass slide functionalized with Ni-NTA.

XPS was utilized in these studies because it can quantify the presence of elements down to <0.5% atomic composition, depending on the sensitivity factor, and only examines the top few atomic layers of a surface. The patterned Ni-NTA surfaces discussed in *Section 3.3.3* were probed with XPS to determine if Ni was present. Several control samples were run, verifying that Ni was indeed irreversibly bound to the patterned surface. Figure 3.24 gives representative XPS spectra from Ni-NTA patterned surfaces indicating the presence of Ni at the surface.

3.7.3 Particle Sizing

Two main methods were employed in order to accurately measure the diameter of colloids used in these studies. The first involves drying out a sample into crystalline domains and then taking a $g(r)$, thereby determining the particle size from the first peak in the distribution. The second method is dynamic light scattering (DLS), in which a monochromatic laser is passed through a colloidal suspension and the time-dependent intensity fluctuations are monitored. Brownian motion of the particles is the source of these intensity fluctuations, so the time scale of movement of the particles is related to the time scale of intensity fluctuations. The second-order autocorrelation function in generated from the intensity vs. time data and used to calculate the diffusion coefficient, which is directly related to the particle's hydrodynamic radius. Additionally, a fairly accurate measure of polydispersity can be obtained from this technique. Results from these two methods applied to sizing nominal 2.34μm silica are given in Figure 3.25. Results from article sizing of 1.5μm silica through the $g(r)$ approach are shown in Figure 3.26.

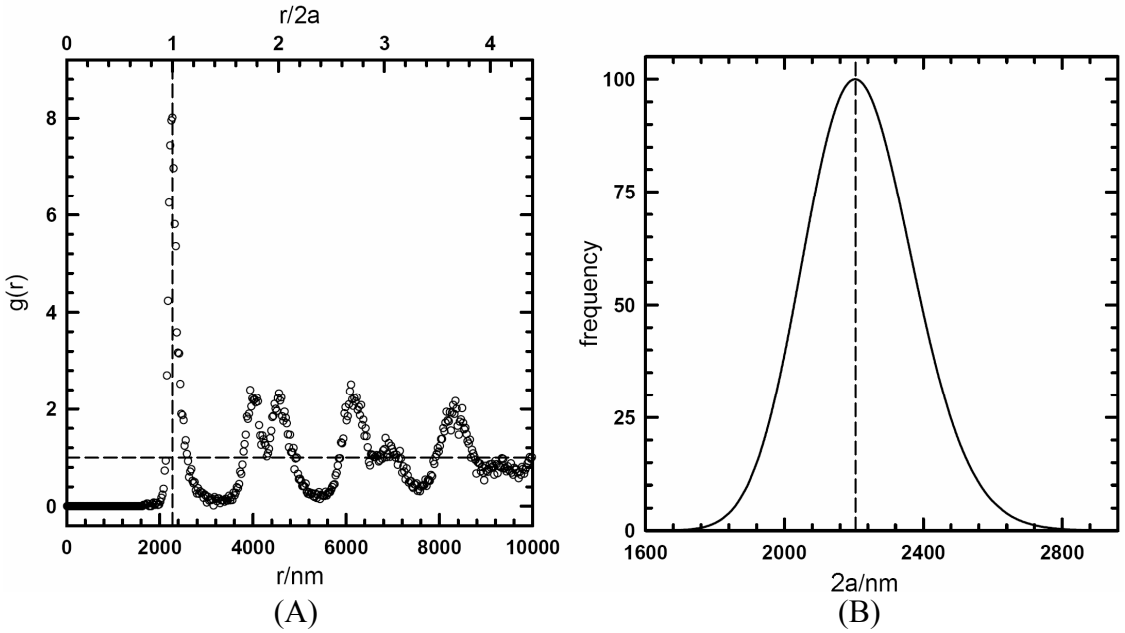

Figure 3.25. (A) CSLM-measured $g(r)$ of nominal 2.34μm silica dried into a crystal, showing a first peak at r=2a=2.22μm. (B) Dynamic light scattering result showing a log-normal distribution of sizes for the same silica particles, with a most probably size at 2a=2.21μm.

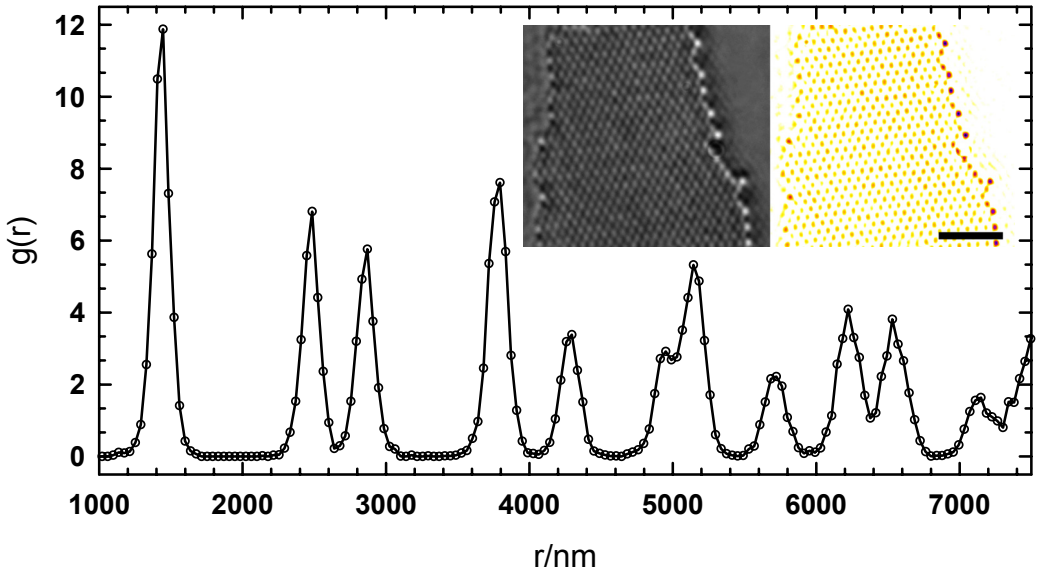

Figure 3.26. VM-measured $g(r)$ of crystal made from nominal 1.58μm silica colloids. First peak is located at 1.46μm, consistent with TIRM fits. Inset is a VM image of the dried crystal with (right) and without (left) processing. Scale bar=10μm.

4. STUDYING INTERACTIONS BETWEEN CELL-CELL ADHESION PROTEINS

4.1 Cell Sorting

Throughout every stage of embryogenesis, cells maintain an intrinsic ability to arrange themselves according to their fated cell type and position in the body. Early in this developmental process, cells sort into three distinct germ layers, providing the necessary segregation for localized cell differentiation and migration into characteristic locations that allow for the organization and formation of more complex tissues. Likewise, the regulation of cell-cell adhesion processes is crucial for the progression of diseased states such as cancer. That is, at a fundamental level, metastasis involves the down- or upregulation of cell-cell adhesion proteins, allowing cancer cells to disengage from their neighbors and migrate across cancerous and native tissue layers. What is more, beyond embryonic development and disease progression, recent studies have implicated adhesion molecules in synaptogenesis, or the formation of neural networks. The development of specific synaptic connections, following neural outgrowth in both the central and peripheral nervous systems, is almost certainly directed by surface receptor recognition and regulation of cell-cell adhesion proteins. It should be noted that there are many other areas of interest in adhesion molecule research, such as expression of adherin in tubulogenesis, asymmetric cell division, somite morphogenesis, cell migration and differentiation, neurogenesis, heart and neural tube morphogenesis, vasculogenesis, etc., that will have their discussions omitted for the sake of brevity.

Holtfreter (1939) was the first to find that tissue layering could be achieved *in vitro*[82] and, soon after (1947), demonstrate that embryonic cells could rearrange themselves and subsequently form recognizable anatomical structures after they were experimentally intermixed.[83] His research revealed that cells expressed a preference, or affinity, in their associations with other cells to the extent that they could adopt a particular *in vitro* arrangement similar to that seen over the course of normal embryonic development. The Differential Adhesion Hypothesis (DAH) is one of the most accepted explanations of this phenomenon and was formulated by Steinberg in the early 1960s.[84,85] The DAH proposes that the inherent sorting of cells and hierarchical envelopment of tissue layers is the result of a recurring exchange of weaker for stronger bonds between motile cells in a tissue that exhibits fluidity. Further, the final arrangement is that which minimizes the interfacial free energy and maximizes the cell-cell adhesion strength. In other words, the sorting out of intermixed embryonic cells and the envelopment (i.e., formation of concentric germ layers) of one tissue by another are analogous, respectively, to the aggregation of a dispersion (or emulsion) and encapsulation of one liquid by another liquid having a lower surface tension. It should be noted that "cell sorting" is not necessarily a morphogenic mechanism but rather a consequence of experimental intermixing of cells;[86] this process can, however, elucidate some valuable and otherwise experimentally unattainable information pursuant to tissue development hypotheses.

4.2 Cell-cell Adhesion Molecules

Studies by Ringer[87] (1880) and Herbst[88] (1900) illustrated that Ca^{2+}-free media could break tissues into cell dispersions. It was later proposed that Ca^{2+} could facilitate adhesion by desolvating the negative charges on the cell membrane,[89] and others hypothesized that Ca^{2+} may act to screen the repulsive electrostatic charges between membranes thus reducing their Debye screening length, κ^{-1}.[90] The work of Gray[91] (1926) inspired Rinaldini[92] (1958) to suggest that Ca^{2+} most likely promotes macromolecular adhesion sites, thereby creating colloidal "intercellular cement." This intermolecular binding was further specified by many[93] as ionic bridges between exposed phosphate and/or carboxyl groups present on the extracellular portion of the cell membrane.

The first major adhesion molecule identified from a vertebrate cell was named N-CAM.[94] Shortly after, it was determined that there are at least two mechanisms controlling the adhesion of cells: one completely independent of Ca^{2+} (at that point, only N-CAM had been identified) and another requiring it. It was shown that each mechanism can be temporarily suppressed with enzymes such as trypsin and cells expressing only one of the mechanisms are able to aggregate with like cells but not with others expressing only the alternate mechanism. Thus, for the first time, adhesion specificity was shown to be directly related to the type of mechanism (i.e., protein) expressed.

Calcium-independent adhesion molecules comprise the "immunoglobulin" (Ig) superfamily of proteins, of which the aforementioned N-CAM was the first discovered. The third and, to this date, only other known cell-cell adhesion molecule family are the "selectins," which are involved in the inflammatory response.

4.3 Cadherins

The first calcium-dependent adhesion protein was discovered by Takeichi[95] in 1977 from his work with V79 (a cell line from hamster lung), trypsin, EDTA (a chemical that sequesters divalent cations), and a host of cations.[96] Many other calcium-dependent adhesion proteins were identified within several years of Takeichi's initial discovery and were found to be genetically similar; therefore, the universal name "cadherin" (a combination of "calcium" and "adhere") was given to the superfamily of these cell-cell adhesion molecules.

Cadherins play a crucial role in tissue morphogenesis and embryonic development.[97] More specifically, they direct cell sorting processes that lead to the formation of distinct tissue layers.[98,99] After development, cadherins regulate the reorganization and turnover of higher-order cell structures and are responsible for maintaining the structural integrity of solid tissues by adhering adjacent cells.[98] Moreover, cadherins have been found to be important in regulating apoptosis, establishing tissue polarity, and maintaining cell differentiation and tissue morphology.[100] Although, for example, VE-cadherins are responsible for sustaining the barrier properties of the vasculature, they must also allow for constant rearrangement (bond breakage and reformation), as cells in the endothelium are highly motile, and blood vessels undergo constant remodeling in response to altered hemodynamic loads.

Four types of cadherins compose the entire cadherin superfamily: desmosomal cadherins, protocadherins, cadherin-like proteins, and classical cadherins. Of these four subgroups, the latter is the most extensively studied. The nomenclature given to classical

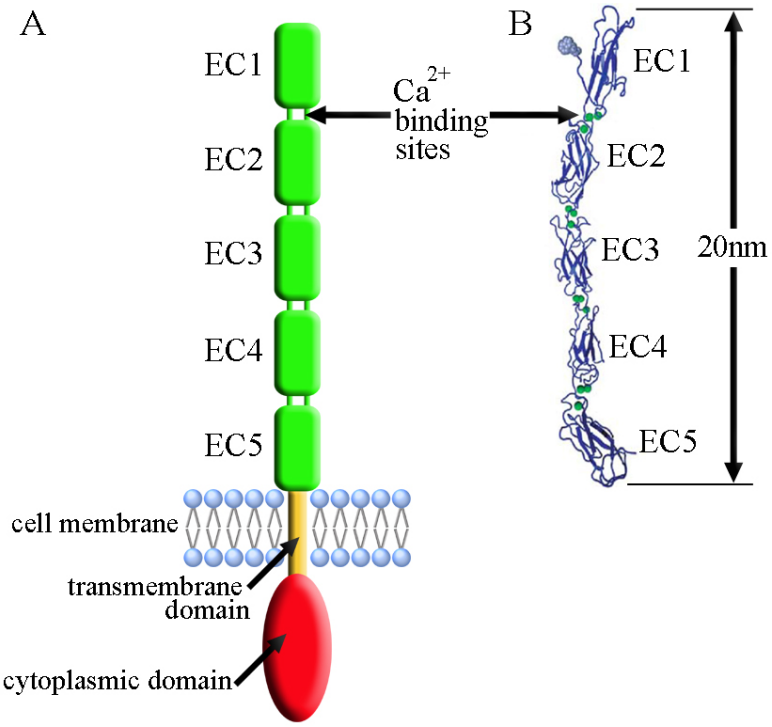

Figure 4.1. (A) Cartoon of cadherin structure showing the three major protein domains and the five extracellular (EC) domains, which are involved in adhesion. (B) Rendering from X-ray crystallography data of the extracellular portion of a cadherin. Part (B) is modified from another source.[101]

cadherins is derived from the location from which they were first isolated. For example, N-, R-, and E-cadherins were first found in neuronal, retinal, and epithelial tissues, respectively. They are, on the other hand, expressed in tissues beyond their namesakes.

Central to understanding the role of cadherins in cell biology and how they can be exploited for biotechnological applications is the determination of the how cell-cell junction formation is mediated by cadherin interactions.[101] The principle challenge is elucidating the mechanisms of adhesive intercellular bond formation. Cadherins are single-pass transmembrane proteins (Figure 4.1), but nearly all experimental attention has been focused on studying how the extracellular domains of cadherins interact. That

is not to say that the transmembrane and endoplasmic domains are irrelevant, but this directed focus merely reflects the scientific view that the extracellular portion of the protein is responsible for adhesive forces following *trans* dimerization. Aside from the function of providing adhesive forces, cadherins have also been implicated in signaling (localized to the cytoplasmic domain), lateral clustering, and selectivity. These specialized functions help congeal cadherin interactions as more than just simple bonding.

In general, cadherins are thought to form homodimers (also known as lateral or *cis* dimers) with other cadherins within the same membrane before dimerizing with cadherins on apposing membranes (forming *trans* adhesive bonds). Yet, research has pointed to variants in this binding that can modulating selectivity and binding strength. Figure 4.2 summarizes all of the hypothesized *cis* and *trans* cadherin associations found in the literature.[101] In these models, *cis* dimers precede *trans* dimers, but only the pathways shown in Figure 4.2F-H require lateral dimerization for adhesion to occur. Not surprisingly, the fully overlapped domains, shown with a maximum of three overlapping bonds, form the strongest adhesive bonds. Further, it is postulated that the N-terminus is the most crucial domain involved in binding selectivity, as mutations of residues within this domain abolish cell-cell adhesion in flow assays.[102]

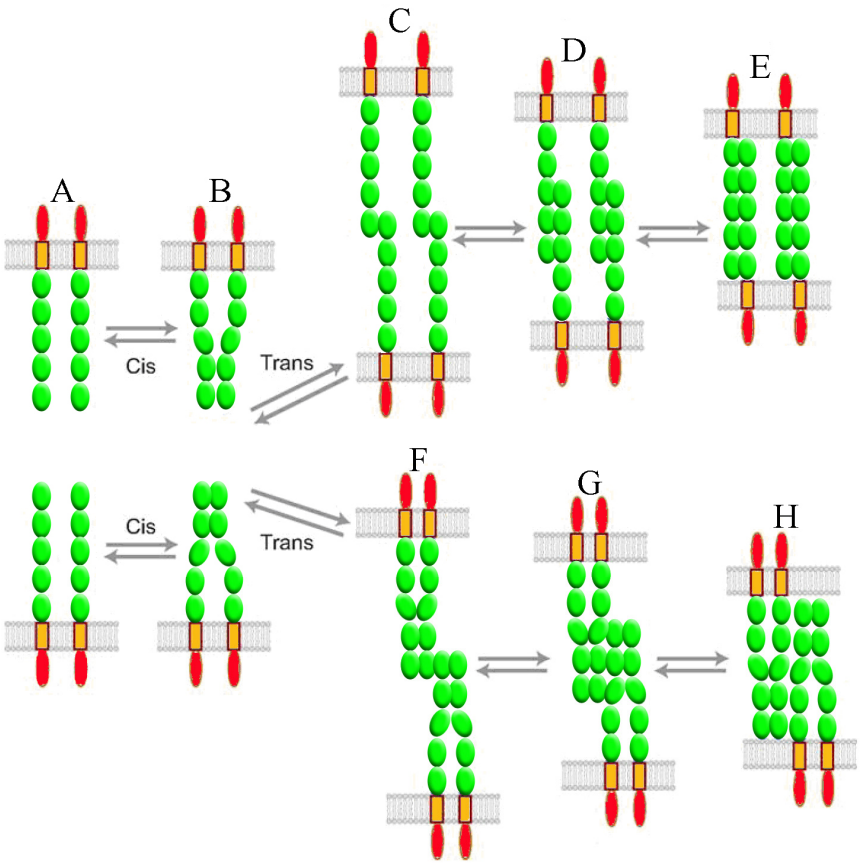

Figure 4.2. Diagram summarizing all experimentally supported cadherin dimer configurations. (A to B) Formation of *cis* or homodimers. Lateral dimers can dissociate but still form *trans* dimers (C) or remain dimerized and form *trans* dimers (F). Additionally, overlapping of non-dimerized (C to E) or *cis* configurations (F to H) can occur. Figure modified from another source.[101]

In all cases, loading of calcium binding sites (Figure 4.1) is required to form *trans* and *cis* dimers, with a maximum of three calcium ions at each of the four domain junctions.[103,104] Likewise, as calcium binds to these sites on the protein, structural changes occur in stages.[105] Important to note is that these five domains remain flexible at low calcium concentrations (low μM range), but at $[Ca^{2+}]$>40μM, the chain becomes more elongated and stiffer.[104,105,106] Experimental evidence also shows that local *trans* dimerization is only initiated when $[Ca^{2+}]$>0.5mM, but this exact threshold concentration

may be cadherin-type specific. As will be shown in a later section, we have observed bond formation between apposing cadherins at 0.2mM and possibly lower. Apart from cadherin type being an issue, the surface concentration could also influence these preliminary results, pointing to the role of lateral clustering in increasing adhesive strength and lower the dissociation constant. Future work beyond this dissertation will involve careful adjustment to cadherin surface density and lateral mobility. In this way, the formation of cadherin clusters can be controlled.

4.4 Differential Adhesion Hypothesis (DAH)

The formulation of the DAH was presented as a qualitative thermodynamic explanation of spontaneous cell sorting, liquid-like tissue segregation, and mutual envelopment behaviors seen in embryonic cells and tissues. Thus far, the DAH has made correct predictions for all cell systems that have been studied experimentally, wherein quantitative surface tension data were collected, generally through the use of tissue surface tensiometers. In all cases, the tissue of lower surface energy envelops its counterpart, and this is independent of the type of surface protein expressed. Foty and Steinberg[107] recently affirmed that cell sorting, spreading, and mutual tissue segregation are only dependent upon the intensity of adhesion between the cells within these tissues (i.e., the absolute number of adhesion molecules expressed on the membrane's surface) and not necessarily the subtype expressed. According to Foty and Steinberg, this was the final postulate that needed to be proven in order to fully validate the DAH. The experimental details of cell sorting experiments, and in particular, the way in which they can be used to test the DAH, are now described briefly.

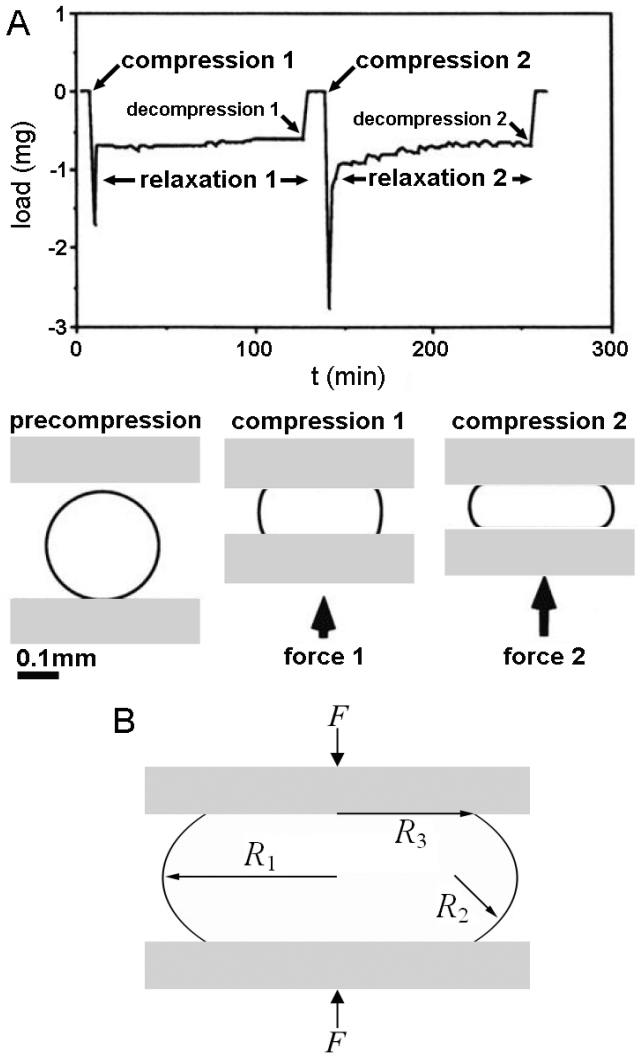

Figure 4.3. (A) Compression data from a cell aggregate. (B) Geometric parameters of relevance in the Young–Laplace equation that are used to calculate surface tension of the tissue aggregate. This figure was modified from Foty et al.[25]

Cell lines, which only express one particular type of cadherin (e.g., L-cad, N-cad, E-cad, P-cad, R-cad, etc.) or Ig protein, are produced through genetic vector modification. Typically, cadherin studies are conducted because it has been shown that cell rearrangements during embryonic development are associated with changes in expression levels of different cadherin subtypes[108] and that severe morphological defects

occur when cadherin function is blocked.[109] Cadherin expression level on the cell surface is quantified using a flow cytometric assay in conjunction with calibrated microbeads that have different binding capacities for Ig antibodies, which are covalently bound to both cadherin molecules and fluorophores before testing; this is currently the most accurate method for determining the density of cadherin proteins on the cell's surface.

Surface tension (interfacial free energy) of the cell aggregate is determined using a parallel plate compression apparatus (Figure 4.3), wherein continuous measurements of the compressive load and aggregate's surface profile are recorded until shape equilibrium is reached (i.e., where the force plateaus). By applying the Young–Laplace equation,[110]

$$\sigma = \frac{F}{\pi R_3^2}\left(\frac{1}{R_1} + \frac{1}{R_2}\right)^{-1}, \tag{4.1}$$

an estimate of *apparent* tissue surface tension (σ) can be found, where F is load, and R_1, R_2, and R_3 are the meridional, equatorial, and polar radii, respectively (Fig. 4.1B). This *apparent* surface tension is only valid if the tissue mass is behaving as a viscous liquid under compression. For elastic bodies, the force required to change the shape of a spherical material increases with increasing strain. Thus, the aggregate is further compressed in order to flatten the tissue more, and another *apparent* surface tension is calculated. If the first and updated σ values are not markedly different, the tissue can be classified as a viscous liquid, and this force-independence is said to validate the *apparent* surface tension as *true* surface tension.[111]

In qualitative visualized cell sorting experiments, mixed aggregates are formed by fluorescently tagging the different cadherin subfamilies with fluorophores displaying different spectral properties so that cells can be distinguished using confocal or fluorescence microscopy. Equal cell concentrations from each line are mixed with a pipette and a small volume is plated and incubated for later observation. Studies of both heterotypic and homotypic mixtures of cell types are conducted. In the latter, a different degree of cadherin expression is the made the independent variable. Results from several cell sorting experiments are summarized in Figure 4.4. In (A-C), L cells were made to express either P-cad (red) or E-cad (green). In (A), E-cad expressing cell line was intermixed with cells expressing P-cad at a higher level, showing envelopment of E-cad cells over P-cad cells. In (B), cells expressing either E- or P-cad at approximately the same level, revealing no sorting. For (C) E-cad levels were elevated in cells relative to intermixed cells with P-cad expression, therefore leading to the envelopment of P-cad over E-cad cells. In (D) L cells, some labeled green while others were labeled red, expressing approximately the same amount of N-cad exhibited no sorting behavior. Part (E) shows L cells expressing 50% higher N-cad expression (red) that are segregated internally to the L cells expressing less N-cad. Finally in (F), aggregates containing equal amounts of B- and R-cad segregated to produce nearly independent cell masses. Note that it can be observed that the cells expressing R-cad (red) are slightly enveloping the B-cad cells (green). This type of experiment proves that cells are able to segregate into different tissue types in the absence of developmental cues, but the underlying cause

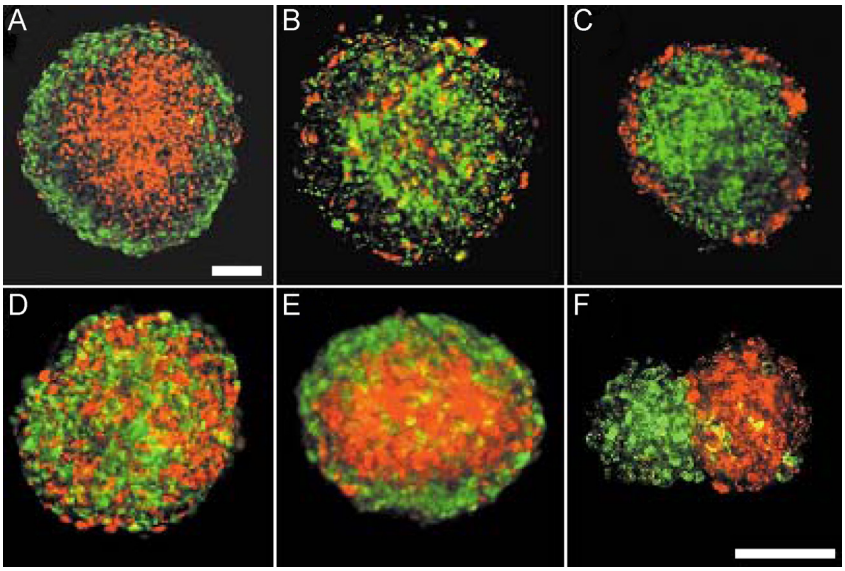

Figure 4.4. Fluorescently labeled cadherins in multiple cell sorting experiments. Scale bars are 100µm. This figure was modified from Duguay et al.[112]

of sorting is still unknown. This qualitative result is incomplete in that little is know about the relative magnitudes of adhesive potential amongst cadherin subtypes.

4.5 The DAH: Wrong, Incomplete, or Both?

As mentioned above, there have been no published experimental results that differ from the predictions set forth by the DAH. The most substantiating aspect of the DAH is that it can predict the entire compendium of liquid-like behaviors observed when embryonic cells are intermixed, which include: the coalescence of smaller cell groups into larger ones (a specific pathway of cell sorting); the envelopment of one tissue mass by another; spreading of one tissue mass over the surface of another; the correlation between envelopment hierarchy and corresponding interfacial free energies; the tendency of spherical masses to form from a collection of irregularly shaped tissue fragments; cell sorting following intermixing.[107] There are competing ideas, some

already proven theoretically and experimentally infeasible and others that have yet to be tested; however, these can only account for and predict the phenomenon of cell sorting and, to a limited extent, tissue envelopment. For example, it has been suggested that cell sorting can be attributed to chemotaxis, differential cell-cell adhesion, homophilic subtype interactions of cadherins, differential timing of adhesive changes within cells, differences in cell migration speed, and differential surface contractions.

Of the above competing hypotheses, there is clearly one that has survived and gained notoriety even after "conclusive" experimentation and theoretical trials; that is, the idea that differential surface contractions drive cell sorting and possibly envelopment. Prior to 1997, the only direct challenge to the DAH was that provided by Harris[113] in 1976. In his critique, Harris questioned the validity of the DAH and proposed a number of alternative mechanisms that could result in cell sorting. From that work, the Differential Surface Contraction Hypothesis (DSCH) is one of the most compelling, postulating (i) cells exhibit surface contractions, (ii) the strength of surface contractions are highest when a cell is in contact with the medium, lower when they interact with a different cell type, and the lowest when they bind with a homologous cell type, and (iii) different cell types exhibit varying degrees of contraction when exposed to culture medium. Chen and Brodland[114] followed up on the DSCH and utilized the finite element method (FEM) to study morphological occurrences such as cell sorting and envelopment. Many technical challenges, seen when utilizing FEM for the study of cell conglomerates with domain irregularities, were overcome by modeling the relative force contributions of cytoplasmic and cytoskeletal constituents such as actin and

microtubules. Moreover, their model simulated cell rearrangements and allowed for the forces produced by passive deformation of the cytoplasm and membrane to be accurately determined. In their follow-up work,[114] they used analytical mechanics to estimate forces generated by contractile elements and showed that the phenomena of cell sorting and envelopment could be driven by imbalances of these forces. In addition, they demonstrate that differential adhesions alone could not account for the forces necessary to promote sorting and envelopment. Their proposed force balance is as follows

$$\gamma^{AB} = F_{MF}^{A} + F_{MF}^{B} + F_{Mem}^{A} + F_{Mem}^{B} - F_{Adhesion}^{AB}, \tag{4.2}$$

where *A* and *B* superscripts denote two different cell types, and the interfacial tension, γ^{AB}, is the sum of F_{MF} (contractile forces generated by microfilaments that lie along the membrane's boundary), F_{Mem} (in-plane contractile forces due to membrane-bound proteins), and $F_{Adhesion}^{AB}$ (the tangential force that arises when normal adhesion forces create a new contact, lower the surface area, and decrease the overall surface energy). When a cell is in contact with the culture medium, it is called a surface tension, as opposed to an interfacial tension. This surface tension in cell type *A* is defined as

$$\gamma^{AM} = F_{MF}^{A} + F_{Mem}^{A} + -F_{Adhesion}^{AM}, \tag{4.3}$$

and in cell type *B* as

$$\gamma^{BM} = F_{MF}^{B} + F_{Mem}^{B} + -F_{Adhesion}^{BM}. \tag{4.4}$$

According to Brodland and Chen,[114] if the above equations (Eq 4.2-4.4) are representative of the interfacial and surface tensions seen in biological colloids, differential adhesions alone cannot be responsible for driving cell sorting, because in-

plane net tensions (i.e., $\gamma > 0$) would not exist and the cell membranes would become flaccid.

Primarily, their analysis,[114] later termed the Differential Interfacial Tension Hypothesis (DITH),[115] refutes the intuitive and popular notion that cells with greater adhesion strengths coalesce more tightly and consequently exclude cells with lower adhesivity; this is also the case for immiscible fluids. The DITH states that cells posessing a greater adhesive strength envelope the ones with lower surface tension, a result which directly contradicts the DAH. The main difference, therefore, between the DITH and the DAH is how surface tension is defined. In the DAH, interfacial free energy is only dependent upon cell-cell adhesion strength. Conversely, the DITH shows that differential adhesion does not necessarily exist and contractile units give rise to in-plane tensions that constitute the interfacial and surface tensions. Hence, even if surface tension differences resulted from differential adhesion, with the other forces being constant and large enough in magnitude to maintain the positive tension necessary to sustain a membrane's mechanical integrity, cells would sort in a fashion contradictory to the DAH and direct experimental observation.

The recent work conducted by Foty and Steinberg,[107] mentioned earlier, seems to directly refute the notion set forth by the DITH that adhesion actually decreases interfacial tension. Perhaps one flaw in the DITH, to my knowledge not mentioned in any of the open literature, is that it disregards the positive change in surface energy associated with the detachment of two cells that continue on to form more energetically favorable bonds with neighboring cell types. Equation 4.2 would have to be modified (as

shown in Eq. 4.5) to include the positive contribution of breaking adhesive bonds and forming new surfaces, leading to

$$\gamma^{AB} = F_{MF}^{A} + F_{MF}^{B} + F_{Mem}^{A} + F_{Mem}^{B} - F_{Adhesion}^{AB} + F_{detachment}^{A(AorB)}, \quad (4.5)$$

where $F_{detachment}^{A(AorB)}$ represents the tension generated by breaking a bond between two cells and forming new cell surfaces.

Furthermore, the DITH is based on the assumption that, when adhesion molecules form bonds, they collapse the cell surfaces into a single shared surface; likened to the phenomenon seen in coalescing soap bubbles. It may be the case that the adhesion molecules are interacting, but energetically, the cell membranes can still be treated as two individual surfaces. In other words, the energy required to combine two overlapping surfaces into a single surface may be much larger than the energy needed to bind complimentary proteins that extend away from the membrane. This assertion may be reasonable based on the fact that adhesive bonds are readily broken and reconstituted during cell sorting.

One additional aspect that neither the DITH nor the DAH consider is that cellular energy from metabolic activity may be utilized for the formation and cleaving of adhesive bonds. For instance, other than a second messenger system linked to adhesion protein activity, how else could one explain the cooperative action of forming new bonds while breaking existing ones. Thus, these colloidal systems cannot be treated as macromolecules; henceforth, the idea that these single entities will prefer one adhesive interaction over another based purely on energetic favorability is without merit.

It should be stated that computer simulations and theoretical studies by Glazier and Graner,[116] Mochizuki et al.,[117] Rieu et al.,[118] Graner,[119] and Palsson[120] (interestingly, no mention of the work by Chen and Brodland) have further legitimized the claims postulated by the DAH. Yet, these simulations are, for the most part, based entirely on assumptions set forth in formulating the DAH, so it is not surprising to see that these simulations and predictions match well with Steinberg's DAH.

4.6 Direct Force Measurements between Cadherins

At present, the only techniques that have been employed to measure forces generated by the *trans* dimerization of extracellular cadherin domains are the bioforce probe (BFP), atomic force microscopy (AFM), and surface forces apparatus (SFA). The quantity measured in these studies is properly characterized as bond rupture force, although findings from SFA measurements have provided seemingly reliable data concerning separation-dependent bond strengths. This subsection will, therefore, present most of the findings from these studies, with a general aim to point out the advantages, limitations, and shortcomings of each study. Likewise, an explanation will be given as to how the methods presented in this dissertation can compliment or improve upon these approaches.

As mentioned in *Section 1*, SFA holds the distinction as the force/energy measurement technique with the best spatial resolution, approaching 1Å in ideal cases. Superb studies have been performed on cadherins, all by Leckband's group, wherein binding strengths are measured at various absolute separations. In this way, domains from apposing cadherins can be precisely overlapped and then pulled apart to collect

bond rupture data vs. the number of overlapping domains. They found that the substrate-substrate separation at cadherin contact was 40nm (22.5nm end-to-end ectodomain length for proteins on apposing surfaces, with an single domain length of 4.5nm[103,104]). An adhering force was found at three separations: 39, 32, and 25nm. The minimum overlap of 39nm corresponded to binding of the two N-terminal domains, 25nm to complete domain overlap, and 29nm to intermediate overlapping of the outer three domains on each cadherin fragment. The bond strengths followed a hierarchical arrangement in that the highest degree of overlapping led to the highest average bond strength while the interaction of the N-termini exhibited the lowest bond strength.[12] In related study, identical SFA measurements of domain deletion mutants pin-pointed the EC domains responsible for the three distinct binding strengths.[121] These studies provide a wealth of information regarding domain importance and bond energies, but these measurements are lacking in two important regards: the calcium concentration was fixed at 1mM and apposing proteins were held at a fixed separation during an "incubation" period to allow bonds to form. First, the calcium ion concentration outside of a cell fluctuates due to activity of ion channels—this is especially true for skeletal and cardiac tissues. Second, proteins *in vivo* are not held at a fixed distance from one another but are very dynamic via cytoskeletal and thermally induced membrane fluctuations and cell motility. In our studies, interactions are measured as a function of $[Ca^{2+}]$, and the diffusing nature of our probes establishes a similar dynamic state of the protein, which more closely mimics the type of bond formation occurring *in vivo*.

BFP offers the largest range of force measurement of any of the highly sensitive techniques available. Given that, BFP is ideally suited for measuring adhesive forces between cadherins. Two key works will be discussed here: Bayas et al.[14] and Perret et al.[122] Bond rupture forces are found for each of three loading conditions that include steady ramp, jump/ramp, and force-clamp modes. Steady ramp is just as it sounds, jump/ramp involves a rapid jump to a baseline force followed by a steady ramp in force, and a force-clamp mode holds interacting proteins at a fixed load until the bond breaks. Since bond rupture events are stochastic, a probability distribution describes the measured rupture forces as a function of pulling rate and bond parameters.[123,124] Importantly, features of the protein-protein potentials and dissociation rates can be extracted from the probability distribution.[124]

Briefly, under an external load, the dissociation rate, k_{off}, of a molecular bond is exponentially related to the applied force through[125]

$$k_{\text{off}} = k_{\text{off}}^{0} \exp\left(F / F_{\beta}\right), \tag{4.6}$$

where k_{off}^{0} is the baseline rate of dissociation under zero applied load, and F_{β} is termed the thermal force, which is directly related to the thermally averaged transition state projection along the line of force, x_{β}, by[126]

$$F_{\beta} = \frac{kT}{x_{\beta}}. \tag{4.7}$$

For conditions where the thermal force is much smaller than the applied load, the probability of reassociation tends to zero, so the likelihood of remaining in the bound state, $S(t)$, can be obtained:

$$\frac{dS}{dt} = -k_{\text{off}} S \,. \tag{4.8}$$

For the constant load case, the normalized probability distribution for bond failure between times t and $t+dt$ is found by

$$p(t) = k_{\text{off}} S(t) = k_{\text{off}} \exp\left(-k_{\text{off}} t\right), \tag{4.9}$$

thus the probability of a bond breaking at times larger than t is[14]

$$P_s(t) = \int_1^{\infty} p(t)\, dt = \exp\left(-k_{\text{off}} t\right). \tag{4.10}$$

Future work analyzing association times from TIRM data will utilize this theory for accurately finding dissociation rates, provided the diffusion of a particle is assumed to apply a constant force. At this point, several aspects of this assumption need to be verified.

The data from these studies suggest several important aspects of cadherin bond formation and rupture. Depending on the domains interacting, a range of maximum rupture forces were found, the weakest breaking below 50pN and obviously corresponding to the fastest dissociation kinetics. Rupture-force histograms from completely overlapped cadherins showed four populations of bound states corresponding to multi-domain binding. Additionally, time-dependent measurements showed that fast, weak bonds form first and are then followed by strong but slow bond formation. By varying the residence times for association, they concluded that cadherins quickly bind through interactions with the outer two domains, but the formation of strong bonds requires the entire group of five extracellular domains.[122] Moreover, it was determined

that the dissociation rates varied for the different classical cadherins. For instance, E-cad bonds were found to possess association rates 25× higher than that of C-cad, despite C-cad exhibiting a much larger absolute binding energy.[14] These findings are important to our research in that we can chose to study classical cadherins with the highest dissociation rate and use macromolecules of various molecular weights to either expose of conceal the number of ectodomains the immobilized cadherins presents for *trans* dimerization. More discussion of this follows in *Section 7*.

Despite the BFP being extremely useful in collecting force- and time-dependent data, it still lacks the capability to spatially resolve the degree of overlapping and distance over which the force is applied. However, by studying the generated force histograms, the authors were able to extrapolate the existence of multiple overlapping bonds. Although they could ensure short residence times (0.1s) for bond formation, they imposed an impingement force of 10pN on each approach, which forces the membrane to overlap and form bonds at more than just a Hertzian contact point. This was unaccounted for in their analyses. Furthermore, like most studies of cadherins, rupture forces were only measured for high [Ca^{2+}] (2mM in this case), where the largest bond strength will be achieved. This, and the lack of spatial resolution, presents an opportunity to compliment the BFP approach with one that is more sensitive to changes in force/energy and has spatial resolution on the order of a single cadherin ectodomain.

Finally, studies of rupture forces between cadherins using AFM are now addressed. As described in *Section 1*, AFM possesses unparalleled lateral spatial resolution, which is a great value to biophysicists, but gathering separation-dependent force data carries

with it unresolved problems. In any case, a few prominent studies described here are excellent examples of well-performed measurements of cadherin interactions using AFM.

Because AFM tips can be easily produced to a yield radius of curvature of <5nm, single-molecule force experiments are fairly straightforward with this technique, and AFM can be used to image a surface to find the location of isolated molecules prior to attempting single-pair binding. Work performed by Baumgartner et al.[127] suggests that cooperativity between lateral VE-cadherin clusters could account for a significant increase in binding strength. They also found a K_D of 1.15mM and k_{off}^0 of 1.8s^{-1} for VE-cadherin; however, these values are specific to VE-cadherins and could be inaccurate due to the limited force resolution of AFM or loading rates and ranges applied. In another set of AFM studies of classical cadherin interactions,[128] VE-cadherin was found to have a k_{off}^0 of 0.45s^{-1}, and depending on the loading rate (10^3 or 10^4pN/s), N-cad interactions possessed a k_{off}^0 of 0.98s^{-1} and E-cad exhibited a k_{off}^0 of 1.09 to 4.00s^{-1}. Additionally, and more importantly, the heterophilic interaction of E-cad with N-cad was investigated. In contrast to other findings,[129] E-cad-N-cad interactions displayed similar potentials to that of non-specific binding and binding between antibody-deactivated cadherins.

Taken together, these AFM studies provide, more or less, much of the same information as work with SFA and BFP. Conflicting results from several groups point to inconsistencies in testing protocols or the lack of absolute sensitivity needed to resolve weak specific cadherin-cadherin interactions. Again, we hope that implementing

diffusing colloidal probes to interrogate interactions throughout a range of [Ca^{2+}] will provide essential information necessary to unraveling the form and magnitude of cadherin interactions throughout a range of physiologically relevant conditions (e.g., surface protein density, calcium ion concentration, existence of surrounding macromolecules that mimic the glycocalix, mixture of heterophilic and homophilic interactions).

4.7 Conclusions

Cellular organization is crucial for the proper development of functional tissues. The role of surface adhesion proteins, such as the cadherins and Ig superfamilies, in the processes of cell sorting and tissue layering has been well established. Yet, the underlying mechanism that explains these phenomena is still under debate. Steinberg's DAH has, thus far, held up to every experimental outcome and to nearly all cell sorting simulations and theoretical models. The fairly recent arguments that differential adhesion cannot alone be the driving force behind self-organization of tissues and cells has some validity, but this model is incomplete and there is no way to justify its accuracy without further revision based on the proper physics and physiology of cell adhesion and detachment.

The true nature of cadherin-cadherin bonds has not been explored beyond: (i) the determination of tissue surface tension from compression tests with parallel plates and (ii) the ultimate rupture strength and rate dependence of *trans* dimer bonds found from SFA, AFM, and BFP studies. Examination of intermolecular bond affinities with TIRM and VM approaches may elucidate weaker interaction potentials that could possibly

translate into signals that dictate localized, dynamic cell adhesive and repulsive responses.

5. NON-SPECIFIC PROTEIN-SYNTHETIC MACROMOLECULE INTERACTIONS

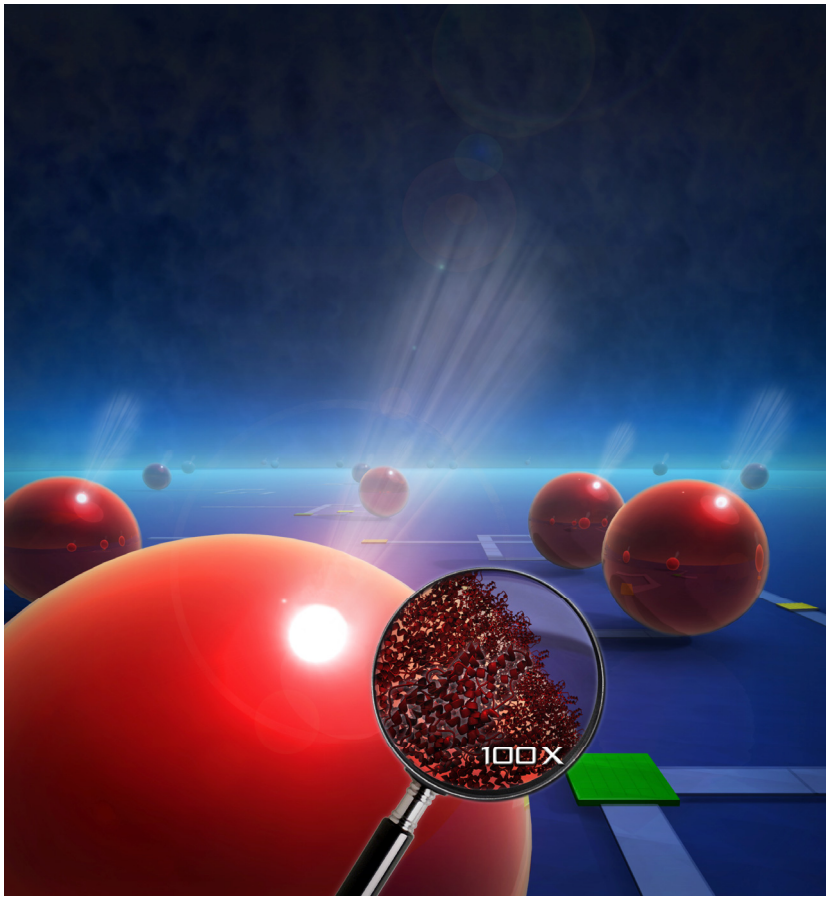

Figure 5.1. Conceptual illustration of protein-modified colloids diffusing and scattering in an EW, with underlying overlays of trajectories and locations of colloid-surface association lifetimes.

5.1 Synopsis

Understanding non-specific interactions of synthetic and biological macromolecules is of great importance to traditional medicine and the interface of nanotechnology and biology.[130] Although nearly all of medicine necessarily involves

interactions of synthetic and biological systems, many emerging applications require robust integration of materials on molecular to micron scales such as novel therapeutics (e.g., nanoparticles, gene delivery), sensors (e.g. insulin), biomolecular chips (e.g., DNA, protein), cellular diagnostics (e.g., microfluidics, arrays), and tissue engineering. Very generally, a net repulsive intermolecular interaction is often required to prevent non-specific binding, adsorption, or aggregation of proteins to other proteins and synthetic materials to permit the retention of specific interactions that are the origins of unique biological function both *in vitro* and *in vivo*.

This section reports data from our novel diffusing probe method in which we directly and non-intrusively measure *kT*- and nanometer-scale interactions between adsorbed bovine serum albumin (BSA) and copolymers with polyethyleneoxide (PEO) moieties. As mentioned before, by utilizing TIRM and VM,[25,28,29] 3D Brownian excursions of many single colloids bearing either adsorbed BSA or copolymers with exposed PEO moieties are monitored near similarly coated wall surfaces (see Figure 5.2C). Statistical mechanical and dynamic analyses of colloid distributions[25,28,29,47,48,131] and trajectories[51,80,81] yield normal potential energy profiles (PEP), lateral mean-square displacements (MSDs), and colloid-surface association (CSA) lifetimes. Simultaneous single and ensemble-average analyses of many diffusing colloids allows for a consistent and unambiguous interpretation of spatial, statistical, temporal, and energetic aspects of BSA-PEO mediated colloid-surface interactions. By passively monitoring Brownian excursions of diffusing colloids on surfaces, our technique exploits natural gauges for time (a^2/D), energy (kT), force (fN), and length (nm) when interrogating protein-

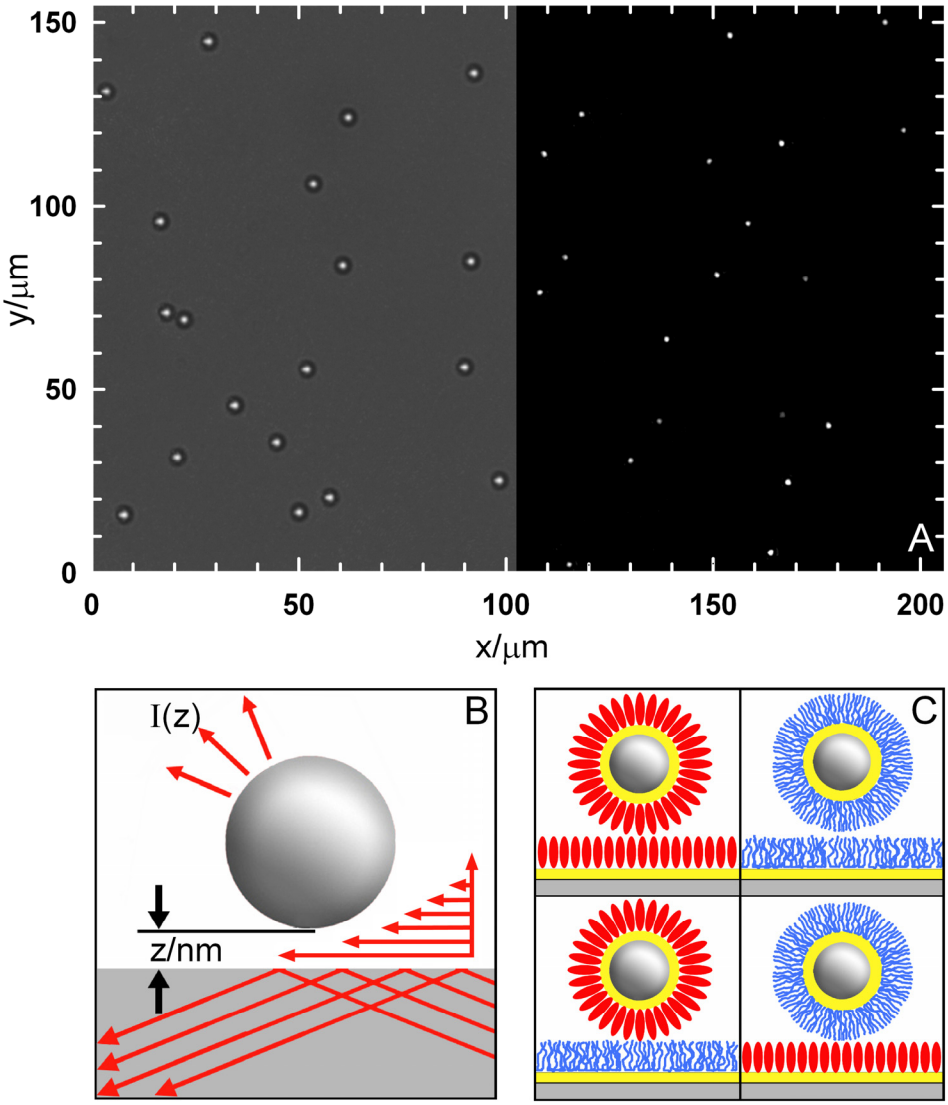

Figure 5.2. (A) Total internal reflection and video microscopy of 2.2 μm silica colloids levitated above a microscope slide with (left) and without (right) transmitted light. (B) Schematic of total internal reflection, EW generation, and colloid-EW scattering. (C) Cartoon of BSA (red ellipsoids) and PEO (blue brush layer) configurations on chemically modified surfaces (yellow).

synthetic macromolecule interactions. Successful measurement of non-specific interactions using this approach provides a basis to measure specific interactions in integrated synthetic-biomolecular materials, devices, and systems.

5.2 Bio-fouling and Controlling Protein Adsorption with PEO

Adsorption of proteins to surfaces, both *in vivo* and *in vitro*, must be controlled in order to realize optimally functional devices for drug delivery, tissue engineering, biosensing, and artificial implantation. Nucci et al.[132] were the first to find that the covalent attachment of PEO to proteins yields a conjugate that increases serum lifetimes and is less immunogenic and antigenic. Since then, the modification of surfaces with PEO, as a grafted single chain or adsorbed as part of a conjugate such as in the triblock copolymer PEO_n-PPO_m-PEO_n (Pluronic®, BASF corporation), has been one of the most effective methods of reducing or inhibiting protein adsorption.[133]

Physisorption of Pluronics is a well-documented method for producing protein-repellant surfaces. Initially based on entropic reasoning, it was thought that the dynamic motion of the surface chains would have a great influence on preventing the adsorption of proteins.[134] Currently, the most widely accepted mechanisms by which these surfactants prevent protein adsorption are as follows. The minimization of surface free energy by the adsorption of the hydrophobic PPO chain provides the requisite anchor for the macromolecule to remain adsorbed to the hydrophobic substrate, even in the presence of other macromolecules and polyelectrolytes. The PEO chains remain solvated and provide steric or osmotic repulsive forces, which perhaps leads to the protein-resistant nature of this adsorbed layer.[135] This steric repulsion picture emerged from the view that the grafted polymer layer forms a brush-like structure on the surface;[136] there are experimental and theoretical suggestions, however, that the typical molecular weights and grafting densities of PEO used to control protein adsorption properties are

such that the Pluronic layer is not within the so-called "brush" regime.[137] Other experimental data directly refute this claim.[138] Furthermore, it is widely accepted that protein and the ethylene oxide component have a repulsive (or possibly non-attractive) interaction.[135]

Several key studies on protein-PEO interactions will be reviewed in the following subsection. The scope, though, is not such that every important study will be summarized or even mentioned.

5.2.1 Varying Pluronic Constituent Molecular Weight

PEO surface density and chain length can be adjusted by manipulating the MW of the PPO and PEO, respectively. The limiting factor for achieving a high PEO-chain density is most likely steric exclusion during polymer adsorption. The balance between the chain elasticity (opposed to stretching) and excluded volume (expanding the chains normal to the surface) determines the brush layer's thickness. In a study by McPherson et al.,[136] protein adsorption was monitored for PEO layers with different densities. They utilized the following Pluronics: F127 (98 EO units; 67 PPO units), F108 (128 EO units; 54 PPO units), and F68 (75 EO units; 30 PPO units). Protein solutions of lysozyme and fibrinogen were radiolabeled, and adsorption profiles were measured. The adsorbed amount of F68 polymer was lower than F108, as expected, because of the shorter PPO chain in the F68. Lysozyme adsorption decreased with an increasing amount of Pluronic, irrespective of PEO chain length. For instance, protein concentration steadily decreased to a minimum of $0.05\mu g/cm^2$ as the Pluronic adsorption increased. Conversely, fibrinogen adsorption decreased to $0.09\mu g/cm^2$ on F68, compared with $0.35\mu g/cm^2$ on

the control surface (glass). The adsorbed amount of fibrinogen was approximately 0.10μg/cm^2 on F127 layers. Protein adsorption on F108 decreased steadily throughout the range of F108 concentrations studied, to a minimum of 0.02μg/cm^2; consequently, F108 was most effective in reducing fibrinogen adsorption. Assuming these results are valid, this study provides some important information on the relationship between the density of PEO chains and protein adsorption. In summary, these findings give evidence that PEO density, and not chain length, directly controls the amount of protein adsorbed. This hypothesis is based on the idea that PEO kinetically blocks protein adsorption and any protein bound to the surface is the result of defects in the Pluronic layer.

One obvious consideration when examining these surfactant-protein systems is the chemistry and geometry of the protein under study. Smaller proteins such as insulin (~3.5×5nm), for instance, have been found to adsorb more readily, as compared to larger globular proteins such as fibrinogen (length ~46nm).[139] The utilization of long- and short-chain PEO mixtures for surface coverage has been developed because of these adsorption discrepancies. The thought is that the movement of longer chains would be less inhibited, and the shorter PEO chains could interdigitate close to the surface, thereby decreasing the size of the surface exposure sites to a value comparable to the smallest adsorption dimension of the protein. Pavey and Ollif[140] demonstrated that these mixtures were, in fact, better suited to inhibit protein adsorption. In their SPR study, BSA adsorption onto a gold surface could be made to be below the discernable limit of their instrumentation. In another study of low-MW Pluronics,[141] protein adsorption was reduced significantly but not completely. When the MW of the Pluronic increased

substantially, protein adsorption decreased to nearly zero. Surprisingly, this non-fouling quality could be attained within only 4min of Pluronic adsorption. It was suggested that a PPO block size greater than 16 monomer units can successfully inhibit BSA adsorption, whereas smaller PPO block sizes lead to sub-monolayer coverages. It is important to note that research has shown PEO may be desorbed and displaced by biomolecules with higher surface activities, suggesting that the PPO within the Pluronic plays an integral role in stabilizing the macromolecule. For the sake of brevity, other studies of protein adsorption dependence on Pluronic MW will not be review.

5.2.2 Possible Protein-Pluronic Interactions

To understand how Pluronic-coated surfaces hinder or inhibit protein adsorption, it is important to be able to describe the general routes through which protein adsorption can be limited or prevented.[142] Firstly, one may alter the short-range (i.e., < 1nm) surface-protein interaction energy. At contact, however, the elimination of surface-protein attraction is difficult. This is the result of surface composition multiplicity within the protein and surface materials.[142] A more realistic approach is to generate an intermediate, long-range (i.e., > 1nm) repulsive interaction that would decrease the number of direct protein-surface interactions or prevent the protein and surface from ever coming into contact. For example, protein adsorption can be limited by reducing the rate of adsorption to an insignificant level, or by shifting the equilibrium in favor of moving from an adsorbed to a desorbed solution state. Thermodynamically speaking, repulsion involves the manipulation of the interaction potentials such that the protein and surface repel each other at any separation. To control adsorption kinetically, a

sufficiently high energy barrier should exist so as to decrease the rate of adsorption to a negligible level on the time scale of interest. Total control over the thermodynamic equilibrium between non-adsorbed and adsorbed proteins seems to be unachievable in practice. At this point, very little is known about charge distribution, protein structure, effect of local pH, etc., and the techniques available to measure these parameters do not allow us to do so with much confidence. On the other hand, decreasing the rate of adsorption is an attractive alternative. Although the equilibrium or long-term behavior will favor the bound state, the amount of protein able to transition across a potential energy (PE) barrier and physisorb may be minute.

The distinction between secondary and primary adsorption must be made to classify relative contributions of the different interactions encountered.[143] Whereas primary adsorption occurs at a PE minimum close to the surface, secondary adsorption occurs further from the surface at PE minima (e.g., at the outer reaches of a PEO brush layer). In the case of a Pluronic-covered surface, a protein must first cross a PE barrier in an activated process to undergo primary adsorption. Generally speaking, a bare surface has no PE barrier so the adsorption is diffusion limited.[144] As mentioned by Leckband et al.,[145] protein adsorption in a secondary minimum is a distinct feature of protein-Pluronic interactions. Yet, the strength of this effect is arguable (as it pertains to PEO brush layers) since van der Waals forces are the major interactions involved, and modeling of these systems is extremely difficult.

Electric double-layer repulsion plays a role in short-range interactions between proteins and PEO. For example, ethylene oxide may be slightly oxidized, thereby

creating a negative formal charge at the end of the Pluronic brush. As a single unit, most proteins are positively charged at physiologic pH. Therefore, proteins may adsorb to those negatively charged ethylene oxide groups in low-salt conditions; however, the ionic strength *in vivo* is around 150mM. Moreover, if the PEO brush layer is not sufficiently dense, the proteins may interact with the underlying substrate and adsorb if the substrate is negatively charged.

Obviously, steric interactions will be important if the protein and Pluronic interact and adsorption occurs. This interaction results directly from the polymer chains resisting compression and interdigitation. Macromolecular compression results in a small elastic recovery component (repulsive), where the local concentration of the PEO and protein will increase the free energy, resulting in a net repulsive interaction. Moreover, if a protein compresses the PEO chains, the available volume for each polymer segment is reduced, conformational freedom of the PEO is temporarily lost, and as a result, a repulsive force is established. Of course, PEO density is important for these types of interactions, because the more polymer available to sterically interact with the protein, the stronger the repulsive force—it is important to remember that smaller proteins encounter fewer chains upon impact. If a protein is sterically held away from the substrate, adsorption will most likely occur at a secondary minimum, and this is important in real-world applications; shear forces, such as those seen in blood flow and around joints, can more easily sweep away these loosely bound proteins.

Hydrophobic interactions occur because of thermodynamically driven removal of water from hydrophobic regions of a macromolecule. The same type of hydrophobic

interactions responsible for the self-assembly of micelles and PPO adsorption onto hydrophobic surfaces dictate the adsorption and subsequent conformational changes of proteins. These interactions are considered short range and are attractive by nature.

5.2.3 Measuring Protein-PEO Interactions

The two most utilized techniques for directly measuring the interaction forces between macromolecules are the SFA and AFM. Israelachvili and Adams developed the SFA in the late 1970s for quantifying molecular forces between thin films as a function of their separation distance (resolution: ±10pN; ±2Å).[146] Ducker et al.[9,147] were the first to modify the AFM tip with a colloidal probe, and since then, this modification has been used to study macromolecular and colloidal forces. As with all direct steric force measurement techniques, there is inherent complication in that the forces measured are the sum of all forces. In order to accurately determine the steric contribution to the net force, it is necessary to theoretically calculate the electrostatic and van der Waals' contributions. These are normally not estimated accurately. Thus, these techniques, while not without merit, are often misleading or unrepresentative of the true nature of interactions.

In an SFA study by Sheth and Leckband,[148] attractive forces between streptavidin and grafted PEO were measured. It was claimed that this was the direct result of polymer-protein adhesion because: the applied forces were much to low to denature the streptavidin; neither the compression of the PEO brush nor the extended incubation period with a second polymer layer resulted in similar adhesion; and adhesive contacts formed readily with streptavidin but not with the PEO chains. They did, however, note

that the compressive energy required for adhesion was probably necessary to facilitate PEO rearrangement. While it is interesting to observe PEO and protein with an attractive force between them, these experiments are not necessarily practical or relevant to protein adsorption. In other words, there is rarely a case in real-world applications where proteins (already adsorbed or grafted to a surface) are compressively forced into contact with these "protein repellant" brush layers.

In a follow-up paper by Efremova et al.,[149] SFA was used to explore protein-PEO "adhesive forces" as a function of MW, temperature, and polymer coverage. They found that protein adhesion was increased at higher temperatures and stated that this might be due to a temperature-dependent increase in *trans* conformers within the brush. Further, this would diminish the solvent quality since it increases the number of hydrophobic conformers on the PEO chain, thereby increasing the PEO-protein attraction. Note, however, the Pluronic brush layer has been shown to collapse as temperature increases.[150] Not only does the protein interact more with the underlying substrate, but the van der Waals attraction generated by the polymer brush increases as solvent conditions become less favorable and water molecules begin leaving the PEO chain. This vdW phenomenon is directly related to the change in the dielectric properties of the brush as a function of temperature and degree of solvation.

McGurk et al.[151] combined SPR and AFM to explore the relation between: (i) the surface concentration of Pluronic and amount of protein adsorbed, (ii) Pluronic surface concentration and degree of protein adhesion, (iii) Pluronic MW and amount of protein adsorption, and (iv) Pluronic MW and degree of adhesion. More specifically, SPR was

utilized to determine the amount of adsorbed Pluronic and protein as a function of time. An AFM cantilever tip was modified with an amine-functionalized glass microsphere (47±2μm) and coated with covalently bound albumin. Force curves were collected for various Pluronic surface concentrations and MWs. It was determined that the higher MW Pluronic (F127) completely masked all adhesion between the modified tip and the surface. On the other hand, with L35 and L61, adhesion was seen, albeit significantly reduced. By equating protein adhesion with effective surface coverage, 40% (for L35) and 15% (for L61) complete monolayer coverage was observed. In summary, the L35 has a ratio of 11:16:11 (PEO-PPO-PEO), yet displayed a reduced effect in antifouling behavior compared with L61, which has a ratio of 3:30:3 (PEO-PPO-PEO). The authors believed this was due to the increased size of the hydrophobic portion in the macromolecule that allows it to bind more strongly to the PS. This hypothesis and these results match well with their findings on F127-modified PS. Hence, like others in this field, they concluded that the PPO chain segment length enables the effective adsorption of Pluronic to the hydrophobic substrate while the length of the hydrophilic segment (PEO) allows for adequate steric repulsion of proteins.

There are many opinions and explanations as to how and why PEO-modified surfaces are protein repellant. In order to optimize these systems, it is necessary to gain a detailed understanding of the underpinnings of protein adsorption to PEO and PEO copolymers. There are several tools available to probe these interactions, but care should be taken when applying these techniques because experimental models may not match well with actual adsorption, especially for the case of adsorption from protein solutions.

Theoretical work in this area has led to advances in an experimental understanding, but these studies should be utilized carefully, as well. If we can elucidate these fundamental protein-PEO interactions, perhaps new anti-adsorption systems can be realized and/or old schemes can be modified to yield high-performance materials for the field of biomedicine.

5.3 Colloid-Surface Association Lifetimes

To a first approximation, the equilibrium CSA lifetime, t_a, depends on the diffusion-limited motion of colloids near surfaces and the colloid-surface interaction potential as[152]

$$t_a \approx \left(l^2/\langle D_\perp \rangle\right) exp\left(|u_{min}|/kT\right), \tag{5.1}$$

which can be rearranged to $\tau_a = t_a\langle D_\perp\rangle/l^2$ and related directly to the potential well depth as

$$ln\left(\tau_a\right) \approx |u_{min}|/kT\,, \tag{5.2}$$

where $(l^2/\langle D_\perp\rangle)$ (from Eq.2.27 and the literature[50]) is the characteristic timescale for colloid diffusion normal to the surface within an energy well with a characteristic length scale l, and $\exp\left(|u_{min}|/kT\right)$ is the Boltzmann probability of a colloid remaining in a attractive energy well. Single colloids are considered to be associated with the surface in a given image if their height excursions in the two preceding and two following images (5 total images) have a standard deviation of $\sigma_h < 1.5$ nm, which is a semi-empirical value obtained for irreversibly deposited colloids on unmodified surfaces. For more a more detailed description of this criteria, see *Section 3.5.3*.

5.4 Levitated Colloidal Probes

Figure 5.2A displays a typical optical microscopy image of 2.2 μm silica colloids levitated above a glass microscope slide against a gravitational potential by non-specific interactions of physisorbed BSA and copolymers with exposed PEO moieties. 3D colloidal positions are monitored using VM with half-pixel resolution in the *x*- and *y*-directions parallel to the surface (Figure 5.2A) and using TIRM with nanometer resolution in the *z*-direction normal to the surface (Figure 5.2B).[25,28,29] Non-specific interactions probed in this work include long-range, colloid-surface van der Waals (vdW) attraction[34,36] and macromolecular interactions due to interpenetration and compression[11,138] of adsorbed BSA and PEO copolymer layers (Figure 5.2C). Three polyethyleneoxide-polypropyleneoxide-polyethyleneoxide copolymers (Pluronic, BASF, Wyandotte, MI) were used with similar block ratios but different nominal MWs (F68-3400/1700/3400, F127-4400/3800/4400, F108-5400/3300/5400). To develop compact and meaningful notation for each copolymer, abbreviations are PEO3k (F68), PEO4k (F127), and PEO5k (F108), based on PEO block MWs. Additionally, electrostatic interactions are unimportant due to screening at distances >0.5nm in 150 mM physiological ionic strength media.

A limiting case of BSA- and PEO-mediated colloid-surface interactions occurs when repulsive macromolecular interactions dominate vdW attraction to produce robustly levitated diffusing colloids. Figure 5.3 shows results for BSA/APS coated colloids levitated above a PEO5k/OTS coated glass slide. Figure 5.3A shows 25 grey

colored diffusing colloidal random walk trajectories with colored pixels corresponding to the natural logarithm of non-dimensional CSA lifetimes, ln(τ_a), through

$$u(h) - u(h_{ref}) = kT\, ln\left[p(h_{ref}) / p(h) \right]. \quad (5.3)$$

The inset in Figure 5.2A shows a histogram of all ln(τ_a) values with the same color scale as the main plot and frequency normalized by the mode. Figure 5.3B shows ensemble-average (red) and single colloid (black) potential energy profiles (PEP), $u(h)$, with and without the confining gravitational potential. Figure 5.3C gives non-dimensional lateral MSDs in the x- and y-directions vs. the non-dimensional diffusive time, $\tau_D = t_D \langle D_{\|} \rangle / a^2$, from an average over all colloids and multiple time origins.

The ensemble-average and all single colloid PEP in Figure 5.3B are identical within the limits of polydispersity,[28,47,48] indicating chemically and physically uniform surfaces and a mean colloid radius of a=1.11 μm, in agreement with independent measurements.[29] The net PEP can be interpreted as a superposition of colloid-surface vdW attraction and non-specific BSA-PEO5k osmotic repulsion to produce a 0.7kT energy well. Using 20nm for the PEO5k copolymer brush thickness,[138] and assuming prolate ellipsoid BSA molecules are oriented along their 14nm major axis,[153,154] the onset of BSA-PEO repulsion can be expected at 34nm. By fitting the measured vdW minimum using rigorous theory,[34,36] the onset of repulsion is estimated to occur at 40nm substrate-substrate separation. The vdW attraction, however, is likely to be weakened by surface roughness,[36,155] such that occurrence of the 0.7kT minimum at smaller separations is consistent with a repulsive BSA-PEO interaction at ~34 nm.

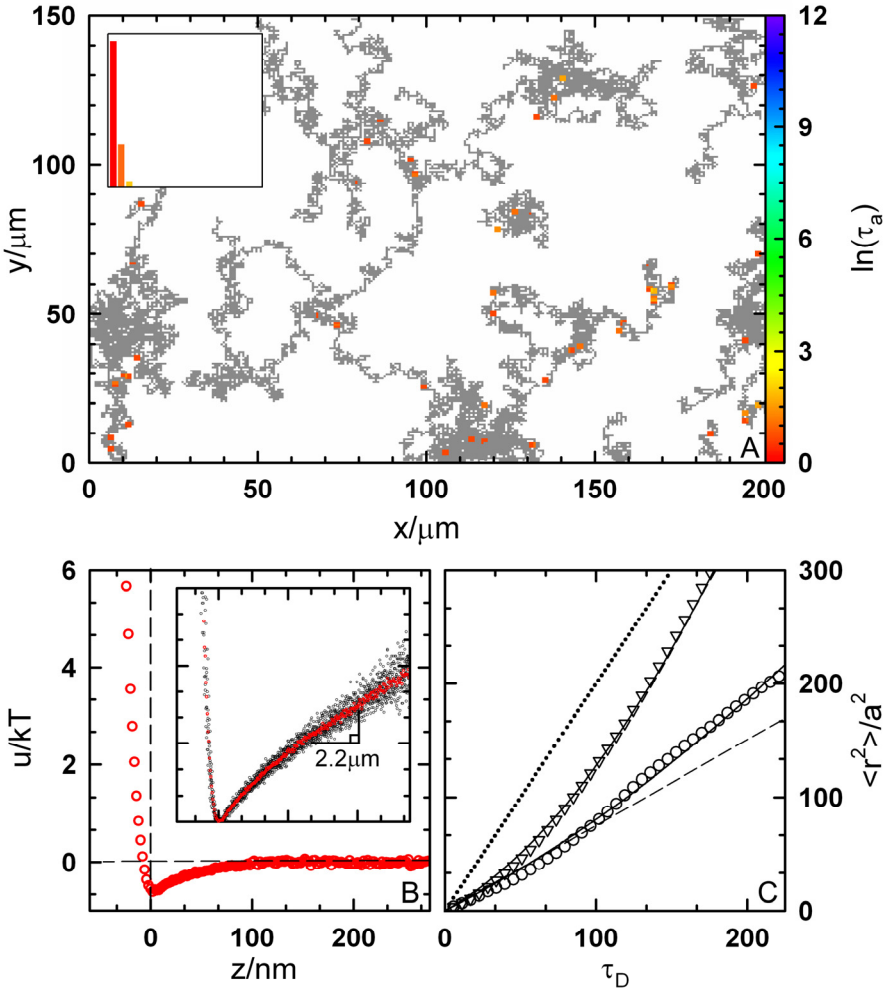

Figure 5.3. (A) Lateral trajectories of BSA/APS-coated colloids on a PEO5k/OTS-coated glass surface. Grey pixels indicate a lack of CSA, and colored pixels indicate CSA times (right-side scale). (B) Single (black) and ensemble (red) colloid PEPs with (inset) and without (main plot) gravitational potentials. (C) Ensemble-average lateral MSDs in x (○) and y (∇) directions with curve fits (—), predictions (– –), and isolated single-colloid diffusion (···).

Lateral diffusion results in Figure 5.3C provide temporal and spatial information consistent with the predominantly repulsive PEP in Figure 5.3B. As expected, the lateral diffusivity is ~(1/2)D_0, due to hydrodynamic interactions between colloids and the underlying wall surface.[81] Predicted lateral diffusivities, based on colloid-surface hydrodynamic interactions with impermeable adsorbed layers,[156] are in excellent

agreement with the short-time x and y MSDs. The parabolic upturn from the initially linear MSD in the y direction is indicative of migration due to a lateral force <1fN, consistent with a misleveling of <1°.

In addition to PEP and diffusivity results in Figures 5.3B and 5.3C, the colored pixels in Figure 5.3A indicate $\ln(\tau_a)$ values identified using the analysis described in *Section 3.5.3*. The most probable CSA lifetime is t_a=32ms from the histogram. This corresponds well to the 0.7kT well in Figure 5.3B with a diffusion-limited timescale of $l^2/\langle D_\perp \rangle$=16ms, based on the predicted value of $\langle D_\perp \rangle$ and a characteristic diffusive length scale of ~14nm within the energy well (Eq. 5.3). The value of l is not obvious *a priori* due to the continuous nature of the attractive interaction, but ~14nm is comparable to the well dimension and gives a reasonable timescale for diffusion-limited motion of levitated colloids in the absence of attraction. The minimal number and duration of association events in Figure 5.3A is consistent with the repulsive PEP in Figure 5.3B that is averaged over all colloids, surface locations, and the total observation period.

A small number of CSA events are observed in Figure 5.3A, but these most likely result from a somewhat conservative criterion for identifying discrete CSA events from probabilistic colloid height excursions. These few CSA events do not obviously correspond to chemical or physical surface heterogeneity that might produce locally stronger attraction. The predominantly grey pixels in Figure 5.3A also indicate temporally and spatially uninterrupted lateral diffusion, consistent with the MSDs in Figure 5.3C, which would be significantly retarded in the presence of either more or longer-lived CSA events. All results in Figure 5.3 demonstrate characteristics of robust

colloidal levitation via net potentials that are mainly repulsive due to long-range, non-specific interactions of adsorbed BSA and PEO macromolecules.

5.5 Irreversibly Deposited Colloidal Probes

At the other extreme of robust colloidal levitation observed in Figure 5.3 is the limiting case of irreversible colloidal deposition, due to strong colloid-surface attraction. Figure 5.4 shows results from this work that most closely approach irreversible deposition for BSA adsorbed to unmodified silica colloids and to 5nm-thick Au films on a microscope slide. Figure 5.4A shows 22 colloid trajectories in gray with colored pixels indicating $\ln(\tau_a)$ values and an inset histogram of $\ln(\tau_a)$ values similar to Figure 5.3A. Figure 5.4B shows the ensemble-average (red) and 11 single colloid (black) PEP with exponential curve fits to both sides of the ensemble-average PEP, having decay lengths of κ^{-1}=5 nm. Figure 5.4C shows lateral MSDs with the same format as in Figure 5.3C.

Results in Figure 5.4 show characteristics of irreversibly deposited colloids resulting from colloid-surface vdW attraction dominating short-range BSA-BSA repulsion. Adsorbed BSA layers are still expected to have repulsive interactions in Figure 5.4, but the range of repulsion is diminished compared to Figure 5.3, due to the formation of much thinner ~3nm layers on unmodified colloid surfaces.[153] Another factor favoring deposition is the ~5× greater vdW silica-Au attraction in Figure 5.4, compared to silica-silica attraction in Figure 5.3.[25] As the result of thin adsorbed layers and strong vdW attraction, the ensemble-average PEP in Figure 5.4B primarily shows colloids confined to the bottom of energy wells that are deep compared to kT.

Curve fits to lateral MSDs in Figure 5.4C yield confinement lengths of 78 and 127nm in the *x*- and *y*-directions and short-time $\langle D_{\|} \rangle$ values remarkably similar to predictions. The latter correspondence is probably somewhat fortuitous given the proximity of the associated length scales to the limited sub-pixel resolution of our CCD camera. Results in Figure 5.4C also show long-time $\langle D_{\|} \rangle$ is suppressed (except for several weakly associated colloids), which is not obvious *a priori*, since normal particle-surface attraction can still allow for lateral diffusion through rolling. Local deformation[157] and interpenetration[143] of adsorbed BSA layers in contact probably provide resistance to translation via rolling. The normal and lateral confinement observed in Figure 5.4C is a general feature of irreversibly deposited colloids, at least in the absence of lateral potential fields.

CSA events reported in Figure 5.4A are a more sensitive measure of colloid deposition than the MSDs in Figure 5.4C, due to the significantly better spatial resolution of TIRM compared to VM (~1nm vs. ~600nm). Some explanation is required for the finite colloid-surface dissociation observed in Figure 5.4A, as truly irreversible deposition should produce the trivial result of all colloids being immobilized for the duration of the ~40min experiment to produce all blue pixels ($\ln(2.3\times10^5 \text{ms}/16\text{ms}) \approx 12$, based on Eq. 5.1 and the diffusion-limited timescale identified in Figure 5.3A). The different colored isolated pixels in Figure 5.4A result from both apparent height excursions, due to signal noise, and actual low-probability excursions of colloids out of ~12*kT* deep wells. For example, any deposited colloid displaying either real or apparent height excursions during the measurement period will overwrite blue pixels (large τ_a)

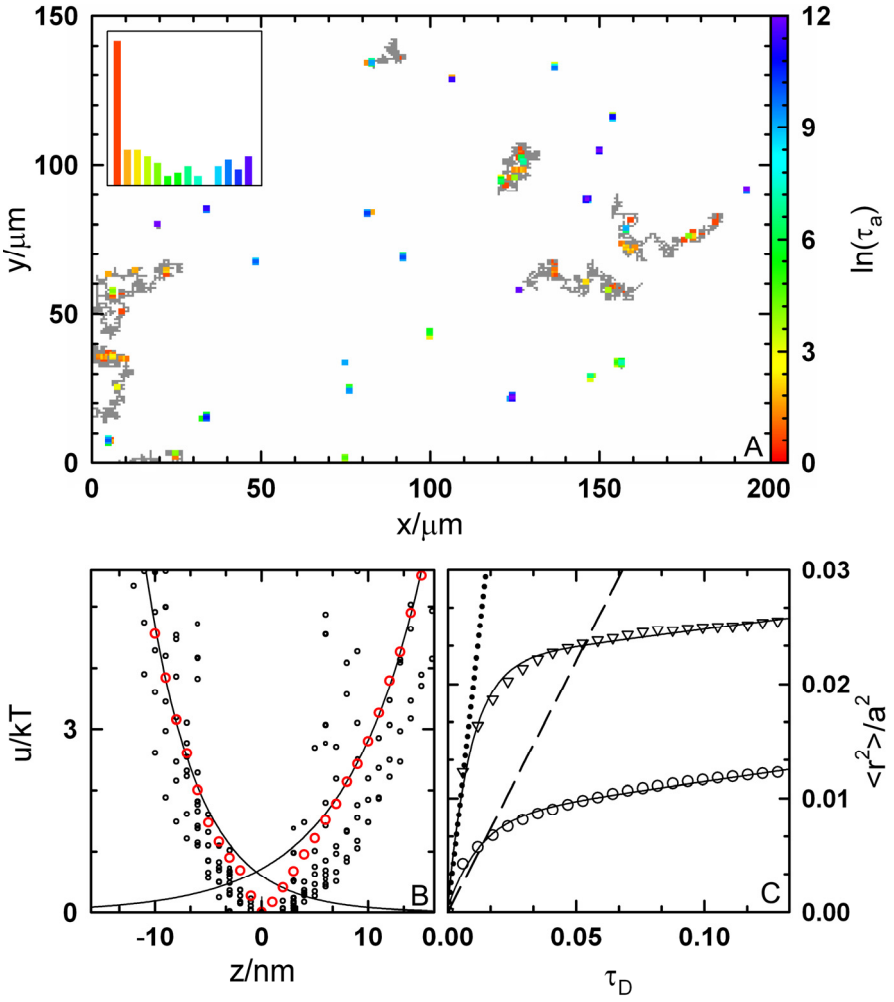

Figure 5.4. (A) Lateral trajectories of BSA/APS-coated colloids on a BSA/Au-coated glass surface. (B and C) PEPs and MSD data presented with same format as Figure 5.3.

with red-shifted pixels (small τ_a). Overwriting occurs due to lateral confinement, which suggests isolated red-shifted pixels still correspond to nearly irreversibly deposited particles.

Although noise can produce apparent dissociation events, 5 colloids in Figure 5.4A clearly display significant lateral diffusion and short-lived CSA events. Such behavior could arise from locally diminished colloid-surface attraction due to surface

nonuniformities,[36] smaller colloids within the sample polydispersity,[29] and variations in the local BSA layer architecture that generate short-range repulsion, thereby weakening attraction at contact. In any case, the small percentage of colloid-surface dissociation events and the occurrence of finite lateral diffusivities in Figure 5.4 suggest >12kT deep attractive wells due to residual repulsion between thin BSA layers that, while insufficient for robust stabilization, still significantly weaken vdW attraction compared to bare surfaces in contact. The results in Figure 5.4 also suggest attraction can be altered on the kT scale in the presence of surface heterogeneity to influence local CSA events.

5.6 Associated Colloidal Probes and Surface Heterogeneity

Intermediate to the limiting cases of robust levitation and irreversible deposition is the case of intermittent CSA. As captured by 5.1, τ_a values are exponentially sensitive to the attractive well depth, u_{min}, and become diffusion limited as $u_{min}\rightarrow 0$ and infinitely long as $u_{min}\rightarrow -\infty$. The non-dimensional quantity, u_{min}/kT, indicates the relative magnitudes of attraction, favoring CSA, and thermal Brownian motion, favoring colloid-surface dissociation. As a result, small changes in u_{min} relative to kT produce exponentially large changes in τ_a, which is important for understanding intermittent CSA as mediated by adsorbed BSA and PEO layers.

Figure 5.5 shows representative results for intermittent CSA with BSA adsorbed to 1-octadecanoic acid (ODA)-coated silica colloids and PEO3k adsorbed to an OTS-coated glass slide. Each plot in Figure 5.5 displays information similar to corresponding plots in Figures 5.3 and 5.4. Figure 5.5A shows uninterrupted lateral colloid random walks in some regions and other regions displaying a spectrum of colored pixels,

indicative of broadly varying τ_as. Figure 5.5B gives 4 single colloid PEPs, with solid red lines showing exponential fits (12-15nm decay lengths) to each attractive potential having minima (indicated by dashed red lines) of -1.6, -2.3, -2.7, -3.8 *kT*.

Results in Figure 5.5B point to varying levels of attraction between BSA-coated colloids and a PEO3k-coated wall that could be misinterpreted as novel BSA-PEO attraction without additional information. Nevertheless, results in Figure 5.5A signify numerous spatially and temporally distributed CSA events, indicative of local attraction on a heterogeneous surface. Because single-colloid PEPs in Figure 5.5B are constructed by averaging all heights over each colloid's random walk without distinction for its local interaction, the resulting net colloid-surface potentials include both levitated (grey pixels) and associated (colored pixels) height excursions. As a result, deeper wells are observed in Figure 5.5B when a greater proportion of height excursions are measured during associated rather than levitated states. By identifying and discarding the "heterogeneous portion" of each average PEP in Figure 5.5B, all single-colloid PEPs can be "corrected" to collapse onto a single curve that is remarkably similar to the PEP in Figure 5.3B. This result shows that the BSA-PEO5k and BSA-PEO3k repulsion in Figures 5.3B and 5.5B are similar once the effects of surface heterogeneity (that are not concealed by the thinner PEO3k layer) are considered.

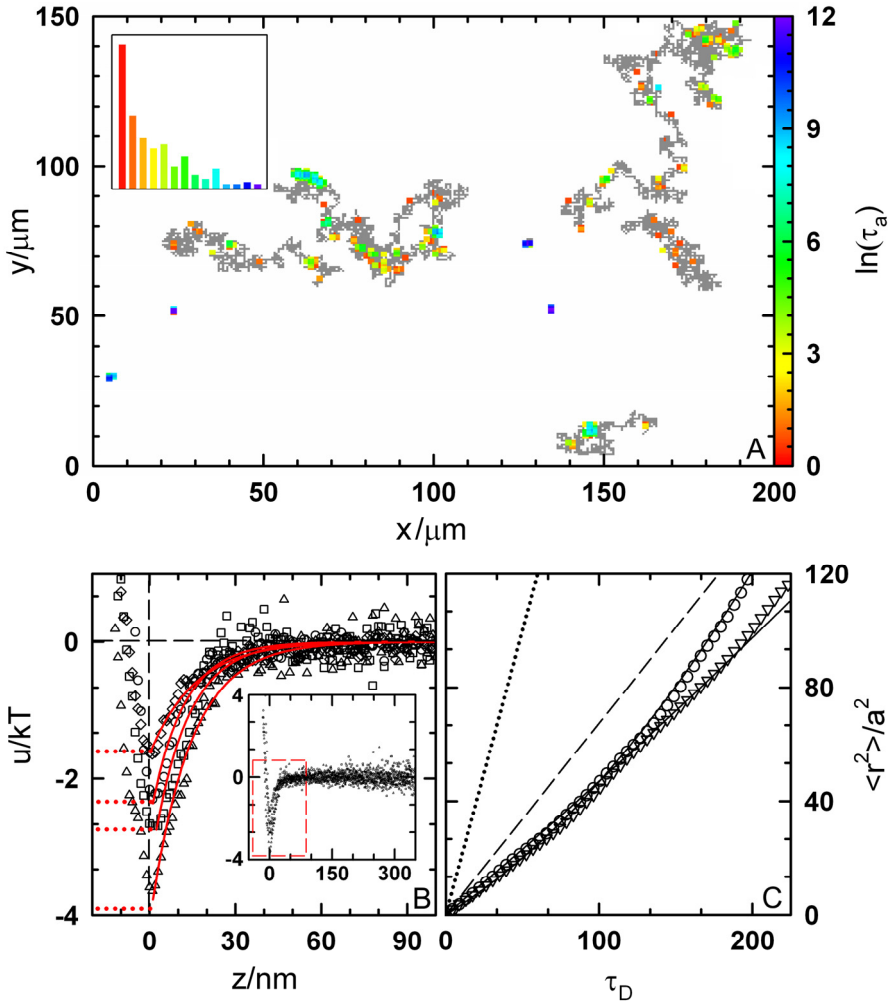

Figure 5.5. (A) Lateral trajectories of BSA/ODA-coated colloids on a PEO3k/OTS-coated glass surface with same format as Figure 5.3. (B) Single-colloid PEPs (black points) without gravitational potential and with exponential curve fits (red lines) to van der Waals attraction. (C) Ensemble-average lateral MSDs with same format as Figure 5.3.

The surface heterogeneity implicated in Figures 5.5A and 5.5B is also consistent with the retarded lateral diffusion in Figure 5.5C, which is apparent from the measured diffusivity, $\langle D_{\|} \rangle / D_0 = 0.2$, being less than the predicted diffusivity, $\langle D_{\|} \rangle / D_0 = 0.3$, from Eq. 2.27. Because colloids are already held near the surface in attractive wells, the diminished diffusion cannot be explained by increased hydrodynamic hindrance but is

consistent with intermittent CSA events hindering the lateral diffusion process.[81] Nearly linear MSD curves in Figure 5.5C also suggest CSA events are spatially random, as anything else would produce characteristic features indicative of diffusion over a periodic landscape.[25] The net interpretation of the results in Figure 5.5 is that the suspected surface heterogeneity is randomly distributed such that locally varying attraction on the 1-10 kT scale produces intermittent CSA events amongst other regions without any CSA.

The algorithm for identifying discrete association events produces consistent results for experiments in Figures 5.3-5.5 that involve levitation, association, and deposition of BSA- and PEO-coated colloids on similarly coated surfaces. Because the statistical nature of CSA events does not allow an *a priori* method for identifying discrete CSA events, a certain fraction of measurements are designated in error as either levitated or associated in all cases. Yet, the validity of the algorithm is justified *a posteriori* since using more or less conservative constraints begins to distort PEPs from agreement with independent measures (e.g., colloid radius via the gravitational potential, colloid diffusivity via Eq. 2.27). By neither removing too many points corresponding to homogeneous vdW interactions (to underestimate the attractive well) nor leaving too many points corresponding to heterogeneous association events (to overestimate the attractive well), the algorithm for identifying CSA events produces self-consistent energetic, spatial, statistical, and temporal results in Figures 5.3-5.5.

5.7 Colloidal Probe Non-uniformity and Migration

Although wall surface heterogeneity appears to be implicated in the intermittent CSA results described in Figures 5.4 and 5.5, there is no obvious indication of colloid non-uniformity. Colloids likely have molecular-scale heterogeneity[158] but also appear to be sufficiently uniform that they can be analyzed as ensembles,[28] which was an unstated assumption up to this point. For comparison, Figure 5.6 reports a unique experiment involving a single outlier colloid with similar plots to Figures 5.3-5.5. Results are shown for BSA/APS coated colloids levitated above a BSA/APS coated glass slide. The flow cell was intentionally misleveled in Figure 5.6 upon observation of the outlier colloid to observe surface association in the presence of lateral migration.

The obvious departure of the single predominantly orange-yellow-green colored trajectory in Figure 5.6A from all other gray trajectories allows for its straightforward identification and its separate analysis from the otherwise robustly levitated colloids. Because the trajectory of the outlier colloid coincides with the same surface locations as a preceding colloid's trajectory, the frequent intermittent association of the outlier colloid with the surface can be attributed to defects on the colloid rather than the wall. The red PEP in Figure 5.6B is the ensemble-average profile of 13 colloids, excluding the outlier colloid, and is typical for robustly levitated colloids (see Figure 5.3B). The black PEP in Figure 5.6B corresponds to the single outlier colloid and displays the parabolic shape characteristic of deposited particles (Figure 5.4), except for its greater width due to larger height excursions. Results in Figure 5.6B demonstrate BSA-BSA mediated colloid-surface interaction can be quantified in the presence of migration and an easily

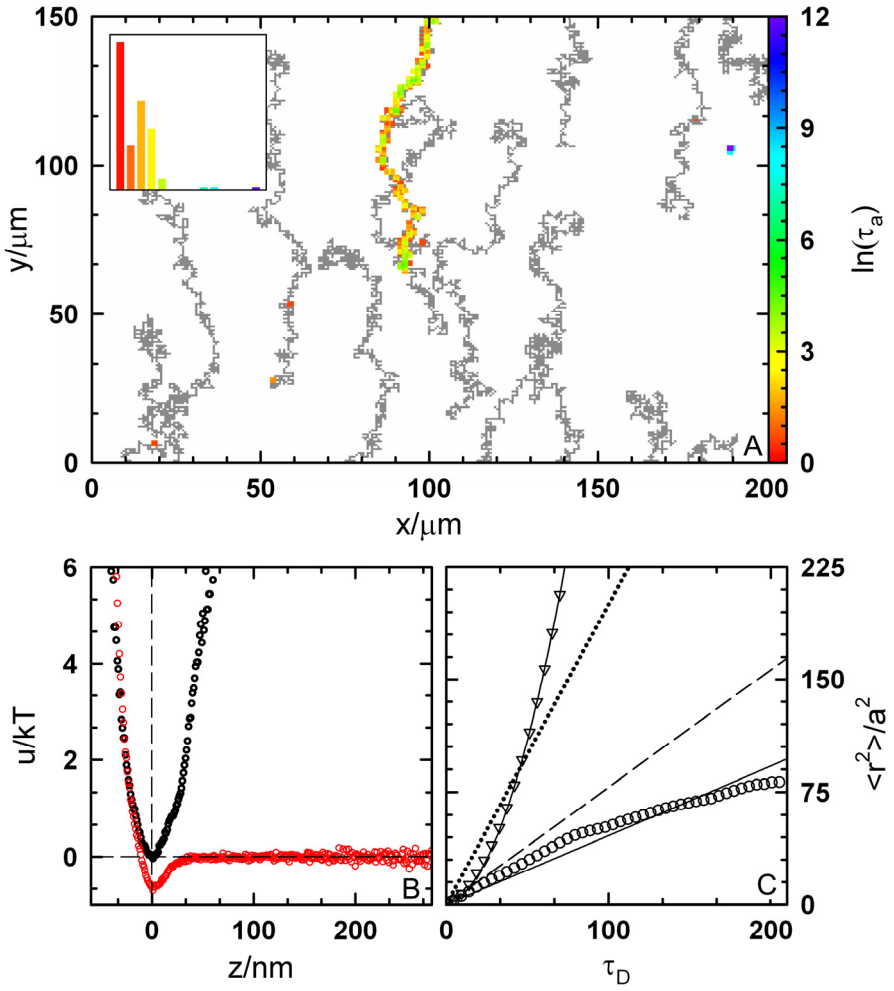

Figure 5.6. (A) Lateral trajectories of BSA/APS-coated colloids on a BSA/APS-coated glass surface with data presented in same format as Figure 5.3. (B) Single associating colloid (black) and ensemble (red) colloid PEPs without the gravitational potential. (C) Ensemble-average lateral MSDs with same format as Figure 5.3

identifiable deviant colloid to produce ~0.7*kT* attractive vdW well, similar to the BSA-PEO5k PEP in Figure 5.3B.

Figure 5.6C shows a parabolic upturn in the MSD in the *y*-direction, consistent with the obvious migration in Figure 5.6A, whereas the MSD in the *x*-direction shows a turnover approaching a constant MSD that is indicative of confinement. Because the colloids should not be confined for any obvious reasons, the turnover in the *x* MSD is

attributed to migration into or out of the window in the *y*-direction leaving suitably sampled short-time trajectory data but statistically deficient long-time data. Analysis of the migration in Figure 5.6C indicates a ~5º tilt in the flow cell, based on a component of gravity acting parallel to the surface. The lateral migration of the associating outlier colloid in Figure 5.6 does not appear to be hindered by any tangential interaction, in contrast to the diffusive behavior in Figure 5.4, which might result from the lateral force exceeding a sort of tangential yield stress. As a side note, the colloid migration in Figure 5.6 is reminiscent of ligand coated colloids and leukocytes on surfaces,[159] which suggests another potentially interesting application for investigation with the new methods reported here.

The outlier colloid's greater association with the surface could result from defects due to the APS silanization procedure, which is performed under metastable conditions such that periodic aggregate formation could produce surface patches altering the local interaction. Observation of non-uniform colloids was also extremely rare; for ~20 colloids interrogated in the nearly 100 ensemble experiments similar to Figures 5.3-5.6, only the single outlier colloid in Figure 5.6 was observed, suggesting an occurrence of less than ~1/2000. Based on the results in this work, non-uniform colloids are rarely observed in comparison to wall surface heterogeneity.

5.8 BSA-PEO Interactions and Surface Heterogeneity

The results in Figures 5.3-5.6 demonstrate the ability to simultaneously observe many single colloids interacting with different surface regions. By averaging over many colloids and surface positions, statistically significant results are obtained but not at the

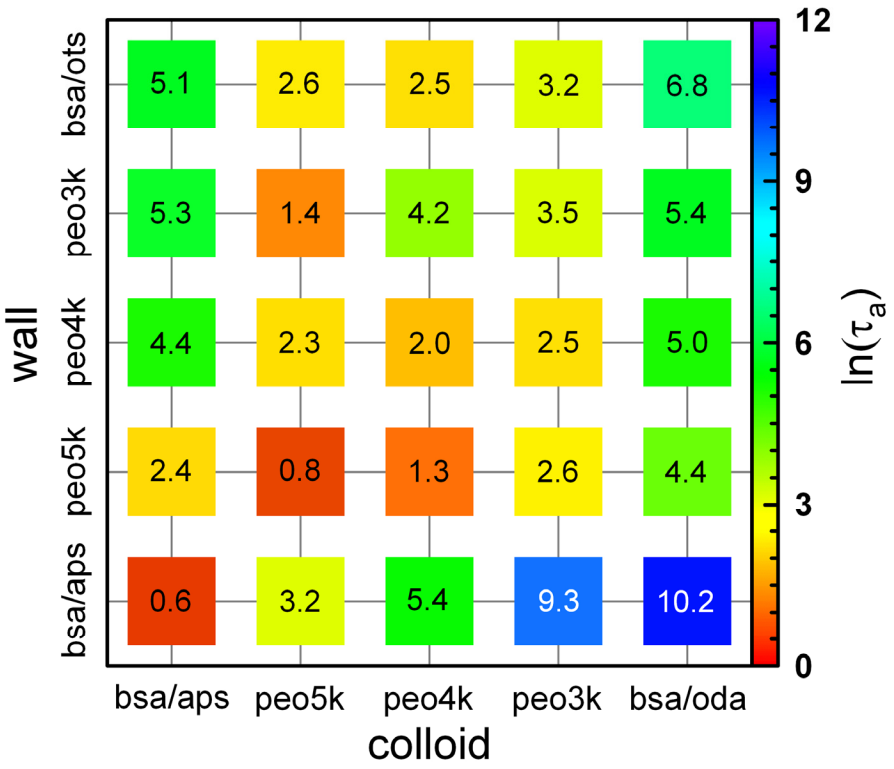

Figure 5.7. Summary of $\ln(\tau_a)$ values for combinations of colloids and surfaces with adsorbed BSA and PEO copolymers.

expense of losing discrete information about single colloids and local surface properties. Figure 5.7 summarizes several trends that emerge from numerous systematic measurements of BSA- and PEO-coated particles and surfaces and reports average $\ln(\tau_a)$ values for 25 experiments performed in triplicate including: (i) BSA adsorbed to APS-modified colloids and surfaces and (ii) BSA, PEO5k, PEO4k, and PEO3k adsorbed to ODA-modified silica colloids and OTS-modified microscope slides. The $\ln(\tau_a)$ values in Figure 5.7 are averaged over all colloids, surface locations, and the total observation time (i.e., average over all grey and colored pixels in Figures 5.3-5.6).

Effects of adsorbed macromolecule MW on $\ln(\tau_a)$ values are apparent from the PEO-PEO layer interactions in Figure 5.7. For example, the highest MW PEO5k copolymer absorbed to OTS and ODA modified surfaces yields ~20 nm thick layers[138] that are expected to produce the observed robust levitation ($\ln(\tau_a)$=0.8). In contrast, adsorption of ~10 nm PEO3k layers[160] to similarly modified surfaces allows significantly more and longer-lived CSA events ($\ln(\tau_a)$=3.5). The general trend that emerges in Figure 5.7 is that thicker layers, due to higher PEO MWs, produce smaller $\ln(\tau_a)$ values. Because all PEO copolymers have similar triblock ratios, their adsorbed layers are expected to have brush architectures with thicknesses determined primarily by MW.[143] PEO interactions are also expected to be purely repulsive for the favorable solvent conditions explored in this work.[138] A likely mechanism leading to decreasing $\ln(\tau_a)$ with increasing PEO MW is that thicker layers are more likely to conceal chemical and physical surface heterogeneities that allow for increased local attraction and CSA.

Effects of adsorbed layer architecture in Figure 5.7 can be deduced from the BSA-BSA data, which consist of monodisperse macromolecules adsorbed with different orientations on different chemically modified surfaces. For example, adsorption of BSA to APS modified silica can produce ~14nm-thick layers via a preferred orientation of BSA parallel to its major axis[154] to produce robust levitation ($\ln(\tau_a)$=0.6). In contrast, adsorption of BSA to OTS modified silica surfaces can produce thin ~3nm layers via a flattened BSA orientation[161] to yield significantly more and longer-lived CSA events ($\ln(\tau_a)$=6.8). BSA conformation may also be perturbed on different chemically modified surfaces to influence adsorbed layer thicknesses. The BSA-BSA data in Figure 5.7

suggest that thicker layers via architectural effects can also better conceal surface heterogeneities, similar to PEO MW effects.

Finally, for the asymmetric BSA-PEO interactions in Figure 5.7, the ln(τ_a) data can be explained based on the concealment of surface heterogeneity due to a combination of PEO MW and BSA orientation. For example, BSA/APS modified surfaces interacting with PEO5k/OTS-ODA surfaces produce robust levitation (ln(τ_a)=3.2, 2.4) whereas BSA and PEO3k adsorbed to alkyl modified surfaces produce comparatively more and longer CSA events (ln(τ_a)=9.3, 5.3). In all cases, BSA-PEO interactions are completely repulsive and, therefore, parallel with standard theories for macromolecular interactions in good solvent conditions. As a result, adsorbed BSA and PEO layers can robustly levitate colloids above surfaces provided layers are thick enough to overcome colloid-surface attraction, particularly in the presence of surface heterogeneity.

A final note about the data in Figure 5.7 is that it is not symmetric about the diagonal; there is a bias toward greater ln(τ_a) for thin adsorbed layers on the colloid instead of the wall. For example, PEO3k adsorbed to colloids interacting with BSA/APS coated walls experience longer CSA lifetimes with ln(τ_a)=9.3 than the reverse case with ln(τ_a)=5.3. The simplest explanation for this bias is differences in the colloid and wall surface modifications. Because stable silica colloids are modified with ODA using a well-established method,[162] the problem is expected to lie with OTS modification of the glass slide surface, which is known to produce OTS aggregates[163] (note that surface roughness <5nm does not significantly scatter the evanescent wave).[36] The dielectric properties of aggregated alkane structures on the wall could reduce vdW attraction

compared to alkane layers on colloids,[34] which would produce the observed bias towards greater ln(τ_a) for thinly adsorbed layers on the colloid compared to the wall.

Data from MSDs can be studied to obtain information pertaining to confinement lengths, lateral migration forces, and two-body hindered particle diffusion coefficients. The MSD data in Figures 5.3 to 5.6 were fit using Eq. 2.27, and Table 5.1 summaries the parameters of interest. Importantly, the superimposed migration force is easily determined so that the true hindered diffusion coefficient can be ascertained and compared with theory.

Table 5.1. Fitted parameters for hindered particle diffusion, migration, and confinement.

Figure	**direction**	$D_{\|\|}$	$V_{x,y}$	F	**slope**	L^2	A_1	A_2	L/a
5.3	*x*	0.2472	0.0264	0.39fN	0.43º				
5.3	*y*	0.3149	0.0548	0.64fN	0.70º				
5.4	*x*					0.0073	0.9537	80.59	78nm
5.4	*y*					0.0193	0.9776	112.316	127nm
5.5	*x*	0.1464	0.0347	0.88fN	0.96º				
5.5	*y*	0.1999	0.0124	0.23fN	0.25º				
5.6	*x*					78.15	1.016	0.0077	8.04μm
5.6	*y*	0.1147	0.1628	5.25fN	5.75º				

5.9 Conclusions

Here, we have described a distinctly new approach for quantitatively measuring interactions of proteins and synthetic macromolecules adsorbed to colloids and wall surfaces. Using an integrated TIRM and VM colloid-tracking technique, equilibrium and dynamic analyses of the 3D trajectories of many freely diffusing colloids provide simultaneous energetic, spatial, statistical, and temporal information about adsorbed BSA and PEO copolymer interactions. Information from such measurements includes single colloid and ensemble-average PEP, lateral diffusivities, and CSA lifetimes. A

consistent analysis of such information in several demonstrative measurements is used to distinguish different colloid-surface interaction regimes as belonging to levitation, association, or deposition.

This newly developed method and associated analyses were then employed in a systematic series of experiments to capture how average colloid-surface interactions are mediated by combinations of chemical surface modifications, adsorbed BSA and PEO layers, and surface heterogeneity. These results reveal how BSA layer architecture on different chemically modified substrates and PEO copolymer MW, together, either conceal or expose underlying substrate heterogeneities to influence colloid-surface attraction and association lifetimes. In all cases, BSA-BSA, BSA-PEO, and PEO-PEO interactions appear to be completely repulsive such that CSA only occurs due to non-specific colloid-surface attraction, particularly in the presence of surface heterogeneity. The results in this work demonstrate non-specific repulsion of proteins and synthetic macromolecules as a basis for creating integrated biomolecular-synthetic devices. More importantly, this work provides a baseline to differentiate specific and non-specific interactions between protein binding partners on colloids and surfaces.

6. LATERAL TRANSPORT WITHIN AND STABILITY OF APPOSING SUPPORTED LIPID BILAYERS

6.1 Synopsis

The functionalization of colloid surfaces with supported lipid bilayers (SLBs) facilitates the investigation of complex biological behavior that has origins in the lateral fluid properties of the bilayer. Gaining insights into how apposing SLBs interact is critical to the development of novel therapeutic treatments, such as gene and protein delivery, and the establishment of meaningful and reliable experimental constructs for studying cell membrane components.

This section outlines the use of confocal scanning laser microscopy (CSLM) and ensemble TIRM to explore the interactions between stable and unstable SLBs on apposing silica colloidal and wall surfaces. Our results reveal (i) the conditions necessary to maintain bilayer integrity and segregation in stabilized systems, (ii) the role of bilayer defects in fusion and neck formation between apposing SLBs, (iii) how surface heterogeneity affects the spatial and temporal distribution of mobile lipids, and (iv) the existence of uniform and complete quasi-2D exchange of lipids between colloids and planar glass surfaces.

Ensemble TIRM data are collected to find separation-dependent potentials of colloids sterically levitated by PEGylated SLBs and irreversibly deposited onto the underlying wall. TIRM and CSLM results for multiple colloid-wall bilayer configurations reveal that SLBs interact through several mechanisms including fusion with complete exchange of lipids and membrane adhesion without lipid exchange.

CSLM of fluorescently tagged bilayer components helps elucidate the role of defects/heterogeneity in fusion and neck formation between apposing SLBs.

Collectively, these results help in the development of robust experimental systems that can be used to study interactions between biomolecules incorporated into a fluid bilayer. Additionally, knowledge gained from this work can be implemented to better design drug delivery vehicles that rely on the fusion between cell membranes and freely diffusing functionalized colloids.

6.2 SLB Formation and Characterization

PEGylated and non-PEGylated bilayers were formed on surfaces according to the vesicle fusion method[61] detailed in *Section 3.2.4*. Figure 6.1 shows a series of CSLM images that capture time-dependent vesicle adsorption, rupture, and spreading at the glass-liquid interface for a vesicle concentration of 25μg/ml. Vesicles were comprised of 5mol% PEG1000 and 1mol% Bodipy. The first image (t=0s) was taken within 1s of

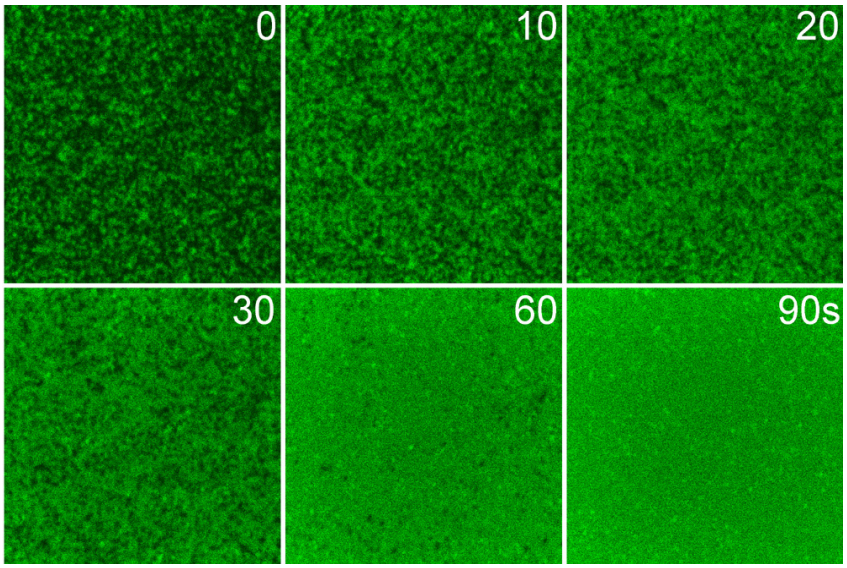

Figure 6.1. CSLM time series of SLB formation. Each image is 10μm wide.

vesicle addition. Clearly, defects in the membrane at 60s are eventually repaired as more vesicles adsorb and fuse and the bilayer spreads laterally. Further, excess, non-fused vesicles can be seen absorbed to the surface subsequent to complete bilayer formation. Their presence, however, is significantly reduced following rinsing, which could be the result of shear flow at the surface during rinsing or the inevitable desorption of PEG-stabilized vesicles. .

The mobility of membrane components was quantified with FRAP measurements using confocal microscopy (see *Sections 2.7 and 3.6* for details). Figure 6.3 gives intensity vs. time data for fluorescence recovery of the following three different lipid compositions with POPC as bulk or background lipid: 3mol% PEG1000 with 1mol% DiA, 1mol% Bodipy, and 1mol%DiA. Note that DiA and Bodipy are simply charged lipophilic tracers used to generate fluorescence within the membrane.

From the fits given in the plot, the diffusion coefficients, D_{bl}, and % recovery in 150mM NaCl were found to be 6.4μm^2/s and 96% for 1mol% Bodipy (○), 4.9μm^2/s and 95% for 1mol% DiA (○), 2.9μm^2/s and 93% for 3mol% PEG1000-1mol%DiA (○). Note that the calculated magnitudes for D_{bl} are within the typical range found for these membrane compositions. When the solution concentration was dropped to 0.1mM, D_{bl} and % recovery for the same 1mol% DiA bilayer decreased to 1.2μm^2/s and 66% (△). The presence of PEG in the bilayer increases the membrane-to-surface separation, therefore decreasing the viscous coupling between the fluorescent lipids and the surface, but PEG incorporation tends to increase the intermembrane viscosity more; hence, D_{bl}

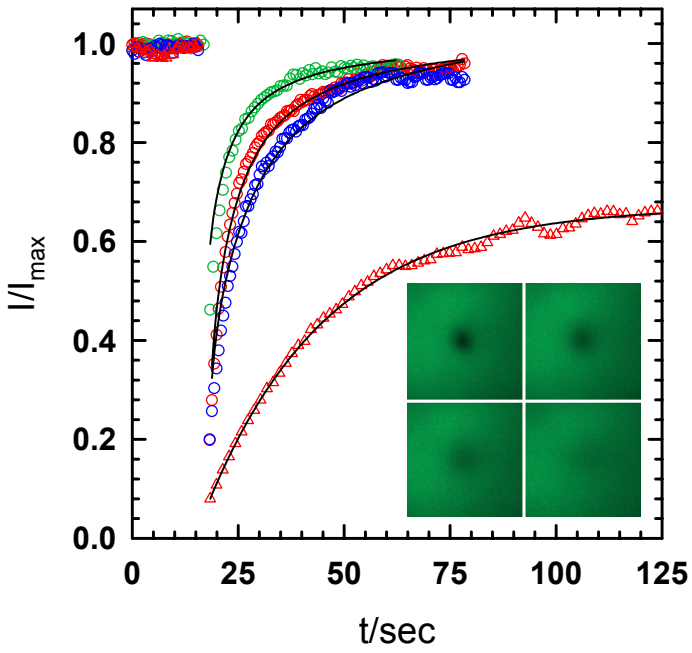

Figure 6.2. FRAP data for three bilayer compositions in 150mM NaCl media with one (○) duplicated in 0.1mM NaCl (△). The initial 15s prebleach period is performed to find the intensity for full recovery. Inset gives a qualitative representation of fluorescence recovery. Pre- and postbleaching was 1/5000th the bleaching intensity.

dropped by approximately 40% between the non-PEGylated and PEGylated membranes..

Although the MW of DiA is 618 and Bodipy is 1067g/mol, Bodipy has a higher D_{bl} than DiA at the same mole fraction. This and the other DiA result can be easily explained by an argument based on electrostatic interactions. Because DiA carries a net positive charge and Bodipy a negative one, DiA is attracted to the negatively charged silica substrate and Bodipy is repelled by it. The silica surface is not atomically smooth, and thus, DiA lipids temporarily in contact with the surface experience a tangential drag force. Moreover, the water layer beneath the membrane becomes thinner due to this attraction, which increases the viscous drag on both the lower and upper leaflets. In the

presence of 150mM NaCl, columbic attraction is screened at distances >0.5nm, thus the affect is not as pronounced as compared with diffusion within the 1mol% DiA membrane in 0.1mM (κ^{-1}=30nm), for which D_{bl} drops significantly as well as the % recovery. Therefore, these FRAP results not only give a quantitative assessment of transport within these membranes, they are also self-consistent in the way they describe the physical systems.

6.3 Non-fused and Sterically Stabilized SLBs

When cell membranes come into contact, several forces arise between the two membranes. For example, steric repulsion between certain molecules within the glycocalix provides a stabilizing force, receptor ligand pairs such as cadherins or SNARE proteins may induce membrane adhesion or fusion and fission,[164] local electrostatic and vdW potentials between the membranes could lead to locally repulsive or attractive interactions, thermal and cytoskeleton-induced undulations in the membrane structure act to provide an entropic barrier to adhesion. Depending on the magnitude, range, and lifetime of these various forces, the cytosol of juxtaposed cells or a cell membrane and a diffusing lipid vesicle either remain partitioned or interconnected. The extent of interconnection (e.g., complete engulfing of the vesicle or the formation of gap junctions between cells) is mediated by the specificity of the ligand-receptor pair or stability of the two membranes.

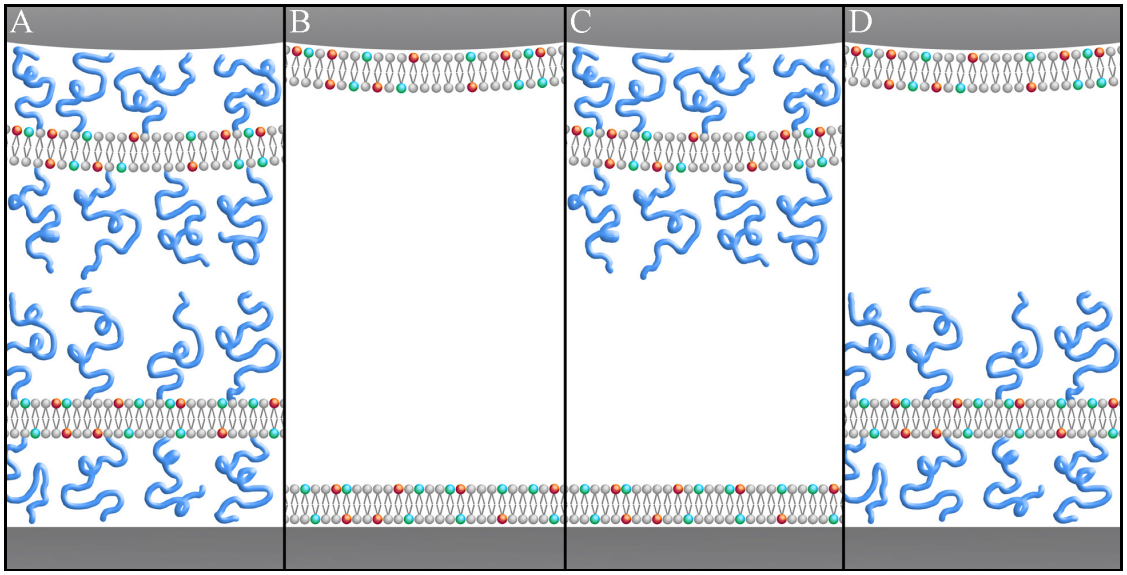

Figure 6.3. Experimental SLB configurations studied.

In this subsection, particle-wall TIRM and CSLM studies of non-fused (but adhered) and sterically and electrostatically stable SLBs are presented. The inherent stability of these systems is a function of absolute separation between particle and wall surfaces (dictated by PEG MW and X_p) and ionic strength of the media and net charge of the lipid components. Figure 6.4 schematically depicts the four variations of interest throughout this entire section. Particle and wall surfaces are: both modified with PEGylated bilayers (A), both modified with non-PEGylated bilayers (B), or exist as an asymmetric mixture (C and D).

In the limiting case of low ionic strength (≤1mM) electrostatic experiments, apposing like-charged and neutral bilayers exhibited purely repulsive interactions and a lack of adhesion. For neural bilayers, the negative surface potential of the underlying silica on the particle and wall surfaces was able to pass through the bilayer and impart electrostatic stability on the particle. Electrostatic interactions also play a role in vesicle

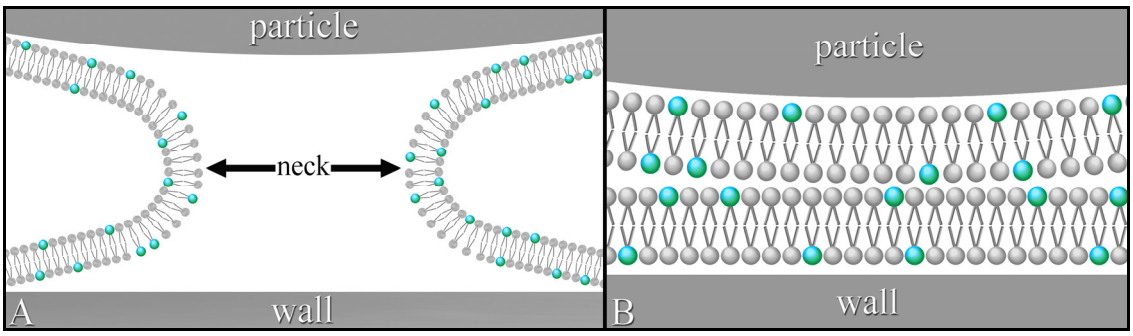

Figure 6.4 (A) Fused SLBs, leading to lipid exchange between the two surfaces. (B) Unstable and adhered but non-fused SLBs.

fusion during the formation of SLB (e.g., vesicles with negatively charged species will only adsorb and fuse on silica particles in the presence of high salt).

Confocal studies of non-fused SLBs revealed a lack of lipid exchange for systems classified as such, thus CSLM results will only be discussed and not shown. For particles functionalized with fluorescently labeled bilayers (all combinations shown in Figure 6.4), CSLM scans were able to image the surface of the particle and show that the POPC-modified (hereafter, the term given to the surface modification with a complete lack of fluorescence) wall was devoid of fluorescent lipids that would be otherwise acquired from the particle. In the case of fluorescently tagged bilayers on the wall and POPC on the particle, the same was also true: stable and non-fused particles remained non-fluorescent, even in the case of adhesion. The previous illustrates why these systems were classified as non-fused and stable. The distinctions between fused and non-fused and stable and unstable are, however, not exclusively given to any particular system but are instead used to describe particle-wall interactions on an individual particle-wall basis. In other words, for nearly every experimental configuration tested, apart from

PEGylated bilayers on each surface, “stable” systems exhibited isolated events of fusion and instability. For reference, the schematic in Figure 6.5 addresses the description of fused vs. non-fused. As will be shown in a later subsection, these discrepancies are the result of surface heterogeneity in the form of bilayer defects that most likely reside on the particle. .

Ensemble TIRM data for 1.5μm silica colloids, sterically stabilized in 150mM NaCl with either 1.5mol% PEG2000 (□) or 0.5mol% PEG5000 (○) on both surfaces, is given in Figure 6.6A. In Figure 6.6B, the vdW portion of each ensemble is compare to the Lifshitz fit for a 1.5μm silica colloid interacting with an infinite silica plate. These reasonably good fits indicate that the onset of repulsion occurs at a particle wall separation of ~50nm for 0.5mol% PEG5000 and ~40nm for 1.5mol% PEG2000. Note that slightly better fits could be attained in the model was rigorously adapted to include the vdW contribution from the SLBs themselves, but that has been left out here.

Using scaling theory to predict brush layer thickness (see *Section 2.8*), hardwall repulsion should occur at ~26nm for 0.5mol% PEG5000 and ~19nm for 1.5mol% PEG2000. Additionally, the 9nm in thickness provided by the two lipid leaflets on each surface should actually be removed from the estimate due to the fact that the Hamaker constant for lipid-lipid interactions is 2-5× larger than silica-silica, thus their presence would actually increase the attractive well at a given separation and shorten the predicted absolute separation at the onset of repulsive contact. A small portion of this 25 to 30nm discrepancy between observed and predicted values for layer thickness could be accounted for by considering the diminishing effect of surface roughness on vdW

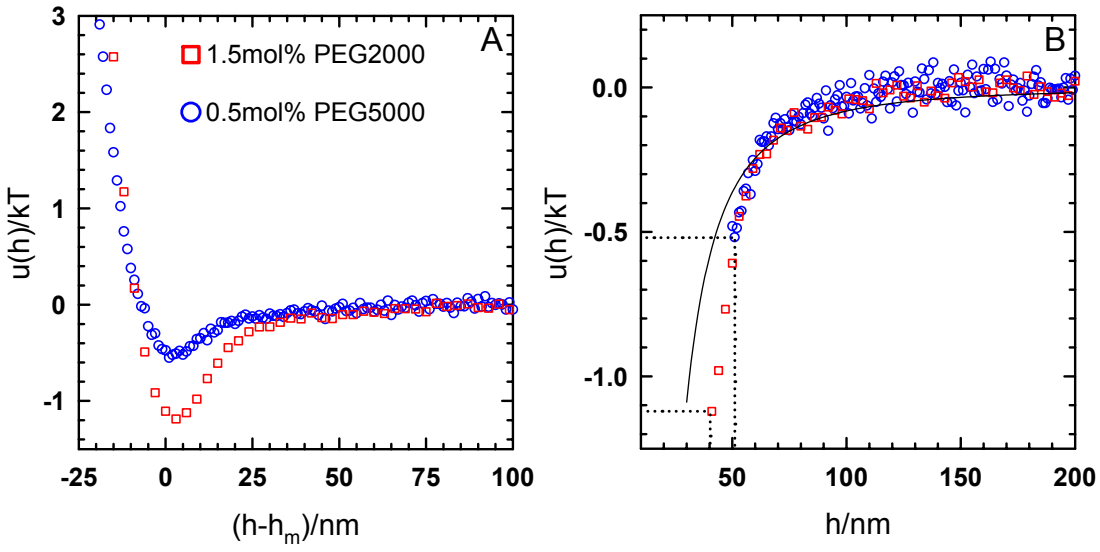

Figure 6.5. (A) Ensemble TIRM profiles for 1.5µm silica particles sterically stabilized by PEGylated bilayers with one of two different compositions. (B) vdW portion of each profile in (A) plotted against the Lifshitz prediction for particle-wall vdW.

potentials,[36] but this could not account for all of the difference. I hypothesize that the additional steric contribution arises from thermal undulations of the PEGylated bilayer.

Multiple studies have modeled[165] and experimentally observed[166] undulations in supported and free-floating and lipid membranes. Figure 6.7 illustrates how undulations of the membrane increase the average thickness of the steric layer. The addition of PEG to the top and bottom leaflets of the bilayer, as is the case here, helps amplify thermal undulations because the lipids are offset from the wall, therefore they experience less vdW attraction with the underlying support and they move more freely. Additionally, the hydrodynamic force that resists the motion of a bilayer away from the wall is diminished the further the lipid bilayer is separated from the support. Collectively, these sited studies and our TIRM measurements of weaker vdW attraction than predicted point to thermal undulations as a phenomenon that occurs in these PEGylated bilayers, with

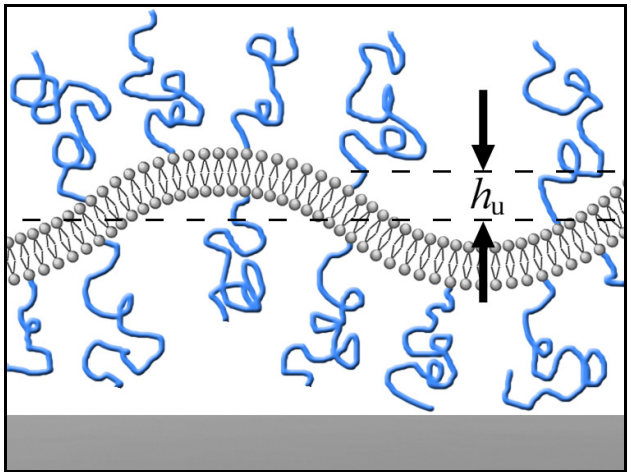

Figure 6.6. Increased steric layer thickness due to thermal undulations with an out-of-plane amplitude of h_u.

amplitudes on the order of ±10nm for 1.5mol% PEG2000 and ±15nm for 0.5mol% PEG5000.

TIRM profiles of adhered but non-fused particles in 150mM NaCl are shown in Figure 6.8. The single-particle data correspond to three different colloid or bilayer systems, with POPC on the wall in each case. They are: POPC-modified 1µm silica (○), POPC-modified 1.5µm silica (△), and 1.5µm silica coated with 3mol% PEG1000 (□). The black symbols are ensemble averages that correspond to the single-particle profiles of same symbol shape. The narrowest well (○) is an ensemble average from bare particles deposited on a bare wall in 150mM NaCl.

For these three configurations, CSLM confirmed that particles were, indeed, deposited onto the wall but not exchanging lipids. The 1.0µm and 1.5µm silica colloids coated with POPC and deposited on a POPC-modified wall exhibited drastically different height fluctuations. Because vdW attraction scales linearly with particle size, the 1.0µm particles should have 33% less attraction at a given separation, thus 1.0µm

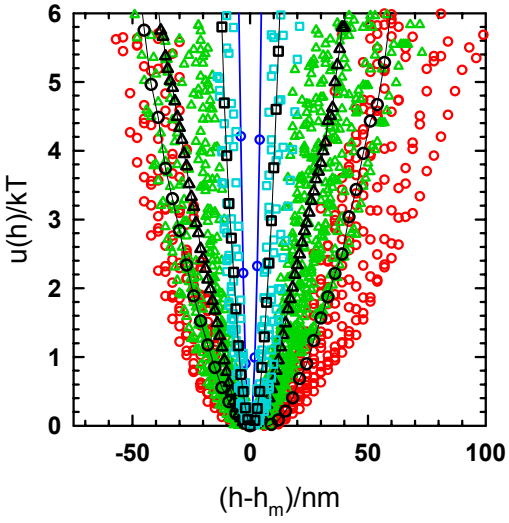

Figure 6.7. Ensemble (black) and single-particle TIRM potential energy profiles of adhered, non-fused bilayer-coated particles. In all cases, the wall has been coated with a POPC bilayer. (○) 1.0μm silica modified with POPC, (△) 1.5μm silica modified with POPC, (□) 1.5μm silica coated with 3mol% PEG1000, and (○) ensemble potential of bare particles deposited on a bare wall.

colloids were able to sample much larger height fluctuations relative to 1.5μm silica, due to a reduced vdW attraction. The interesting thing to note about the wells for all cases is the weakness in the repulsive side of each profile.

Compared to bare particles deposited onto a bare wall, data from the POPC-modified particles reveal that apposing SLBs are adhered to each other and are being pulled from away the supporting surfaces as the particle diffuses perpendicularly. If this were not the case, the particles would be able to escape this adhesive well and sample gravity at these ranges of relative separations reached. It is possible that the particles are coated with adsorbed, non-fused vesicles, but CSLM data shows that SLBs formed on particles with this protocol create uniform and fluid bilayers on the particle and wall

surfaces. More investigation is needed to determine the exact cause of wells with this width.

6.4 Fusion and Lipid Exchange between Apposed SLBs

Primarily, this subsection presents (i) CSLM evidence of fusion and quasi-2D lipid exchange between apposing SLBs and (ii) TIRM results that describe time-dependent fusion behavior with potential energy profiles. The key characteristics of fusion between two apposing SLBs are pinhole neck formation at the membrane-membrane interface and formation of a continuous and fluid single bilayer that encapsulates the deposited particle. Figure 6.9A-D illustrates the fusion process and free exchange of membrane components between the particle and wall surfaces. Assuming the wall provides an infinite source of lipid, relative to the particle, mobile lipids on the wall will completely exchange with the mobile fraction on the particle.

The set of CSLM images presented in Figure 6.9E-H show proof of fused SLBs and neck formation within a continuous membrane that encloses the deposited particle. In this particular experiment, a POPC-modified 4μm silica particle was deposited onto a 1mol% Bodipy SLB. Figure 6.9E gives an x-y slice from the mid-plane (diameter) of the particle, showing fluorescent lipids have completely exchanged with the POPC on the particle. Figure 6.9F is a “zoomed out” view of several fused particles. The bright diffuse ring around the fused particles is the result of the point-spread function leading to focal bleed-through from the fluorescent lipid on the portion of the particle that is outside of the focal plane.

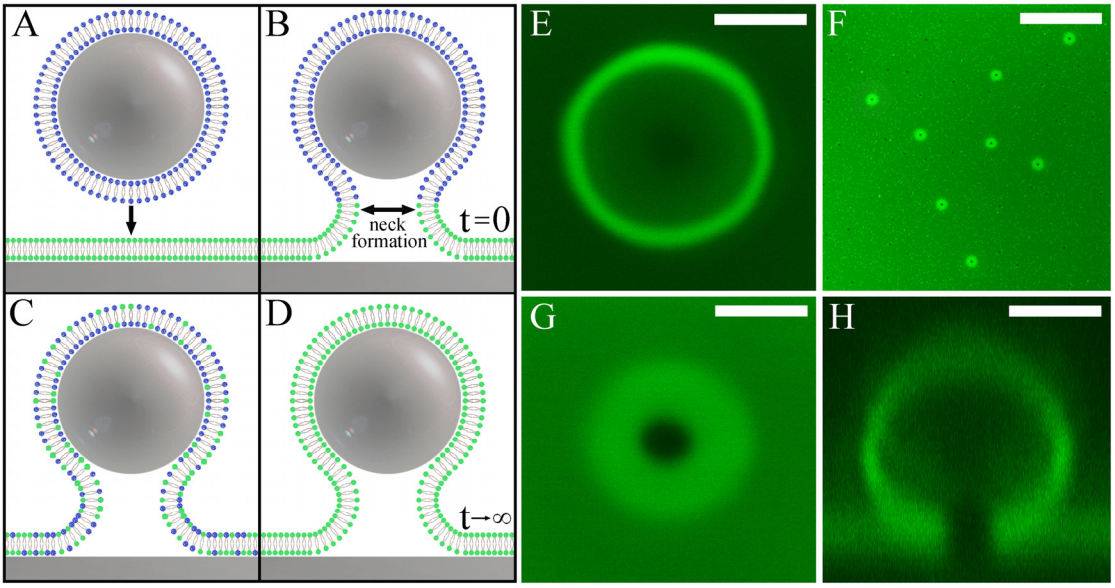

Figure 6.8. (A) Bilayer-coated particle approaching a SLB on a wall that contains fluorescent tracer lipids. (B) Interpenetration of leaflets and fusion forming a neck and continuous, two-leaflet membrane. (C) Exchange of mobile lipids. (D) Complete exchange, where the bilayer on the wall is represented as an infinite source and sink. (E) x-y CSLM slice from the mid-plane of a 4μm silica particle fused and exchanging lipids with the underlying SLB. (F) SLB-SLB interface showing several fused particles with pinholes at their centers. (G) x-y slice of SLB-SLB interface for same particle in (E). (F) x-z vertical slice from same particle in (E) showing neck formation and the continuous bilayer. Scale bars are 2μm for (E, G, H) and 30μm in (F).

Interestingly, not all of the particles in the window exchange lipids with the wall, but the vdW attraction between the particle and wall is strong enough to squeeze lipid out from beneath each particle and thereby forming pinholes at every particle location. Note that this does not happen for 2.2μm and 1.5μm particles, most likely the result of reduced vdW relative to the larger particle size. This aspect of fusion will be discussed in a later section, but for now, we will assume that lipid exchange did not happen for all particle-wall cases because of the existence or lack of surface heterogeneity on the wall and/or particle. Figure 6.9G is an x-y slice at the particle-wall interface that shows a pinhole in the center of the particle, which results from neck formation. Again, the

diffuse ring around the pinhole is caused by a limitation of the confocal (and all optical systems for that matter) to block ambient light from outside the focal plane along the optical axis. Finally, Figure 6.9H shows an x-z (vertical) slice through the same particle in particle G and E. This image leaves little doubt as to the existence of fused and continuous SLBs on particle and wall surfaces.

Beyond forming a fluorescent bilayer on particles that were initially non-fluorescent, a qualitative FRAP experiment was performed to verify the mobility and free exchange of lipids between the two surfaces. Figure 6.10 shows an isolated particle being bleached at its mid-plane, followed by nearly complete fluorescent recovery after 30s of zero laser exposure. By significantly lowering the pinhole to reduce ambient light from the SLB on the wall, meaningful FRAP data could not be collected on this particle. It is likely, though, that the mobility at and around the neck is only restricted from a geometrical sense and not thermodynamically, although this is speculation at this point.

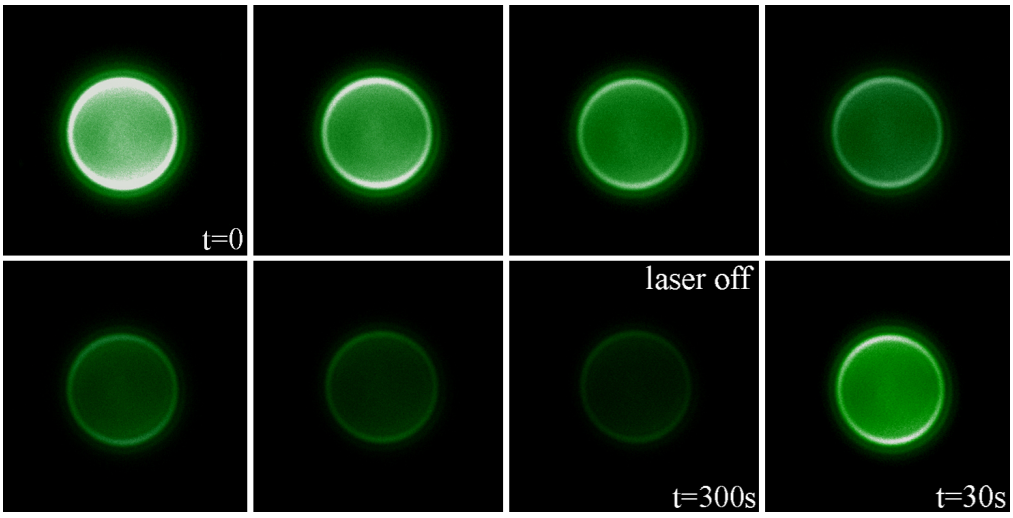

Figure 6.9. Qualitative single-particle FRAP experiment demonstrating lipid exchange between the fused particle and wall bilayers.

Note that monitoring the exchange between a POPC-modified wall and particles with fluorescently labeled bilayers was attempted but had little successful, due to the fact that the wall disperses the tracer lipid over a large area, whereas the POPC-modified particle concentrates fluorescent lipids on the particle surface as lipids are freely exchanged. Thus, fusion in this configuration was captured from CSLM images but only a drop in fluorescent intensity of the particle was observed; fluorescent lipid around particle-wall interfaces was not observed.

Aside from verifying lipid exchange between two apposing lipid bilayers, lipid spreading from particles onto bare walls and from walls onto bare particles was studied. Figure 6.11 show confocal images from the particle wall interface, where 1.5μm silica particles were functionalized with a 1mol% Bodipy bilayer and then deposited onto a bare glass coverslip in 150mM NaCl. There are two important remarks to make concerning this image. For one, the lipid only creeps or spreads onto the wall surface a minimal amount and the spreading is asymmetric. Secondly, the same pinhole geometry, seen in fusion between apposing SLBs, is formed at the particle-wall interface.

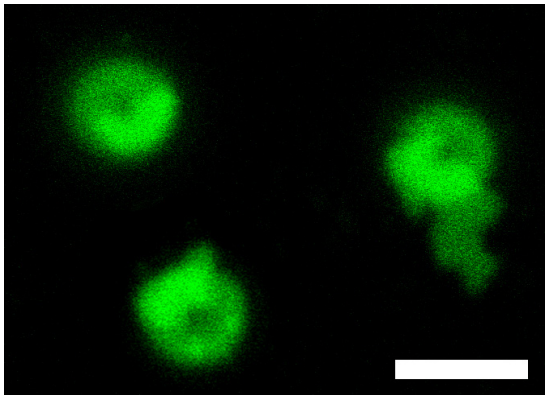

Figure 6.10. Lipids spreading from 1.5μm particles onto a bare silica wall.

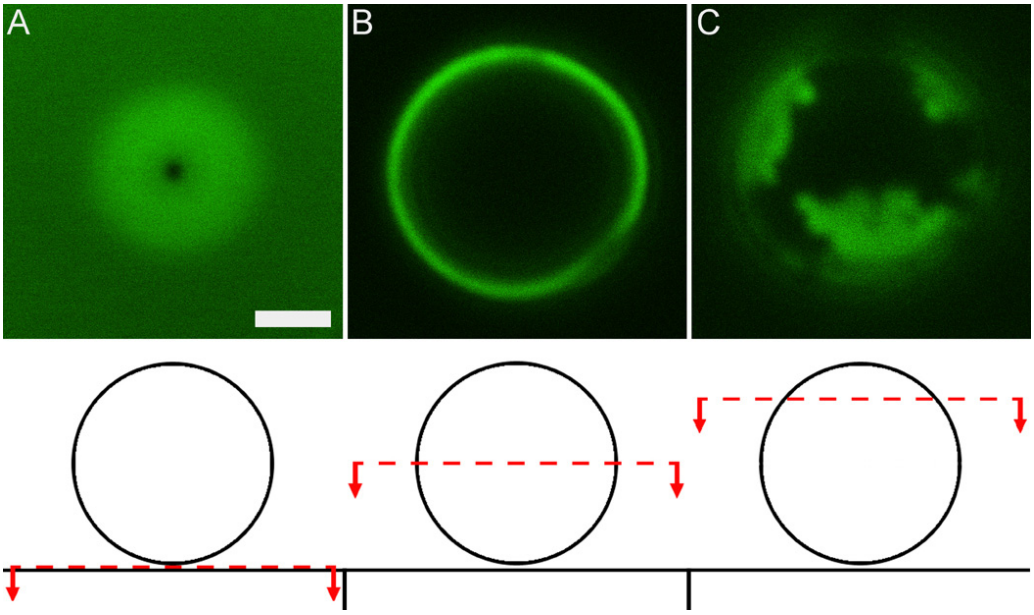

Figure 6.11. CSLM images of lipid spreading from a 1mol% Bodipy-coated wall onto a bare 4µm particle. Schematics below images show approximate scanning planes.

Figure 6.12 shows CSLM images from a bare 4µm silica particle deposited onto a 1mol% Bodipy bilayer-modified wall. At the particle-wall interface (Figure 6.12A), fusion and neck formation exist, just like that seen for fusion between apposed SLBs (see Figure 6.9). However, scans taken further from the interface reveal heterogeneity that results from partial spreading of the lipid bilayer onto the particle surface.

Incomplete spreading could be the result of a poorly prepared particle surface, but it most likely occurs due to an increase in interfacial tension within the lipid bilayer as it expands to cover more surface area. At least 20% of the particles at this interface exhibited this type of behavior; therefore, the bilayer expansion was being applied over more surface area than just this isolated particle. Independent proof of this hypothesis was gathered by adding more particles to the surface (Figure 6.13). After the particle concentration was increase 10 fold, bilayers receded from the surface of the particles.

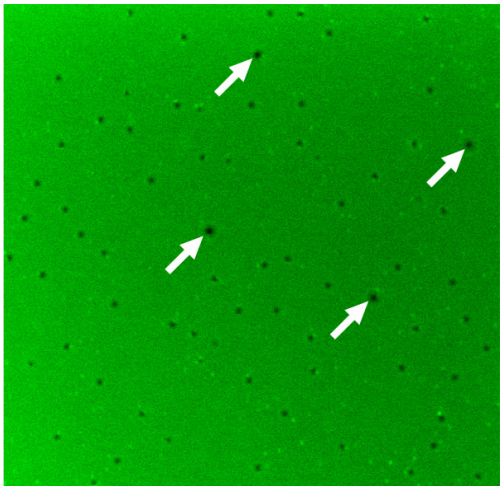

Figure 6.12. CSLM image showing bilayers have receded off of bare particles after more particles are deposited and fuse. Arrows indicate pinholes from particles that were fused before the increase in particle concentration. They appear to have increased in size. Window size = 60μm.

Pinhole and neck formation persisted, but the degree of spreading was equally spaced among all particles, thereby increasing the interfacial membrane tension and causing the lipids to undergo a form of de-wetting from the surface. The practical aspect to this finding is that surface free energy within lipid membranes could be tuned with the addition of microparticles into the system.

6.5 Conclusions

The importance of stability of SLBs in this work cannot be overstated. Without apposing layers maintaining their integrity, colloid-surface association lifetimes and potentials will be severely misrepresentative of interactions that are governed strictly by specific protein-protein attraction. The work described in this section was a crucial part of developing a robust experimental construct for measuring weak specific interactions. Additionally, these findings will be of interest to anyone working with SLBs.

7. CALCIUM-MEDIATED CADHERIN-CADHERIN INTERACTIONS

7.1 Synopsis

This section reports preliminary TIRM, VM, and confocal results of specific and non-specific cadherin-cadherin and cadherin-antibody binding, proving the potential efficacy of the devised experimental system. VM data of particle-particle interactions revealed that nearly all particles can be made robustly stable in high-salt conditions through the application of PEGylated SLBs to particle and wall surfaces. TIRM experiments confirm that particle-wall vdW attraction is reduced (in the absence of Ca^{2+}), following the binding of cadherin to both PEGylated surfaces. This evidence confirms non-specific repulsion between cadherins when they are unable to form *cis* or *trans* dimers. Independent of VM and TIRM studies, the presence and activity of cadherins incorporated into PEGylated SLBs is shown qualitatively with confocal microscopy, following the successful binding of fluorescently labeled antibodies to cadherin fragments. Moreover, specificity is demonstrated through observation of particle-particle aggregation behavior of cadherin-functionalized colloids within a large range of calcium ion concentration (i.e., $0 < [Ca^{2+}] < 5$mM). Taken together, these preliminary data prove that specific calcium-mediated interactions between cadherins can be quantified using the methods outlined in previous sections.

7.2 Types of Cadherins Studied

Two cadherins were investigated in these preliminary studies: recombinant human (i) neuronal cadherin (N-cadherin or N-cad) and (ii) epithelial cadherin (E-cadherin or E-cad). N-cad is a type 1 classic cadherin that exists *in vivo* with a propeptide sequence,

five extracellular cadherin repeats with a conserved His-Ala-Val motif in the N-terminal domain, and a highly conserved cytoplasmic portion that interacts directly with the actin cytoskeleton through intermediate catenins (α, β, and γ). Interestingly, in the absence of association with catenins, cadherins have been found to lose their adhesiveness *in vivo*. In adult tissues, N-cad is highly expressed in neuronal cells and cardiac and muscle tissue, while it is relatively ubiquitous during early vertebrate development. N-cad primarily mediates cell-cell adhesion through homophilic interactions, though some studies have shown N-cad to form equally strong heterophilic bonds with E-cad[167] and R-cad. Aside from regulating cell-cell adhesion, N-cad-mediated adhesion also activates signaling cascades that function in various cellular processes such as heart development, establishment of left-right asymmetry, somitogenesis, neural tube morphogenesis, axon guidance, maintenance of neural tube integrity, neural cell proliferation, and synapse formation and plasticity.[168] On the other hand. E-cad is responsible for upholding the integrity of the epithelial layer, which is found, for example, within the intima of the vasculature. E-cad may also play a role in tumor development, as loss of E-cad function has been associated with an increase in tumor invasiveness.

Recombinant human chimera proteins expressed in a mouse myeloma cell line (NS0) were purchased from R&D Systems, and they come as the extracellular fragment of the cadherin fused to the carboxyl-terminal 6X his-tagged Fc region of human IgG via a peptide linker (see Figure 3.5 in *Section 3.2.6*) The samples are lyophilized from a 0.2μm filtered solution of either 50mM Tris-citrate buffer, 0.25M NaCl, 2mM $CaCl_2$ (100μg of E-cad) or 50mM Tris-citrate buffer (50μg of N-cad) each with pH 6.5. Protein

samples were reconstituted with 1ml of DI water to yield either 50μg/ml (N-cad) or 100μg/ml (E-cad) protein concentrations, stored at 4ºC, and used within one month. Protein binding to bilayers bearing Ni-NTA ligands was carried out for 1hr at a protein concentration of 5μg/ml, which is well above the limit for complete Ni-NTA ligand saturation on bilayers with His-tagged proteins in the absence of PEGylated lipids.[23]

In other studies, allophycocyanin-conjugated mouse monoclonal anti-human E-cad (a fluorescently labeled E-cad antibody) was bound to E-cad for 1hr at a concentration of 10μg/ml. This was used to quantify the amount of protein present on particle and wall surfaces and to block cadherin function in control studies. The conjugated fluorophore was excited at 633nm and emission was collected >650nm with a confocal scanning laser microscope.

7.3 Cadherin Activity in PEGylated Bilayers

The most important initial control experiment to run before attempting to characterize cadherin interactions between functionalized colloidal and wall surfaces is the verification of cadherin oriented and activity present within the PEGylated SLBs. Initial experiments conducted with (i) PEGylated, Ni-NTA-containing bilayers and (ii) Ni-NTA bearing surfaces prepared through multi-stage silane chemistry (see *Section 3.3.3*) showed that bound cadherins were, in fact, active at these interfaces. This proof was obtained by binding a fluorescently labeled antibody to surface-immobilized E-cad within the PEGylated bilayer (Figure 7.1). Non-specific adsorption of antibodies to surfaces not bearing cadherin was also quantified, and the fluorescent intensity difference between the two conditions conclusively proved that cadherins were oriented

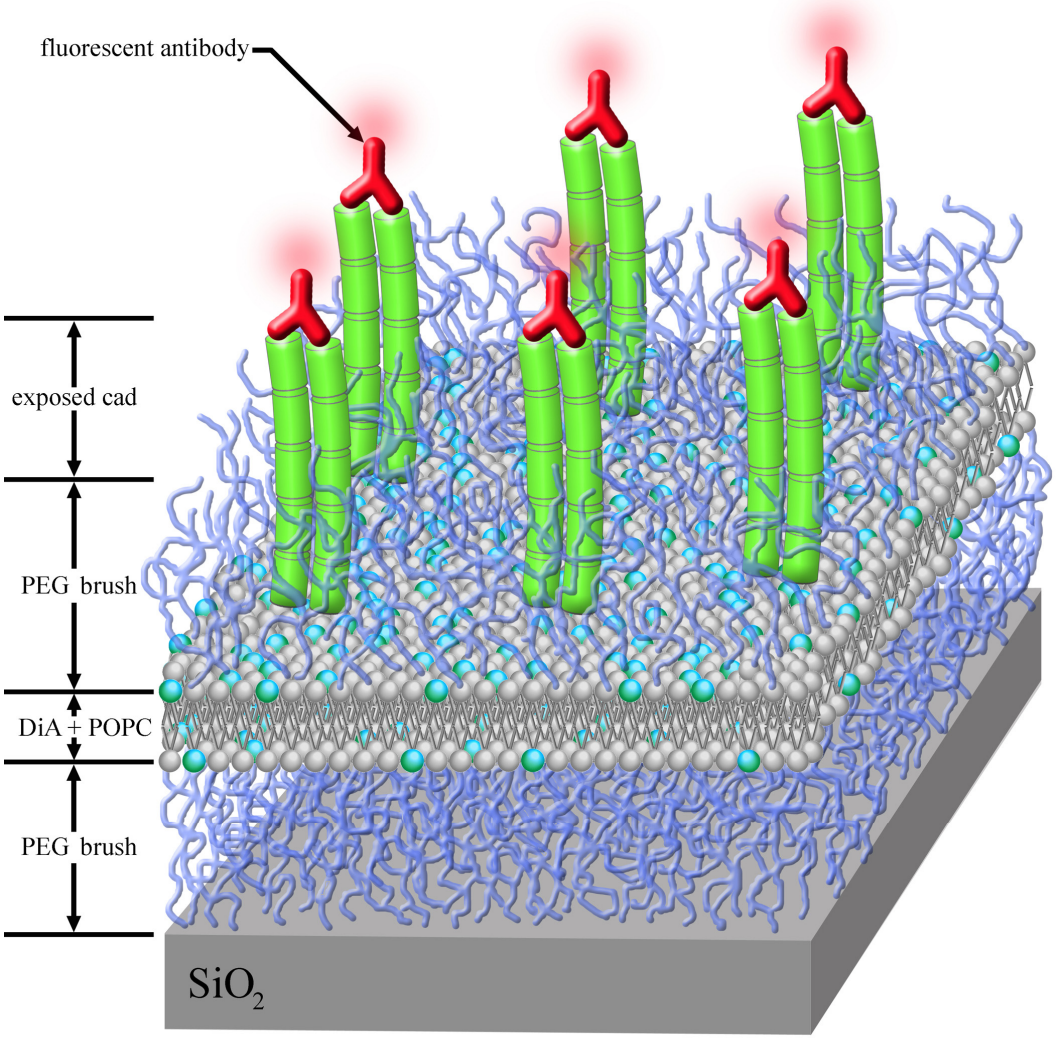

Figure 7.1. Illustration of antibody labeling of cadherin cis-dimers (lime) immobilized on a PEGylated SLB with incorporated DiA fluorescent lipids (cyan).

and active on the surface. Figure 7.2 gives confocal images of a SLB containing 5%Ni-NTA/3%PEG1000 with (Figure 7.2B) without (Figure 7.2A) bound E-cad after incubation with the fluorescent antibody for 1hr. As shown, the PEGylated bilayer prevented non-specific adsorption of antibody in the absence of cadherin but did not interfere with cadherin and antibody binding.

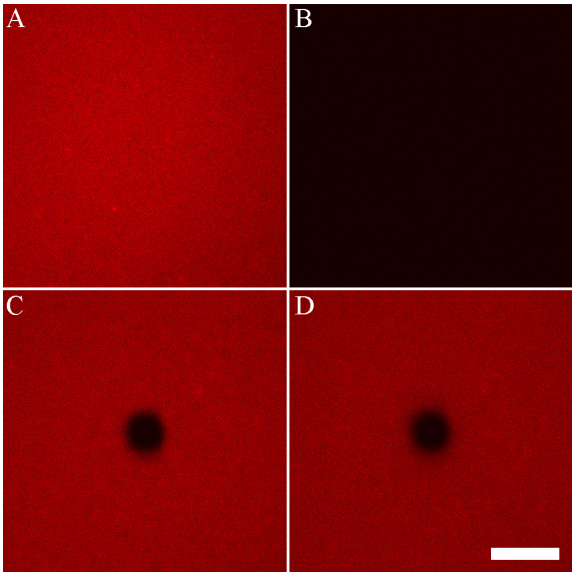

Figure 7.2. (A) Antibody association to a bilayer following cadherin binding. (B) Non-specific antibody binding to the same bilayer composition in (A) except without bound E-cad. Confocal settings were identical in both scans. (C and D) Qualitative FRAP experiment at (C) t=0s and (D) t=700s after photobleaching. Scale bar =10μm.

E-cad mobility within the PEGylated bilayer was qualitatively checked with a FRAP experiment. For 5mol%Ni-NTA/3mol%PEG1000 bilayer, antibody-cadherin complexes were nearly immobile, as can be seen in Figure 7.2C and D. Some intermixing surrounding the bleached zone can be observed, which indicates that cadherins may move substantially faster at lower X_p of PEG and Ni-NTA. Additional follow-up experiments to this work are discussed in *Section 10.2*.

For 0.05mol%Ni-NTA ligands imbedded in 3 and 5mol%PEG1000 bilayers, E-cad and antibody binding reveal the presence of protein domains (Figure 7.3B). These types of cadherin clusters have been observed in live cell experiments, where active remodeling of membrane components is induced.[169] Because Ni-NTA ligands should be evenly distributed throughout the bilayer, these preliminary results point to cadherin

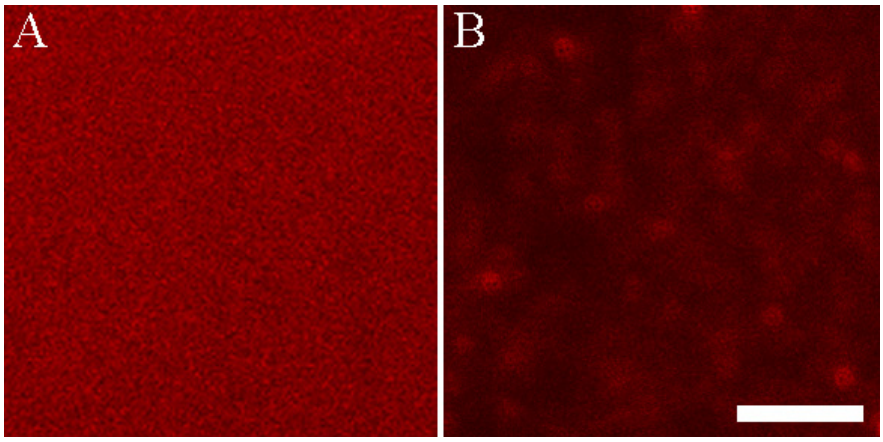

Figure 7.3. CSLM images of antibody bound to E-cad immobilized on (A) 5mol%Ni-NTA-5mol%PEG2000 and (B) 0.05mol%Ni-NTA-5mol%PEG2000 bilayers. (B) The non-uniformity in (B) may indicate the presence of lateral E-cad association. Scale bar is 5μm.

clustering and indicate that cadherins can form large domains within bilayers. Clusters are more easily viewed in low concentration systems compared with dense protein binding, due to lateral saturation effects (as seen in Figure 7.3).

7.4 VM Measurements of Particle-Particle Interactions

For meaningful particle-particle data to be collected, it is imperative that particles remain stable with each other and the wall during the course of the entire experiment. In purely repulsive systems, such as electrostatic experiments, this is easily accomplished. In high-salt conditions (>15mM), however, surface homogeneity and a minimum steric-layer thickness are crucial for maintaining a completely stable dispersion.[170] Therefore, these arrangements are normally very difficult to establish, and as far and we know, these are the first known pair potential experiments performed under strictly steric conditions. Our particle-particle arrangement is shown in Figure 7.4, with PEGylated

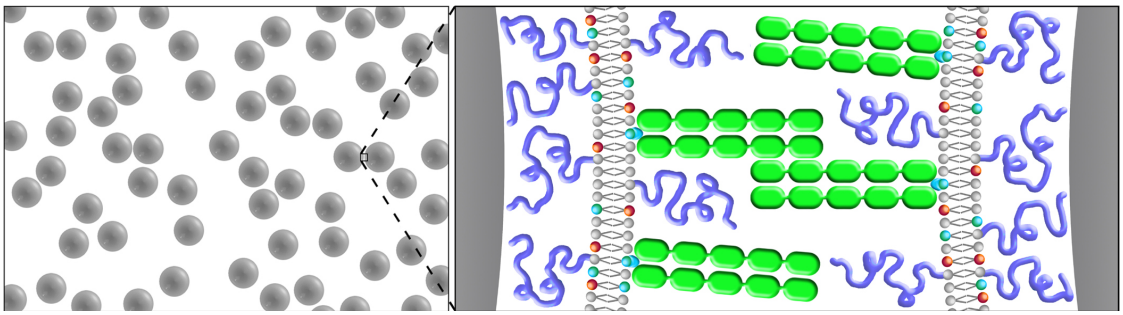

Figure 7.4. Stable particle-particle interface for studying specific cadherin-cadherin interactions. PEG is shown as blue coils and cadherins are green.

bilayers serving to reduce baseline particle-particle vdW between the two underlying surfaces and keep the particles from aggregating prior to protein binding in high salt.

For our steric layers, the primary adjustable parameters are PEG MW and concentration. The minimum requirement for the PEG2000 layers is that they reside in the brush regime, and particles must be large enough so that "hopping" doesn't occur (see *Section 2.5.1*). Because these SLBs are formed through vesicle adsorption and fusion, particle curvature and PEG brush density are important factors in determining whether or not a uniform and continuous SLB can form. As a vesicle collapses onto to surface of the particle and begins to fuse laterally with surrounding vesicles, PEG in the interior of the vesicle resists collapse, and PEG chains on the exterior of the vesicle resist lateral compression resulting from vesicle deformation during adsorption onto the curved particle surface. As will be shown, VM and TIRM data support evidence of incomplete vesicle fusion onto particles having radii of curvature below a critical value for a particular combination of PEG density and MW.

To keep particles robustly levitated above the wall during VM experiments, dispersions were monitored in polystyrene (PS) wells that had been coated with a layer

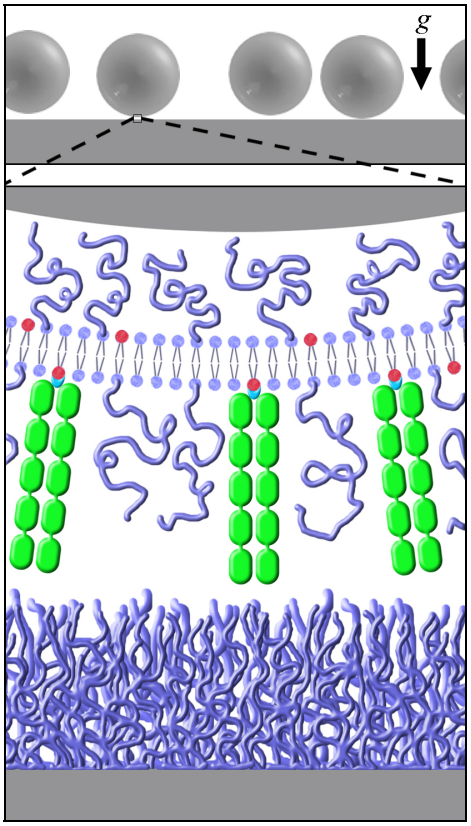

Figure 7.5. Schematic showing particle-wall configuration with F108 used as a stabilizing layer adsorbed to a polystyrene wall.

of F108 (Figure 7.5). PS wells were chosen because no preparation is required to make the entire surface hydrophobic, the PPO block of the F108 copolymer chain readily adsorbs to PS and forms a uniform and ~20nm-thick[138] PEO brush layer, and multiple wells can be set up simultaneously to test different media conditions and particle concentrations in parallel.

A series of 2000 images were collected to generate a $g(r)$ for each particle-particle experiment, with frame rates varying from 0.1 to 0.2fps, depending on the particle radius, area fraction, and window size. All sequences were collected through a 63× objective with a 2.5× magnifier at 1 binning to yield a pixel size of 38.5nm. Average

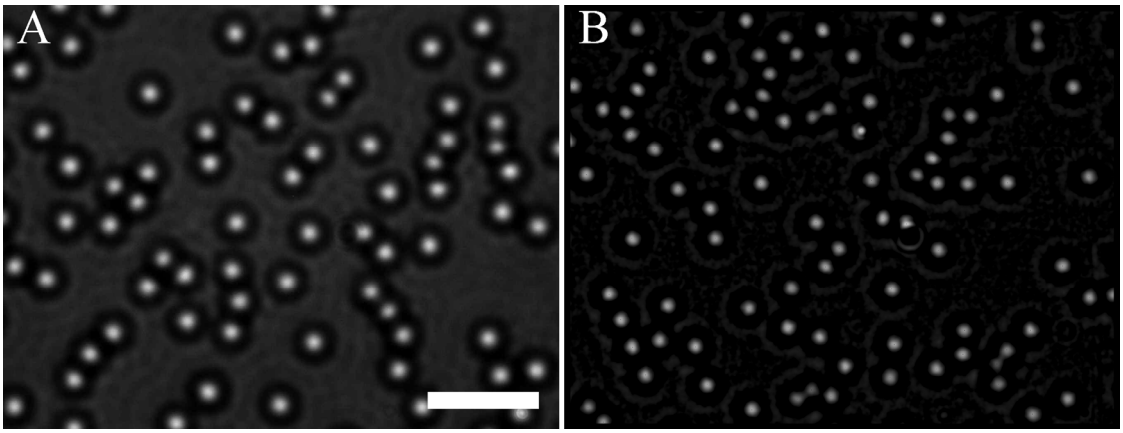

Figure 7.6. (A) VM CCD snapshot from a sequence of diffusing silica particles ($2a$=2.2μm) stabilized with a PEGylated SLB and N-cad in 150mM NaCl, 50μM $CaCl_2$ solution. (B) Processed CCD image of diffusing silica particles ($2a$=1.5μm) stabilized with an identical layer to that in (A) and in the same media. Scale bar=10μm.

particle area fractions were kept at 0.098–0.121 for $2a$=1.5μm particles and 0.174–0.192 for $2a$=2.2μm particles. Figure 7.6 shows snap shots from two different VM experiments. In Figure 7.6B, the image has been processed with our image analysis code (see *Section 3.5.2*) to reduce local random noise and find particle centers with half-pixel resolution. Examination of multiple randomly selected post-processed frames throughout each experiment confirmed that false centers were not being accidentally located by the analysis.

Figure 7.7A and B show experimental radial distribution functions, $g(r)$, for silica particles ($2a$=1.5μm) modified with 5mol%Ni-NTA-5mol%PEG2000 bilayers with and without bound N-cad and for various Ca^{2+} concentrations with a constant background of 150mM NaCl. Note that the $g(r)$ datasets have not yet been corrected for optical distortions, polydispersity, and multiparticle effects (see *Section 2.5*). Although preliminary, there are several important insights that can be gleaned from this data.

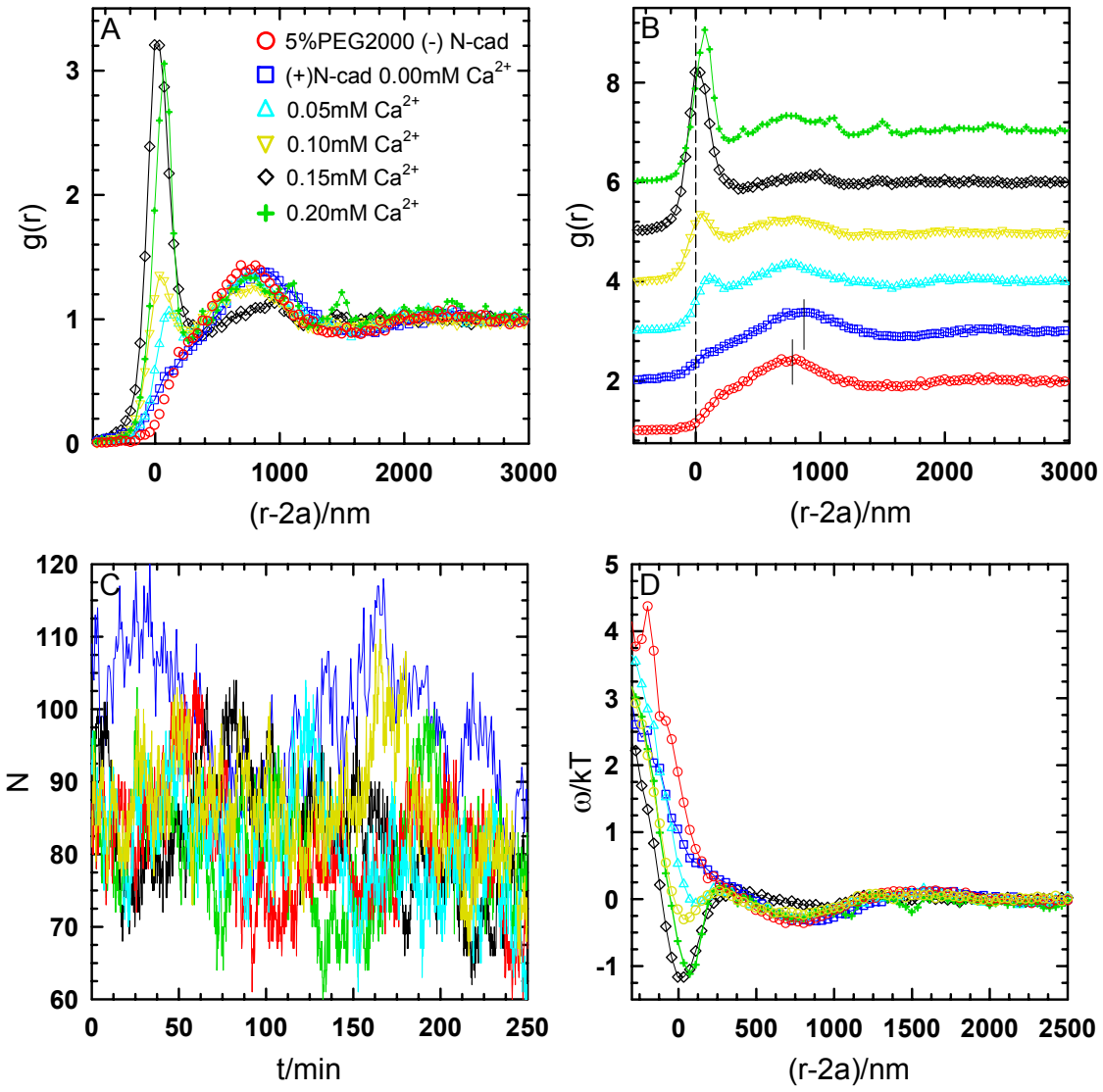

Figure 7.7. (A) Six experimental $g(r)$ vs. absolute separation corresponding to the conditions given in the legend. (B) Same $g(r)$ datasets, but with each offset by 1.0 to help compare their characteristics. Note the ~60nm shift after protein addition, demarcated by the two solid lines (C) Number of particles, N, vs. time for all six experiments. (D) PMF for all $g(r)$ shown in (A) and (B).

In the absence of N-cad (○), the particles experienced an extremely soft repulsion with an onset at approximately 900nm. Following the addition of N-cad to the system (□), the $g(r)$ peak magnitude remains unchanged within experimental error. This finding is consistent with a lack of specific cadherin-cadherin interaction in the absence of calcium. One interesting observation to point out is that the separation at contact for weak repulsion is shifted ~60nm (Figure 7.7B), which would be the approximate thickness expected after binding protein (2 × 25nm-long cadherin fragments). This is most likely fortuitous given the limited resolution of our VM system that results from polydispersity and optical distortion; however, these errors are systematic, which could mean that the observation is real. As shown in Figure 7.8B, after properly accounting for multi-body packing effects, the difference in absolute separation at contact between the PMF and iOZ $u(r)$ is actually shifted -150nm and the well width is ~25% narrower.

After adjusting the media to a $[Ca^{2+}]$=50μM, 10μM above the concentration at which domains stiffen and the protein becomes more elongated,[104,105,106] a peak begins to evolve (△) at what is expected to be near bare particle-particle contact (r-2a=0nm). As the $[Ca^{2+}]$ increases from 0.1 to 0.2mM, the magnitude of the first peak increases. For a different perspective, the potential of mean force (ω) is plotted for each $g(r)$. This observed behavior could be interpreted as an increase in specific cadherin-cadherin interactions, and that is most likely part of the contribution. Yet, the soft repulsive peak at ~750nm begins to drop in magnitude, suggesting the structure of the surface is changing.

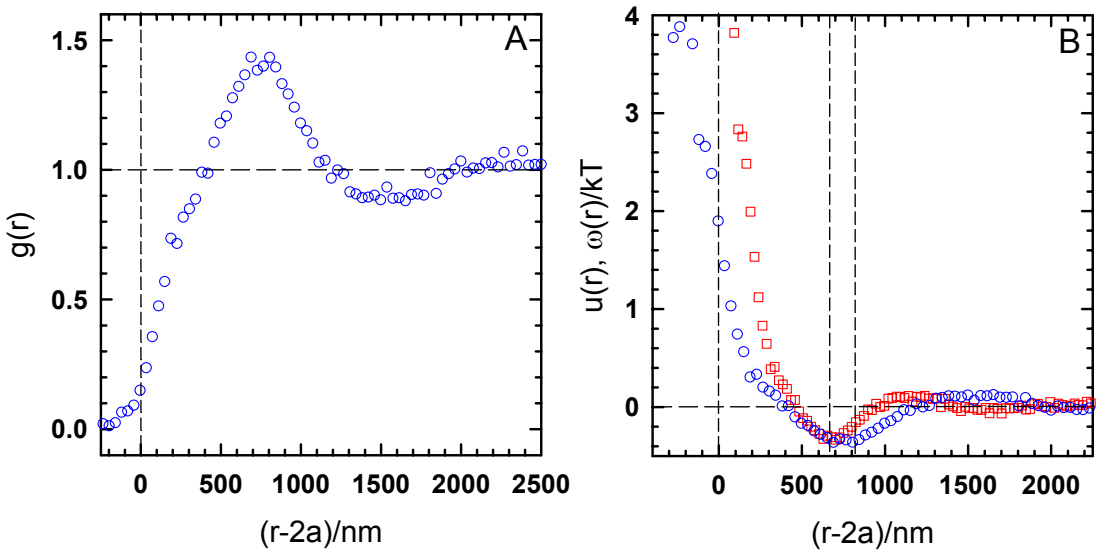

Figure 7.8. (A) Experimental $g(r)$ vs. absolute separation. (B) Corresponding PMF (○) and pair potential, $u(r)$, (□) found from inverse OZ analysis, which corrects for multiparticle effects.

The most likely explanation of why the $g(r)$ is evolving in this manner as a function of $[Ca^{2+}]$ is a combination of (i) an increase in specific attraction between cadherin *trans* dimers and (ii) desorption of non-fused vesicles from the surface as cadherins become more rigid (thereby increasing the stabilization of vesicles) and adhesion between non-fused vesicles begins to tear vesicle aggregates from particle surfaces. Another contributing factor in how these $g(r)$ data sets evolve is experiment time. Because each data set takes approximately 5hr to collect, the time between initial particle preparation and the final data set is nearly 28hr. In this time span, the odds of particle pairs sampling localized defects increases, eventually leading to non-specific binding of particles as bare (non-stabilized) surfaces come into contact. For instance, an increase in associated particle doublets due to non-specific aggregation would lead to an increase in the first peak of the $g(r)$, irrespective of cadherin mediated attraction.

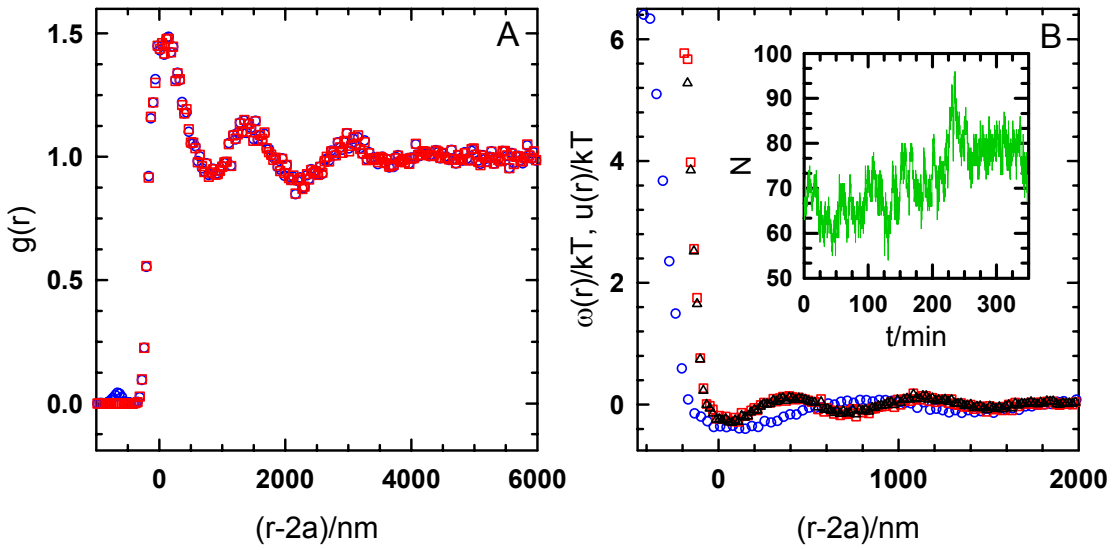

Figure 7.9. (A) Experimental (○) and iMC (□) $g(r)$ vs. absolute separation for 2.2μm modified with same SLB as in Figure 7.7 plus N-cad. (B) Corresponding PMF (○) and $u(r)$ from iOZ (△) and iMC (□) with an inset of N vs. time

With this knowledge, the experimental system was re-evaluated, and it was determined that particle curvature and PEG X_p were the main contributors to poor lipid bilayer formation and an increase in surface defects. CSLM images confirmed that this specific vesicle formulation led to surface aggregates and not continuous bilayers on 1.50μm particles, a behavior not observed previously when using vesicles containing 1.5mol%PEG2000. Follow-up CSLM data showed the formation of uniform and fluid bilayers on 2.2μm silica particles using the exact same vesicles. Thus, new $g(r)$ data was collected for the same system with $2a$=2.2 instead of $2a$=1.5μm silica particles. Note that, for PEG5000 up to 2mol%, uniform and fluid bilayers were readily formed on wall surfaces; hence, SLB quality on the wall should not be a concern for any PEG5000 vesicle formulation up to 2mol%. Nevertheless, DiA lipids are added in for every vesicle

recipe so that wall surfaces can be checked with confocal scans prior to protein binding and TIRM experiments in order to remove one avenue of uncertainly.

The $g(r)$ shown in Figure 7.9 was collected from 2.2µm silica, stabilized with 0.5mol%Ni-NTA-5mol%PEG2000 and bound N-cad, diffusing above an F108-coated wall in 150mM NaCl and 0mM $CaCl_2$. Scanning through the entire well, there was no evidence of non-specific particle association (irreversible doublets), and <0.5% of particles were deposited on the underlying wall. Hence, this experimental system meets or exceeds all requirements for studying specific protein-protein interactions. Figure 7.9A presents the experimental $g(r)$ (○) and the $g_s(r)$ (□) found with iMC analyses (see *Section 2.5.1*), showing that $g_s(r)$ converged to the measured $g(r)$ nicely. In Figure 7.9B, three separation-dependent potentials are plotted: the PMF (○), $u(r)$ from iOZ (△), and $u(r)$ from iMC (□). The extracted potentials from iMC and iOZ are nearly identical, and they both show a steeper repulsion and shorter-range attraction compared to the basic analysis of calculating the PMF.

Finally, rudimentary VM particle-particle association experiments were conducted on cadherin-modified silica colloids as a function of $[Ca^{2+}]$ to determine relevant calcium ranges for future studies. Bilayers consisting of 10mol%Ni-NTA (no PEG) were formed on 2.2µm silica, and E-cad was then bound to the surface. Although PEGylated lipids were not added to provide a stabilizing layer, 10mol%Ni-NTA allowed cadherins to bind at nearly their highest surface concentration possible, thus the protein acted as the steric layer under the high-salt conditions (150mM NaCl). Because of the potentially negative effects from forced protein crowding, non-physiologically relevant protein

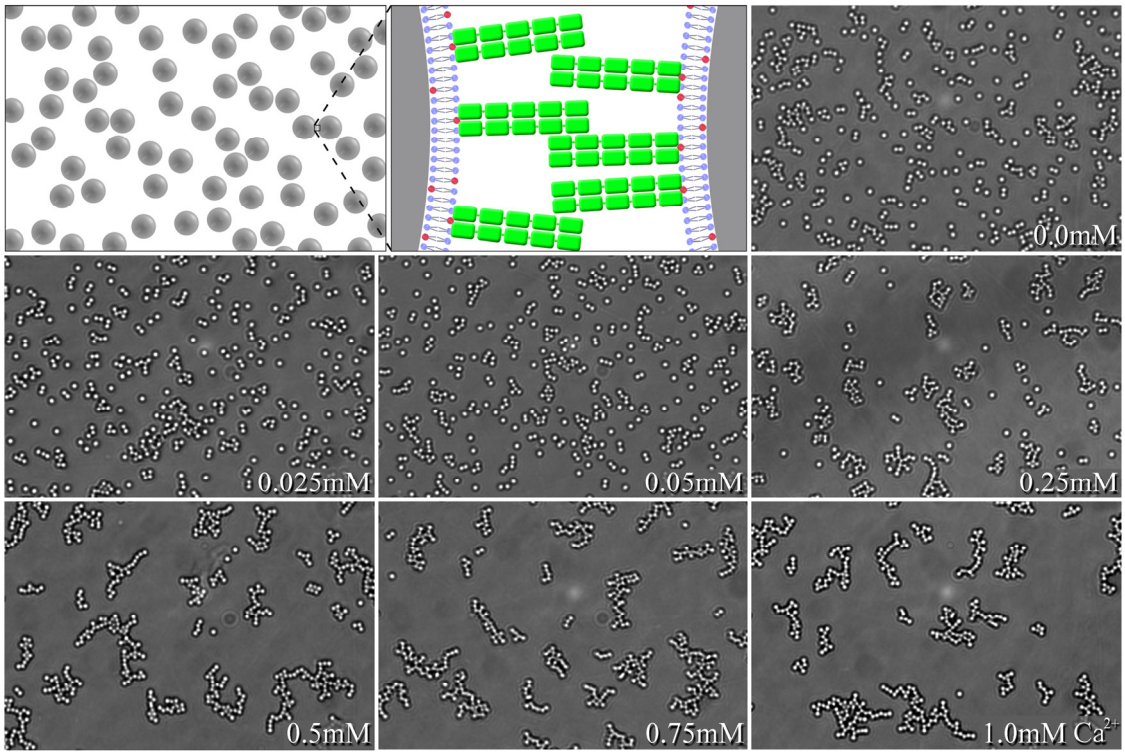

Figure 7.10. VM snapshots showing particle-particle behavior at seven different Ca^{2+} concentrations for 2.2μm silica particles bearing E-cad.

concentrations, and a lack of robust stability that result from this system, it was not considered a valid candidate for studying cadherin-cadherin interactions, however it serves its purpose well in these preliminary experiments.

The association behavior of E-cad-modified particles is graphically illustrated with VM snapshots at different calcium concentrations (Figure 7.10). At the visible onset of attraction (0.05mM < $[Ca^{2+}]$ < 0.25mM), diffusion-limited aggregation caused particles to form kinetically arrested gels. These seven experiments were performed in seven different wells, and a key observation was that particles aggregated at a faster rate as the $[Ca^{2+}]$ increased from 0.25 up to 0.75mM. This may indicate $[Ca^{2+}]$-dependent differences in binding kinetics within a fairly large range of $[Ca^{2+}]$, which could be

exploited in future TIRM studies. Nevertheless, these types of simple experiments only provide information pertaining to the onset of strong attraction, and the immobilized protein concentrations used to stabilize the particles may no yield reliable results.

7.5 TIRM Measurements of Particle-Wall Interactions

PEGylated SLB thicknesses can be inferred from macromolecular scaling arguments that describe mushroom-to-brush transitions based on the Flory radius and surface concentration of the PEG.[57] Using our available techniques, the most direct way to gauge these layer thicknesses experimentally with a reasonable degree of certainty is to functionalized particle and wall surfaces with bilayers, measure the separation-dependent potential with TIRM, and indirectly calculate absolute particle-particle separations using Lifshitz theory.[171] These experiments were performed prior to measuring specific protein-protein interactions between cadherins in order to quantify baseline potentials of non-specific interactions with and without bound protein in the absence of calcium. Data were collected from 1.5 and 2.2μm silica particles modified with a variety of bilayer compositions.

Figure 7.11A shows TIRM data for 1.5μm silica modified with 1.5mol%PEG2000 (□) and 0.5mol%PEG5000 (○) SLBs. Here, gravity has been subtracted in order to help compare the relative well depths. Interactions are symmetric with regard to the particle and wall modifications. The ensemble data reveal that SLB with 0.5mol%PEG5000 are approximately 5nm thicker than those with 1.5mol%PEG2000, despite the PEG X_p being 300% lower. The scaling theory, presented in *Section 2.8*, predicts the difference to be 4nm, which agrees well with the TIRM data. Figure 7.11B shows the vdW portions of

each potential shifted from h_m to h and compared with the Derjaguin-modified[172] Lifshitz theory[171] (solid black line) for retarded vdW attraction between a 1.5μm silica particle and silica wall. It is important to comment here that a possible vdW contribution from interacting bilayers was not incorporated into the Lifshitz estimate for separation-dependent vdW. If it were, the fit would most likely agree with experimental data to a greater extent, but the accuracy in estimating particle-wall separations is not significantly affected by this incomplete modeling. Finally, these two combinations of PEG X_p and MW yielded >80% stable particles at this particle diameter. Although not at a sufficient level for TIRM and VM studies of cadherin interactions, this data does prove that fully formed SLBs with PEGylated lipids can be properly deposited onto smaller particle sizes, provided the X_p is not too large for a given PEG MW.

As seen from VM experiments, when the X_p is too high for a given PEG MW and particle diameter, vesicles do not fuse but simply adsorb to particle surfaces. Figure 7.12 gives TIRM data from 1.5μm silica particles, modified with 5.0mol%PEG2000 vesicles, diffusing above a SLB possessing the same functional lipid composition. Gravity has not been subtracted so that the separation-dependent potentials are more easily interpreted. It is clear from these data sets that particles sample two different energy wells: one exhibiting a soft repulsion at a separation of 100nm, and the other presenting a steep repulsion at $h=h_m$. The outer well at h=100nm appears to be the result of contact between the uniform SLB on the wall and adsorbed, non-fused 80-100nm vesicles on the surface of the particle. A soft repulsion is expected to exist for compression of a non-fused vesicle layer against the non-compliant wall, and this is consistent with particle-particle

VM data showing a soft repulsion at several hundred nanometers. The other interesting aspect to this result is that particles experienced transient deposition events onto the wall that led to the formation of the deeper energy wells near contact. This recurring non-specific association is expected for particles with surface defects that are the product of desorption or incomplete coverage by lipid vesicles.

As particles diffuse, they undergo rotational translation (see *Section 2.4*), which exposes different portions of the particle surface to the underlying wall during the course of the experiment. When a defect is proximal to the wall, the particle may drop into a deeper energy well and temporarily deposit. However, if the well is shallow enough (i.e., <6kT), particles can escape and freely rotate, thereby exposing more stable portions of

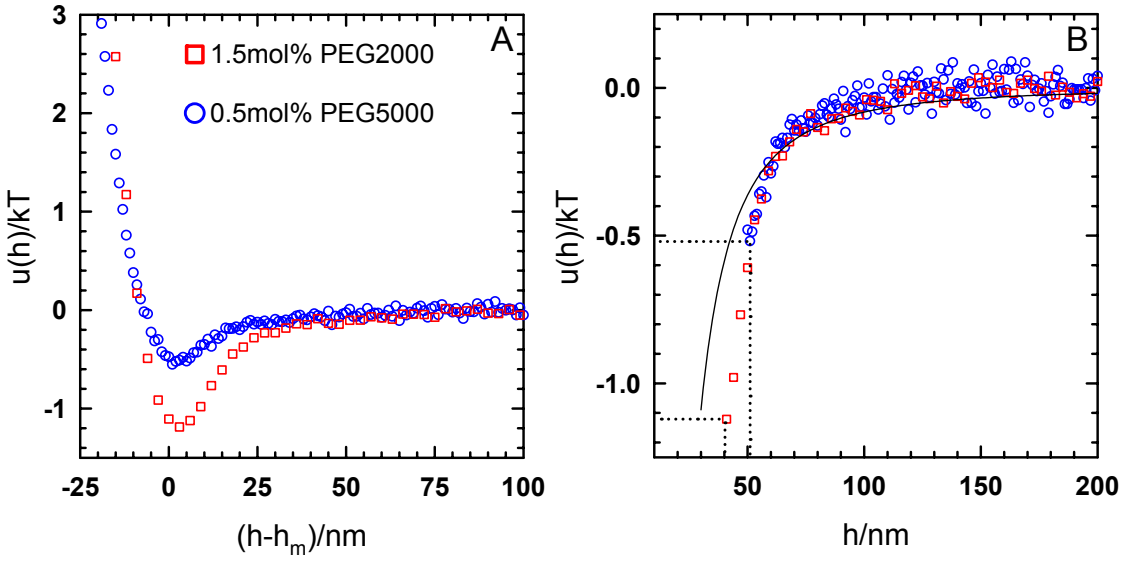

Figure 7.11. (A) TIRM-generated ensemble average potential energy profiles (minus gravity) of SLB-modified 1.5µm silica particles sterically levitated above an identically coated wall surface in 150mM NaCl. Bilayer compositions are given in the legend. (B) vdW portions of the curves in (A) compared with Lifshitz theory to gauge layer thicknesses.

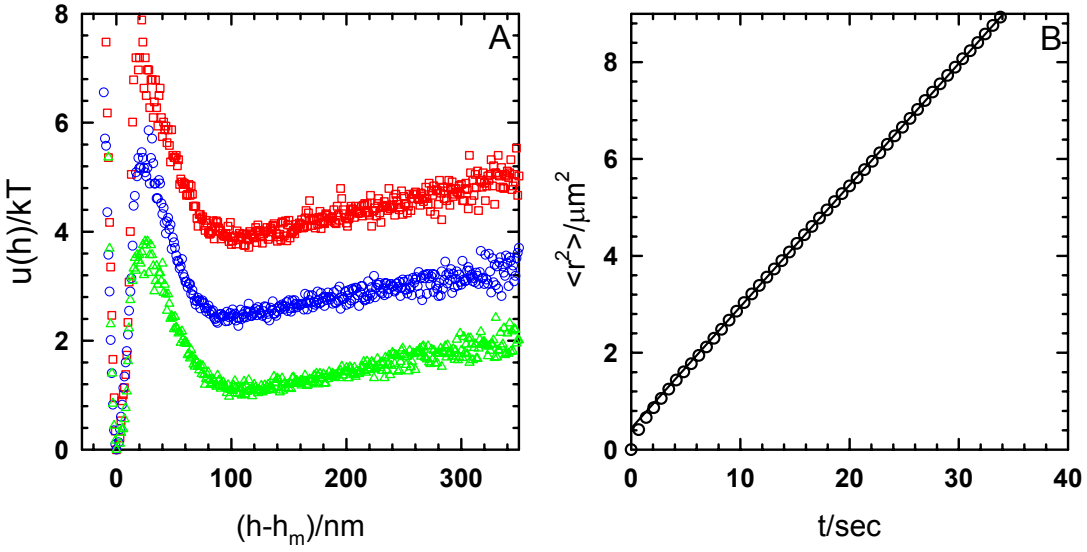

Figure 7.12. (A) Three single-particle profiles of nominal 1.5μm particles, modified with 5.0mol%PEG2000, sterically levitated above an identically coated wall. Fitted particle diameter $2a$=1.45μm. (B) Time- and particle-averaged lateral MSD data from the three colloids shown in (A). Fit to short-time diffusivity yielded a particle diameter of $2a$=1.49μm.

the particle's surface to the underlying wall and temporarily maintaining particle stability. In this way, the three potential energy profiles shown in Figure 7.12A were formed. Particles with deeper wells at h=h_m merely associate with the wall for a larger percentage of the experimental time. It is also important to keep in mind that these potentials are not truly continuous, because transient deposition events bias particle-wall sampling.

Another independent type of analysis to prove or disprove the presence of adsorbed, non-fused vesicles on particle surfaces is to calculate the particle radius from lateral MSDs using a correction factor for two-body hydrodynamics and a properly weighted diffusion coefficient based on the distribution of sampled heights (see *Section 2.6*). Figure 7.12B gives average short-time lateral MSD data for the three particles in

Figure 7.12A. After correcting for separation-dependent hydrodynamic dissipation, the unbiased diffusion coefficient can be calculated. Note that data for lateral translation during deposited states was removed from the analysis in order to find $<D_{\|}>$ for levitated states only. The average particle diameter was estimated to be 1.49μm from these analyses, and 1.45μm from TIRM fits to gravitational slopes. Because the lateral diffusion coefficient scales as h/a^2 this parameter is a reliable and sensitive measure of particle size, provided precautions are taken to account for multi-body hydrodynamics and association events. Since non-fused vesicles adsorbed to particle surfaces would affect the average hydrodynamic radius but not the buoyant weight of the particles, this comparison independently confirms the existence of adsorbed lipid vesicles to particle surfaces.

TIRM data from 2.2μm silica is given in Figure 7.13. Particles were modified with SLB containing 5mol%PEG2000, which would generally form defect-laden bilayers on 1.5μm. Observation of the entire batch sedimentation cell revealed that >95% of particles were stable, consistent with VM and confocal results presented in the previous two subsections. To determine if the particle-wall potential was time-varying for this system, which would be an important factor in interpreting particle-particle VM data over a 30hr period, TIRM profiles were collected for the same particles at different times. Figure 7.13 shows three ensemble-average profiles corresponding t=0 (□), 2.5 (○), and 8hr (△). In the first dataset, particles reside in two separate potential energy wells. The height analysis algorithm (described in *Section 3.5.3*) was applied to the data, and it was discovered that particles remained levitated during the entire experiment.

Thus, the energy well near $h=h_m$ is continuous and not a result of biasing from random short-time association events. Of note is that the peak of the near-contact (20nm) energy barrier ($0.38kT$) plus the offset of the second completely repulsive well ($0.18kT$) corresponds nicely with the vdW well depth for the two other ensemble profiles, which indicates that the particle ensemble sampled both uniform and non-uniform (adsorbed vesicles) portions of the particle surfaces during the course of the experiment.

After 2.5hr, another ensemble profile was collected from the same sedimentation cell (Figure 7.13A (○)). Careful study of the entire cell revealed that the percentage of levitated particles remained unchanged from the previous experiment, but the particles appeared to be sampling much deeper wells. These findings point to complete SLB formation on particle surfaces, however the difference between the first dataset and the

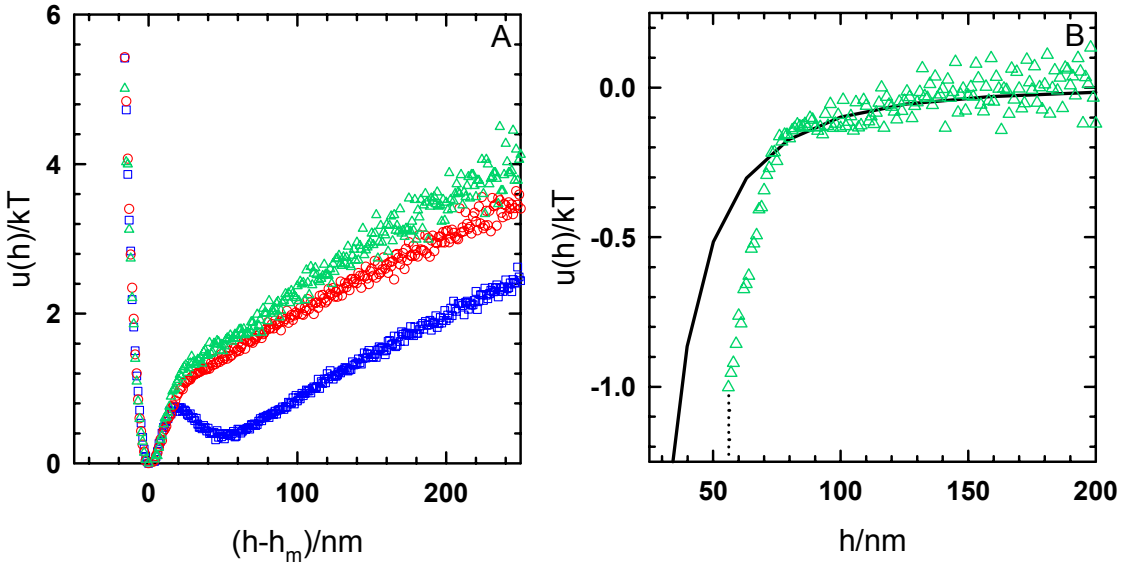

Figure 7.13 Potential energy profiles of 2.2µm silica modified with 5.0mol%PEG2000 SLBs taken at t=0 (□), 2.5 (○), and 8hr (△), showing the slow formation of SLB. Ensembles are formed from >15 particles for each profile, and ensemble profiles are representative of single-particle behavior.

second indicate the slow process of vesicle rupture and spreading on curved surfaces. The additional dataset collected at t=8hr is identical to the second, within the experimental error of TIRM, which verifies that the bilayer remains unchanged over that time period.

In order to corroborate the CSLM results that proved PEGylated bilayers in the brush regime still allow for cadherin binding at and below those explored PEG MWs and X_p values, particle-wall TIRM experiments were conducted on cadherin-modified SLBs with 2.2μm silica particles (Figure 7.14). The same SLB composition used to generate data in Figure 7.13 (0.5mol%N-NTA, 5mol%PEG2000) was implemented in these cadherin-cadherin experiments. Figure 7.14A presents potential energy profiles from N-cad-bearing particle and wall surfaces in a 150mM NaCl, 0mM $CaCl_2$ solution. Interactions for this experiment are limited strictly to non-specific repulsion. Particle-wall data from Figure 7.13A (△) is given along side non-specific cadherin-cadherin potentials (○), and the difference in well depths conclusively proves that the surfaces have been functionalized with N-cad and that N-cad displays a repulsive interaction in the absence of calcium. Figure 7.14B shows the vdW portion of (○) from Figure 7.14A plotted against the Lifshitz estimate for a 2.2μm silica particle levitated above a silica wall. The data matches theory more closely than the previous datasets, which is not completely understood at this point. At any rate, the onset of repulsion occurs at an absolute particle-wall separation of ~35nm. Although cadherin fragments have an end-to-end distance of 22nm, these molecules are only elongated at $[Ca^{2+}]$>40μM.[104] Thus, the chain would freely bend in these solution conditions, which would lead to a

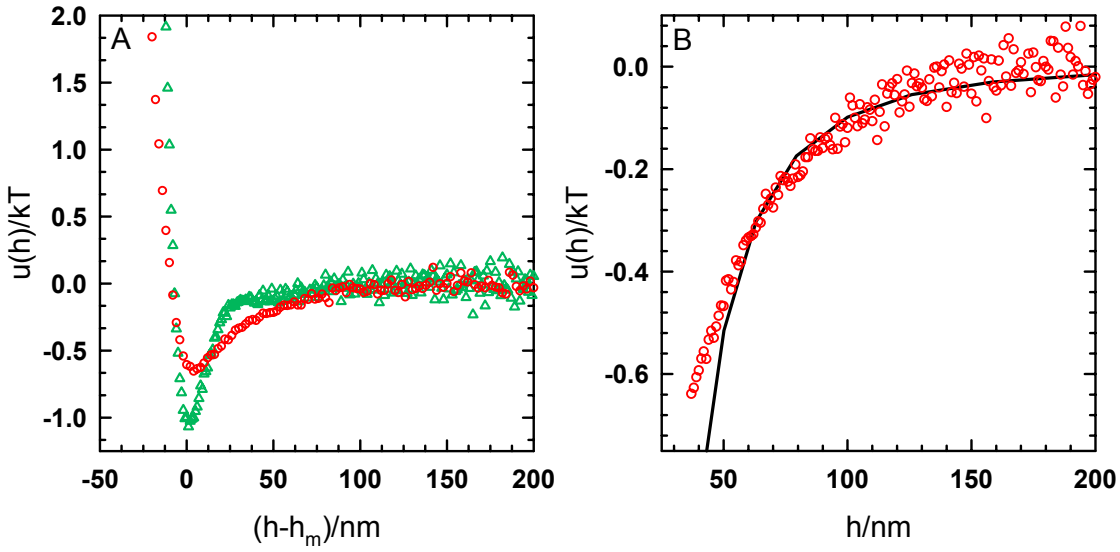

Figure 7.14 (A) Potential energy profiles of 2.2µm silica modified with 5.0mol%PEG2000 SLBs before (△) and after (O) binding of N-cad in 150mM NaCl and 0mM $CaCl_2$. Ensembles are formed from >20 particles for each profile. (B) Lifshitz fit to N-cad-modified particle ensemble from (A), showing the onset of repulsion at approximately 35nm. The well depth is approximately half of the original magnitude following N-cad binding.

markedly reduced N-cad layer thickness compared with what it would be in the presence of calcium. Also, the repulsive portion of the curve is less steep compared to the system without N-cad, indicating a more compliant layer. When calcium-dependent changes in the potential are finally recorded, it is expected that the protein layer thickness will increase upon addition of Ca^{2+}. Hence, the particle-wall vdW well is expected to initially decrease before increasing as the frequency of cadherin-cadherin *trans* dimerization rises.

7.6 Comparison of VM to TIRM Results

Since these two approaches are essentially measuring identical potentials, after considering geometric corrections, it is prudent exercise to compare data and explain

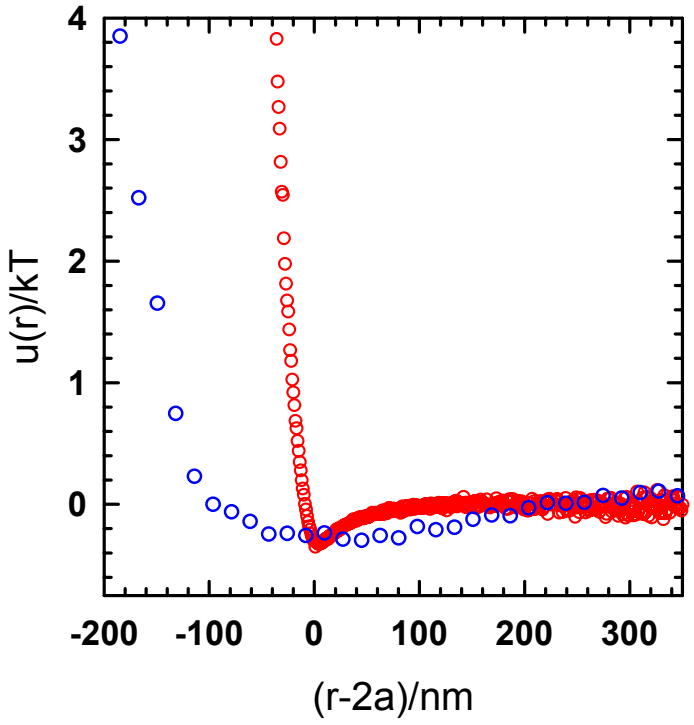

Figure 7.15. VM vs TIRM potential energy profiles for the interaction of N-cad-modified surfaces in the absence of calcium.

differences and commonalities between findings. Figure 7.15 shows separation-dependent potentials from VM and TIRM experiments for N-cad-modified surfaces (data from Figure 7.9B and 7.14A). To properly compare the magnitudes of each data set, the TIRM potential has been multiplied by a factor of 0.5, in accordance with the Derjaguin approximation. The most glaring similarity between the two profiles is that the depths of the potential wells estimated from TIRM and VM approaches are nearly identical (~0.4kT). Although this only represents two experiments, the fact that particle ensembles were analyzed helps increase the confidence in these datasets.

Examining the two potentials further, it is obvious that the width of the two potential wells and repulsive parts of the curves are strikingly different. The VM data has been corrected for multiparticle effects but not for polydispersity and optical distortion; we are currently only able to correct for these two distortions for 1.5μm silica particles. Once the distortions are handled properly, the potentials are expected to match more closely, but VM will never approach the spatial resolution needed capture vdW and specific interactions, which is possible with TIRM. Thus, the only potential utility that VM has for studying attractive systems is to observe changes in well depth.

7.7 Conclusions

Preliminary VM and TIRM data reported in this section denote a significant role that surface defects play in mediating particle-particle and particle-wall interactions. In order for future studies to be successful, particle surfaces must be coated with uniform and continuous PEGylated SLBs that maintain particle stability but do not hinder protein-Ni-NTA binding and *trans* dimerization. The presence of oriented and active cadherins on particle and wall surfaces was verify directly by CSLM images and indirectly by changes in particle-wall and particle-particle potentials.

Calcium-mediated specific interactions were observed between immobilized cadherins in particle-particle experiments. TIRM experiments were used in initial trials to verify the absolute particle-wall separations and monitor changes in surface potentials after cadherin binding to particle and wall surfaces. As expected, protein layers in the absence of calcium demonstrate non-specific repulsion that manifests itself as a reduction in the vdW well. These results also indicate that the PEG X_p on the particle

should be reduced to between 2 and 3mol%, while the stability provided by the wall can be bolstered by using either PEG3000 or PEG5000 lipids to yield and increased PEG brush thickness without interfering with His-tag-to-Ni-NTA binding and cadherin-cadherin *trans* dimerization. Initial CSLM trials are underway to verify that the latter point is a non-issue.

VM has proven to be a useful technique, but resolving separation-dependent potentials or even binding lifetimes becomes impractical at the ranges of interest in this problem. Additionally, particle-particle experiments are limited to studying homophilic interactions between cadherins, apart from novel cell sorting studies proposed in *Section 10.3*. Despite these drawbacks more VM measurements will be collected once the system is perfected, and this data will be used to show that TIRM is a superior technique when performed with the appropriate set of experimental parameters (e.g., particle radius and SLB thicknesses).

8. LUMINESCENCE TOTAL INTERNAL REFLECTION MICROSCOPY

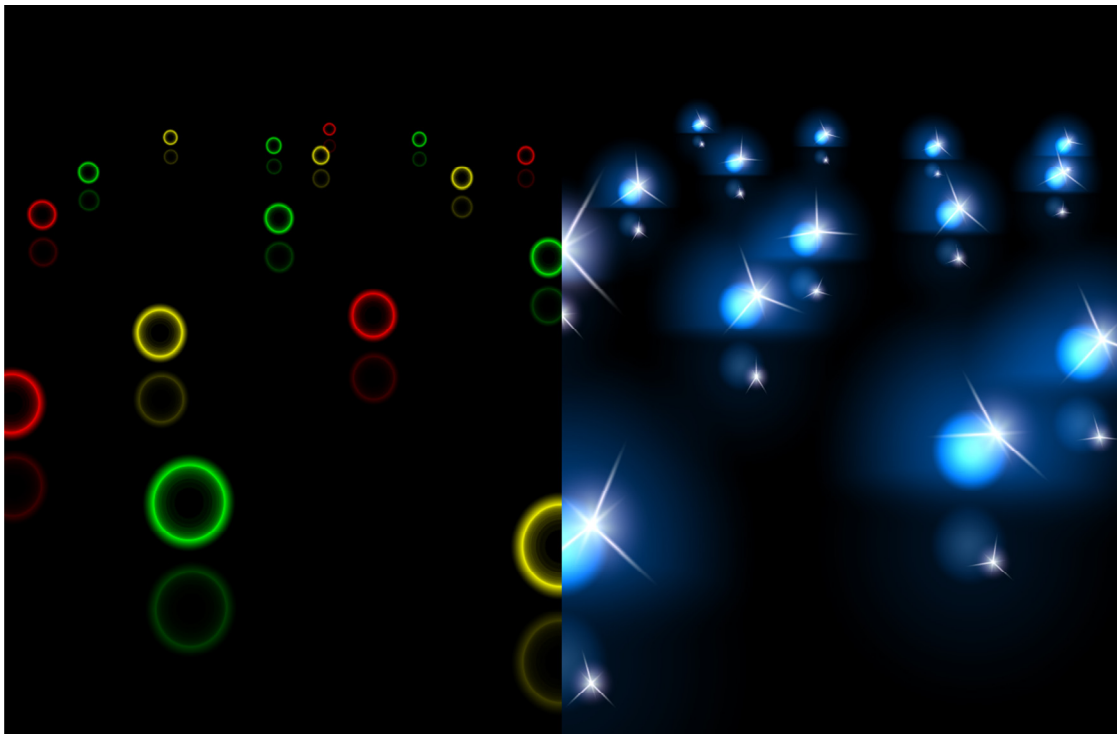

Figure 8.1. Graphic illustration of quantum dot modified colloids luminescing (left) and scattering (right) in an evanescent wave; scattering is filtered on the left side.

8.1 Synopsis

Measurement of absorbance, fluorescence, and scattering of macromolecules and colloids in evanescent waves (EWs) provides the basis for a variety of techniques capable of characterizing interfacial chemical and physical phenomena on nanometer length scales. Examples of such techniques include attenuated total reflection,[173] total internal reflection fluorescence (TIRF),[174] surface plasmon resonance,[175] and TIRM.[176] When EW methods are combined with optical microscopy and digital imaging methods, it is possible to simultaneously measure spatial and temporal behavior of single-particles

and particle ensembles near surfaces.[25,177] With TIRM,[26,178] EW scattering is typically used to monitor Brownian motion of single colloids levitated above planar surfaces, which can be utilized to quantify potential energy profiles[6,36,138,179] and hydrodynamic interactions.[51,180] As discussed in previous sections, TIRM has been combined with VM to track 3D excursions of many colloids near surfaces to measure single and ensemble colloid-surface potentials,[28] particle-particle potentials,[29] particle interactions with patterns,[25] and local protein-macromolecule interactions.[181]

The utility of TIRM lies in its ability to sensitively resolve colloid-surface interactions on nanometer length scales and the scale of *kT*. While *kT*-scale energy resolution is obtained using a clever experimental design involving a statistical mechanical inversion, access to nanometer dimensions with TIRM is due to the properties of colloidal EW scattering. Figure 8.2 schematically depicts a single colloid in an EW generated via total internal reflection of a laser at a glass-water interface.[26] In this configuration, the scattering or luminescence intensity, I, is exponentially sensitive to the instantaneous particle-surface separation height, h, via[182,183]

$$I(h) = I_0 \exp(-\beta h), \tag{8.1}$$

where $\beta = (4\pi/\lambda)\left[\left(n_g \sin\theta\right)^2 - n_w^2\right]^{1/2}$, I_0 is the intensity at colloid-surface contact (h=0), and β^{-1} is the EW decay length determined by glass and water refractive indices, n_g and n_w, and the laser's incident angle, θ. Although the validity of Eq 8.1 has recently been contested for variations of the arrangement in Figure 8.2 (e.g., adsorbed films, AFM tips, small βa),[184,185] the overwhelming majority of TIRM studies have directly or indirectly

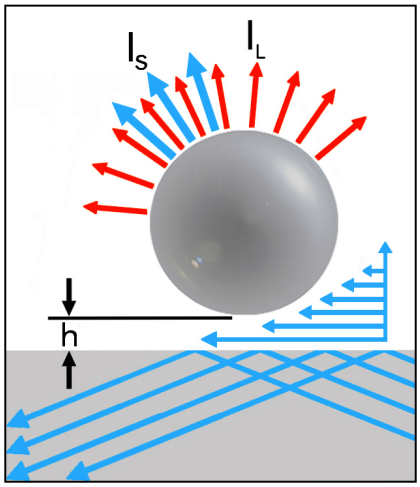

Figure 8.2. Schematic of height-dependent scattering (I_S) and luminescence intensities (I_L) from a QD-doped particle interacting with an evanescent wave. Incident and scattering wavelengths are identical and can be filtered out, while the higher wavelength luminescence can be gathered for particle-wall analysis.

confirmed the exponential relationship between scattering intensity and height, through colloid-surface interaction measurements.[6,25,26,28,29,36,51,138,176,177,178,179,180,181,182,183]

Despite the fact that TIRF is commonly used to interrogate fluorescent macromolecules near interfaces, only a few studies have investigated EW excitation of fluorescent colloids, and those tended to focus on interfacial particle image velocimetry[186] rather than colloid-surface interactions. Reasons for the lack of such studies probably include lower absolute fluorescence intensities compared to scattering and the role of photobleaching in producing undesirable temporal intensity changes additional to the height dependence in Eq 8.1. Despite these drawbacks, monitoring fluorescence has benefits that include: capabilities for spectral multiplexing,[78,187] measurements in index matched media,[188] lowering the signal-to-noise ratio by limiting interference from background scattering,[189] and avoiding optical distortion[49] in integrated VM approaches.[29]

Here, we monitor EW-excited luminescence of quantum dot (QD) modified polystyrene (PS) colloids (QDPS) to measure potential energy profiles for ensembles of QDPS particles levitated above a glass surface. The rationale for using QDs in the present work is to exploit their superior quantum yield in terms of absolute intensity, their resistance to photobleaching, and the large range of emission wavelengths accessible with a single excitation wavelength. The goal is to determine whether the height-dependent EW-excited QDPS luminescence is accurately described by Eq 8.1 to allow quantitative, nanometer-scale measurements of colloid-surface interactions. Potential issues are whether the luminescent shell-nonabsorbing core geometry influences the validity of Eq 8.1 and whether temporal luminescence variations due to the ensemble QD response for each QDPS colloid are significant.[190]

To investigate the use of QDPS with EW excitation, our results characterize QDPS luminescent properties and then compare potential energy profiles obtained from scattering and luminescence modes. Specifically, we report confocal scanning laser microscopy (CSLM), emission spectra, and flow cytometry (FC) results for QDPS colloids prepared using three PS colloid sizes modified with three QD sizes. We then compare scattering and luminescence temporal intensity variations for electrostatically levitated and irreversibly deposited QDPS colloids. Finally, we measure colloid-surface potential energy profiles using both scattering and luminescence intensity measurements. These results demonstrate that EW-excited luminescence of QDPS colloids can be used to obtain quantitative colloid-surface potential energy profiles. Furthermore, these findings should enable the use of similar QDPS colloids in future studies (see *Section*

10) that exploit their unique spectral and optical properties for novel measurements in interfacial colloidal systems.

8.2 QDPS Colloids in Evanescent Waves

Results from CSLM are given in Figure 8.3, showing either luminescence from a set of uniform particles or a mixture of three different sized QDPS colloids (4.0μm, 5.2μm, 5.9μm) modified with QDs having different emission wavelengths (540nm, 590nm, 640nm). In Figure 8.3A, it is evident that there are small aggregates on the surface of the microspheres, but these are absent in the multi-channel confocal image in Figure 8.3B. This is primarily from the reduced resolution that results when performing spectral mixing of three channels, compared with the single-channel data gathered in Figure 8.3A. As will be evident in a later discussion, the presence of these small aggregates can be considered negligible in the context of error in absolute luminescence intensity data. The true-color, multi-channel CSLM image of all three QDPS demonstrates the ability to perform spectral multiplexing by identifying different QDPS colloidal probes via their spectral signature.[25,28,29,181] Although the present work only explores QD luminescence as a "tag" for colloid size that can be verified independently via direct visualization, the following results demonstrate how such an approach could be exploited to probe specific biomolecular interactions in a combinatorial fashion.

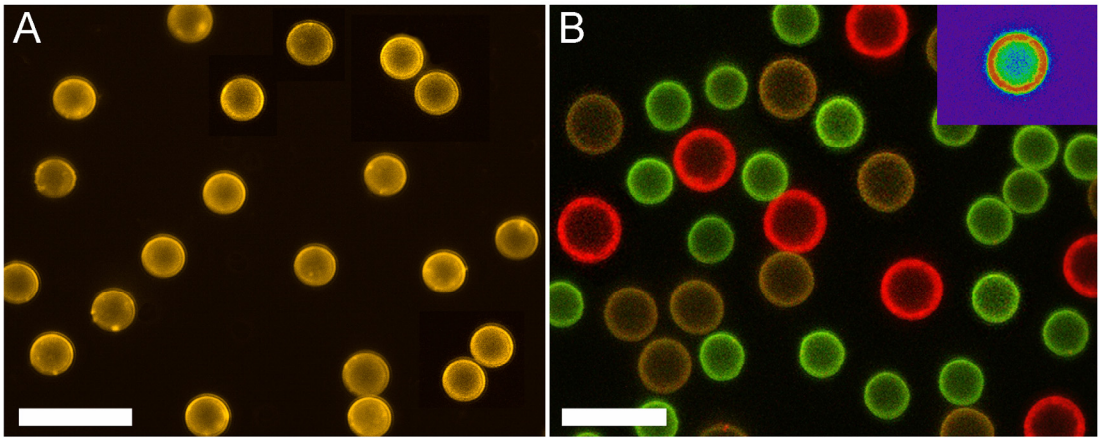

Figure 8.3. (A) CSLM image of single 4µm QDPS particles emitting at 590nm after being excited with 488nm. (B) True-color multi-channel CSLM image of 4µm, 5µm, and 6µm QDPS emitting at 540, 590, and 540, respectively. Inset in (B) is a contour plot of intensity distribution. Scale bars are 10µm.

The angular independence of the luminescence intensity from each QDPS colloid in Figure 8.3 with uniform illumination indicates the homogeneous distribution of the QD coatings. The CSLM images in Figure 8.3 also shows the general uniformity in intensity between different QDPS colloids, which offers a number of potential advantages in ensemble TIRM measurements (e.g., single particle intensities do not have to be renormalized for ensemble analyses).[25,28,29] Because the apparent thickness of the bright shell region in the CSLM images is approaching the visible diffraction limit (~200nm), it is not possible to accurately determine the radial shell thickness that contains the majority of the QDs, but it can be assumed to be less than ~100nm.

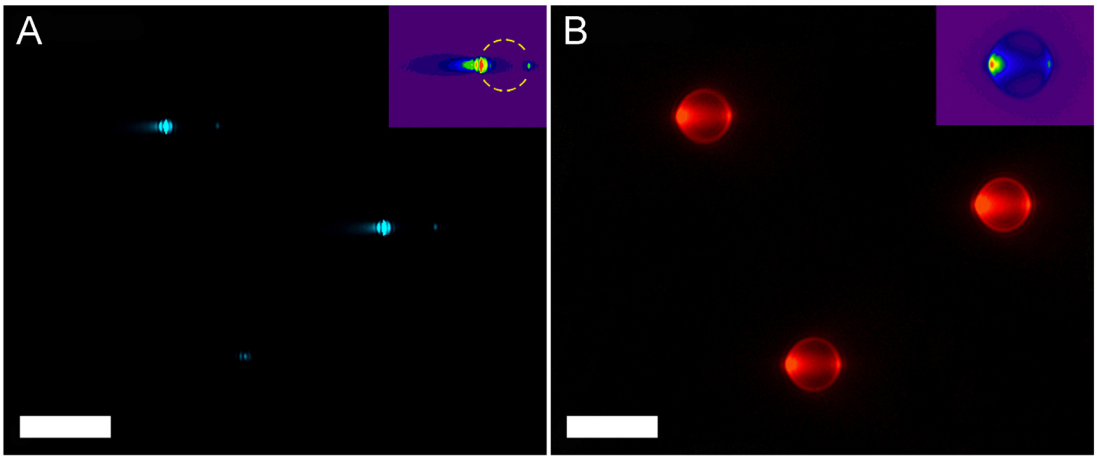

Figure 8.4. (A) 488nm EW scattering from three 6μm QDPS. (B) EW-excited luminescence from the same three colloids diffusing in 1mM NaCl. Insets are contour plots of representative intensity distribution. Scale bars are 10μm.

Figures 8.4A and 8.4B show images of scattering and luminescence of levitated QDPS colloids in a 488nm wavelength EW; both are false-colored 12-bit grayscale images. Each image includes an inset contour plot showing the spatial distribution of the scattering or luminescence intensity. In the scattering case, QD luminescence is not filtered since the scattering dominates luminescence by as much as a factor of 10^3, whereas in the luminescence case, the scattered 488nm light is filtered (>500 nm). Although both scattering and luminescence arise from EWs with the same penetration depth (β^{-1}=88nm), the resulting intensity distribution is distinctly different in the two images. The measured spatial intensity distributions depend on the microscope objective numerical aperture in terms of the solid angle over which light is collected. When comparing the images in Figure 8.3 and 8.4, it should be noted that a 100× (NA=1.4) oil objective was used for the CSLM image in Figure 8.3, and a 63× (NA=1.4) oil objective

was used for the EW images in Figures 8.4. Additionally, all potential energy profiles were measured using a 40× (NA=0.6) objective.

In the case of scattering in Figure 8.4A, two spots appear at forward and backscattering positions, with significantly brighter forward scattering. The luminescence in Figure 8.4B appears to be more distributed over the colloid volume, although local maxima still occur at the forward and backscattering positions. Of course, these two signals are not unconnected; the intensity distribution that results from scattering is essentially the excitation source for luminescence, and attenuation in the scattering pattern due to local absorbance will be captured in the distribution of luminescence intensity. One advantage of luminescence over scattering is that background noise from the EW scattering from other particles and surface roughness[189] is removed by high pass filtering to produce a lower signal-to-noise ratio and higher lateral resolution measurements of colloid-surface interactions.[28,29] Multi-particle EW luminescence may also be less of a problem than multi-particle EW scattering after including the net effect of excitation light attenuation, re-absorbance of emitted light, and the isotropic nature of luminescence, although thorough examination of this topic is well beyond the scope of the present work.

8.3 QDPS Colloid Luminescence

Before analyzing QDPS luminescence for the purpose of measuring colloid-surface interactions, results in Figure 8.5 help to more fully characterize the anticipated spectral properties of QDPS luminescence. Figure 8.5 shows emission spectra for three different sized QDs using a 400nm excitation source (before their addition to PS colloids).

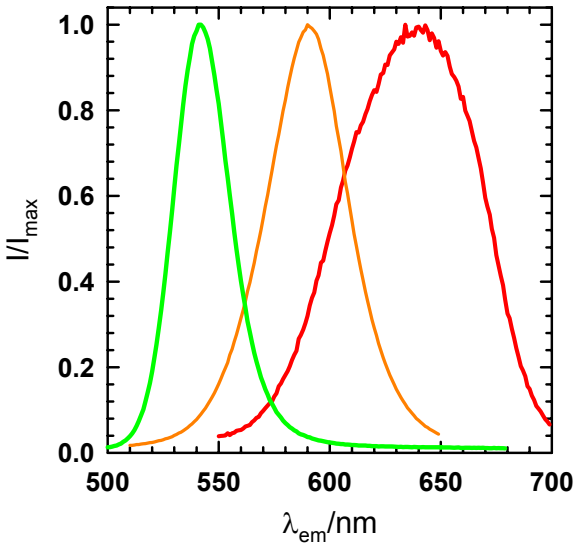

Figure 8.5. Emission spectra of three different sized CdSe-ZnS QDs with peaks at 542, 591, and 640 nm.

Despite the considerable overlap between emission spectra, presumably as the result of QD polydispersity, the ensemble luminescence from QDPS colloids (with as many as 10^4 QDs/colloid[190]) is clearly distinguishable, as already shown in Figure 8.3B.

Figure 8.6 shows FC results for the three sets of QDPS colloids each modified with one of the three batches of QDs characterized in Figure 8.5. The two bandpass filters in Figure 8.6 capture luminescence signatures in three distinct groups. These results indicate retention of spectral separation from ensemble QD luminescence signals for each of the three batches of QDPS colloids. In addition to the CSLM image in Figure 8.3B that demonstrates detection of each QDPS population on a separate channel, the FC data provides statistical information on the distribution and separation of spectral properties for each batch of QDPS colloids, including all variations introduced during their synthesis and preparation. The results in Figures 8.6, along with the CSLM image

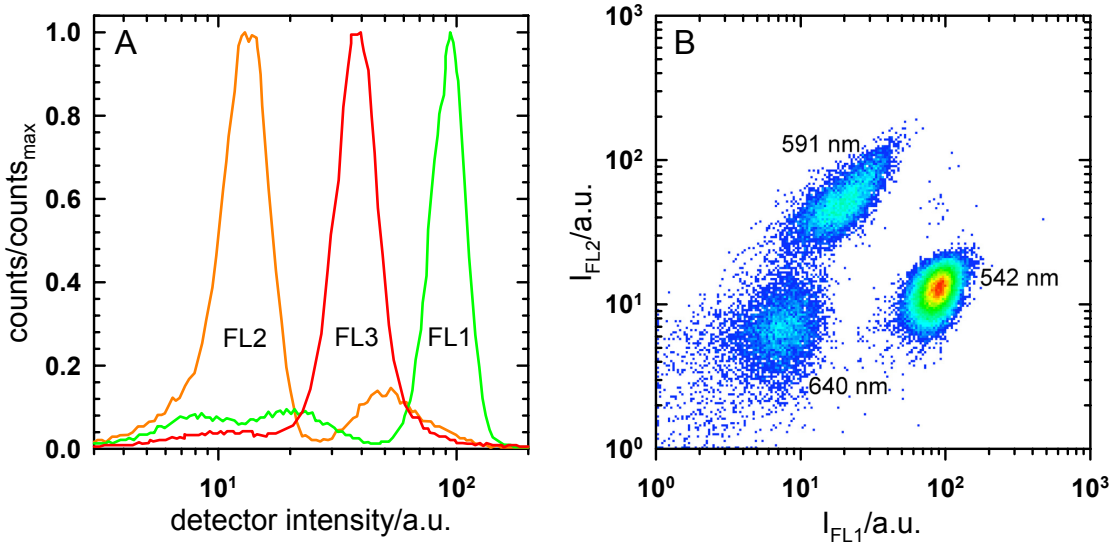

Figure 8.6. (A) FC results for a mixture of QDPS particles showing the normalized particle counts vs. intensity distribution for each detector. (B) Scatter plot of FC result from the same QDPS mixture showing simultaneous intensity capture using filters FL1 and FL2. The color gradient within each grouping represents the absolute particle count at that FL1-FL2 intensity location.

in Figure 8.3B, clearly demonstrate that such QDPS colloids could be used in spectral multiplexing applications.

Because single QDs and QD ensembles are known to display time-variant luminescence,[190,191] Figure 8.7A reports temporal intensity fluctuations from EW scattering and luminescence of single, levitated QDPS colloids. Regression lines indicate that scattering gradually decreases with time, whereas luminescence gradually increases with time. In both cases, the short-time intensity fluctuations are primarily the result of Brownian excursions of the levitated colloids within the EW.[51] In the scattering case, the long-time decrease in the average intensity with time is probably due to drift from several sources including the laser, stage, and detection system. The gradually increasing slope in the luminescence data is comparable in magnitude to the decreasing slope in the

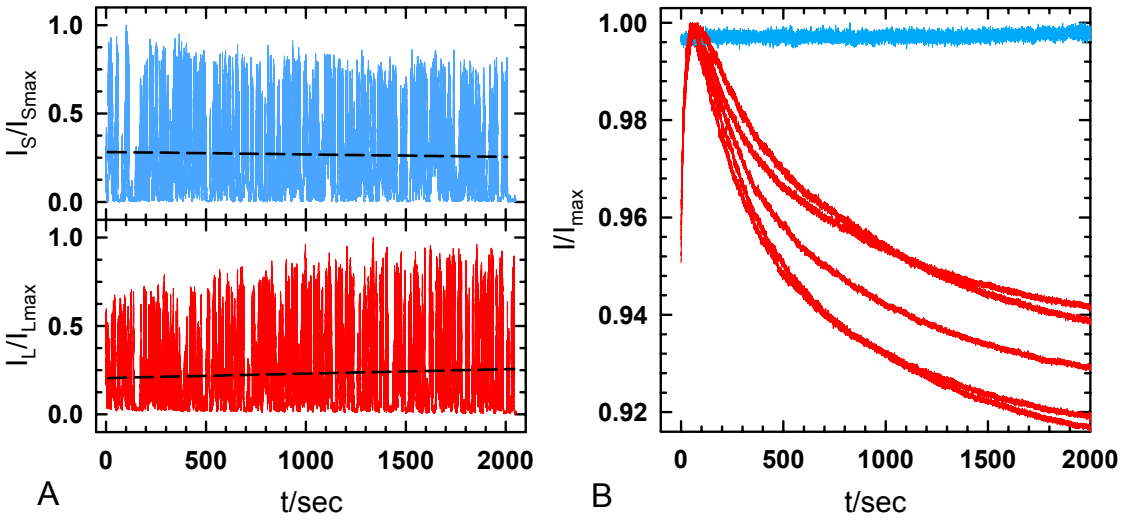

Figure 8.7. (A) Scattering (blue) and luminescent (red) intensities for 488nm excitation of single 6μm levitated colloids in 1mM NaCl as a function of time. (B) Scattering (red) and luminescence (blue) intensities from stuck colloids as a function of time. Intensities are normalized by the maximum values for each data set.

scattering data and could also be attributed to long-time drift. However, luminescent QDPS colloids can display time-dependent intensity fluctuations over a broad range of time scales based on the collective statistical behavior of QD ensembles,[190] which cannot be dismissed as a contributing factor to the long-time increase in Figure 8.7A.

Because the intensity variations in Figure 8.7A are dominated by Brownian excursions of the levitated QDPS and subtle changes cannot be extracted, Figure 8.7B reports time-dependent scattering and luminescence intensity data for QDPS colloids irreversibly deposited on the underlying glass surface. The intensity fluctuations in the scattering case now characterize the cumulative noise inherent to our apparatus, since Brownian excursions no longer contribute to the intensity fluctuations. While scattering intensity fluctuations due to residual thermal motion of deposited colloids (possibly allowed by surface roughness, adsorbed molecules, etc.) cannot be absolutely dismissed,

such contributions have previously been shown to be minimal compared to system noise.[40]

The luminescence intensities from the deposited QDPS in Figure 8.7B display small amplitude fluctuations due to noise that are superimposed on a more obvious non-monotonic, long-time dependence. As noted earlier, the signal-to-noise ratio in the luminescent case is greater than that in the scattering case since background scattering of the EW is removed via filtering. Luminescence results in Figure 8.7B show an initial ~5% intensity increase occurring over ~100s, which is then followed by a ~10% decrease over a ~2000s period. These variations are not unlike other literature results[190] in that an initial short-time increase is observed followed by a longer decay. However, the time constants associated with these intensity changes in Figure 8.7B appear to be different from other ensemble QD measurements, which might result from the mere glancing illumination of the QDPS colloid bottom surface by the EW (see Figure 8.2).

Because intensity data are often acquired over a ~2000s period in TIRM experiments, the temporal luminescence variations of ~10% in Figure 8.7B could adversely affect potential energy profile measurements. However, an inconsistency to be resolved between Figures 8.7A and 8.7B is the gradually increasing luminescence intensity for the levitated colloid in Figure 8.7A, in contrast to the deposited colloid in Figure 8.7B. One explanation is that free rotation of levitated QDPS colloids affects the residence time of QDs that experience full EW illumination, which could influence their net temporal intensity response compared to irreversibly deposited QDPS colloids that remain fixed. In addition, deposited colloids have ~10% of their surfaces illuminated by

the EW (spherical cap intersecting EW within $4\beta^{1}$) compared to ~2% for levitated colloids in ~1mM aqueous media. It is possible that the increasing intensity in Figure 8.7A (bottom) is the result of QDs with shorter residence times in the EW effectively all being on the initial part of the time-dependent luminescence curves in Figure 8.7B.

Ultimately, it is nontrivial to know exactly the time-dependent ensemble QD luminescence characteristics for levitated QDPS colloids without extensive control experiments and modeling work beyond the scope of this initial investigation. The problem is much more complex than simply including the spherical cap of colloids directly illuminated by the EW, since scattering excites QDs at varying intensities over the entire colloid surface (see Figures 8.4A and 8.4B).[182,183] In addition, the incident EW intensity experienced by QDPS colloids fluctuate in time, based on Brownian excursions. The average rotational diffusion coefficient of levitated QDPS colloids also depends on the relative frequency at which different heights are sampled above the surface, which depends on the colloidal-surface interaction potential.[51] With consideration of these complexities and the fact that the long-time luminescence change in Figure 8.7A could be attributed to drift in the laser and detection system, we proceed with measurements of potential energy profiles to assess the validity of Eq 8.1 for describing height-dependent EW-excited QDPS luminescence.

8.4 Colloid-Surface Potential Energy Profiles

We now analyze EW-excited QDPS luminescence in the same manner that height-dependent EW scattering is typically analyzed in TIRM[26] to construct potential energy profiles, $u(h)$, and to indirectly test the validity of Eq 8.1. Although it would be desirable

to directly measure the height dependent EW luminescence intensity profile for QDPS colloids, established methods for performing such measurements using deposition on MgF_2 films[183,192] or AFM cantilever tips[184,193] would interfere with QDPS Brownian rotation and dynamic aspects of their luminescence, as discussed above. Instead, we simply check whether $u(h)$ are obtained in agreement with theory, which provides evidence that the exponential intensity dependence is retained for the luminescent, levitated QDPS colloids investigated in this work.

Figure 8.8 shows six plots of $u(h)$ obtained from both scattering and luminescence measurements of ensembles of QDPS colloids that were characterized in Figures 8.3-8.7. Each of the three QDPS batches is measured at two ionic strengths that are sufficiently low so that van der Waals attraction does not contribute to the net $u(h)$. The absence of van der Waals simplifies the analysis of measured potentials since effects of roughness, retardation, QD dielectric properties, etc. do not have to be considered.[36] Measurements of $u(h)$ via luminescence were performed immediately prior to scattering measurements to minimize temporal luminescent intensity variations that could occur as the result of scattering 488nm light for 40min prior to measuring luminescence. Simultaneous measurement of several colloids in each case was used to compare single and ensemble colloid-surface $u(h)$. The results for all cases in Figure 3 are the same for scattering and luminescence measurements. This fact demonstrates that no obvious difference exists between $u(h)$ constructed from Brownian height excursions of levitated QDPS measured using either scattering or luminescence intensities and analyzed with Eq 8.1.

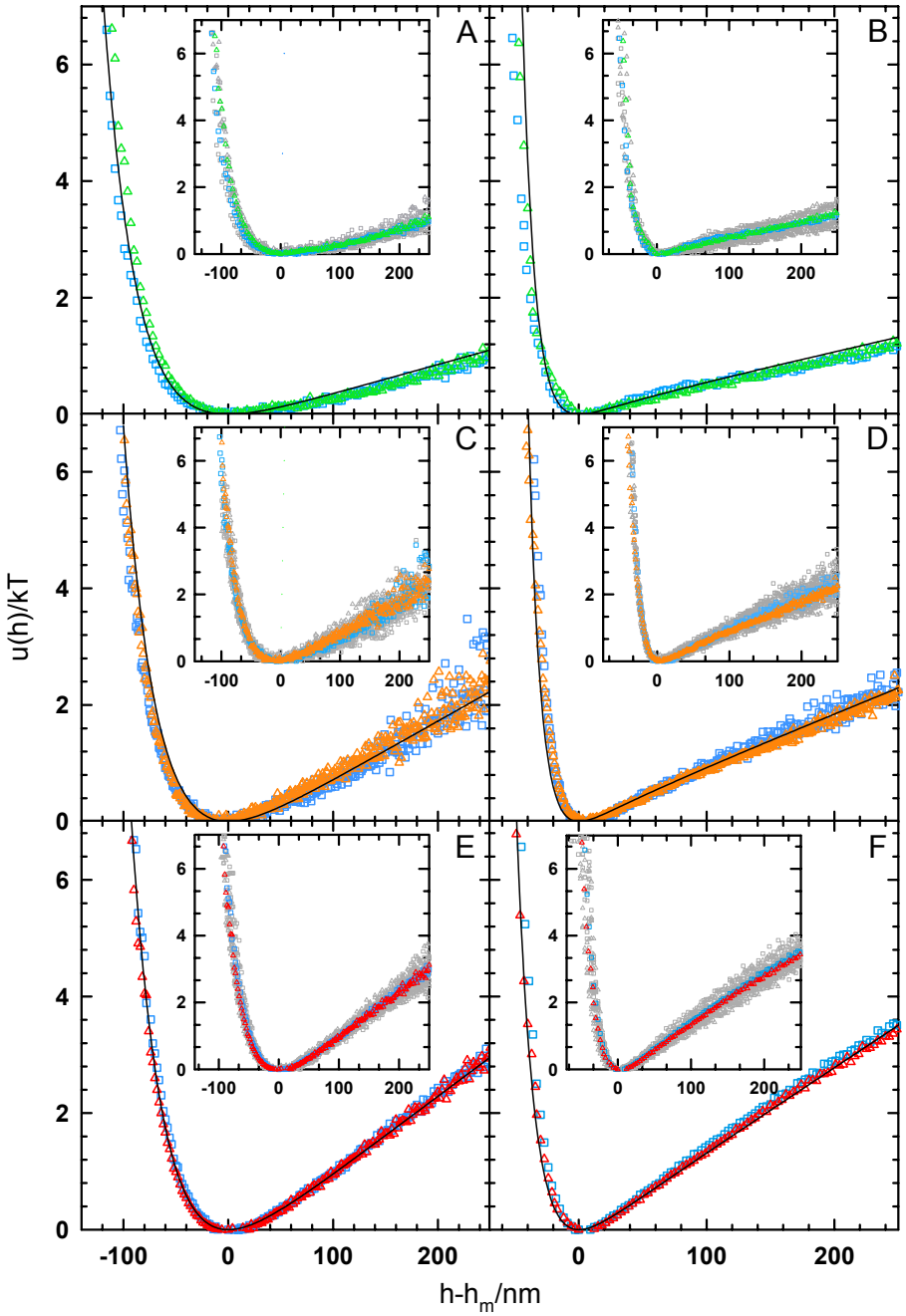

Figure 8.8. (A) Ensemble average colloid-surface potential energy profiles for (□) scattering and (Δ) luminescence from QDPS colloids with diameters/emission maxima of (A,B) 4μm/540nm, (C,D) 5μm/590nm, (E,F) 6μm/640nm. Ionic strengths are (A,C,E) 0.1mM, (B,D) 1.0mM, and (F) 0.5mM. Insets in each plot show single-colloid and ensemble-average potential energy profiles. Ensemble profiles are fit with Eqs 2.3 to 2.7, giving parameters reported in Table 8.1.

Fitting the theoretical potential with Eqs 2.14 produces values of colloid radius (Eq 2.7) and solution ionic strength (Eq 2.6) in excellent agreement with independent measurements, as reported in Table 1. Colloid size is estimated using the commonly reported density for PS (1055 kg/m^3), which assumes that a relatively low concentration of QDs within a <100nm surface shell (~10-14% of colloid volume) does not significantly alter the net QDPS colloid density. This assumption appears justified by the agreement between measured and manufacturer reported colloid sizes in Table 1. In addition to verifying Eq 8.1 for describing the height-dependent luminescence of EW-excited QDPS colloids, the agreement between experiment and theory in Figure 8.8 also indicates that QDPS core-shell optical properties do not invalidate EW scattering measurements from such colloids.

Table 8.1 Fitted parameters profiles given in Figure 8.8. (a) manufacturer reported diameters, (b) nominal electrolyte concentrations as prepared, (c) Debye lengths from conductivity measurements, (d) signal measured; scattering (sca) or luminescence (lum), (e) number of single particles measured to construct each ensemble average profile, (f) Debye lengths from curve fits to ensemble profiles in Figure 8.8 (g) diameters from curve fits to ensemble profiles in Figure 8.8.

$2a$/μm[a]	4.0±0.17 μm				5.2±0.29 μm				5.9±0.58 μm			
***C*/mM**[b]	0.1		1.0		0.1		1.0		0.1		0.5	
κ^{-1}/nm[c]	28.9		9.6		31.2		9.7		30.0		13.4	
signal[d]	sca	lum	sca	lum	sca	lum	sca	lum	sca	lum	sca	lum
number[e]	3	3	4	4	3	3	3	4	7	5	10	10
κ^{-1}/nm[f]	31.2	30.1	11.2	10.7	31.9	32.5	10.1	10.6	28.9	30.7	12.4	13.5
$2a$/μm[g]	4.30	4.34	4.02	4.18	5.02	5.18	5.04	4.88	5.68	5.72	5.56	5.72

All single and ensemble $u(h)$ for each case in Figure 8.8 are also in excellent agreement for both scattering and luminescence measurements. This agreement demonstrates that there are no significant effects of physical non-uniformities (e.g.

colloid size polydispersity, surface charge heterogeneity)[25,28,29,47] or optical/spectral non-uniformities (e.g. QD aggregates) that produce different $u(h)$ for different QDPS colloids. Simultaneous measurements of multiple colloids in each experiment in Figure 8.8 demonstrate the robust nature of these measurements, since results for single colloids could be unrepresentative of average statistical properties.

Finally, with knowledge of the QDPS colloid-surface $u(h)$, the extent of EW exposure of QDPS colloids can be more quantitatively estimated, which can be used to revisit the discussion of time-variant luminescence in Figure 8.7. The average exposure of particles, $\langle I \rangle$, can be estimated through

$$\langle I \rangle = \int I(h) n(h) dh \Big/ \int n(h) dh \tag{8.2}$$

where Eq 8.1 is used to find $I(h)$, and $n(h)$ can be obtained from either the measured histogram or $u(h)$ by inverting Eq 2.17. Eq 8.2 provides a relative weighting for the EW intensities sampled by levitated colloids having the same size and observation times but with different $u(h)$. For the 4-6μm QDPS colloids investigated in Figure 8.8, Eq 8.2 indicates deposited colloids have an EW exposure ~40-80 times that for colloids levitated in 0.1mM media and ~10 times for those in 1.0mM media. This ~10-100 factor in average exposure could explain why the time variant luminescence for deposited QDPS in Figure 8.7B over ~2000s differs from levitated QDPS in Figure 8.7A over the same observation period. When allowing for the additional effect of Brownian rotation on QD residence time within the EW for levitated QDPS colloids, it is possible that the time-variant luminescence in Figure 8.7A may correspond to only the initial "charging

up" portion of the temporal response for deposited QDPS colloids in Figure 8.7B.

8.5 Conclusions

We have demonstrated quantitative measurements of colloid-surface $u(h)$ by monitoring the EW-excited luminescent intensity of QD-modified PS colloids. Agreement of $u(h)$, determined from scattering and luminescence measurements, with theoretical predictions and independently measured parameters indirectly confirms an exponential relationship between height and luminescence intensity. Luminescence intensities of levitated QDPS colloids do not display obvious time-dependent behavior, although this is nontrivial to confirm directly for levitated colloids. Time-varying luminescence is observed for irreversibly deposited colloids, which might occur as a result of the significantly greater EW exposure compared to levitated colloids. In future studies, care should be taken to check for the relative importance of time-dependent luminescence. From CSLM, spectral, and FC results, QDs are uniformly distributed within each colloid and amongst all colloids, and QDPS particles retain the luminescent emission properties of single QDs.

Based on our findings, EW-excited luminescence of QDPS colloids can be used to quantitatively measure nanometer-scale colloid-surface interactions. Such luminescence measurements do not appear to offer any disadvantages compared to scattering measurements, beyond an additional effort in synthesis. In some cases, luminescence intensity measurements of QDPS colloids in EWs could offer several advantages including lower noise, contrast in index-matched media, and spectral multiplexing capabilities. Examples of measurements in interfacial colloidal systems that might

exploit QDPS luminescence could include combinatorial measurements of different colored diffusing probes, each bearing different biomacromolecules,[181] or measurements of interfacial self assembly of index-matched colloids using integrated TIRM and CSLM measurements.[194]

9. CONCLUSIONS

Spatial and temporal tracking of passively diffusing functionalized colloids continues to be an improving and auspicious approach to measuring weak specific and non-specific biomolecular interactions. Evidence of this is given by the recent increase in published studies involving the development and implementation of these methods. The primary aim of the work presented in this dissertation was to modify and optimize VM and TIRM methods to permit the collection of equilibrium binding and sampling data from interactions of surface-immobilized biomolecules.

In this pursuit, several procedures were developed and optimized to meet this goal. For instance, a distinctly new approach for quantitatively measuring interactions of proteins and synthetic macromolecules adsorbed to colloid and wall surfaces was developed. Information from such measurements included single-colloid and ensemble-average potential energy profiles, lateral diffusivities, and colloid-surface association (CSA) lifetimes. A consistent analysis of such information in several demonstrative measurements was used to distinguish different colloid-surface interaction regimes as belonging to levitated, associated, or deposited. This newly developed method and associated analyses were then employed in a systematic series of experiments to capture how average colloid-surface interactions are mediated by combinations of chemical surface modifications, adsorbed BSA and PEO layers, and surface heterogeneity. Results comprehensively reveal how BSA layer architecture on different chemically modified substrates and PEO copolymer MW, together, either conceal or expose underlying substrate heterogeneities to influence colloid-surface attraction and association lifetimes.

In all cases, BSA-BSA, BSA-PEO, and PEO-PEO interactions appear to be completely repulsive such that CSA only occurs due to non-specific colloid-surface attraction, particularly in the presence of surface heterogeneity. Most importantly, the results and developed analyses from this work severe as a baseline to differentiate specific and non-specific interactions between protein binding partners on colloids and surfaces. Further, the proven capability to measure non-specific interactions provides a basis for future direct measurements of weak specific protein-protein interactions.

Supported lipid bilayers were chosen as the model surface system for functionalizing colloid and wall surfaces. By incorporating PEG into the upper and bottom leaflets of these SLBs, we are able to instill baseline stability into the system. This was a key achievement in order to prevent non-specific association of colloids to the underlying wall and the surfaces of other colloids prior to and following protein binding. Importantly, control studies were performed that proved conclusively that cadherin was active and oriented on PEGylated SLBs.

Preliminary VM and TIRM data denote the significant role that surface defects play in mediating particle-particle and particle-wall interactions. In order for future studies to be successful, particle surfaces must be coated with uniform and continuous PEGylated SLBs that maintain particle stability, yet they cannot hinder protein-Ni-NTA binding and *trans* dimerization. The presence of oriented and active cadherins on particle and wall surfaces was verify directly by CSLM images and indirectly by changes in particle-wall and particle-particle potentials.

Calcium-mediated specific interactions were observed between immobilized cadherins in particle-particle experiments. TIRM experiments were used in initial trials to verify the absolute particle-wall separations and monitor changes in surface potentials after cadherin binding to particle and wall surfaces. As expected, protein layers in the absence of calcium demonstrate non-specific repulsion that manifests itself as a reduction in the vdW well. These results also indicate that PEG X_p for fusion onto particle surfaces should be reduced to between 2 and 3mol%, while the stability provided by the wall can be bolstered by using either PEG3000 or PEG5000 lipids to yield and increased PEG brush thickness without interfering with His-tag-to-Ni-NTA binding and cadherin-cadherin *trans* dimerization. Initial CSLM trials are underway to verify that the latter point is a non-issue.

VM has proven to be a useful technique, but resolving separation-dependent potentials or even binding lifetimes becomes impractical at the ranges of interest in these problems. Additionally, particle-particle experiments are limited to studying homophilic interactions between cadherins, apart from novel cell sorting studies proposed in *Section 10.3*. Despite these drawbacks, more VM measurements will be collected once the system is perfected, and this data will be used to show that TIRM is a superior technique when performed with the appropriate set of experimental parameters (e.g., particle radius and SLB thicknesses).

And finally, other work, which may seem to be a slight departure from the rest of the dissertation, was conducted to collect quantitative measurements of colloid-surface $u(h)$ by monitoring the EW-excited luminescent intensity of QD-modified PS colloids.

Agreement of $u(h)$, determined from scattering and luminescence measurements, with theoretical predictions and independently measured parameters, indirectly confirms an exponential relationship between height and luminescence intensity, just as in conventional TIRM. Luminescence intensities of levitated QDPS colloids did not display obvious time-dependent behavior, although this is nontrivial to confirm directly for levitated colloids. Time-varying luminescence is observed for irreversibly deposited colloids that might occur as a result of the significantly greater EW exposure compared to levitated colloids. In future studies, care should be taken to check for the relative importance of time-dependent luminescence. From CSLM, spectral, and FC results, QDs are uniformly distributed within each colloid and amongst all colloids, and QDPS particles retain the luminescent emission properties of single QDs.

Based on our findings, EW-excited luminescence of QDPS colloids can be used to quantitatively measure nanometer-scale colloid-surface interactions. Such luminescence measurements do not appear to offer any disadvantages compared to scattering measurements, beyond an additional effort in synthesis. In some cases, luminescence intensity measurements of QDPS colloids in EWs could offer several advantages including a lower signal-to-noise ratio, contrast in index-matched media, and spectral multiplexing capabilities. Examples of measurements in interfacial colloidal systems that might exploit QDPS luminescence could include combinatorial measurements of different colored diffusing probes each bearing different biomacromolecules or measurements of interfacial self assembly of index-matched colloids using integrated TIRM and CSLM measurements.

10. FUTURE RESEARCH

10.1 Homophilic and Heterophilic Cadherin-Cadherin Interactions

The promising results presented in *Section 7* suggest a capability to measure separation-dependent potentials and bond lifetimes between immobilized extracellular cadherin fragments. Even for deposited particles, the length scale of each cadherin domain lends itself to the possibility of being able to resolve (with TIRM) time-variant changes in bond length as the proteins ratchet down the length of the five domains. Hypothetically speaking, this could only be observed if very few proteins are interacting simultaneously and they have nearly the same behavior.

Current work is underway to optimize the baseline stability of colloids and incorporate cadherins into the SLB at physiologically relevant concentrations. Flow cytometry assays will be performed to quantify the concentration of cadherins on each particle, relative to a prepared bead standard. After homophilic interactions have been studied, the characteristics of heterophilic binding between various classical cadherins will be compared with previous results from homotypic adhesion and values reported in the literature. Specifically, the interaction between E-cadherin and N-cadherin, found in some studies not to exhibit an attractive potential at any $[Ca^{2+}]$,[128] will be the first heterophilic system investigated with these newly developed methods. All of these experiments will be performed at multiple cadherin surface concentrations. If cadherin clustering experiments reveal interesting phenomenon, SLBs possessing T_m>room temperature will be used to “freeze” cadherins into place on the surface following

binding, so as to inhibit lateral clustering through the significant reduction of protein mobility.

10.2 Mobility and Lateral Association of Cadherins in SLBs

Current work is underway to characterize the spatial distribution of cadherins throughout a fluid SLB in order to verify the existence of localized cadherin clusters. How the existence of clustering affects potentials and binding lifetimes will also be evaluated through TIRM experiments. In addition to qualitative confocal data, FRAP will be conducted on SLBs containing cadherins at various surface densities and for different PEG mole fractions and MWs. By systematically adjusting these parameters, optimal conditions can be found for cluster formation or inhibition. Additionally, I will attempt to establish the relationship between mobility of cadherins and other fluorescently labeled lipids within the membrane, which will be approached through capturing data from two confocal channels simultaneously. By incorporating a fluorescently tagged lipid into the SLB, recovery by the antibody-labeled cadherins and fluorescent lipid can be monitored simultaneously, provided they emit at different wavelengths but can be excited by the same laser.

10.3 Utilizing Quantum Dot-Modified Probes

Following the successful synthesis of silica core-shell QD-modified probes (described in *Section 3.4.4*), multiple experiments are planned. First, electrostatic interactions of an ensemble of probes will be measured in index-matched media. This will be performed at low (ϕ<0.01, Figure 10.1A) and near-monolayer concentrations (ϕ≈0.4 Figure 10.1B). Efforts will focus on forming ensemble particle-wall averages at

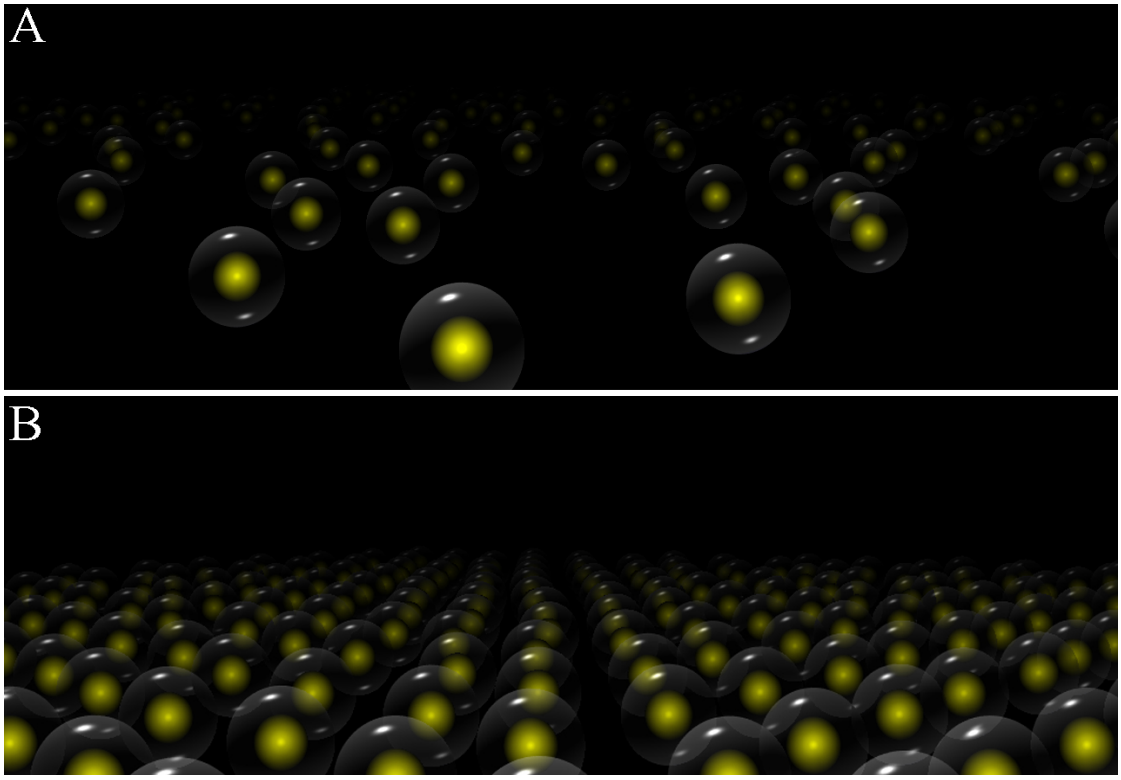

Figure 10.1. (A) Rendering of QD-modified silica particles luminescing from EW excitation within an index-matched system at a low area fraction. (B) Same system but at a high enough area fraction to yield a hexagonally close-packed electrostatic crystal.

pixel locations to spatially map out the particle-wall potential across an entire window[25] at the highest probe concentrations possible. In comparison with non-index-matched systems (conventional TIRM), index matching permits us to perform these experiments without substantial noise from scattering overlapping and intensity crosstalk between neighboring particles.[28,29]

A QD-tag will also facilitate the collection of microrheological data from an index-matched particle self-diffusing in a concentrated dispersion of index-matched nanoparticles. While acquiring MSD data, instantaneous height information can be gathered simultaneously. These novel microrheology experiments would be the first to

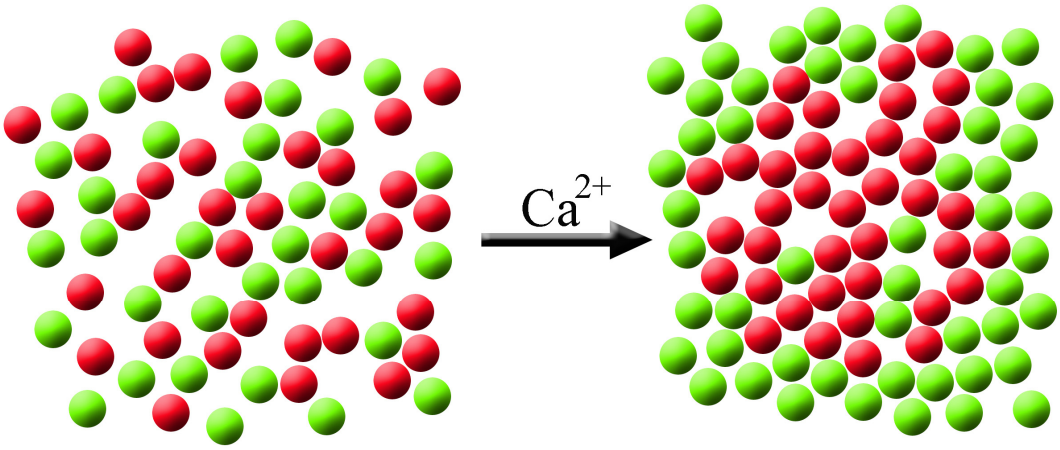

Figure 10.2 (A) Mock cell sorting experiment with QD-modified probes bearing two different types of cadherins. (e.g., green probes N-cad, red probed E-cad).

account for the separation-dependent multi-body hydrodynamics between a particle and a wall with a nanoparticle dispersion acting as the viscous media. Recent investigations of nanoparticle dispersions have yielded non-Einstein-like diffusivities.[195] By exploring the diffusion of particles at various size ratios, we may be able to help better explain the phenomenon occurring at these length scales. Furthermore, silica nanoparticles <100nm would be used in confined and index-matched systems to check the limit of detectable luminescence as a function of particle size. This information could help us design experiments wherein small QD aggregates or possibly single QDs could be used in microrheology studies[196] or for measuring biomolecular interactions.[197]

Once cadherin-cadherin potentials and binding affinities are ascertained, mock cell sorting experiments will be conducted using QD-tagged probes emitting at two different wavelengths (Figure 10.2). By forming SLBs on two differently emitting groups of QD-modified silica particles, splitting them into two populations, and binding two different cadherins (e.g., E-cad and N-cad) to each population, cell sorting can be approached

from a strictly thermodynamic standpoint. In other words, protein-protein interactions will dictate any type of phase separation, without the influence of active processes that exist in cell sorting studies with living cells. Results from this work could help to prove or disprove the DAH set forth by Steinberg nearly half a century ago.[84]

In addition, we have developed an interesting experimental idea in which an ensemble of index-matched QD-modified particles could be tracked in an EW as they diffuse above a topographically modified substrate (e.g., MgF_2) that is also index-matched. This would be the first time an EW has been used to map out physical features, and we hypothesize nanometer-scale vertical resolution would be achieved. These physical maps found with diffusing probes could be easily compared with AFM height data from the same features. In this way, we would be developing a procedure for simultaneously imaging physical and chemical heterogeneity on a surface with *kT*-scale sensitivity.

10.4 Patchy Particles and Measurements of Anisotropic Potentials

Future structures and materials for molecular electronics, photonics, sensors, and drug delivery devices will require precise self-assembly of synthetic nanostructures with reliability comparable to that of biological self-assembly.[198] One emerging approach to solve this problem is to confer upon colloids a predetermined set of building instructions in the form of anisotropically decorated domains, hence the term "patchy." This strategy would then rely on assembly of particles into specific structures based on the location of these attractive patches, liken to Lego toys. Several examples of these types of structures range from polyhedral, plate-like particles to particles having hydrophobic and

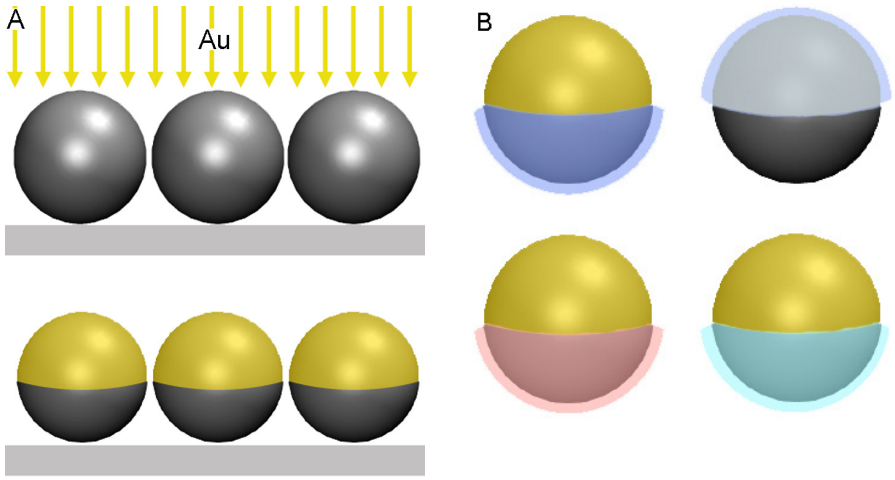

Figure 10.3. (A) Procedure for fabricating Au/silica Janus particles. (B) Functionalization of the silica hemisphere (top left), Au hemisphere (top right), or modification of the silica hemisphere with two different fluorophores (bottom two). Note that Au quenches fluorescence, so fluorophores would never be attached to the Au hemisphere.

hydrophilic poles. Because of the experimental complexity involved in synthesizing the types of particles that can assemble into 3D structures, successful demonstrations have been limited to millimeter and micrometer (100s of microns) sized particles. Theoretical modeling has predicted that these nanostructures would self-assembly properly if particles were produced in a precise manner.[198,199]

The aim of my work with anisotropic particles branches into two main areas: (i) fabricating Janus particles for studying biomolecular interactions and measuring anisotropic potentials and (ii) modification of particles with several anisotropic patches for use in self-assembly applications. Towards the first goal, I have devised an experimental approach that involves preparing particles with one hemisphere coated with Au (termed Au/silica Janus particles[200]). This is done by vapor depositing a thin Cr/Au layer atop a monolayer of dried silica colloids (Figure 10.3A). After this layer is

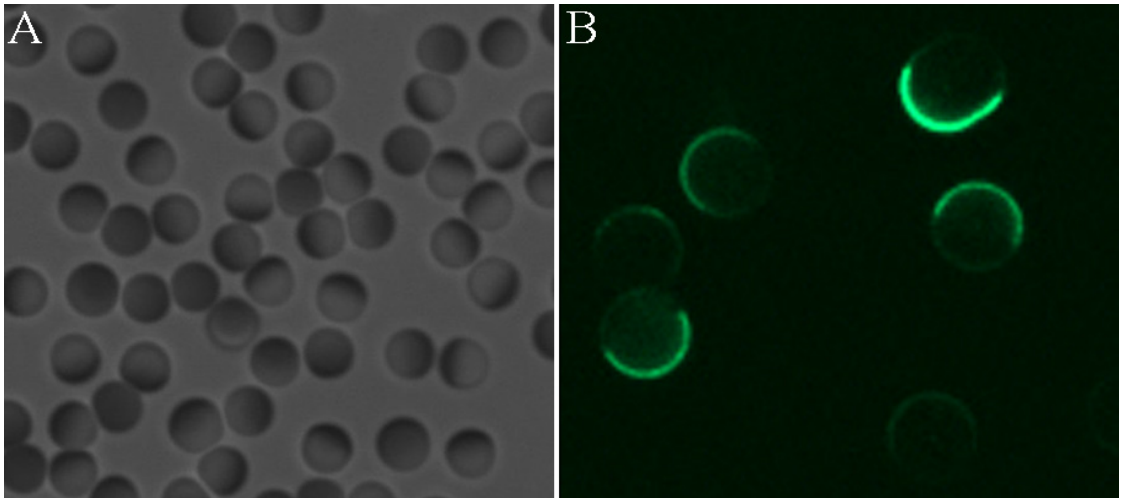

Figure 10.4. (A) Optical microscopy image of diffusing 1.5μm Au/silica Janus particles. (B) CSLM image of fluorescent silica Janus particles made through microcontact printing.

formed, the surface of the Au or silica can be modified according to need (Figure 10.3B). An image of 1.5μm Au/silica Janus particles is shown in Figure 10.4A. Janus particles can also be fabricated through microcontact printing methods. For example, a PDMS stamp inked with a reactive silane, such as APS, can be brought into contact with a dried monolayer of silica colloids. After removal and rinsing, one hemisphere of the silica particles is coated with APS, which can then be reacted with a fluorophore to yield fluorescently labeled Janus particles (Figure 10.4B). These types of particles could be used, for instance, for measuring the rotational diffusion coefficient of a particle from a series of CSLM scans.

One goal of working with patchy particles is to directly measure a potential using TIRM or VM methods. Preliminary TIRM data has been collected from Au/silica Janus particles, and intriguing preliminary results have been found. Before interpreting the data, it is important to predict (i) how a thin Au film will affect the scattering intensity as

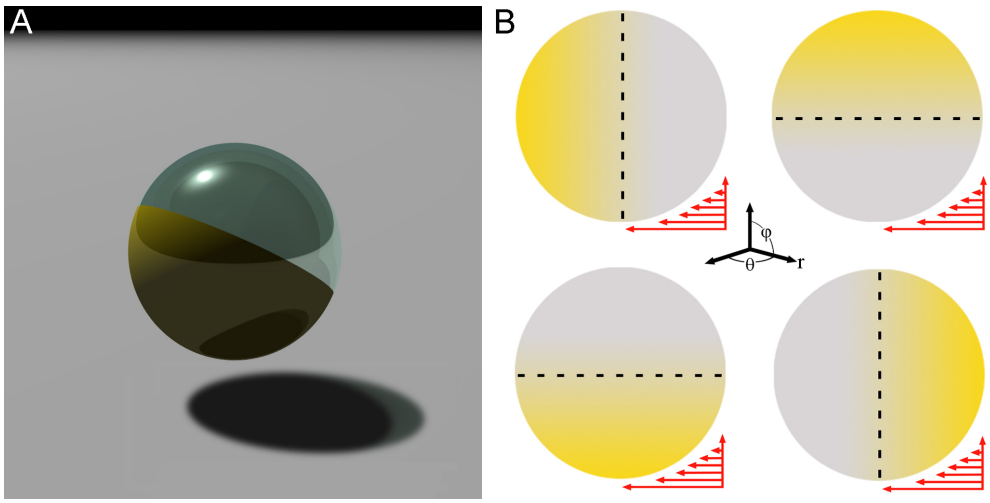

Figure 10.5 (A) Graphic illustration of a Au/silica Janus particle. (B) Important orientations of a Janus particle relative to the glancing EW.

a function of Au hemisphere orientation and (ii) if differences could be used to figure out particle-wall potentials from each half of the Janus particle. This is crucial because the dielectric properties of Au are such that even ultrathin films possess indices of refraction much different from that of silica, which yield drastically different optical properties.

Figure 10.5A is a graphic illustration of a Au/silica Janus particle, and Figure 10.5B represents the four primary optical configurations which that type of anisotropic particle will posses relative to the incoming EW and most intense scattering directions. Initial TIRM data from these Janus particles in electrostatic experiments showed two primary scattering populations. These were isolated by their relative offsets in EW intensity and, thus, relative heights (Figure 10.6).

Assuming the Au hemisphere is not truly a complete hemisphere but more of a Au cap with a circumferentially thinning thickness as it approaches the equator (similar what is drawn in Figure 10.5B), a majority of the sampling would occur with the thicker

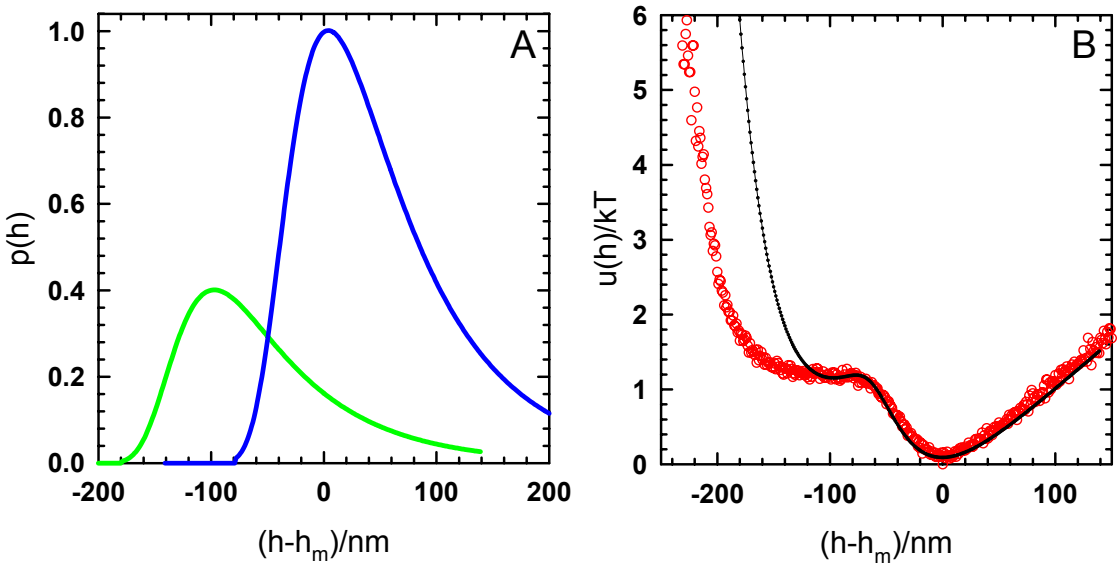

Figure 10.6 (A) Two model probability distributions with attenuated (blue) and un-attenuated (green) intensities. (B) Experimental (red circles) and model (black line) potential energy profiles of a Au/silica Janus in 1.0mM NaCl.

Au region pointing away from the wall, simply due to relative surface area. Thus, the scattering population exhibiting the lowest intensity would be the result of the Au layer adsorbing and reflecting light that would normally escape and be collected by the objective. Knowing this, the relative amount of sampling of one scattering population relative to the other is related through a Boltzmann distribution. Thus, if the Au cap were to preferentially sample in an orientation facing the wall e^2 times as often as the opposite orientation, then the scattering population with the lowest intensity would correspond to the wall region having $2kT$ more attraction relative to the remainder of the particle.

By forming two model probability distributions based on intensity attenuation, relative sampling frequency, ionic strength and particle size (Figure 10.6A), a separation-dependent potential can be generated that fits the experimental data fairly well (Figure 10.6B black curve). Further testing is required to validate the hypotheses set

forth here, but these initial experiments prove that two sampling populations could be separated based on intensity attenuation. By systematically varying the potential between the Au hemisphere and the underlying wall, a relationship that describes the relative shape and heights of the two sampling peaks can be developed. Varying this potential can be accomplished by adjusting the ionic strength or changing the thickness of the Au layer. Once figured out, experiments with two different biomolecules on each half of the particle could reveal preferential sampling for one biomolecular interaction over the other, but a much greater amount of work needs to be done in order to prove that this is a robust experimental approach to measuring anisotropic potentials.

REFERENCES

[1] D. Leckband and J. Israelachvili, Q. Rev. of Biophys. **34** (2), 105 (2001).

[2] D. Leckband, Annu. Rev. Biophys. Biomol. Struct. **29**, 1 (2000).

[3] E. Evans, Annu. Rev. Biophys. Struct. **30**, 105 (2001); C. Bustamante, Y. R. Chemla, N. R. Forde, and D. Izhaky, Annu. Rev. Biochem. **73**, 705 (2004); A. Rohrbach, C. Tischer, D. Neumayer, Ernst-Ludwig Florin, and E. H. K. Stelzer, Rev. Sci. Inst. **75** (6), 2197 (2004); J. K. H. Horber and M. J. Miles, Science **302**, 1002 (2003); M. Patra and P. Linse, Nano Lett. **6** (1), 133 (2006); M. Patra and P. Linse, Macromolecules **ASAP** (2006); S. R. Sheth and D. Leckband, Proc. Nat. Acad. Sci. USA **94**, 8399 (1997); R. A. Vijayendran and D. E. Leckband, Anal. Chem. **73**, 471 (2001).

[4] S. C. Schuster, R. V. Swanson, L. A. Alex, R. B. Bourret, and M. I. Simon, Nature **365**, 343 (1993); C. F. Wertz and M. M. Santore, Langmuir **15** (26), 8884 (1999); P. Schuck, Annu. Rev. Biophys. Biomol. Struct. **26**, 541 (1997); J. S. Shumaker-Parry and C. T. Campbell, Anal. Chem. **76**, 907 (2004).

[5] E. A. Smith and R. M.Corn, Appl. Spectrosc. **57**, 320A (2003); E. A. Smith, W. D. Thomas, L. L. Kiessling, and R. M. Corn, J. Am. Chem. Soc. **125**, 6140 (2003).

[6] R. B. Liebert and D. C. Prieve, Biophys. J. **69** (July), 66 (1995).

[7] S. K. Robertson and S. G. Bike, Langmuir **14**, 928 (1998); S. K. Robertson, A. F. Uhrick, and S. G. Bike, J. Colloid Interface Sci. **202** (1), 208 (1998); M. Singh-Zocchi, S. Dixit, V. Ivanov, and G. Zocchi, Proc. Nat. Acad. Sci. **100** (13), 7605 (2003); J. Schilling, K. Sengupta, S. Goennenwein, A. R. Bausch, and E. Sackmann, Phys. Rev. E **69**, 021901 (2004); J. Gelles, B. J. Schnapp, and M. P. Sheetz, Nature **331**, 450 (1988); D. A. Schafer, J. Gelles, M. P. Sheetz, and R. Landick, Nature **352**, 444 (1991).

[8] G. Binnig, C. F. Quate, and C. Gerber, Phys. Rev. Lett. **56** (9), 930 (1986).

[9] W. A. Ducker, T. J. Senden, and R. M. Pashley, Nature **353** (6341), 239 (1991).

[10] J. N. Israelachvili and F. R. S. D. Tabor, Proc. R. Soc. Lond. A. **331**, 19 (1972).

[11] J. N. Israelachvili, *Intermolecular and Surface Forces*, 2nd ed. (Academic Press, New York, 1992).

[12] S. Sivasankar, N. Lavrik, W. Brieher, B. Gumbiner, and D. Leckband, Biophys. J. **76** (1), A151 (1999).

[13] R. M. Hochmuth, J. Biomech. **33** (1), 15 (2000); D. E. Discher, N. Mohandas, and E. A. Evans, Science **266** (5187), 1032 (1994); M. Sato, M. J. Levesque, and R. M. Nerem, Arteriosclerosis **7** (3), 276 (1987).

[14] M. V. Bayas, A. Leung, E. Evans, and D. Leckband, Biophys. J. **90** (4), 1385 (2006).

[15] K. Svoboda and S. M. Block, Annual Review of Biophysics and Biomolecular Structure **23**, 247 (1994).

[16] K. Svoboda, C. F. Schmidt, B. J. Schnapp, and S. M. Block, Nature **365** (6448), 721 (1993).

[17] M. D. Wang, H. Yin, R. Landick, J. Gelles, and S. M. Block, Biophy. J. **72** (3), 1335 (1997); T. T. Perkins, S. R. Quake, D. E. Smith, and S. Chu, Science **264** (5160), 822 (1994).

[18] C. Bustamante, J. C. Macosko, and G. J. L. Wuite, Nature Reviews Molecular Cell Biology **1** (2), 130 (2000).

[19] R. Karlsson, A. Michaelsson, and L. Mattsson, J. Immun. Meth. **145** (1-2), 229 (1991).

[20] M. Benes, D. Billy, A. Benda, H. Speijer, M. Hof, and W. T. Hermens, Langmuir **20** (23), 10129 (2004).

[21] G. Jin, P. Tengvall, I. Lundstrom, and H. Arwin, Anal. Biochem. **232** (1), 69 (1995).

[22] S. P. Fang, H. J. Lee, A. W. Wark, and R. M. Corn, J. Am. Chem. Soc. **128** (43), 14044 (2006); H. J. Lee, A. W. Wark, and R. M. Corn, Langmuir **22** (12), 5241 (2006); A. W. Wark, H. J. Lee, and R. M. Corn, Anal. Chem. **77** (13), 3904 (2005).

[23] E. Gizeli and J. Glad, Anal. Chem. **76** (14), 3995 (2004).

[24] R. J. Davenport, G. J. L. Wuite, R. Landick, and C. Bustamante, Science **287** (5462), 2497 (2000); N. B. Becker, S. M. Altmann, T. Scholz, J. K. H. Horber, E. H. K. Stelzer, and A. Rohrbach, Phys. Rev. E **71** (2) (2005); M. M. Baksh, M. Jaros, and J. T. Groves, Nature **427** (6970), 139 (2004).

[25] H.-J. Wu, W. N. Everett, S. G. Anekal, and M. A. Bevan, submitted (2006).

[26] D. C. Prieve, Adv. Colloid Interface Sci. **82**, 93 (1999).

[27] J. C. Crocker and D. G. Grier, J. Colloid. Interface Sci. **179**, 298 (1996).

[28] H. J. Wu and M. A. Bevan, Langmuir **21** (4), 1244 (2005).

[29] H.-J. Wu, T. O. Pangburn, R. E. Beckham, and M. A. Bevan, Langmuir **21** (22), 9879 (2005).

[30] W. N. Everett, H. J. Wu, S. Anekal, H.-J. Sue, and M. A. Bevan, accepted in Biophys.J.

[31] A. Noy, Surf. Inter. Anal. **38** (11), 1429 (2006).

[32] S. K. Robertson, A. F. Uhrick, and S. G. Bike, J. Colloid and Interface Sci. **202** (1), 208 (1998).

[33] D. F. Rosenbaum and C. F. Zukoski, J. Crystal Growth **169** (4), 752 (1996); D. Rosenbaum, P. C. Zamora, and C. F. Zukoski, Phys. Rev. Lett. **76** (1), 150 (1996).

[34] V. A. Parsegian, *Van der Waals Forces: A Handbook for Biologists, Chemists, Engineers, and Physicists*. (Cambridge University Press, Cambridge, 2005).

[35] J. Mahanty and B. W. Ninham, *Dispersion Forces*. (Academic Press, New York, 1976).

[36] M. A. Bevan and D. C. Prieve, Langmuir **15** (23), 7925 (1999).

[37] B. A. Pailthorpe and W. B. Russel, J. Colloid Interface Sci. **89** (2), 563 (1982).

[38] P. A. Temple, Appl. Opt. **20** (15), 2656 (1981).

[39] D. C. Prieve and B. M. Alexander, Science **231** (4743), 1269 (1986).

[40] M. Bevan, PhD Dissertation, Carnegie Mellon University, 1999.

[41] A. J. Goldman, R. G. Cox, and H. Brenner, Chem. Engr. Sci. **22**, 637 (1967).

[42] J. P. Hansen and I. R. McDonald, *Theory of Simple Liquids*. (Academic Press, London, 1986).

[43] F. Lado, Journal of Chemical Physics **47** (11), 4828 (1967); F. Lado, Journal of Chemical Physics **49** (7), 3092 (1968); F. Lado, J. Comput. Phys. **8**, 417 (1971).

[44] A. K. Soper, Chemical Physics **202** (2-3), 295 (1996).

[45] C. G. Gray and K. E. Gubbins, *Theory of molecular fluids*. (Oxford University Press, Oxford, 1984).

[46] J. C. Crocker and D. G. Grier, Phys. Rev. Lett. **77** (9), 1897 (1996); Y. Han and D. G. Grier, Phys. Rev. Lett. **91** (3), 038302 (2003); D. G. Grier, J. Phys.: Condens. Matt. **12**, a85 (2000).

[47] T. O. Pangburn and M. A. Bevan, J. Chem. Phys. **123**, 174904 (2005).

[48] T. O. Pangburn and M. A. Bevan, J. Chem. Phys. **124**, 054712 (2006).

[49] J. Baumgartl and C. Bechinger, Europhys. Lett. **71**, 487 (2005).

[50] H. Brenner, Chem. Eng. Sci. **16** (3-4), 242 (1961).

[51] M. A. Bevan and D. C. Prieve, J. Chem. Phys. **113** (3), 1228 (2000).

[52] A. Kusumi, Y. Sako, and M. Yamamoto, Biophys. J. **65** (5), 2021 (1993).

[53] H.-J. Wu, W. N. Everett, S. G. Anekal, and M. A. Bevan, Langmuir submitted (2006).

[54] D. Axelrod, D. E. Koppel, J. Schlessinger, E. Elson, and W. W. Webb, Biophys. J.**16** (9), 1055 (1976).

[55] D. M. Soumpasis, Biophys. J. **41** (1), 95 (1983).

[56] D. W. M. Marr and A. P. Gast, Phys. Rev. E **53** (4), 4058 (1995).

[57] D. Marsh, R. Bartucci, and L. Sportelli, Biochimica Et Biophys.Act.-Biomem.**1615** (1-2), 33 (2003).

[58] E. Evans, D. J. Klingenberg, W. Rawicz, and F. Szoka, Langmuir **12** (12), 3031 (1996).

[59] F. Schreiber, Progress in Surface Science **65** (5-8), 151 (2000).

[60] E. Sackmann, Science **271** (5245), 43 (1996); H. M. McConnell, T. H. Watts, R. M. Weis, and A. A. Brian, Biochimica Et Biophysica Acta **864** (1), 95 (1986).

[61] E. Kalb, S. Frey, and L. K. Tamm, Biochimica Et Biophysica Acta **1103** (2), 307 (1992).

[62] T. M. Bayerl and M. Bloom, Biophys. J. **58** (2), 357 (1990); S. J. Johnson, T. M. Bayerl, D. C. McDermott, G. W. Adam, A. R. Rennie, R. K. Thomas, and E. Sackmann, Biophys. J. **59** (2), 289 (1991); A. Lambacher and P. Fromherz, Appl. Phys. A-Mat. Sci. Process.**63** (3), 207 (1996).

[63] M. Tanaka and E. Sackmann, Nature **437** (7059), 656 (2005); E. Sackmann and M. Tanaka, Trends in Biotechnology **18** (2), 58 (2000).

[64] H. Hillebrandt, G. Wiegand, M. Tanaka, and E. Sackmann, Langmuir **15** (24), 8451 (1999).

[65] J. H. Felgner, R. Kumar, C. N. Sridhar, C. J. Wheeler, Y. J. Tsai, R. Border, P. Ramsey, M. Martin, and P. L. Felgner, Journal of Biological Chemistry **269** (4), 2550 (1994).

[66] R. C. Macdonald, R. I. Macdonald, B. P. M. Menco, K. Takeshita, N. K. Subbarao, and L. R. Hu, Biochimica Et Biophysica Acta **1061** (2), 297 (1991).

[67] N. K. Subbarao, R. I. Macdonald, K. Takeshita, and R. C. Macdonald, Biochimica Et Biophysica Acta **1063** (1), 147 (1991); S. Y. Jung, M. A. Holden, P. S. Cremer, and C. P. Collier, Chemphyschem **6** (3), 423 (2005).

[68] A. R. Sapuri, M. M. Baksh, and J. T. Groves, Langmuir **19** (5), 1606 (2003).

[69] P. S. Cremer and S. G. Boxer, J. Phys.Chem. B **103** (13), 2554 (1999).

[70] Y. Xia and G. M. Whitesides, Angew. Chem. Int. Ed. **37**, 550 (1998).

[71] A. van Blaaderen, R. Ruel, and P. Wiltzius, Nature **385** (23), 321 (1997); W. Lee, A. Chan, M. A. Bevan, J. A. Lewis, and P. V. Braun, Langmuir **20** (12), 5262 (2004).

[72] T. R. Weikl, J. T. Groves, and R. Lipowsky, Europhys. Lett. **59** (6), 916 (2002); S. Y. Qi, J. T. Groves, and A. K. Chakraborty, Proc. Nat. Acad. Sci. **98** (12), 6548 (2001).

[73] K.-B. Lee, S.-J. Park, C. A. Mirkin, J. C. Smith, and M. Mrksich, Science **295**, 1702 (2002).

[74] J. T. Groves, N. Ulman, and S. G. Boxer, Science **275** (5300), 651 (1997).

[75] Z. A. Peng and X. G. Peng, J. Amer. Chem. Soc. **123** (1), 183 (2001).

[76] D. V. Talapin, A. L. Rogach, A. Kornowski, M. Haase, and H. Weller, Nano Lett. **1** (4), 207 (2001).

[77] R. D. Yang, S. Tripathy, Y. T. Li, and H. J. Sue, Chem. Phys. Lett. **411** (1-3), 150 (2005).

[78] M. Han, X. Gao, J. Z. Su, and S. Nie, Nature Biotechnol. **19**, 631 (2001).

[79] J. F. Brady and G. Bossis, Ann. Rev. Fluid Mech. **20**, 111 (1988).

[80] S. Anekal and M. A. Bevan, J. Chem. Phys. **122**, 034903 (2005).

[81] S. Anekal and M. A. Bevan, J. Chem. Phys. accepted (2006).

[82] J. Holtfreter, Wilhelm Roux Archiv Fur Entwicklungsmechanik Der Organismen **139** (1), 110 (1939); J. Holtfreter, Wilhelm Roux Archiv Fur Entwicklungsmechanik Der Organismen **139** (2), 227 (1939).

[83] J. Holtfreter, Journal of Morphology **80** (1), 25 (1947); J. Holtfreter, Journal of Morphology **80** (1), 57 (1947).

[84] M. S. Steinberg, Science **141** (357), 401 (1963); M. S. Steinberg, Proc. Nat. Acad. Sci. **48** (10), 1769 (1962); M. S. Steinberg, Proc. Nat. Acad. Sci. **48** (9), 1577 (1962).

[85] M. S. Steinberg, Science **137** (3532), 762 (1962).

[86] M. S. Steinberg, Develop. Biol. **180** (2), 377 (1996).

[87] S. Ringer, J. Pysiol. **11**, 79 (1890).

[88] C. Herbst, Archiv Fur Entwicklungsmechanik Der Organismen **9** (3), 424 (1900).

[89] F. O. Schmitt, Proc. Nat. Acad. Sci. **42** (11), 806 (1956).

[90] A. S. G. Curtis, Proc. R. Phys. Soc. Edinburgh **26**, 25 (1957); A. S. G. Curtis, Nature **200** (491), 1235 (1963).

[91] J. Gray, Brit. J. Exp. Biol. **3** (3), 167 (1926).

[92] L. M. J. Rinaldini, Int. Rev. Cytol. **7**, 587 (1958).

[93] D. R. Coman, Cancer Research **14** (7), 519 (1954); M. S. Steinberg, American Naturalist **92** (863), 65 (1958); A. D. Bangham, Ann. New York Acad. Sci. **116** (A3), 945 (1964).

[94] J. P. Thiery, R. Brackenbury, U. Rutishauser, and G. M. Edelman, J.Biol. Chem. **252** (19), 6841 (1977).

[95] M. Takeichi, J. Cell Biol.**75** (2), 464 (1977).

[96] D. Sipp and M. Takeichi, International Journal of Dev. Biol. **48** (5-6), 387 (2004).

[97] M. Takeichi, Curr. Opn. Cell Biol. **7** (5), 619 (1995).

[98] B. M. Gumbiner, J. Cell Bio. **148** (3), 399 (2000); B. M. Gumbiner, Cell **84** (3), 345 (1996).

[99] D. Godt and U. Tepass, Nature **395** (6700), 387 (1998); M. Takeichi, Science **251** (5000), 1451 (1991); A. Gonzalez-Reyes and D. St Johnston, Development **125** (18), 3635 (1998).

[100] A. Makrigiannakis, G. Coukos, M. Christofidou-Solomidou, B. J. Gour, G. L. Radice, O. Blaschuk, and C. Coutifaris, Amer. J. Path. **154** (5), 1391 (1999); L. L. Ong, N. Kim, T. Mima, L. Cohen-Gould, and T. Mikawa, Developmental Biology **193** (1), 1 (1998).

[101] D. Leckband and A. Prakasam, Ann. Rev. Biomed. Eng. **8**, 259 (2006).

[102] O. Y. Laur, J. Klingelhofer, R. B. Troyanovsky, and S. M. Troyanovsky, Arch. Biochem. and Biophys. **400** (1), 141 (2002); W. S. Shan, H. Tanaka, G. R. Phillips, K. Arndt, M. Yoshida, D. R. Colman, and L. Shapiro, J. Cell Biol. **148** (3), 579 (2000); K. Tamura, W. S. Shan, W. A. Hendrickson, D. R. Colman, and L. Shapiro, Neuron **20** (6), 1153 (1998); A. Nose, K. Tsuji, and M. Takeichi, Cell **61** (1), 147 (1990).

[103] T. J. Boggon, J. Murray, S. Chappuis-Flament, E. Wong, B. M. Gumbiner, and L. Shapiro, Science **296** (5571), 1308 (2002).

[104] B. Nagar, M. Overduin, M. Ikura, and J. M. Rini, Nature **380** (6572), 360 (1996).

[105] S. Pokutta, K. Herrenknecht, R. Kemler, and J. Engel, Euro. J. Biochem.**223** (3), 1019 (1994).

[106] A. W. Koch, S. Pokutta, A. Lustig, and J. Engel, Biochemistry **36** (25), 7697 (1997).

[107] R. A. Foty and M. S. Steinberg, Dev. Biol. **278** (1), 255 (2005).

[108] M. Takeichi, Development **102** (4), 639 (1988).

[109] R. J. Detrick, D. Dickey, and C. R. Kintner, Neuron **4** (4), 493 (1990).

[110] J. T. Davies and E. K. Rideal, *Interfacial Phenomenon*. (Academic Press, New York, 1963).

[111] R. A. Foty, C. M. Pfleger, G. Forgacs, and M. S. Steinberg, Development **122** (5), 1611 (1996).

[112] D. Duguay, R. A. Foty, and M. S. Steinberg, Dev. Biol. **253** (2), 309 (2003).

[113] A. K. Harris, Journal of Theor. Biol. **61** (2), 267 (1976).

[114] G. W. Brodland and H. H. Chen, J. Biomech. **33** (7), 845 (2000).

[115] G. W. Brodland, J. Biomech. Eng.-Trans. ASME **124** (2), 188 (2002).

[116] J. A. Glazier and F. Graner, Phys. Rev. E **47** (3), 2128 (1993).

[117] A. Mochizuki, Y. Iwasa, and Y. Takeda, Journal of Theor. Biol. **179** (2), 129 (1996).

[118] J. P. Rieu, N. Kataoka, and Y. Sawada, Phys. Rev. E **57** (1), 924 (1998).

[119] F. Graner and Y. Sawada, J. Theor. Biol. **164** (4), 477 (1993); F. Graner, J. Theor. Biol. **164** (4), 455 (1993).

[120] E. Palsson, Fut. Gen. Comp. Syst. **17** (7), 835 (2001).

[121] B. Zhu, S. Chappuis-Flament, E. Wong, I. E. Jensen, B. M. Gumbiner, and D. Leckband, Biophys. J. **84** (6), 4033 (2003).

[122] E. Perret, A. Leung, H. Feracci, and E. Evans, Proc. Nat. Acad. Sci. **101** (47), 16472 (2004).

[123] M. Balsera, S. Stepaniants, S. Izrailev, Y. Oono, and K. Schulten, Biophys. J. **73** (3), 1281 (1997); G. Hummer and A. Szabo, Biophys. J. **85** (1), 5 (2003).

[124] E. Evans and K. Ritchie, Biophys. J.**72** (4), 1541 (1997).

[125] G. I. Bell, Science **200** (4342), 618 (1978).

[126] E. Evans, Ann. Rev. Biophys. Biomol. Struct. **30**, 105 (2001).

[127] W. Baumgartner, P. Hinterdorfer, W. Ness, A. Raab, D. Vestweber, H. Schindler, and D. Drenckhahn, Biophys. J.**76** (1), A351 (1999); W. Baumgartner, P. Hinterdorfer, W. Ness, A. Raab, D. Vestweber, H. Schindler, and D. Drenckhahn, Proc. Nat. Acad. Sci. **97** (8), 4005 (2000).

[128] P. Panorchan, J. P. George, and D. Wirtz, J. Mol. Biol. **358** (3), 665 (2006); P. Panorchan, M. S. Thompson, K. J. Davis, Y. Tseng, K. Konstantopoulos, and D. Wirtz, J. Cell Sci. **119** (1), 66 (2006).

[129] C. M. Niessen and B. M. Gumbiner, J. Cell Biol. **156** (2), 389 (2002).

[130] R. Langer and N. A. Peppas, AIChE Journal **49** (12), 2990 (2003); J. L. West and N. J. Halas, Ann. Rev. Biomed. Eng. **5**, 285 (2003).

[131] M. Lu, M. A. Bevan, and D. M. Ford, J. Chem. Phys. **122**, 224710 (2005).

[132] M. L. Nucci, R. Shorr, and A. Abuchowski, Adv. Drug Delivery .Rev. **6** (2), 133 (1991).

[133] J. H. Lee, H. B. Lee, and J. D. Andrade, Prog. Poly. Sci. **20** (6), 1043 (1995); J. D. Andrade and V. Hlady, Adv. Poly. Sci. **79**, 1 (1986); J. S. Tan and P. A. Martic, J. Colloid Inter. Sci. **136** (2), 415 (1990); K. L. Prime and G. M. Whitesides, J. Am. Chem. Soc. **115** (23), 10714 (1993); C. Schroen, M. A. C. Stuart, K. V. Maarschalk, A. Vanderpadt, and K. Vantriet, Langmuir **11** (8), 3068 (1995); W. R. Gombotz, W. Guanghui, T. A. Horbett, and A. S. Hoffman, J. Biomed. Mater. Res. **25** (12), 1547 (1991); Y. Ikada, Adv. Poly. Sci. **57**, 103 (1984).

[134] J. Lee, P. A. Martic, and J. S. Tan, J. Colloid Inter. Sci. **131** (1), 252 (1989).

[135] M. Amiji and K. Park, J. Biomater. Sci. **4** (3), 217 (1993).

[136] T. McPherson, A. Kidane, I. Szleifer, and K. Park, Langmuir **14** (1), 176 (1998).

[137] I. Szleifer, Curr. Opn. Colloid Inter. Sci. **1** (3), 416 (1996); I. Szleifer and M. A. Carignano, in *Advances in Chemical Physics, Vol Xciv* (1996), Vol. 94, pp. 165.

[138] M. A. Bevan and D. C. Prieve, Langmuir **16** (24), 9274 (2000).

[139] M. Malmsten, K. Emoto, and J. M. Van Alstine, J. Colloid Inter. Sci. **202** (2), 507 (1998).

[140] K. D. Pavey and C. J. Olliff, Biomaterials **20** (9), 885 (1999).

[141] R. J. Green, M. C. Davies, C. J. Roberts, and S. J. B. Tendler, J. Biomed. Mater. Res. **42** (2), 165 (1998).

[142] D. Leckband, S. Sheth, and A. Halperin, J. Biomater. Sci. **10** (10), 1125 (1999).

[143] G. J. Fleer, M. A. C. Stuart, J. M. H. M. Scheutjens, T. Cosgrove, and B. Vincent, *Polymers at Interfaces*. (Chapman & Hall, New York, 1993).

[144] P. M. Claesson, E. Blomberg, J. C. Froberg, T. Nylander, and T. Arnebrant, Adv. Colloid Inter. Sci. **57**, 161 (1995).

[145] D. Leckband and S. Sivasankar, Coll. Surf. B **14** (1-4), 83 (1999).

[146] J. N. Israelachvili, Faraday Disc., 20 (1978); J. N. Israelachvili and G. E. Adams, J. Chem.Soc.-Faraday Trans. I **74**, 975 (1978).

[147] W. A. Ducker, T. J. Senden, and R. M. Pashley, Langmuir **8** (7), 1831 (1992).

[148] S. R. Sheth and D. Leckband, Proc. Nat. Acad. Sci. **94** (16), 8399 (1997)

.

[149] N. V. Efremova, S. R. Sheth, and D. E. Leckband, Langmuir **17** (24), 7628 (2001).

[150] M. A. Bevan, S. N. Petris, and D. Y. C. Chan, Langmuir **18** (21), 7845 (2002); M. A. Bevan and P. J. Scales, Langmuir **18** (5), 1474 (2002).

[151] S. L. McGurk, R. J. Green, G. H. W. Sanders, M. C. Davies, C. J. Roberts, S. J. B. Tendler, and P. M. Williams, Langmuir **15** (15), 5136 (1999).

[152] S. Chandrasekhar, Rev. Mod. Phys. **15** (1), 1 (1943); P. Hanggi and P. Talkner, Rev. Mod. Phys. **62** (2), 251 (1990).

[153] D. Bendedouch and S. H. Chen, J. Phys. Chem. **87**, 1473 (1983).

[154] R. Kurrat, J. E. Prenosil, and J. J. Ramsden, J. Colloid Inter.Sci. **185** (1), 1 (1997).

[155] R. R. Dagastine, M. Bevan, L. R. White, and D. C. Prieve, J. Adhes. **80** (5), 365 (2004).

[156] A. A. Potanin and W. B. Russel, Phys. Rev. E **52** (1), 730 (1995).

[157] K. L. Johnson, K. Kendall, and A. D. Roberts, Proc. R. Soc. Lond. A **324**, 301 (1971).

[158] J. D. Feick and D. Velegol, Langmuir **18** (9), 3454 (2002).

[159] D. A. Hammer and S. M. Apte, Biophys. J.**63** (1), 35 (1992).

[160] J. A. Baker and J. C. Berg, Langmuir **4**, 1055 (1988).

[161] C. F. Wertz and M. M. Santore, Langmuir **17** (10), 3006 (2001).

[162] A. K. van Helden, J. W. Jansen, and A. Vrij, J. Colloid Interface Sci. **81** (2), 354 (1981).

[163] A. Ulman, Chem. Rev. **96**, 1553 (1996).

[164] J. S. Bonifacino and B. S. Glick, Cell **116** (2), 153 (2004); L. V. Chernomordik and M. M. Kozlov, Ann. Rev. Biochem. **72**, 175 (2003).

[165] J. Y. Walz and E. Ruckenstein, J. Phys. Chem. B **103** (35), 7461 (1999); Y. Kaizuka and J. T. Groves, Biophys. J. **86** (2), 905 (2004); M. Kraus and U. Seifert, Journal De Physique Ii **4** (7), 1117 (1994); U. Seifert, Phys. Rev. E **49** (4), 3124 (1994).

[166] Y. Kaizuka and J. T. Groves, Phys. Rev. Lett. **96** (11) (2006); A. P. Wong and J. T. Groves, J. Am. Chem. Soc. **123** (49), 12414 (2001); J. B. Manneville, P. Bassereau, S. Ramaswamy, and J. Prost, Phys. Rev. E **6402** (2) (2001); R. Hirn, T. M. Bayer, J. O. Radler, and E. Sackmann, Faraday Discus., 17 (1998).

[167] A. K. Prakasam, V. Maruthamuthu, and D. E. Leckband, Proc. Nat. Acad. Sci. **103** (42), 15434 (2006).

[168] S. Hirano, S. T. Suzuki, and C. Redies, Frontiers in Bioscience **8**, D306 (2003); Z. Lele, A. Folchert, M. Concha, G. J. Rauch, R. Geisler, F. Rosa, S. W. Wilson, M. Hammerschmidt, and L. Bally-Cuif, Development **129** (14), 3281 (2002); G. L. Radice, H. Rayburn, H. Matsunami, K. A. Knudsen, M. Takeichi, and R. O. Hynes, Dev. Biol. **181** (1), 64 (1997).

[169] O. Bozdagi, W. Shan, H. Tanaka, D. L. Benson, and G. W. Huntley, Neuron **28** (1), 245 (2000); H. Tanaka, W. S. Shan, G. R. Phillips, K. Arndt, O. Bozdagi, L. Shapiro, G. W. Huntley, D. L. Benson, and D. R. Colman, Neuron **25** (1), 93 (2000); V. Vasioukhin, C. Bauer, M. Yin, and E. Fuchs, Cell **100** (2), 209 (2000); C. L. Adams, Y. T. Chen, S. J. Smith, and W. J. Nelson, J.Cell Biol. **142** (4), 1105 (1998); C. L. Adams, W. J. Nelson, and S. J. Smith, J.Cell Biol. **135** (6), 1899 (1996).

[170] W. N. Everett, H. J. Wu, S. G. Anekal, H. J. Sue, and M. A. Bevan, Biophys. J. **92** (3), 1005 (2007).

[171] E. M. Lifshitz, J. Exp. Theor. Phys. USSR **29**, 94 (1955).

[172] B. V. Derjaguin, S. S. Dukhin, and V. N. Shilov, Adv.Colloid Interface Sci. **13**, 41 (1980).

[173] N. J. Harrick, *Internal Reflection Spectroscopy*. (Wiley, New York, 1967).

[174] D. Axelrod, T. P. Burghardt, and N. L. Thompson, Ann. Rev. Biophy. Bioeng. **13**, 247 (1984).

[175] E. Stenberg, B. Persson, H. Roos, and C. Urbaniczky, J. Colloid Inter. Sci. **143, No. 2, May 1991** (2), 513 (1991).

[176] D. C. Prieve, F. Luo, and F. Lanni, Faraday Disc. **83**, 297 (1987).

[177] J. M. Brockman, B. P. Nelson, and R. M. Corn, Annu. Rev. Phys. Chem. **51**, 41 (2000); X. Qu, D. Wu, L. Mets, and N. F. Scherer, Proc. Nat. Acad. Sci. **101** (31), 11298 (2004).

[178] J. Y. Walz, Curr.Opn. Colloid Inter. Sci. **2** (6), 600 (1997).

[179] S. G. Bike and D. C. Prieve, Int. J. Multiphase Flow **16** (4), 727 (1990); J. Y. Walz and D. C. Prieve, Langmuir **8**, 3043 (1992); D. L. Sober and J. Y. Walz, Langmuir **11** (7), 2352 (1995); D. Rudhardt, C. Bechinger, and P. Leiderer, Phys. Rev. Lett. **81** (6), 1330 (1998).

[180] N. A. Frej and D. C. Prieve, J. Chem. Phys. **98** (9), 7552 (1993); E. S. Pagac, R. D. Tilton, and D. C. Prieve, Chem. Eng. Comm. **148**, 105 (1996).

[181] W. N. Everett, H.-J. Wu, S. G. Anekal, H.-J. Sue, and M. A. Bevan, Bio. J. **92**, 1005 (2007).

[182] H. Chew, D. S. Wang, and M. Kerker, Appl. Opt. **18**, 2679 (1979).

[183] D. C. Prieve and J. Y. Walz, Appl. Opt. **32** (9), 1629 (1993).

[184] C. T. McKee, S. C. Clark, J. Y. Walz, and W. A. Ducker, Langmuir **21** (13), 5783 (2005).

[185] E. Eremina, N. Grishina, Y. Eremin, L. Helden, and ThomasWriedt, J. Opt. A: Pure Appl. Opt. **8**, 999 (2006); N. Rieflera, E. Ereminaa, C. Hertleinb, Laurent Heldenb, Y. Ereminc, T. Wriedtd, and C. Bechinger, J. Quant. Spectrosco. Rad.Trans. in press (2007).

[186] C. M. Zettner and M. Yoda, Exp. Fluids **34**, 115 (2003); S. Pouya, M. Koochesfahani, P. Snee, M. Bawendi, and D. Nocera, Exp. Fluids **39**, 784 (2005); P. Huang, J. S. Guasto, and K. S. Breuer, J. Fluid Mech. **566**, 447 (2006).

[187] J. M. Nam, S. J. Park, and C. A. Mirkin, J. Am. Chem. Soc. **124** (15), 3820 (2002).

[188] L. Helden, R. Roth, G. H. Koenderink, P. Leiderer, and C. Bechinger, Phys. Rev. Lett. **90** (4), 048301 (2003).

[189] P. A. Temple, Appl. Opt. **20** (15), 2656 (1981).

[190] I. Chung, J. B. Witkoskie, J. P. Zimmer, J. Cao, and M. G. Bawendi, Phys. Rev. B **75**, 045311 (2007).

[191] K. T. Shimizu, R. G. Neuhauser, C. A. Leatherdale, S. A. Empedocles, W. K. Woo, and M. G. Bawendi, Phys. Rev. B **63**, 205316 (2001).

[192] J. Radler and E. Sackmann, J. Phys. II France **3**, 727 (1993).

[193] A. Sarkar, R. B. Robertson, and J. M. Fernandez, Proc. Nat. Acad. Sci. USA **101** (35), 12882 (2004).

[194] R. E. Beckham and M. A. Bevan, in preparation (2007).

[195] M. E. Mackay, T. T. Dao, A. Tuteja, D. L. Ho, B. Van Horn, H. C. Kim, and C. J. Hawker, Nat. Mater. **2** (11), 762 (2003).

[196] S. Yamada, D. Wirtz, and S. C. Kuo, Biophys. J. **78** (4), 1736 (2000); T. G. Mason, K. Ganesan, J. H. vanZanten, D. Wirtz, and S. C. Kuo, Phys. Rev. Lett. **79** (17), 3282 (1997).

[197] J. Choi, Y. H. Zhao, D. Y. Zhang, S. Chien, and Y. H. Lo, Nano Lett. **3** (8), 995 (2003).

[198] Z. L. Zhang and S. C. Glotzer, Nano Lett. **4** (8), 1407 (2004).

[199] Z. L. Zhang, A. S. Keys, T. Chen, and S. C. Glotzer, Langmuir **21** (25), 11547 (2005); S. C. Glotzer, Science **306** (5695), 419 (2004).

[200] K. E. Paul, M. Prentiss, and G. M. Whitesides, Adv. Funct. Mater. **13** (4), 259 (2003); J. C. Love, B. D. Gates, D. B. Wolfe, K. E. Paul, and G. M. Whitesides, Nano Lett. **2** (8), 891 (2002).

[201] A. S. Barnard, Nat. Mater. **5** (4), 245 (2006).

[202] T. J. Brunner, P. Wick, P. Manser, P. Spohn, R. N. Grass, L. K. Limbach, A. Bruinink, and W. J. Stark, Environ. Sci. Tech. **40** (14), 4374 (2006).

APPENDIX A

A.1 Cytotoxicity of ZnO Nanocrystals

The surge in nanotechnology research over the past decade has led to an increased awareness of how advancements can have both positive and negative consequences. Often, economic and technological gains may outweigh any legitimate concern regarding an innovation's impact on society—at least in the short-term. More specifically, researchers and public officials have started turning their attention towards nanomaterial-related health hazards[201] and how to establish the proper framework from which generalizations can be drawn that relate the danger of a material to its physical properties (e.g., size, shape, surface chemistry). The difficulty lies in the fact that there are too many variables to accurately predict *a priori* how a living cell will react to a nanomaterial, or whether results from animal models and *in vitro* cell experiments can be extrapolated back to humans. Our current level of exposure to nanomaterials in the products we buy and industrial waste we produce is, of course, expected to increase significantly in the near future; hence, these concerns are valid and need our immediate attention.

This section of my dissertation addresses the first study of size- and concentration-dependent effects of ZnO nanoparticles on cells and tissues via the exposure of a cultured tumor cell line (PC12 cells) to a relevant range of ZnO particle sizes and concentrations. Currently, nanometer-sized ZnO particles (~50 to 100nm) can be found in many sunscreens, cosmetics, and dental products, but few studies have been

conducted[202] to determine any potential hazards posed by a continually reduction in ZnO particle size. If it is cost-effective, manufacturers in many areas of industry either introduce nanomaterials into their products or reduce the size of the nano-ingredient in order to "improve" performance. In the case of the latter, there is normally little concern over how this change in physical dimension could lead to unintended consequences, since the ingredient composition and concentration remain unaltered. While the assumption of bulk property values at length scales greater than 10s of nanometers is reasonable for most materials, a reduction in size down to <20nm causes the material to behave in a much different way, especially since this length scale approaches that of biomolecules such as proteins. For this specific reason, I am performing this research to help elucidate any hazardous effects that may result from reducing ZnO down to the smallest particle size that will still yield the necessary adsorption properties desired by product manufactures for UV absorbing applications.

A.1 ZnO Nanoparticle Preparation and Characterization

The most important aspect of this study is that a synthesis method was devised to control ZnO aggregate size in aqueous media from the micrometer range down to the single particle level (~3nm). This was accomplished through the incorporation of an amphiphilic surfactant called polyvinyl pyrrolidone (PVP) during ZnO synthesis and after purification (discussed in more detail in *Section 3.4.3*). By varying the ratio of PVP to ZnO from 0:1 to 300:1, a wide range of aggregate sizes was produced, all the way down to the single QD level (Figure A1). Importantly, aggregate and particle size was quantified with dynamic light scattering (DLS), and other characterization techniques

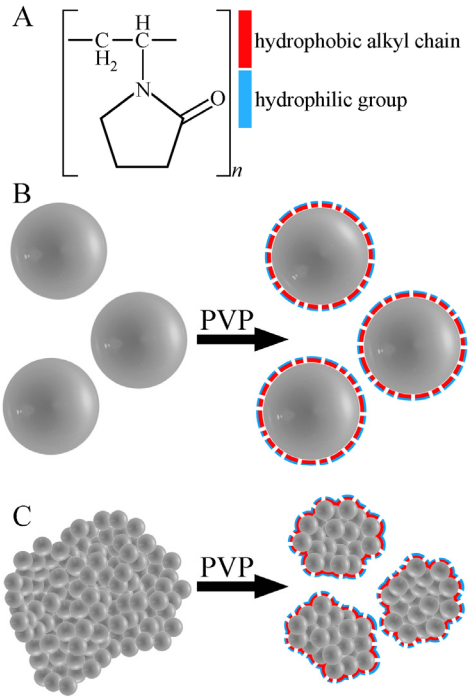

Figure A1. (A) Chemical structure of PVP showing its amphiphilic nature. (B) Schematic illustrating stabilization of ZnO QDs with PVP down to the single-particle level. (C) Dissolution of large aggregates into smaller aggregates following the addition of PVP.

were employed to ensure that ZnO was not chemically or structurally modified in any way.

Figure A2 shows X-ray diffraction (XRD) data with a high-resolution TEM image inset of ZnO synthesized in the presence of PVP. The atomic structure remains unchanged between the synthesis routes with (blue) and without (black) PVP, suggesting the polymer only acts as a surfactant during ZnO formation and does not interfere with the final chemical composition. Broad peaks also point to small crystal domain sizes, consistent with existence of single nanoparticles.

In addition to the atomic structure being examined, the spectral properties of the dispersion were checked with UV/vis adsorption spectroscopy to determine whether or

not the addition of PVP at high concentrations interferes with quantum confinement. Although this is not particularly important for cytotoxicity studies, it does show that transforming ZnO into a water-soluble form can be accomplished through a facile approach without affecting the distinctive opto-electrical properties of the material; hence, ZnO could be introduced into water-based composite systems. UV/vis spectra are show in Figure A3, and they reveal that PVP-stabilized ZnO exhibits nearly identical wavelength-dependent absorption characteristics compared with purified and unpurified ZnO QDs.

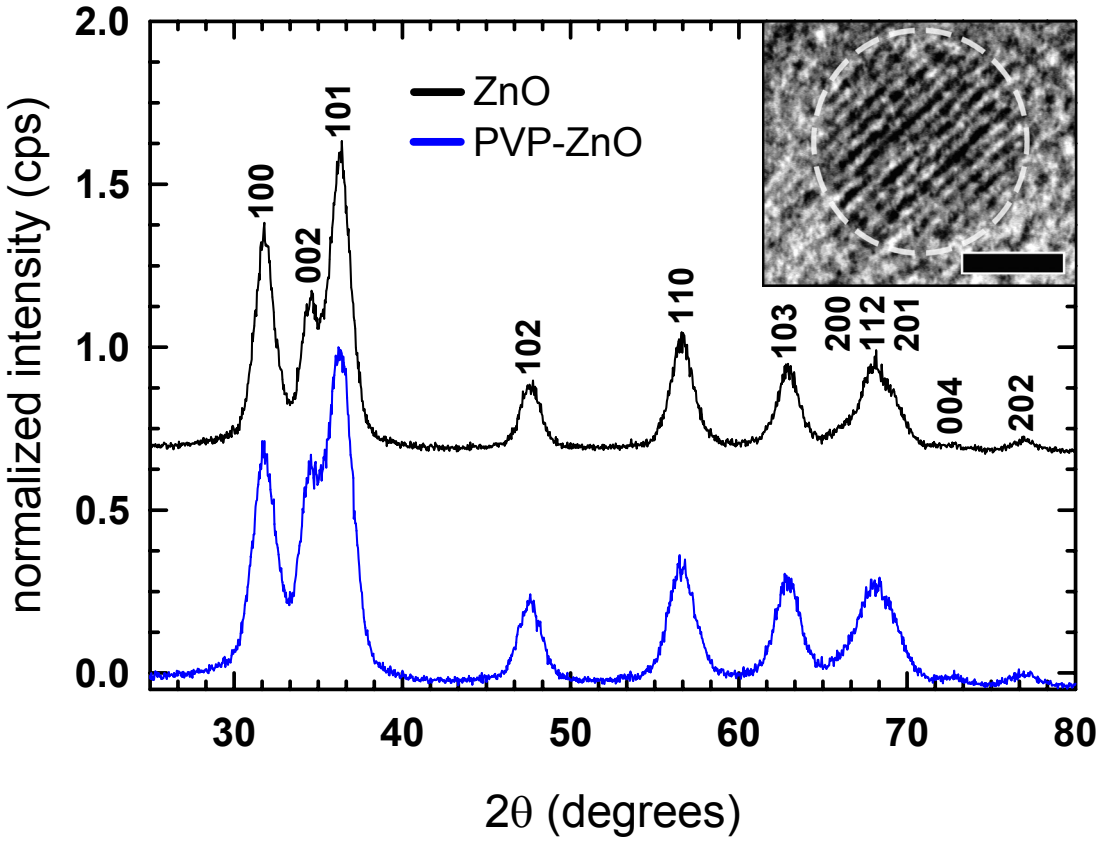

Figure A2. XRD data from ZnO powder displaying all of the typical peak locations of the Wurtzite structure. Inset is a high-resolution TEM image of a single ZnO QD, with the scale bar=2nm.

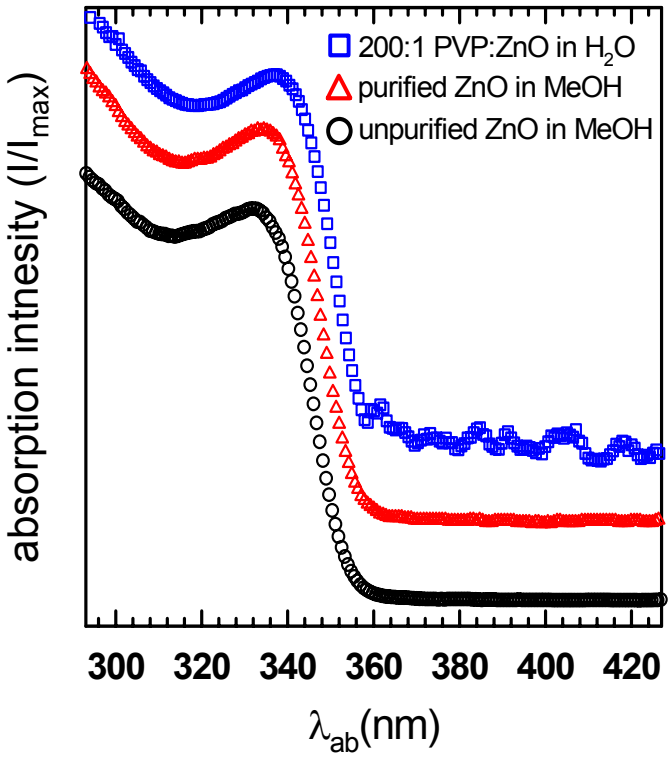

Figure A3. UV/vis spectra from PVP-modified ZnO and unmodified ZnO.

Particle and aggregate sizes were determined with DLS. Diluted samples of 300:1, 200:1, and 150:1 PVP to ZnO were sized, with data given in Figure A4. Individual QDs were observed in the 300:1 and 200:1 samples, and a PVP solution was tested to ensure that PVP molecule scattering was not skewing the data. Results show that PVP displays a peak at 1.8nm, which is near the maximum reliable resolution of the technique. 300:1 and 200:1 samples were run at three different concentrations, and the results were identical in all cases for each sample type. These results, along with evidence provided by UV/vis and XRD, point to the definite existence of ZnO QDs at the single-particle level. To date, single QDs dispersed in an aqueous phase have not been shown in any of the open literature

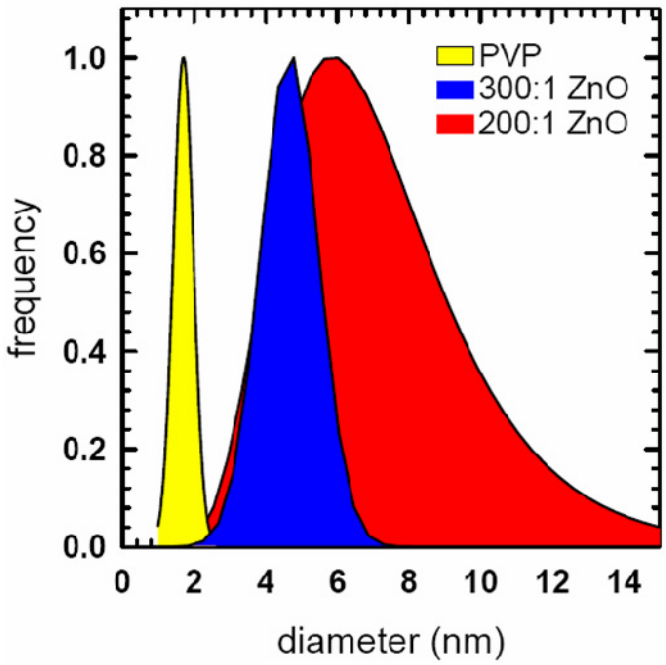

Figure A4. Dynamic light scattering data proving the existence of individual ZnO QDs for 300:1 ratio of PVP to ZnO. Results from the 200:1 dispersion point to slightly larger aggregates among individually dispersed QDs.

Not shown in Figure A4 are results from particle sizing of 150:1 samples. The aggregates exhibited a large polydispersity with a bimodal distribution: one peak at 150nm and another at 50nm. DLS the 100:1 sample was conducted, but meaningful results were not obtained because aggregates were >1μm, so sedimentation led to misrepresentative data. Optical microscopy observation of this sample revealed aggregate sizes on the order of 1 to 4μm.

One very important consideration when performing cell cytotoxicity experiments with synthesized particulates is to account for the presence of excess free ions remaining from the reaction, as certain ions can dramatically affect the viability of cells. In order to remove that variable from the testing protocol and only examine the effects of ZnO on

cellular function, free ions were systematically removed from the ZnO dispersions. K and Zn ions are of particular concern here, since they are byproducts of the synthesis. A rinsing procedure was developed to remove free ions from the dispersion without losing ZnO nanoparticles. By "crashing out" the nanoparticles in hexane, free ions could be rinsed away through several cycles of crashing and restabilization in methanol.

Figure A5 gives atomic absorption spectroscopy survey data of K^+ after successive rinse cycles. The [K^+] dropped nearly three orders of magnitude nearing the detection limit of the instrument after only four rinses. Obviously, any free Zn^{2+} in the solution would be removed as well, so the levels of K^+ are indicative of every other soluble contaminant in the dispersion.

After thorough characterization of the particle dispersion, cell cytotoxicity experiments were conducted on PC12 cells (Figure A6). The PC12 cell line is derived

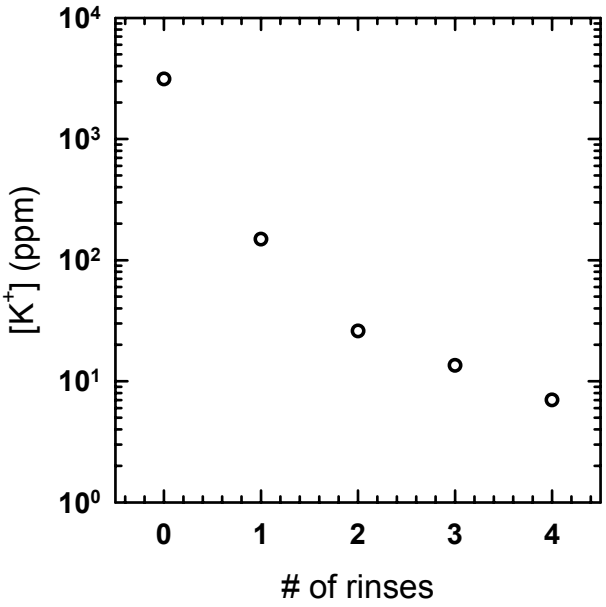

Figure A5. Atomic absorption spectroscopy data tracing potassium levels following each rinse cycle.

from cloned rat adrenal pheochromocytoma, and it is a useful model for studying neuronal development, since they can be induced to differentiate into a neural phenotype following exposure to nerve growth factor (NGF). Specifically, these cells have been successfully utilized in studies of gene regulation and cellular development.

PC12 cells were maintained in RPMI media supplemented with 10% equine serum, 5% FBS, and 1% penestrep (antibacterial agent) and kept in an incubator at 37ºC with 5% CO_2. In all instances, media was replaced every 2-3 days. For all experiments, PC12 cells were plated at a concentration of 300,000 cells/well in six-well plates that had been coated with laminin (5mg/ml) overnight. Cells were maintained throughout the course of these experiments in media containing 25ng/ml of NGF and allowed to differentiate for 7 days for all cell-counting studies and for measurement of lactose dehydrogenase (LDH) activity. This incubation period also provided adequate levels of protein for DNA fragmentation studies. Following 7 days of differentiation, proliferation, and maturation, the cells were dosed with the appropriate amounts of ZnO and left for 1 day.

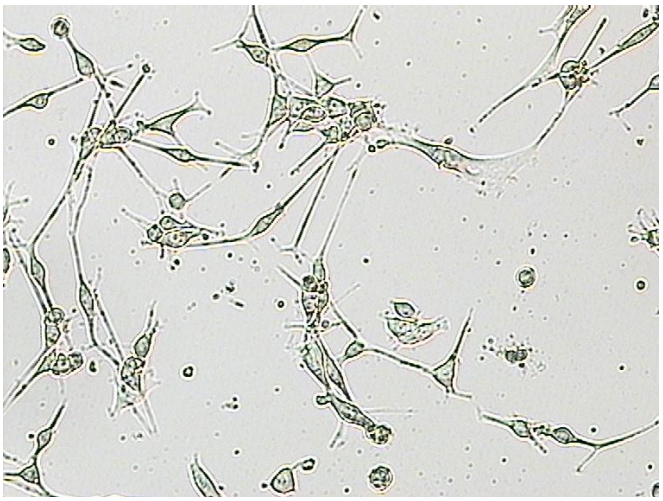

Figure A6. Optical microscopy image of differentiated PC12 cells.

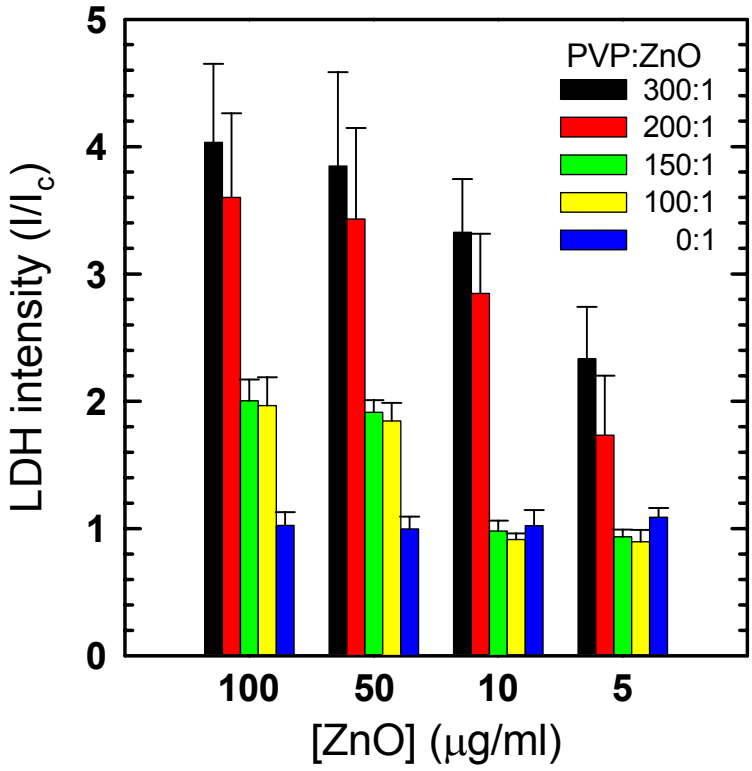

Figure A7 Results from LDH assays revealing cytotoxic effects down to 5μg/ml for ZnO dispersions with individual QDs.

Supernatant was collected from each well and analyzed for LDH levels. When cells begin to die, their membrane integrity is weakened and permeability to most molecules significantly increased. One cell death marker is LDH, which can be easily tested for using a covalently linked dye and a transmission absorption plate reader. Results from LDH studies are presented in Figure A7. Data has been normalized against the control wells for each data set. The sample number, *n*, is between 20 and 25 for each tested condition. For the 300:1 and 200:1 PVP to ZnO ratios, cell death is marked, and present even at 5μg/ml. As proven before, these preparations lead to single ZnO QDs in the dispersion, thus the cytotoxicity of ZnO is substantially increased with particles are

dropped to low nanometer length scales. Note that cells were also exposed to concentrated PVP at levels above those seen for the 300:1 and 200:1 samples. Data indicate that the free PVP has a marginal affect on the viability of cells.

The precise mechanism leading to cell death has not been determined. What is important to point out in this study is that cells responded to ZnO levels as low at 5µg/ml, which is at least one order of magnitude lower than that reported for nanoparticle cytotoxicity of any material including those synthesized from heavy metals such as Cd. Current work is underway to quantify the degree of DNA fragmentation vs. protein concentration. In this way, the mechanism of death, apoptosis or necrosis, can be determined. Preliminary data from DNA fragmentation assays point towards apoptotic pathways lead to the eventual lysis of these cells in the presence of ZnO at all concentrations but not at every particulate size.

VITA

William Neil Everett graduated with a Bachelor's degree in Biomedical Engineering from Texas A&M University in December 2000 as part of the "Fast-track Program." In December 2002, he graduated with a Master of Science degree in Biomedical Engineering. His thesis work was guided by Professor Jay D. Humphrey, and it concerned the development and testing of a bi-plane video microscopy technique for measuring 3D surface strains in arterial bifurcations. In 2002, he simultaneously enrolled in the doctoral program in mechanical engineering, with Professor Hung-Jue Sue as his advisor, and began work for one year as a research scientist at the Institute of Materials Research and Engineering in Singapore. After returning to the U.S. in 2003, he joined the Materials Science and Engineering Program and began to be co-advised by Drs. Michael A. Bevan and H.-J. Sue, starting in the spring of 2005. Neil received his Ph.D. in Materials Science and Engineering through the Department of Mechanical Engineering on August 10, 2007. His current research interests are: colloidal and interfacial science, protein and membrane biophysics, colloidal assembly, microscopy techniques, and microfabrication for biomedical applications.

He can be reached at wne1454@hotmail.com or by contacting Dr. Michael Bevan, Department of Chemical Engineering, Texas A&M University, College Station, TX 77843-3122, or Dr. H.-J. Sue, Department of Mechanical Engineering, Texas A&M University, College Station, TX 77843-3123.